

An aerial photograph of a city, likely Rotterdam, with a color overlay representing urban atmosphere modeling. The overlay uses a color scale from green to red, indicating varying levels of atmospheric concentration or temperature. The city's dense urban core is predominantly red and orange, while surrounding areas and water bodies are green. The text is overlaid on the upper left portion of the map.

Advancements in modelling and mapping the urban atmosphere in a temperate maritime climate

Sytse Koopmans

Propositions

1. Exceedance maps to assess human thermal comfort are more representative than heat maps for a single day and are therefore preferred in heat legislation.
(this thesis)
2. The construction of high-rise buildings with preservation of greenery is less detrimental for heat stress than the extension of low-rise residential areas at the cost of greenery.
(this thesis)
3. Consultancy research should be a preferred option as training activity of the research school.
4. Climate mitigation cannot be accompanied by continued economic growth.
5. Publishing research computer code is required for a long-term utility of research by society.
6. Small research projects by the government are typically too short to be innovative.

Propositions belonging to the thesis, entitled

Advancements in modelling and mapping the urban atmosphere in a temperate maritime climate

Sytse Koopmans

Wageningen, 14 September 2021

Advancements in modelling and mapping the urban atmosphere in a temperate maritime climate

Sytse Koopmans

Thesis committee

Promotor

Prof. Dr A.A.M. Holtslag
Emeritus Professor of Meteorology
Wageningen University & Research

Co-promotor

Dr G.J. Steeneveld
Associate Professor, Meteorology and Air Quality Group
Wageningen University & Research

Other members

Prof. Dr A.K. Bregt, Wageningen University & Research
Prof. Dr R. Hamdi, KMI, Royal Meteorological Institute, Belgium
Prof. Dr J.E. Stoter, TU Delft
Dr G. van der Schrier, KNMI, Royal Netherlands Meteorological Institute, De Bilt

This research was conducted under the auspices of the Graduate School for Socio-Economic and Natural Sciences of the Environment (SENSE)

Advancements in modelling and mapping the urban atmosphere in a temperate maritime climate

Sytse Koopmans

Thesis

submitted in fulfilment of the requirements for the degree of doctor
at Wageningen University

by the authority of the Rector Magnificus,

Prof. Dr A.P.J Mol,

in the presence of the

Thesis Committee appointed by the Academic Board

to be defended in public

on Tuesday 14 September 2021

at 4 p.m. in the Aula.

Sytse Koopmans

Advancements in modelling and mapping the urban atmosphere in a temperate maritime climate

168 pages.

PhD thesis, Wageningen University, Wageningen, the Netherlands (2021)

With references, with summary in English

ISBN: 978-94-6395-933-9

DOI: <https://doi.org/10.18174/551416>

Table of contents

1. Introduction7

2. Effects of urbanization on a homogenized temperature record19

3. Fine-scale urban data assimilation and weather reanalysis for Amsterdam45

4. Urban planning strategies on heat stress for current and future climates71

5. Mapping thermal comfort on a 1-m scale with meteorological and geographical tools91

6. Perspectives125

7. Summary137

References141

Authorship Statement161

Dankwoord / Acknowledgements163

List of Publications165

Graduate school certificate166

Chapter 1

Introduction

Most people experience variations in daily thermal comfort in cities. Outside as a commuter, doing leisure activities or shopping, and inside their houses. Urban areas alter local weather and climate through the presence of buildings, impervious surfaces and other typical urban infrastructures. Although the observations and main weather forecasts are performed for rural areas, city specific weather gains attention especially during relatively hot periods. This thesis explicates urban climate as determined at different spatial scales for the temperate maritime climate of the Netherlands. As such different numerical tools and techniques are utilized, of which some of them are applied for future urban planning. This chapter introduces the concept of urban climate, points at physical transformation due to urbanisation and effects of climate change, and describes the different tools and models to study urban weather and climate.

1.1 Urban climate and health

Urban environments have distinguished properties that alters their meteorology (Oke, 1982). Often this results in higher urban temperatures and the difference of urban temperature with the rural surroundings is known as the Urban Heat Island (UHI) effect. When analysing long observational records, urban areas can be easily identified from their rural counterparts because of the regular occurrence of the UHI. Therefore, we can speak of an urban climate. In contrast to the Köppen climate classification, the urban climate is often described in relation to the reference rural climate, where Köppen absolutely defines thresholds of seasonal temperatures and precipitation for climate allocation (Köppen et al., 1936; Kottek et al., 2006). In this thesis the urban climate is studied in a temperate maritime climate of western Europe applied for case studies in the Netherlands. First this chapter summarizes the need for urban climate knowledge and research.

1.1.1 Health

Urban climate is important to study because elevated temperatures during heat waves often lead to thermal discomfort and heat stress with adverse effects on human health. In cities more people suffer from heat stress compared to the rural counterparts, which also results in higher mortality rates during heat waves (Clarke, 1971; Basu et al., 2002; Grize et al., 2005). The awareness and urgency increased in western Europe after the heat wave of 2003, where an excess mortality of over 80,000 people was found (Robine et al., 2008). Especially France was hit hard suffering by a long intense heat wave with 15,000 excess deaths in the period between August 1st and August 20th (Fouillet et al., 2006).

In the Netherlands, about 1400–2200 heat related deaths were reported in 2003 (Garssen et al., 2005), and another 1000 during the two heat waves of 2006 (Salcedo Rahola et al., 2009). More recently, in the June and July heat waves of 2019 observed record breaking maximum temperatures were observed in France, Belgium, UK, Germany and the Netherlands (Vautard et al., 2020). In France and the Netherlands, old national records were broken by a large margin of 2 °C (France went from 44.1 °C to 46.0 °C and the Netherlands from 38.6 °C to 40.7 °C). These events were given the dubious honour of the deadliest event globally in 2019 (CRED, 2020).

It appears that during heat events air pollution in the form of ozone and particulate matter (PM₁₀) is detrimental (Analitis et al., 2014), and usually air quality is poorer in urban regions. Ground-level ozone levels are typically raised during heat waves as it is formed under warm and sunny conditions by photochemical reactions (Fischer et al., 2004; Pyrgou et al., 2018). To some extent PM₁₀ is also raised in heat waves under calm high pressure dominated weather. It is still debated to what extent heat deaths are reinforced by air pollution/ozone. Some studies report the joint effect on mortality of heat stress and air pollution (Katsouyanni et al., 1993; Analitis et al., 2014), whereas Katsouyanni et al. (1993) even states that the combination effect seems to be larger than each factor acting alone. Other studies, on the other hand, do not find a clear effect of air pollution on mortality during heat waves (Hales et al., 2000; Zanobetti et al., 2008).

The high mortality rates have been observed mostly under the elderly and people with cardiovascular diseases during the severe heat waves of 2003 and 2006 (D'Ippoliti et al., 2010; Fouillet et al., 2006). Apart from mortality, heat exposure leads to a reduction of labour productivity (Pogačar et al., 2018). Also high night temperatures, preventing an adequate recovery from daytime heat and inducing sleep deprivation, reduces labour productivity (Bergan et al., 2015) and amplifies health effects (Fischer & Schär, 2010). There are positive correlations of productivity loss with the

proportion of time working outside (26–32%) and physical exertion (22–43%), based on a large survey under respondents from Australia (Zander et al., 2015). The smaller but significant productivity loss for office workers inside is probably mainly caused by sleep deprivation. Mortality and morbidity are not insurmountable. Adverse health effects of heat waves are largely preventable by preparing healthcare and early meteorological warning system for the general public (WHO, 2008; Martinez et al., 2019). Individual European countries anticipated by creating heat-health action plans on a national level. In France, the prevention measures reduced the number of heat-related deaths with ~68% in 2006 compared to the absence of those measures (Fouillet et al., 2008).

1.1.2 Processes

Which processes contribute to a UHI? To answer this question, we must look at the radiation and energy balance differences between the city and the surrounding rural area (Oke, 1982). The radiation balance of the surface reads as

$$Q^* = K^\downarrow * (1 - \alpha) + L^\downarrow - L^\uparrow \quad (1.1)$$

Q^* = net radiation (Wm^{-2})

K^\downarrow = incoming shortwave radiation (Wm^{-2})

α = albedo

L^\downarrow = incoming longwave radiation (Wm^{-2})

L^\uparrow = outgoing longwave radiation (Wm^{-2})

According Equation 1.1, urban areas absorb on average more downwelling shortwave radiation K^\downarrow from the sun (lower albedo) than a flat open rural environment (Oke, 1982). This has two causes. First, the nature of most urban materials, like asphalt, brick roads and brick walls and most types of roofing have a lower albedo than grass (Oke et al., 2017). Second, multiple reflections between buildings close together lowers the net amount reflected solar radiation (Kanda et al., 2007), reducing the “effective” albedo (Aida, 1982).

Another difference in the radiation balances between urban and rural areas lies in the upwelling longwave radiation. The latter is related to the typically higher urban surface temperature in the energy balance (Equation 1.2).

$$Q^* + AH = H + L_vE - G \quad (1.2)$$

Q^* = net radiation (Wm^{-2})

AH = anthropogenic heat flux (Wm^{-2})

H = sensible heat flux (Wm^{-2})

L_vE = latent heat flux (Wm^{-2})

G = storage heat flux (Wm^{-2})

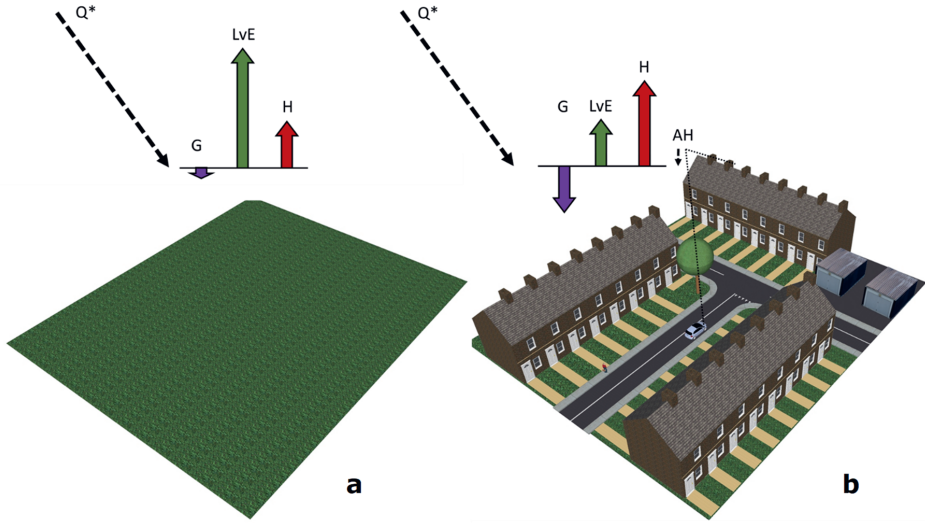


Figure 1.1: a) Typical energy balances for rural tile and b) a urban tile with low-rise buildings (compact low-rise) for a clear summer afternoon in a mid-latitude city (Moriwaki & Kanda, 2004; Oke et al., 2017). The length of the energy balance arrows represents their magnitude.

The energy budget terms are visualised in Figure 1.1 for a rural and urban surface. The net radiation is together with the anthropogenic heat emission the driver for the energy partitioning on the urban surface. Anthropogenic heat (AH) emissions comprise fossil fuel energy emissions from transit and building heating, as well as heat production from electricity and air conditioning, and the small source of human metabolism (Sailor and Lu, 2004). AH emissions are more significant in the UHI in the winter compared to the summer. In summer, the atmosphere is less susceptible for AH, because of a deeper boundary layer. Apart from highly densely populated areas (TMG, 2005), AH emissions remain below 20 Wm^{-2} in summer, based on estimates for Dutch cities as Utrecht and Amsterdam. To put this in perspective, average summer afternoon sensible heat fluxes observations range from $190\text{--}290 \text{ Wm}^{-2}$ for different mid-latitude cities (Oke et al., 2017). A larger part of the net radiation is used for the sensible heat flux at the expense of latent heat flux for urban areas. The latent heat flux is reduced, because of a limited fraction of vegetation and pervious surfaces, thus less evapotranspiration.

A part of the longwave radiation released from the ground surface is trapped between the buildings, resulting in higher surface temperatures. The fraction upwelling longwave radiation released to space strongly correlates with the fraction open sky from a ground surface and is called the sky-view factor (according to definition of view factors in Steyn (1980). An example for downtown Rotterdam is displayed in Figure 1.2. Though, daily urban–rural net radiation differences virtually disappear (Oke & McCaughey, 1983; Christen et al., 2013). This is mainly explained by an increased amount of upwelling longwave radiation, because of higher surface temperatures (Oke et al., 2017).



Figure 1.2: Example of a low sky-view factor (~ 0.35) due to tall buildings in the near surrounding. The fraction open sky is relatively low compared to an open rural environment. Courtesy to Bert Heusinkveld.

The typical energy balance and UHI vary strongly between different urban configurations relating to properties as impervious surface fraction, building height, sky-view factor and anthropogenic heat. The Local Climate Zone is a plain classification methodology which defines different types of built-up areas based on a zonal representation of these climatic properties (Stewart & Oke, 2012). One of them is compact low-rise, as shown in Figure 1.1b, and the ratio between the sensible heat flux and the latent heat flux (known as the Bowen ratio H/LvE) amounts to around 1.8. For more dense urban environments with very little natural fractions Bowen ratios can exceed 4 (Oke, 1982). Natural environments have Bowen ratios of around 0.4 (Oke, 1982) with a range between 0.1–1.5 depending on the availability of soil moisture or irrigation. A typical Bowen ratio of 0.4 in the Netherlands leads to a sensible heat flux which is $\sim 100 \text{ Wm}^{-2}$ lower as compared to an urban environment (Figure 1.1).

Another urban–rural difference is perceived in the storage heat flux. The urban fabric stores more heat at daytime because the urban fabric materials has generally a higher heat conductivity and heat capacity (Oke, 1988) than natural vegetation and the soil beneath. Moreover, the 3D structure of buildings increases the total surface area allowing for a larger heat storage total. It takes longer to release this surplus of stored heat at nighttime. This phenomenon triggers the typical high UHI in the evening and around midnight. Finally, large urban–rural differences in UHI arise in summer for clear sky weather combined with low wind speeds (higher wind speeds dissipate the heat formed by UHI more effectively) (Oke et al., 2017). The net radiation is largest at daytime allowing for the largest absolute differences in the energy balance terms.

To grasp the basic understanding of diurnal UHI differences it is necessary to explain differences in urban–rural boundary layers. Also at night, differences between city and rural environment are largest for clear sky weather conditions with relatively low wind speeds. In such cases the rural cooling rate is larger, and in the rural area a shallow stable boundary layer typically forms. The air volume to be cooled is small and therefore the temperature can quickly drop after sunset. For the urban area, this shallow stable boundary layer is not formed or at least to a lesser extent later in the night, due to the release of the storage heat (Oke, 1982; Theeuwes et al., 2015). Therefore

urban-air temperatures decrease gradually slower. Mostly because of these urban–rural boundary layer stability differences the nocturnal UHI can reach 4–10 °C in summer at clear-sky weather in mid-latitude climates (Oke, 1973; Eliasson, 1996; Heusinkveld et al., 2014). Shallow boundary layers are also more susceptible for anthropogenic heat emissions. Note that the relatively deep daytime boundary layer for both the urban and rural areas result in a relatively low temperature response even for large differences in the sensible heat fluxes.

1.2 Urbanisation and climate change

The urban climate is gaining increasing attention, which is reflected in a greater role in spatial planning of cities and more often cities are specifically mentioned in temperature forecasts during heat waves. Due to regional (Kysely, 2008) and global warming, the health impact of higher temperatures is further enhanced. In addition, a growing number of people are affected by higher temperatures due to a worldwide urbanization trend. From 2009 the urban population has increased from 50% to 55% in 2018. By 2050, this is expected to increase to 68% (United Nations, 2019). Note, that the overall growth in world population leads to an even larger absolute growth of population in urban areas. Urban land cover is projected to expand by 56–310% between 2000 and 2030 (IPCC, 2014b). A factor is the decrease in urban population density by a world-wide trend in smaller households.

Concerning the Netherlands, there is an urgent need for additional housing, with a challenging building assignment of 1 million houses in 2040 starting from 2010 (EIB, 2015). A large part of this assignment must be realised within the existing city borders. This densification of cities results in additional pressure on the thermal environment. In Chapter 4 the heat impact of densification is investigated for The Hague by evaluating different urban planning strategies. In addition, urbanization can impact temperature records of WMO-standard weather stations (WMO = World Meteorological Organization). Therefore, Chapter 2 evaluates the influence or urbanisation on the temperature record of the main weather station of the Netherlands (De Bilt).

Globally WMO standard stations are disproportional sited near populated areas, which have been extended in the last century. On average this urbanization effect for WMO land stations in the global HadCRUT climate dataset is small compared to the climate trend, viz. 0.06 °C per century (one sided 1 σ uncertainty) (Jones et al., 1990; Folland et al., 2001). This urbanization uncertainty further decreases to 0.02 °C per century in the global temperature trend, blended with zero UHI effect for oceans (Trenberth et al., 2007). Local trends for stations facing rapid urban expansion in the past were much higher from 0.2 °C up to 0.54 °C per decade in Beijing (Yan et al., 2010) and 0.4 °C increase between 1949 and 1980 for airport Heathrow at London (Jones & Lister, 2009). Furthermore, Lee et al. (2013) showed statistically significant higher trends in minimum temperatures for South-Korean stations near cities with high populations, and urbanization accounts for more than 30% of the observed temperature trend at the end of the 20th century for all national stations in Northern China (Ren et al., 2008).

Worldwide land temperatures rose 1.53 °C between the pre-industrial period 1850–1900, and 2006–2015 period (climate trend of 1.17 °C per century) (Shukla et al., 2019) and this is ~50% larger than the combined land–ocean temperature rise (Stocker et al., 2013). Land surfaces including urban areas react faster on the CO₂ forcing than oceans, the latter having larger thermal inertia. By 2050, the temperature is projected to increase to just below 2 °C to 4 °C compared to pre-industrial period, depending on mitigation targets and variability between the used climate models

(IPCC, 2014b). Specifically for warm summer extremes, there are signals that days with high temperatures increase faster or become more frequent than based on the climate trend alone. In central Europe (including France, Belgium and southeastern half of the Netherlands), maximum temperature extremes warmed about 50% more than the corresponding summer mean temperatures (Lorenz et al., 2019). Also warm summer night extremes ($> 95^{\text{th}}$ percentiles of minimum temperatures) increased consistently with the maximum temperature extremes.

Other parts of Europe, including the Mediterranean land surfaces do not experience such amplification of observed heat extremes compared to the rise of summer mean temperatures, and this is neither a global phenomenon (Choi et al., 2009; Lee et al., 2013). The increasing heat extremes in central Europe are related to a change in circulation patterns. Blocking central European highs and southerly circulations, favourable for heat waves, are more frequent and persistent (Kysely, 2008). This is accompanied by longer observed sun durations (Tang et al., 2012) and increasing droughts, both of which promote high daily temperatures (Douville et al., 2016). Furthermore, the rapid decline of spring Arctic sea ice and snow cover in high-latitudes is conducive to more persisting blocking weather favouring heat wave events in mid-latitudes (Francis & Wu, 2020).

The shift toward more heat extremes is clearly visible for weather stations in the Netherlands as demonstrated in the histograms of Figure 1.3. These histograms present the distribution of daily average summer temperatures in rural areas for the current climate (1991–2020) and a climate period in the past (1951–1980). The current climate distribution is more flattened, meaning that diurnal temperatures around the median occurs less frequent. Instead, the current climate has a larger right tail towards more heat extremes.

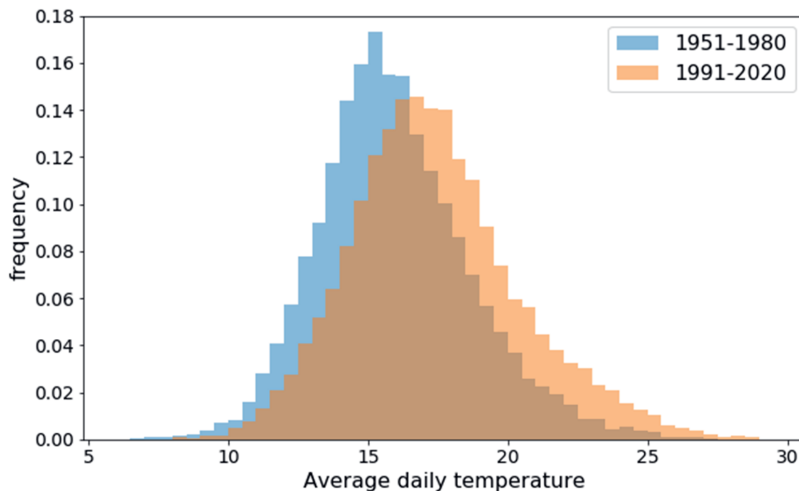


Figure 1.3: Histogram of average daily temperatures in the summer period (June–August) for five Dutch weather stations (De Bilt, Maastricht, Eelde, Den Helder, Vlissingen) from the KNMI (Royal Netherlands Meteorological Institute). The recent 30-year climate period (1991–2020) is compared with an older climate period (1951–1980).

1.3 Urban climate research tools

The urban climate can be studied with various meteorological models that serve different spatial scales and are characterised by contrasting degree of parameterization. The three types of models are presented in Figure 1.4, accompanied with the main key points.

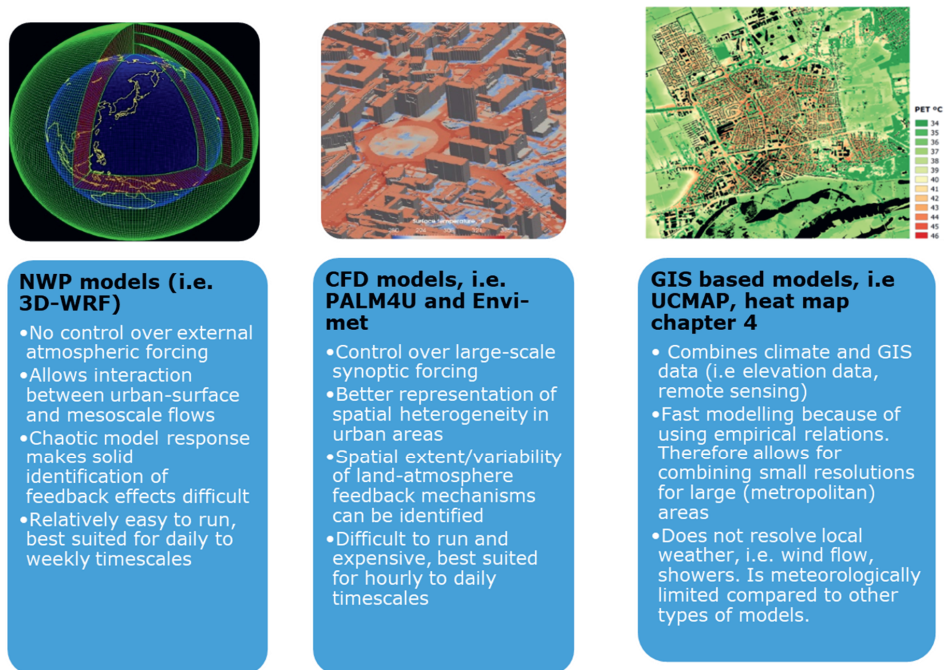


Figure 1.4: Schematic of three types of models with which can be used for urban climate modelling.

First, we discuss numerical weather prediction (NWP) models as research instruments. NWP models can be described as a mathematical model solving equations of motion and uses discretized time steps and grid points to calculate a weather state from a starting point to different times ahead. The Weather Research and Forecasting model (WRF) (Skamarock et al., 2008) is an example of a NWP model, which has been used in Chapter 2 and 3. WRF is a regional atmospheric model, and can be used either for regional forecasts, hindcasts (Chapter 2) and reanalyses (Chapter 3), including data assimilation. WRF is controlled by input of a global weather forecast model, like ECMWF, GFS or global reanalysis data like ERA-Interim (Dee et al., 2011) or ERA5 (Hersbach et al., 2020). A strength of WRF is the option of nested domains. This enables to bridge a coarse spatial resolution of the global weather model which is used as large synoptic forcing, with a resolution of ~ 70 km to a scale of 100–500 m in the inner domain. The inner domains often operate in the so called “grey zone” (between 200 m and 10 km) where turbulence and convective transport can be partially resolved, while parameterizations are still needed (Honnert et al., 2020). The transition between nested domains with different degree of parameterization, may lead to uncertainties in cloudiness and precipitation (Field et al., 2017; Kramer et al., 2020)

At higher resolutions down to 1 m, Computational Fluid Dynamics (CFD) models apply as research tool in the urban environment. One of them are Large-Eddy Simulation (LES) models. Turbulence is resolved to a great extent and they allow for fine subgrid turbulence parameterization

(Deardorff, 1980; Zhou et al., 2019). To describe turbulent flows, LES uses a reduced-order description to remain computationally attractive (Pope, 2010). In an urban environment, wind flows around building obstacles can be modelled as well as a reliable dispersion of contaminants dispersion (Letzel et al., 2008). An example of such a model is PALM-4U (Maronga et al., 2020). Applications of LES in urban modelling is relatively new and has been conducted much less than RANS (Reynolds Averaged Navier-Stokes) models (Toparlar et al., 2017). RANS models are a different type of CFD models on this scale based on the Navier-Stokes budget equations for heat, moisture and momentum, such as ENVI-met (Bruse & Fleer, 1998; Crank et al., 2018). Also, such models are able to calculate complex wind flows around buildings and trees but at lower computational cost than LES.

The difference of RANS with LES, is that turbulence at a smaller scale than the grid size is not resolved but parameterized (Fröhlich & von Terzi, 2008). Therefore, RANS model results fluctuate less on short time scales, while these fluctuations are part of the chaotic behaviour of turbulence. In practise, this gives less performance in the wake of buildings (Mirzaei & Haghighat, 2010), where small-scale turbulence is relatively important due to low horizontal wind speeds. Both for CFD and LES models large synoptic forcings are typically prescribed instead of fed by a global weather model. This type of models is useful for urban planners to reshape neighbourhoods or small districts. Larger areas are computationally too expensive. Besides, this type of models can help to further unravel the mechanisms of the urban physics. This especially holds for LES models which are least parameterized and therefore have less assumptions

A different fast approach to calculate fine scale urban thermal comfort for large areas is the use of empirical meteorological - and GIS methods, usually presented in a quantitative urban heat map or qualitative urban climate map. It avoids numerical simulations which needs costly small time steps. The empirical relations are ideally based on in situ urban observations, wind tunnel experiments or LES to find typical wind profiles in the urban canopy. Because of the statistical methods, short and local weather fluctuations are filtered out and this approach serves well for urban climate maps or urban heat maps representing a typical warm day or climatology. An example is the use of a diagnostic equation to calculate maximum diurnal UHI (Theeuwes et al., 2017), which is based on routine weather observations on a rural reference station and urban density and sky-view factor.

In Chapter 4, we present 95th percentile UHI maps for the Hague with this diagnostic equation. In Chapter 5 heat maps of the Physical Equivalent Temperature are calculated, incorporating urban wind and radiation differences on 1-m resolution. Concerning other urban climate maps, neighbourhood observations and numerical model output were used to define Local Climate Zones. Local Climate Zones have a characteristic temperature regime based on common urban features that horizontally span 100 meters to several kilometres (Stewart & Oke, 2012). Other urban climate maps based on a combined modelling approach of geographical and meteorological observations include urban climatic maps for Hong Kong and Arnhem (the Netherlands) (Ng, 2012; Ren et al., 2012) and the Thermal Environment Map of Tokyo (Ren et al., 2011). A downside is that these models are meteorologically limited compared to the other described numerical models. However, the fast calculations enable to create maps covering large (metropolitan) areas, maintaining a relative high resolution. Therefore, this approach suits many (large scale) urban planning purposes.

1.4 Thesis outline with research questions

The combined effects of urbanization and climate change urges to understand the urban atmosphere and create smart solutions to ameliorate urban heat effects. For many cities around the world, UHIs have been modelled and measured (Chapman et al., 2017). Insights in urban weather from these studies give already a profound understanding of the urban climate. Despite the progress, still important questions remain open and further qualitative and quantitative modelling improvements can be made. Hence, in this thesis we formulate five scientific research questions that will be addressed in the thesis.

1.4.1 Effects of urbanization on a homogenized temperature record

Above we reported that the global effect of urbanization on the climate records is very small. However, in densely populated areas this effect can be much higher, as mentioned for mid-latitude climates as North-China and South Korea. For the populous country of the Netherlands it also seemed interesting to investigate this effect. We noticed that the majority of stations are not located in the vicinity of a substantial urban area. However the main station De Bilt, with the longest historical record, is situated close to expanding urban areas (especially Utrecht ~360,000 inhabitants). By conducting a model study, we aim to investigate the role of urbanization on the climate record. The corresponding research question posed in Chapter 2 is as follows:

Research question 1:

What is the influence of urbanization on the climate record of a nearby rural weather station?

1.4.2 Fine-scale urban data assimilation and weather reanalysis for Amsterdam

Until now numerical simulations of the urban environment do not have the temporal length to describe a full climatology. Alternatively, also urban observations miss this temporal scale and lacks the spatial coverage to explain the spatial variability in an urban climate. As computational power increases and NWP models progress towards finer spatiotemporal scales, we performed a 15-year urban hindcast on a spatial resolution of 167 m for the city of Amsterdam. For such long periods it is essential that models are fed with interim observations with data assimilation techniques. In the atmospheric sciences this is called a reanalysis.

A reanalysis is the best-known state of the weather at any moment by merging model information with local observations. The best-known examples include ERA-interim and successor ERA5 from the ECMWF (Berrisford et al., 2011). Applications of these reanalysis datasets range from renewable energy, e.g. siting of favourable areas for wind farms and solar power plants (Boilley & Wald, 2015; Lorenz & Barstad, 2016), and climate research in general (Boilley & Wald, 2015). However, these reanalysis products miss the spatiotemporal scale which is necessary for studying the climate of urban areas. Therefore, we pose the following research question in Chapter 3 about an urban reanalysis dataset:

Research question 2:

How can we develop modelling techniques to best create and validate an urban reanalysis dataset?

1.4.3 Urban planning strategies on heat stress for current and future climates

In the Netherlands, there is a societal request for heat resilient solutions for a redesign of city districts. The main concern is an urgent need for additional housing of 1 million houses, which has to be realized by 2040. Although this study focuses on the Netherlands (The Hague as test case), a large part of the housing has to be built within the urban borders. Hence, the question to be answered in Chapter 4 is as follows:

Research question 3:

What is the best approach to densify an urban environment with least effects on urban heat?

For this task a straightforward data-driven approach will be proposed. Geo-information as population density, sky-view factor and vegetation fraction will be linked to UHIs. Different urban planning strategies will be evaluated on the impact on UHI. These urban planning strategies differ in constructing low- and mid-rise buildings versus high-rise buildings on green spaces at different places. As the implementation of additional housing reshapes the cities for a longer time, a climate outlook is also given for different climate scenarios by 2050.

1.4.4 Mapping thermal comfort on 1-m scale with meteorological and geographical tools

In Chapter 4 a next step is made by developing urban heat map, where a thermal comfort index is applied which indicates how people experience heat. Factors as wind, humidity and radiation together with air temperature determine how efficient humans can release heat (mainly by transpiration for hot days), and that is included in a thermal comfort index. We develop a heat map of this thermal comfort index on 1-m resolution based on a variety of geographical and meteorological tools. The underlying variables such as air temperature, wind, humidity and radiation have urban–rural differences and also vary within the urban environment. To achieve this, established verified methods are used, e.g. wind reduction for the city (MacDonald, 2000), and methods are elaborated e.g. the diagnostic equation for UHI (Theeuwes et al., 2017) for hourly values. Accordingly, we pose the following research questions in Chapter 5:

Research question 4:

What meteorological and geographical inputs are needed to create a high-resolution urban heat map for city planning purposes and climate stress tests?

Research question 5:

Is a heat map based on empirical meteorological and geographical relations sufficiently accurate to describe the urban climate?

Chapter 2

Effects of urbanization on a homogenized temperature record

Abstract

Many cities have expanded during the 20th century, and consequently some weather stations are currently located closer to cities than before. Due to the urban heat island (UHI) effect, those weather stations may show a positive bias in their 2-m temperature record. In this study we estimate the impact of urbanization on the temperature record of WMO station De Bilt (the Netherlands). This station has a long historical record, but the nearby city of Utrecht and its suburbs expanded during the 20th century. The temperature rise due to urbanization is estimated by conducting representative mesoscale model simulations for the land use situation for the years 1900 and 2000. This is performed for 14 different episodes of a week, each representing a typical large-scale flow regime (Grosswettertypes) in both the winter and the summer season. Frequency distributions of these flow regimes are used to estimate an average temperature rise. We find that the model results with two rather different atmospheric boundary-layer schemes, robustly indicate that the urbanization during the 20th century has resulted in a temperature rise of 0.22 ± 0.06 K. This is more than a factor of two higher than a previously estimated temperature trend by using observed temperature records of stations close to De Bilt.

This chapter is based on:

Koopmans, S., Theeuwes, N. E., Steeneveld, G. J., & Holtslag, A. A. M. (2015). Modelling the influence of urbanization on the 20th century temperature record of weather station De Bilt (The Netherlands). *International Journal of Climatology*, **35**(8), 1732-1748. doi:<https://doi.org/10.1002/joc.4087>

2.1. Introduction

Many observational studies of climate change report a substantial rise of the globally averaged 2-m temperature in the last century (e.g. Jones et al., 1986a,b; Hansen & Lebedeff, 1987; Brohan et al., 2006; Smith et al., 2008). Based on this research, the IPCC documented a global combined land and ocean temperature increase of ~ 0.89 °C over the period 1901–2012 (Stocker et al., 2013). Observational temperature records close to urban areas, however, may be influenced by nearby city expansion and consequent heat advection from the city towards the observing stations (Oke, 1982; Karl et al., 1988; Schaefer and Domroes 2009; Fall et al., 2010). Although on the global scale, urbanization contributes only for 0.02 K to the global temperature trend in the 20th century (Jones et al., 1990; Trenberth et al., 2007), the local trend for urbanized areas might be substantially higher, i.e. ~ 0.3 K (Karl et al., 1988; Balling et al., 1998; Kalnay & Cai, 2003; Fujibe et al., 2007).

With a numerical study Adachi et al. (2012) showed for Tokyo that urbanization leads to higher temperatures on top of the enhanced greenhouse effect. Van der Schrier et al. (2013) report urbanization as one of the key aspects of which its contribution to the northwest European temperature rise is not completely understood. Urbanization may lead to elevated temperatures in the surroundings due to heat advection from the city (Oke, 1982), and can affect the temperature of a nearby weather station in two ways. Firstly, the urban heat island (UHI) intensity (in the urban boundary layer) may change when the urban thermal properties, the urban vegetation fraction, or population density changes for a constant city area (Oke, 1973; Sailor and Lu, 2004; Steeneveld et al., 2011a). Secondly, the influence of the city increases when the city area expands and the distance between the weather station and city margin decreases (Oke, 1982).

In brief, the elevated urban temperatures occur because of the modified surface energy budget compared to the countryside. Typically, the urban street canyon structure triggers an efficient entrapment of solar radiation and thus provides a rather small albedo (Kanda et al., 2007). Overall, up to 30% of the incoming solar radiation is stored during daytime and is subsequently released at night (Oke, 1982). Also, street canyons limit the sky view for outgoing longwave radiation. Moreover, the rather high fraction of impervious surface initiates a relatively high Bowen ratio (ratio of surface sensible and surface latent heat flux). Anthropogenic heat production is mainly important in winter (Sailor and Lu, 2004). Overall, the largest and most intense UHI occurs in the evening, because of the large heat capacity of the urban fabric, and the reduced turbulent diffusion on the countryside.

Focusing on the Netherlands, the surroundings of the weather station in De Bilt (52°06'N, 5°11'E) have been gradually urbanized during the previous century. Weather station De Bilt's nearest city, Utrecht, expanded by a factor of 5 between 1899 and 2003, and accommodated 44% of the current inhabitants in 1899 (Brandsma et al., 2003, henceforth B03). In the 20th century, the screen level temperature at weather station De Bilt has risen ~ 1.3 K, van der Schrier et al., 2011), of which 0.2 K is due to modifications in the large-scale flow pattern (van Oldenborgh and van Ulden, 2003). In addition, spatially averaged temperature series such as the Central Netherlands Temperature series (CNT), consisting of time series from six Dutch weather stations, also show a significant temperature increase. However, the homogeneous temperature trend (without urban contamination correction) in De Bilt is 12% higher than the CNT trend over 1906–2008 (van Ulden et al., 2009), and is so far unexplained (van Oldenborgh et al., 2009).

The observations at weather station De Bilt have a high scientific value for climate research, because it covers the longest homogenized record of historical data series of the Netherlands since

1901 (Visser, 2005; Brandsma, 2011). Part of the De Bilt time series also covers the Zwanenburg/De Bilt series, which already started in 1706. Weather station De Bilt (also abbreviated as DB) is also known as the main station in the Netherlands, in particular for the general public. Its observations are used to compose monthly and yearly evaluations, which are often adopted by the media. Hence, it is important to estimate the contribution of urbanization on this particular temperature record.

So far, the impact of urbanization on DB has solely been studied by means of observational campaigns by bike traverses, and comparisons of observed temperature trends at weather station De Bilt with other nearby rural weather stations, i.e. Soesterberg ($52^{\circ}08'N$, $5^{\circ}17'E$, 7 km to the northeast of DB) and Herwijnen ($51^{\circ}51'N$, $5^{\circ}09'E$, 31 km to the south of DB). The Urbanization Induced Temperature Effect (UITE) is then determined by comparing temperatures with a rural and urbanized upwind footprint. The observational study by B03 found that mainly the city of Utrecht and the town of De Bilt are responsible for the UITE of DB. Another observational campaign by bike traverses found a nocturnal temperature difference between Utrecht and DB of 0.5 K during westerly winds (Brandsma, 2010). However, the intercomparison study between DB and nearby weather stations revealed that the yearly averaged UITE is of minor importance, i.e. 0.10 K (B03). This UITE has been adopted in homogenizing the DB temperature series.

In this study, we extend the earlier studies by estimating the UITE by a high-resolution mesoscale modelling approach, which was suggested as future work by B03, since computational resources for such a modelling approach were limited in the early 2000s. In a model approach one can also explicitly account for a variety in soil types, topography and surface roughness in simulations that are used to derive the UITE (van Weverberg et al., 2008, henceforth VW08). In addition, modelling allows us to reconstruct the effect of urbanization where field observations are lacking. The current mesoscale modelling was inspired by VW08, who quantified the UITE for the weather station Uccle, located close to Brussels (Belgium). VW08 ran the Advanced Regional Prediction System (ARPS) model for four different circulation types for the land use in 1833 and 2000. Depending on wind direction, they found a 0.77–1.13 K temperature rise due to the urbanization, while the observed temperature increase from 1867 to 2002 amounts to 1.4 K (Yan et al., 2002). As such, a substantial part of the recorded temperature rise could be explained by urbanization in the surroundings. In order to draw more statistically sound conclusions, we estimate the UITE with simulations of the seven dominant circulation types both for the summer and winter season (14 periods in total).

The paper is organized as follows: Section 2.2 presents the selection of episodes to perform our analysis, the model set-up including specifications of the current and historic land use. Section 2.3 describes the modelled results for the urban heat island characteristics. Section 2.4 describes the resulting Urbanization Induced Temperature Effect, discusses the diurnal evolution and the wind direction dependence and how the UITE compares to the observational analysis of B03, and we draw conclusions in Section 2.5.

2.2 Methodology

2.2.1 Case selection

Using the advanced research Weather Research and Forecast mesoscale model (WRF-version 3.1.1; Skamarock et al., 2008), two land use scenarios are applied; one run with the land use for the year 2000 and a run with the land use for the year ~1900, further labelled as R2000 and R1900 respectively. The difference between these two runs estimates the UITE, since the R2000 has a larger urban area than the historical run (see Section 2.2.4 for a description of the land use and land cover). In order to cover a wide and representative range of weather situations, this strategy is repeated for seven one-week lasting episodes in summer, and seven one-week lasting episodes in winter during 1999-2005. Each of the seven cases represents a particular large-scale circulation type. The summer half year comprises the period April–September, and the winter half year comprises the period October–March.

Each episode represents a specific large-scale circulation type at 500 hPa defined by Grosswettertypes (GWT, Werner and Gerstengarbe, 2010). In total, our simulations cover 7 GWT's (Table 2.1). Four of the choices of weather periods are inspired by VW08. The other periods are selected based on the distinctness of the 500 hPa flow according the GWT descriptions. Together all simulated episodes explain the vast majority of the flow directions, i.e. 97% for winter and 96.3% for the summer. Consequently, the annual mean UITE of weather station De Bilt can be quantified, based on the known frequencies of occurrence of these circulation types (Table 2.1).

Table 2.1: A description of the seven main atmospheric circulation (“Grosswetter”) types influencing the Netherlands, divided per season. The percentage indicates the frequency of the Grosswettertype in that particular season.

Gross-wetter type	Description	Winter season	Summer season
W	Westerly circulation Predominantly south-westerly winds, mostly cyclonic. In the winter period this is accompanied by strong winds, above-normal temperatures and cloudy and rainy weather. In the summer period the Netherlands is often situated in polar air masses and fronts and troughs pass by. This results in cool and rainy weather.	1-7 December 1999 28.8 %	28 June- 5 July 2004 25.0%
SW	South-westerly circulation The winter period is characterized with exceptionally high temperatures and southerly winds. The summer period is characterized with above-normal temperatures, south-westerly winds and almost all days have periods of rain.	1-7 December 2000 6.3%	27 April- 4 May 2003 3.8%
NW	North-westerly circulation The winter period shows above normal temperatures, especially at night and is relatively cloudy. In the summer a deep low at the North Atlantic brings cool weather. This low is cut off halfway during the period in the Baltic resulting in a strong cyclonic north-westerly winds and lots of rain	16-23 January 2000 7.9%	5-12 September 2001 9.0%
HM	Calm weather High pressure over central parts of Europe, coincides with calm weather and light continental winds for the Netherlands. The winter period has light variable winds between northeast and south and there is a strong temperature inversion with below normal temperatures at the surface. The period is very dull and no rain occurs. The summer period has variable light winds with a slight preference for the NE direction. All days show above normal temperatures and are relatively sunny with little developing cumulus clouds in afternoon.	7-14 December 2004 17.2%	23-30 July 2001 16.0%
N	North circulation In the winter period a large north-south oriented trough is located from Scandinavia towards the Balkan. In the last days a new low pressure enters the North Sea area with a deep northerly flow at the west side. Relatively cold upper air temperatures together with maritime north(westerly) winds results in a well-mixed atmosphere and normal temperatures. The summer period shows well below normal temperatures, which is related to the cold air advection from the north and maritime influences of the north-westerly winds.	14-21 February 2005 13.4%	24 June- 1 July 2000 18.4%
E	Easterly circulation In the winter a large high-pressure system brings cold continental air towards the Netherlands. Average temperatures are below 0 °C, which is well below normal. Furthermore, this period has clear skies and is completely dry. The summer period shows a deep easterly flow from Russia. This means for April slightly above normal temperatures and April also shows clear skies and no rain.	14-21 February 2003 15.4%	4-11 April 2002 15.5%
S	Southerly circulation In the winter period warm air from the south is transported in the upper air and the ground surface. Temperatures are exceptionally high and it is dry and relatively sunny. In the summer period a trough moves from France to Denmark. Aloft there is a southerly flow over the Netherlands, while the surface wind is predominantly north-east.	14-21 October 2000 8.0%	1-8 May 2001 8.6%

2.2.2 Model set-up

WRF is a non-hydrostatic mesoscale model and has the capability to translate large-scale circulations into micro-scale transport and dispersion which is needed for smaller grid scales (Chen et al. 2010). This is realized by four two-way nested domains, with gradually increasing resolutions towards the innermost domain (Table 2.2 and Figure 2.1). Our model simulations utilize initial and boundary (6 hourly) conditions ($0.5^\circ \times 0.5^\circ$, at pressure levels) from the European Centre for Medium-Range Weather Forecasts (ECMWF) operational analysis. For July 2001 (HM) an exception is made by running the model one-way nested due to technical reasons. For the transition of the domains, relaxation zones of 4 grid cells are used.

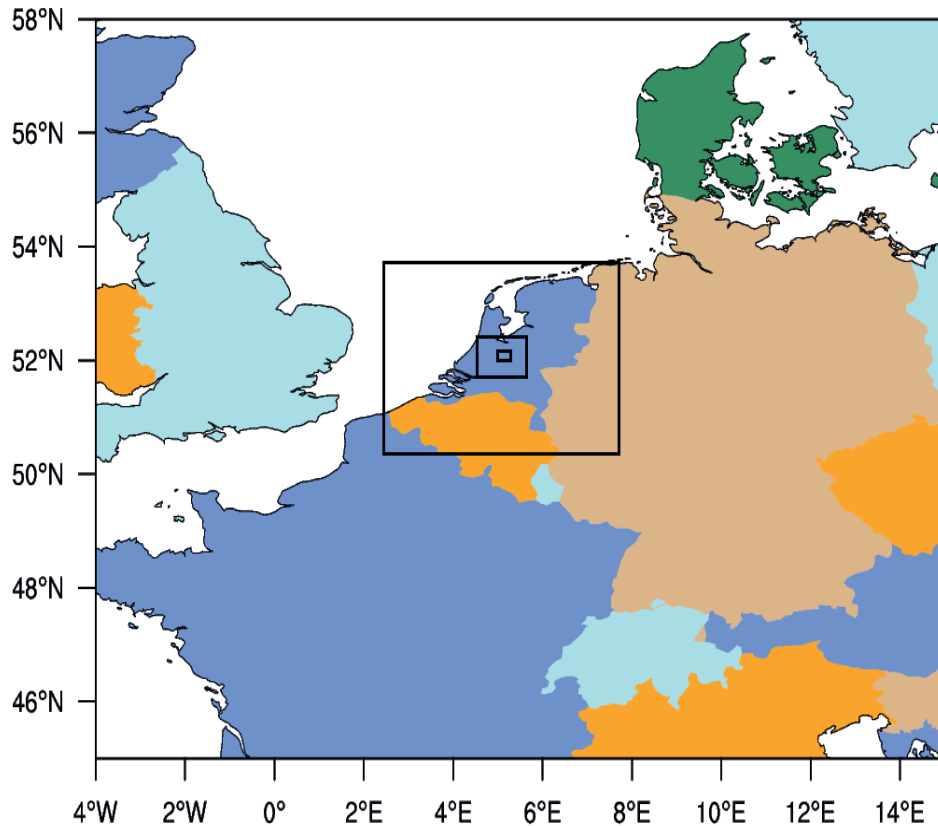


Figure 2.1: Overview of the set-up of the 4 domains. De Bilt is in the centre of the smallest domain. Domain 4 is the smallest domain.

Table 2.2: Configuration of four domains used in the WRF model.

	Resolution (km)	Number of grid cells
Domain 1	62.5	24 * 24
Domain 2	12.5	30 * 30
Domain 3	2.5	30 * 30
Domain 4	0.5	40 * 40

For the innermost domain a resolution of 500 m was used. Since Utrecht is a relatively small city, a high horizontal model resolution is required. The other domains use a coarser resolution and form a bridge to the ECMWF boundary conditions. One day of spin up was applied in all model runs. WRF utilizes 35 vertical sigma levels analogous to VW08, with the first model level at 15 m.

Considering the required domain size and the number of grid cells with each domain, it is important to remark that Warner et al. (1997), Leduc and Laprise (2009) and Leduc et al. (2011) performed limited area modelling experiments for varying domain size. They found that for a domain size that was too small, relatively small-scale meteorological phenomena were underrepresented. Although their studies showed that this effect is most pronounced for precipitation and is most evident in the middle troposphere, it is important to evaluate whether this also plays a role in our case. Hence, we have re-run the winter W case (1-7 December, 1999) with a larger innermost domain, i.e. with 61 x 61 grid cells, instead of 41 x 41 grid cells, and compared the UITE from both runs. The UITE of the two simulations only differs 0.013 K, which is far below the uncertainty estimate of our final UITE estimate (see below). This experiment illustrates that the runs with the 41 x 41 grid cells are sufficient for the performed analysis.

The impact of urbanization is typically an atmospheric boundary-layer (ABL) phenomenon, and the selected ABL parameterization is of key importance (e.g. Stensrud, 2009). However, a priori it is not clear which of the available ABL schemes performs best. Therefore, the UITE has been estimated using two different schemes, namely MRF (Troen & Mahrt, 1986; Holtslag & Boville, 1993) and MYJ (Janjić, 2001). MYJ has a local turbulent kinetic energy closure scheme based on local vertical gradients of the governing variables. MRF employs a non-local first order closure scheme which also accounts for counter gradient transport by large eddies (Holtslag et al., 1995; Shin & Hong, 2011). Earlier experiments revealed that local schemes such as MYJ represent the stable ABL better than non-local schemes (Steenneveld et al., 2008). In particular, MRF experiences too much mixing at the cold surface layer at night. On the other hand, MYJ underestimates the mixing during daytime, and often produces too moist and too cold ABLs (Holtslag et al., 1995; Pino et al., 2004). MRF typically produces a drier surface layer and at this point better represents the urban climate than MYJ (Pino et al., 2004). Hence, both schemes will be employed and evaluated and the corresponding UITE is discussed. This evaluation is based on the 2-m temperature, 2-m specific humidity, 10-m wind speed and global radiation at the surface (Table 2.5). Important differences between models are explained and offer the possibility to define a measure of uncertainty of the estimated UITE.

The choice for the MRF scheme instead of the more recently developed YSU scheme (Hong et al., 2006) came forward due to a recently discovered bug (in 2014 at the time of publication) in the YSU scheme as implemented in WRF version 3 (Richardson et al., 2013; Sterk et al., 2013). The deficiency affects the connection between the surface layer and boundary-layer stability, particularly at night, and is as such a key to our research question. Therefore, MRF was selected as the non-local boundary-layer scheme in this study.

Table 2.3: Used specifications of the Single Layer Urban Canopy model developed by Kusaka et al. (2001).

Roof level	7.5 m
Roof width	9.4 m
Road width	9.4 m
Heat capacity of roof	$1.0 \times 10^6 \text{ Jm}^{-3}\text{K}^{-1}$
Fraction Urban	0.9
Heat capacity of building wall	$1.0 \times 10^6 \text{ Jm}^{-3}\text{K}^{-1}$
Heat capacity of ground (road)	$1.4 \times 10^6 \text{ Jm}^{-3}\text{K}^{-1}$
Thermal conductivity of roof	$0.67 \text{ Wm}^{-1}\text{K}^{-1}$
Thermal conductivity of building wall	$0.67 \text{ Wm}^{-1}\text{K}^{-1}$
Thermal conductivity of ground (road)	$0.4004 \text{ Wm}^{-1}\text{K}^{-1}$
Surface albedo of roof	0.2
Surface albedo of ground (road)	0.2
Surface emissivity of roof	0.9
Surface emissivity of ground (road)	0.95
Roughness length for momentum, over roof	0.01 m
Roughness length form momentum over building wall	0.0001 m
Roughness length for momentum, over ground (road)	0.01 m
Hourly weights of maximum anthropogenic heat flux, from 0 -> 23 UTC.	0.16; 0.13; 0.08; 0.07; 0.08; 0.26; 0.67; 0.99; 0.89; 0.79; 0.74; 0.73; 0.75; 0.76; 0.82; 0.90; 1.00; 0.95; 0.68; 0.61; 0.53; 0.35; 0.21; 0.18
Monthly values of daily maximum anthropogenic heat flux (Wm^{-2}), from Jan -> Dec.	44.7; 41.1; 38.2; 31.1; 26.3; 22.9; 22.5; 22.1; 23.9; 30.2; 36.2; 42.8

WRF has furthermore been equipped with the NOAH land surface model (Ek et al., 2003), with the Monin-Obukhov similarity surface layer and for MYJ with an adapted Monin-Obukhov scheme (Janjić, 1996). Since we study the role of urbanization on the temperature record, the urban surface energy balance should be well represented. The special characteristics of the city surface require specific treatment in terms of modelling. Therefore, we use the single-layer urban canopy model in WRF as developed by Kusaka et al. (2001) and Chen et al. (2010), which has been validated for Beijing (Miao et al., 2008), Osaka (Shresta et al., 2009), Phoenix (Grossman-Clarke, 2009),

and participated in the PILPS-urban model intercomparison (Grimmond et al., 2011). This model consists of parallel infinite street canyons, and the energy balance is calculated for each of the three facades, i.e. wall, street and roof surfaces. In addition, the anthropogenic heat (AH) source strength is prescribed (see Section 2.2.5). Note that in the Netherlands, the contribution by air conditioning in summertime is so far rather small. For the hourly fractions of the AH, the default settings are chosen as described in Chen et al. (2010). Finally, the grid cells with a dominant urban land use utilized 10% grass vegetation cover as a sub-tile. See Table 2.3 for the complete overview with settings for the urban canopy model.

For completeness, our WRF configuration utilizes the Grell (1991) cumulus parameterization in the two outermost domains. The resolution of the smaller domains is sufficiently fine to assume that convection is resolved explicitly (Skamarock et al., 2008). Third order Runge-Kutta time integration is used, with a time step of 9 s in the innermost domain. Finally, the RRTM radiation scheme and the WSM3 microphysics schemes have been selected.

2.2.3 Statistical analysis

The model validation has been performed on four frequently occurring flow regimes, as indicated by VW08. These are the westerly circulation (W) and south-westerly circulation (SW) in the winter, and the southerly circulation (S) and calm weather episode (HM) in the summer. The evaluation of the selected ABL schemes is performed based on the bias, the root mean square error ($RMSE$), the systematic root mean square error ($RMSE_s$) and Pearson correlation, between hourly observations and hourly simulation output for weather station DB. For a good model the $RMSE_s$ vanishes (Willmott, 1982). The remaining unsystematic root mean square error ($RMSE_u$) is a measure of random model errors. The variables are related as follows:

$$RMSE^2 = RMSE_s^2 + RMSE_u^2 \quad (2.1)$$

The significance of temperature differences between the R2000 and R1900 will be tested with a Student t -test and the non-parametric Wilcoxon signed χ -test. Time series are considered. Therefore, we account for autocorrelation, which is a measure of similarity between consecutive model outputs as a function of the time lag. Since statistics are estimated on an hourly basis, the autocorrelation with 1 h lag is considered. The variance increases with the rate of autocorrelation according to

$$var = \frac{s^2}{n} \left(\frac{1+\rho}{1-\rho} \right) \quad (2.2)$$

where ρ is the autocorrelation, s the standard deviation, and n is the sample size (Wilks, 2006). The autocorrelation, on average amounts to 0.61 for a 1 h time lag, so that the variance increases with a factor 4–5 and the correction is therefore substantial.

2.2.4 Land Use

In order to model the atmospheric state over and around Utrecht, the land use should be represented correctly. The United States Geological Survey (USGS) land use map has been used for the three outermost domains. For the innermost domain the Coordinated Information on the European Environment (CORINE) land use map (Commission of the European Communities, 1995), last modified in 2007, has been used and reclassified such that it corresponds to the land use classification of the USGS. The CORINE land use map is required in model domain 4, because CORINE has, in contrast to USGS, a sufficiently high resolution. This is respectively 250 m for

CORINE and 900 meter for USGS. Note that VW08 also utilized CORINE. The basis of the constructed historical land use map is the topographic map of the province Utrecht, produced around 1905 (Wieberdink, 1989; Knol et al., 2004; Breedveld, 2005). This map has been gridded corresponding to the innermost WRF domain. The present and historical land use maps are shown in Figure 2.2. The growth of urban areas around weather station De Bilt is obvious between the present and historical land use map. Furthermore, the land use class for weather station De Bilt is the same in both land use configurations, i.e. pasture and grassland.

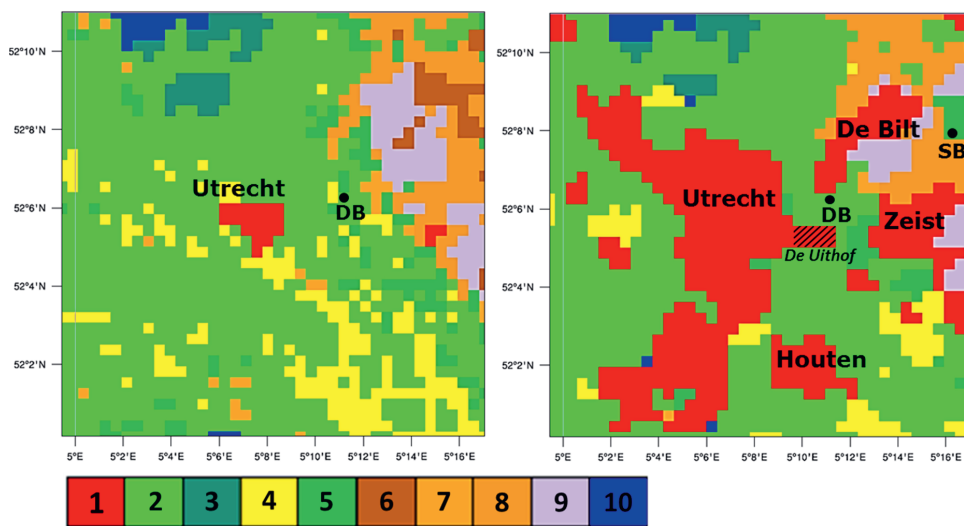


Figure 2.2: Land use map of domain 4 used for the model simulations. R1900 left and R2000 right. Used land use categories of the USGS land use table are urban area (1), pasture and grassland (2), wetlands (3), cropland / grassland mosaic (4), cropland / woodland mosaic (5), heather (6), Deciduous broadleaf forest (7), deciduous needle leaf forest (8), evergreen needle leaf forest (9), water bodies (10). Weather stations Soesterberg and De Bilt are abbreviated as SB and DB respectively. The dashed lines indicate the outskirts De Uithof.

The constructed historical land use map depicts a more patchy structure of different land use types than the present CORINE land use map, which is because the land use type in the historical run is determined per grid cell. In CORINE some generalizations were already made, just as the minimal inventory unit has to be 25 ha (Buttner et al., 2002). For the constructed historical land use map this minimal inventory unit is not always desirable, because USGS also utilizes mixed land use types like the cropland/grassland mosaic. As an illustration, in case of a cropland patch < 25 ha is surrounded by pasture, the cell would be assigned as cropland/grassland mosaic. In R2000, however, the cropland is not detected by CORINE when the patches of cropland cover < 25 ha. Then, the land use of the grid cell is reclassified into the type “pasture and grassland” instead of a cropland/grassland mosaic. The different detection procedure between the historical run and the present run explains the difference in patchiness of the land use map.

2.2.5 Anthropogenic heat

Another crucial model input parameter is the anthropogenic heat flux (AH), which is expected to be a substantial urban heat source, especially in winter because of building heating (Klok et al. 2010; Allen et al., 2011). Generally, the AH consists of three components, i.e. natural gas consumption, electricity and transport. Heat release from human metabolism is considered as well (Table 2.4).

Table 2.4: Estimated anthropogenic heat fluxes in 1900 and 2000 (in Wm^{-2}). The fossil fuel energy usage comprises i.e. transit, building heating and electricity.

Anthropogenic heat	1900	2000
Gas consumption	-	8.57
Electricity	-	3.96
Transit	-	4.7
Fossil fuel energy usage (Gas consumption + electricity)	15.15	-
Metabolic rate	3.76	0.90
Total	18.91	18.13

Due to the privatization of the gas market, the natural gas consumption is difficult to estimate for Utrecht. Therefore, we follow Klok et al. (2010) who quantified the AH for Rotterdam (the Netherlands), and we assume the gas consumption per capita of the complete country is also valid for Utrecht. In summer less natural gas is used than in winter, and therefore we distinguish the natural gas consumption per month (CBS, 2001). With the population density of Utrecht, the AH contribution is $\sim 8.6 \text{ Wm}^{-2}$.

The Central Office for Statistics (CBS, 2001) also provides monthly values for electricity consumption, consisting of consumption by the public network and by companies. In total, 387.7 PJ is consumed, which gives 3.96 Wm^{-2} . We assume that all electricity consumption is dissipated as heat in the local environment (as in Klok et al. (2010) and VW08).

In estimating the contribution by traffic, we take the same heat contribution as in Klok et al. (2010) for Rotterdam. We assume no large differences in traffic compared with Rotterdam, and therefore 4.7 Wm^{-2} is used. Finally, the human metabolic rate amounts on average $\sim 175 \text{ W}$ per person (Sailor & Lu, 2004; Klok et al., 2010). With a population density of 5155 inhabitants per km^2 in Utrecht, the metabolic rate amounts to 0.90 Wm^{-2} .

The AH for 1900 (18.9 Wm^{-2}) corresponds closely with the AH of 2000 (18.1 Wm^{-2} , Table 2.4). At first sight, this looks surprising, because the energy consumption per capita increased by a factor 5 in the 20th century (CBS, 2001). However, the four times larger population density in Utrecht compensated this completely. The metabolic rate rose by a factor four, and the energy consumption per m^2 does not differ much compared with the present. Due to the small differences the same AH values are used for the R1900 and R2000. Finally, the reported AH values in Table 2.4 are yearly averaged numbers, while for our model analysis monthly and seasonal data are required.

For the validation of the boundary-layer schemes MRF and MYJ (Section 2.3.1 and 2.3.2), we utilize specific monthly AH averages. These are respectively; 12 Wm^{-2} for the July (HM) case, 15 Wm^{-2} for the May (NW) case, and 26 Wm^{-2} case for the December cases WW and SW (CBS, 2001). The fourteen episodes used for the model analysis (Section 2.3.3 and 2.3.4) are run with a distinct representative AH for the summer half year and winter half year, i.e. 14 Wm^{-2} and 22 Wm^{-2} . This is preferred, because this filters the intra-seasonal variability in AH which otherwise interacts with the circulation types. For instance, the AH is higher in December compared to October due to more building heating. The ratio of the AH in winter half year and summer half year, i.e. 1.6, is close to findings for London (Hamilton et al., 2009; Allen et al., 2010). Our WRF simulations account for a diurnal and monthly cycle of AH (see Table 2.3) (Kimura & Takahashi, 1991; Kusaka & Kimura, 2004).

2.2.6 Available observations

We utilize routine hourly observations of the weather station De Bilt ($52^{\circ}06' \text{ N}$, $5^{\circ}11' \text{ E}$, 1.9 m above sea level) to estimate the UITTE from field observations as well as for model validation. This station is located on a grass field over a sandy soil, and its surroundings are characterised by half open landscape with grass and arable land as well as forests and built up area. In addition, we use routine observations of Herwijnen ($51^{\circ}51' \text{ N}$, $5^{\circ}09' \text{ E}$, 0.9 m above sea level about 30 km south of DB) which is located in a polder covered with grass vegetation and a river clay soil. The latter station is used to independently estimate the UITTE from an observational perspective. At both stations temperature is recorded by electronic sensors in a multi-plate screen. More detailed background information is available in van der Meulen and Brandsma (2008), and at KNMI (2013).

2.3 Model results for urban heat island characteristics

2.3.1 Sensitivity to boundary-layer scheme

In general, we note that atmospheric boundary layer (ABL) schemes still pose many challenges (e.g. Holtslag et al., (2013)). Here we evaluate the ABL schemes MRF and MYJ for four key variables, i.e. temperature (T_2), wind speed (U_{10}), specific humidity (q_2) and global radiation (K_d) over the entire period of 7 days for each case (Table 2.5); an overview of these associated time series is presented in Figure 2.3. Statistics over these relatively long time series are more robust than over a shorter series as in VW08 who used 4 of the 7 modelled days. Overall, the utilized statistical measures indicate that the model skill for the selected key variables does not uniformly improve by removing the worst three days (as done in VW08) from our analysis.

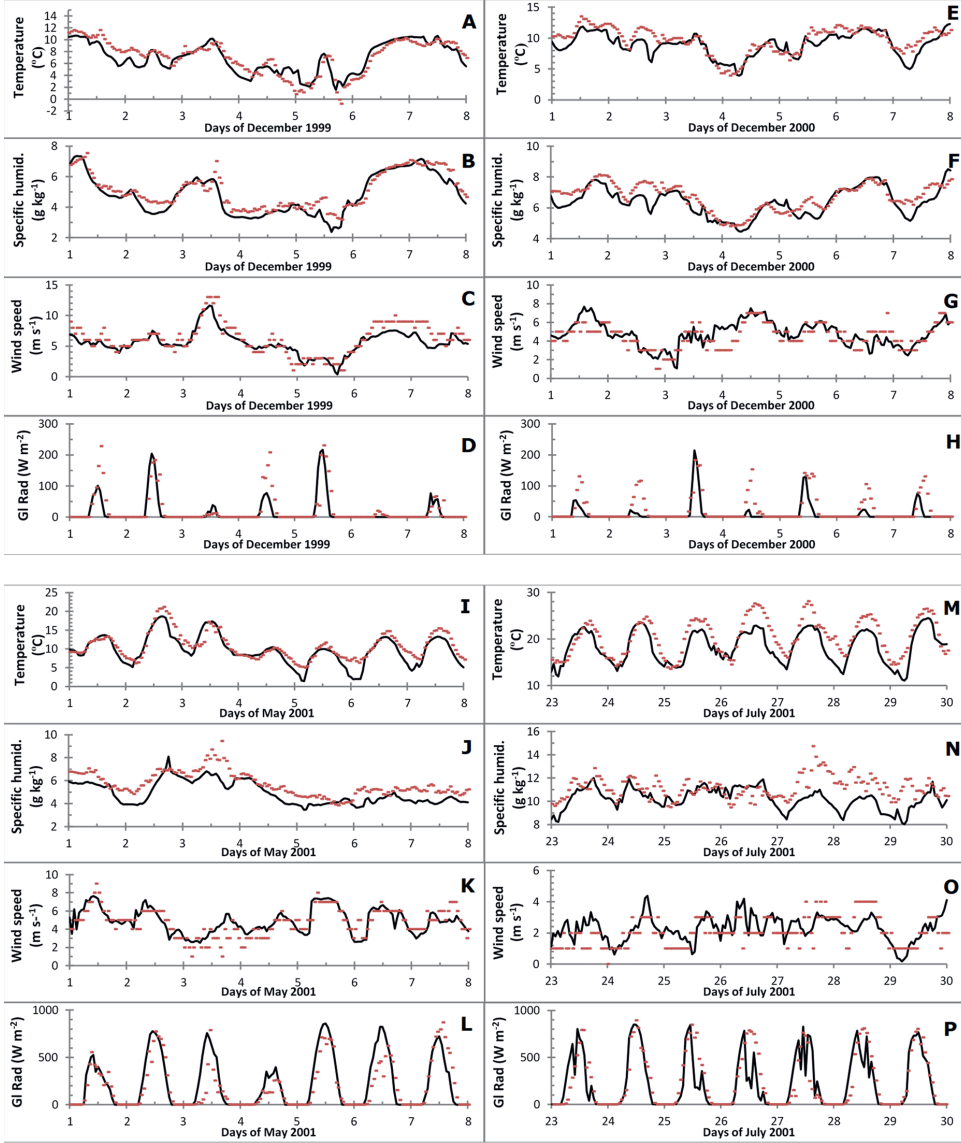


Figure 2.3: Simulated (MRF) and observed values of temperature, specific humidity, wind speed and global radiation for the four episodes, i.e. A-D: WW; E-H: SW; I-L: NW; M-P: HM. Asterisk symbols represent the observations and the solid line corresponds to model simulations.

From this analysis MRF appears to outperform MYJ for most criteria, although the differences between the schemes are rather small (Table 2.5). In general, we find the score for temperature is best for MRF based on (systematic) RMSE and bias. MYJ shows too low T_2 , especially during daytime, and is moister than MRF, which corresponds with results from earlier sensitivity studies (Pino et al., 2004, García-Díez et al., 2012). This is related to the local mixing of MYJ, which underestimates the vertical mixing and the accompanying entrainment at daytime (Hu et al., 2009). Compared to observations, however, MYJ is not too moist and has a smaller bias than MRF.

Table 2.5: Evaluation of the WRF model results for the MRF and MYJ by statistics of the key variables temperature (T_2), specific humidity (q_2), wind speed (U_{10}) and global radiation (K_{\downarrow}) for the four episodes. Italic numbers indicate the best performing ABL scheme.

	WW (Dec 1999)		SW (Dec 2000)		NW (May 2001)		HM (July 2001)	
	MRF	MYJ	MRF	MYJ	MRF	MYJ	MRF	MYJ
2-m temperature (T_2)								
RMSE (K)	<i>1.32</i>	1.39	<i>1.45</i>	2.03	<i>1.87</i>	2.46	<i>2.81</i>	3.15
RMSEs (K)	<i>0.60</i>	1.14	<i>0.95</i>	1.62	<i>1.05</i>	1.73	2.22	2.64
Bias (K)	<i>-0.16</i>	-0.95	<i>-0.76</i>	-1.44	<i>-1.05</i>	-1.97	<i>-2.06</i>	-2.38
Correlation	0.88	<i>0.94</i>	<i>0.81</i>	0.74	0.91	<i>0.92</i>	<i>0.87</i>	0.85
2-m specific humidity (q_2)								
RMSE (g kg ⁻¹)	0.49	<i>0.41</i>	0.62	<i>0.54</i>	0.96	<i>0.58</i>	1.47	<i>1.29</i>
RMSEs (g kg ⁻¹)	0.28	<i>0.25</i>	0.35	<i>0.31</i>	0.80	<i>0.25</i>	1.18	<i>0.86</i>
Bias (g kg ⁻¹)	-0.27	<i>0.06</i>	-0.33	<i>-0.28</i>	-0.77	<i>-0.18</i>	-0.95	<i>-0.69</i>
Correlation	<i>0.95</i>	0.94	0.83	<i>0.85</i>	0.84	<i>0.85</i>	<i>0.83</i>	0.43
10-m wind speed (U_{10})								
RMSE (ms ⁻¹)	<i>1.33</i>	2.73	<i>1.06</i>	1.83	<i>0.99</i>	1.31	<i>0.94</i>	1.49
RMSEs (ms ⁻¹)	<i>1.03</i>	2.30	<i>0.42</i>	1.45	<i>0.26</i>	0.66	<i>0.83</i>	1.14
Bias (ms ⁻¹)	<i>-0.62</i>	2.30	<i>0.23</i>	1.43	<i>0.14</i>	0.70	<i>0.25</i>	1.02
Correlation	<i>0.89</i>	0.86	0.69	0.69	<i>0.77</i>	0.74	<i>0.46</i>	0.41
Surface downwelling radiation (K_{\downarrow})								
RMSE (Wm ⁻²)	<i>22.23</i>	30.60	<i>30.74</i>	38.36	<i>113.89</i>	142.27	<i>161.30</i>	170.90
RMSEs (Wm ⁻²)	<i>12.92</i>	17.20	<i>24.02</i>	35.81	<i>34.20</i>	73.31	<i>0.84</i>	48.61
Bias (Wm ⁻²)	<i>-6.03</i>	-9.08	<i>-13.74</i>	-18.03	32.16	<i>-19.98</i>	<i>-19.71</i>	-20.02
Correlation	<i>0.90</i>	0.81	<i>0.76</i>	0.63	<i>0.92</i>	0.82	<i>0.84</i>	0.83

Considering the HM case (July), the T_2 is substantially underestimated with a bias of -2.06 K. The modelled T_2 of MRF is still better than that of MYJ (bias = -2.38 K). In addition, MRF underestimates the q_2 by -0.95 g kg⁻¹. Two possible reasons for the underestimated T_2 are the overestimated soil moisture content in the model, and the temperature at 850 hPa is ~ 2 K too low compared to sounding observations from weather station De Bilt (not shown). This too low 850 hPa temperature inhibits the T_2 to rise towards the observed maximum temperatures. The K_{\downarrow} is negatively biased for July, which can be explained by the fact that more cumulus clouds have been

observed (based on satellite clouds observation (not shown)) than were present in the model simulation. Finally, the U_{10} is well represented in the model with the largest positive bias at night (mean bias = 0.25 ms^{-1}).

The episode in December 1999 (WW) is relatively easier to model than the previously described summer case, because the ABL is relatively neutral. This episode is characterized by moderate to strong winds ($\sim 5 \text{ ms}^{-1}$), which results in a better representation of T_2 . Exceptions are the calm nights occurring at December 5th and December 6th. The observed T_2 was 3 K colder than modelled, especially because the wind vanished in reality, but not in the model run. On the contrary, considering the full episode, WRF slightly underestimates U_{10} . The modelled q_2 corresponds with the observations with a bias of only -0.27 g kg^{-1} and a RMSE of 0.49 g kg^{-1} . $K\downarrow$ is of relatively smaller importance in winter, but is still correctly forecasted (bias = -6 Wm^{-2} and RMSE = 22 Wm^{-2}).

In the case of December 2000 (SW) the model forecasts also indicate a lower T_2 than observed (bias = -0.76 K). Especially the first two days are too cold in the model (1.6 K). Cloud differences, which may affect the energy balances, cannot explain this deviation. In addition, a small bias is found for q_2 (-0.33 g kg^{-1}). The forecasted U_{10} is close to the observed U_{10} with a bias of 0.23 ms^{-1} and a RMSE_s of 0.42 ms^{-1} .

For the May 2001 case (NW) the modelled T_2 is negatively biased by -1.05 K . A relatively large part of this bias is due to the cold nights of 5 and 6 May, which were not correctly simulated by WRF. In particular, observations showed that these nights had partly cloudy skies, while the model forecasted clear skies. The lack of clouds is also the reason behind the overestimated $K\downarrow$ ($\sim 32 \text{ Wm}^{-2}$). The observed clouds on May 5th and 6th were hardly reproduced in the model. Also, q_2 is almost always negatively biased, on average -0.77 g kg^{-1} . The forecasted U_{10} corresponds relatively well with the observations with a RMSE of 0.99 ms^{-1} and a bias of 0.14 ms^{-1} .

Considering the fact that VW08 performed a comparable mesoscale model study using a different model, i.e. the ARPS model (Xue et al., 2000) for the same episodes, it is interesting to compare the model skill of WRF with that of ARPS (VW08 Table 2). Based on both the bias and RMSE for T_2 , WRF performs slightly better for the WW and NW cases, and slightly worse in the HM and SW cases. Interestingly, the bias for q_2 is larger for WRF than for ARPS, while for RMSE WRF performs better than ARPS for all cases, except HM. Concerning U_{10} , the RMSE is typically 0.2 ms^{-1} higher in WRF than for ARPS for all cases. This is consistent with the enhanced mixing in the MRF scheme utilized in WRF (e.g. Steeneveld et al., 2011b), compared to the moderate mixing in the TKE-based ABL scheme in ARPS. Finally, WRF performs considerably better than ARPS for $K\downarrow$ based on both the bias and RMSE. Particularly in the NW case the RMSE amounts to $\sim 60 \text{ Wm}^{-2}$ less than by ARPS.

Despite the fact that the WRF model results contain a number of systematic biases, especially for the HM case, we consider the model results suitable to estimate UITE. Note also that the largest contribution to UITE is by the SW case (see next section), for which WRF produces the best forecast (and outperforms ARPS). For further evaluation of WRF for Dutch conditions we refer to Steeneveld et al. (2011b).

2.3.2 Surface Energy balance

The surface energy balance in R2000 is not substantially different from R1900 for weather station De Bilt (not shown). Since the grid cell of De Bilt shares the same land use, soil and initial soil moisture, this is not surprising. However, for the winter episode December 1999 (WW) a difference in the sensible heat flux downstream of Utrecht is observed in the order of $10\text{--}15\text{ W m}^{-2}$ at daytime. In R2000, the sensible heat flux is more negative downstream of Utrecht than in R1900. This is because the urban plume causes a larger temperature gradient between screen level and ground level. With cloudy days in the winter, it is quite normal that the sensible heat flux is directed downwards during a large part of the day (in winter the atmosphere is stably stratified approximately 60% of the time in coastal wind climates (Barthelmie, 1999)). Cities generally show positive values for the sensible heat flux in winter at daytime, due to the addition of AH.

In order to illustrate the differences in energy balance for a relatively clear spring week, Figure 2.4 shows the energy balance components for the centre of Utrecht compared with weather station De Bilt (over grass) for May 2001 (NW). The storage flux is clearly larger in Utrecht, due to the larger heat capacity of the urban fabric. The difference in partitioning of the latent heat flux and sensible heat flux are characteristic for these areas. Due to the relatively small amount of vegetation and high fraction of impervious surfaces in urban areas, a large part of the net radiation is used for the sensible heat flux instead of the latent heat flux. However, the net radiation itself is slightly lower for urban areas in all seasons. This is the result of higher temperatures in the city which supports emission of longwave radiation.

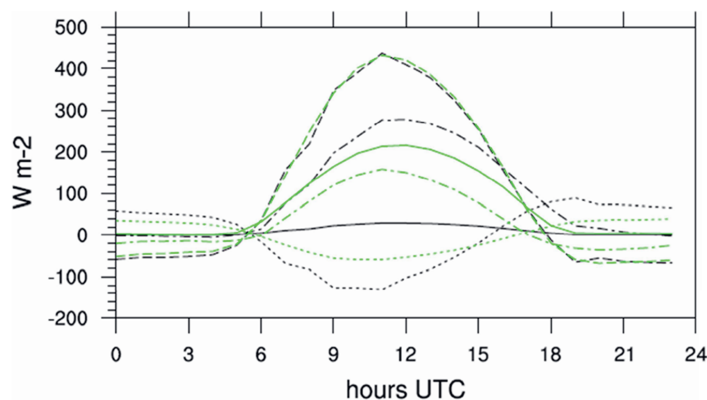


Figure 2.4: The 7-day averaged modelled energy fluxes for weather station De Bilt (green) and the energy fluxes for the centre of Utrecht (black) for the May 2001 episode. All energy fluxes are counted positive upward. Net radiation (dashed line); sensible heat flux + anthropogenic heat (dotted dashed line); latent heat flux (solid line); storage heat flux (dotted line).

2.4 Urbanization Induced Temperature Effect (UITE) for weather station De Bilt

2.4.1 Yearly average UITE

From the fourteen model simulations comprising all atmospheric circulation types (GWT) for summer and winter, we can estimate an average UITE for DB, since the frequencies for the 14 chosen episodes are known (Table 2.6) (Werner and Gerstengarbe, 2010). These frequencies are calculated between 1881 and 2008, and are also assumed to be representative for the present situation. The

modelled total average temperature difference (UITE) then becomes 0.22 ± 0.06 K (Figure 2.5), which is significant at the 0.95 level. The standard error is calculated considering autocorrelation. WRF simulations using the MYJ ABL scheme confirm the UITE estimate of MRF (also 0.22 ± 0.06 K). Within these episodes, the average UITE differs with a maximum of 0.08 K between MYJ and MRF. The main difference between both schemes is that MRF clearly simulates substantially warmer cities than MYJ which is in the order of 25%. The relatively close correspondence of the two estimates indicates an apparently small sensitivity to the boundary-layer scheme.

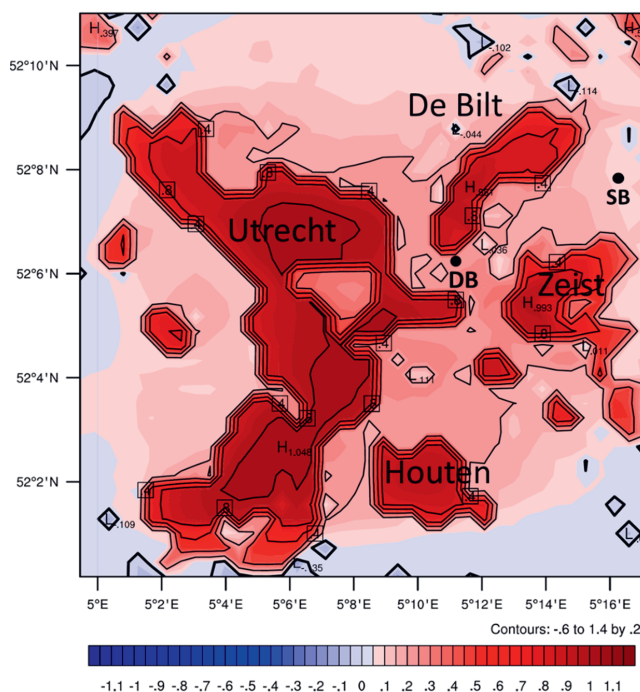


Figure 2.5: Yearly averaged UITE (K), which is composed by the difference in temperature between R2000 and R1900 averaged with frequencies over all weather episodes using MRF. SB and DB indicate the weather stations in Soesterberg and De Bilt, respectively. Names of cities and towns are also indicated.

Figure 2.5 also shows the spatial distribution of the yearly averaged UITE, and indicates that the largest temperature differences between R2000 and R1900 in rural areas can be found North-East of the urban areas. This is a result of the predominantly south-westerly flow in the Dutch climate. Another important result is that other locations between Utrecht, De Bilt, Zeist and Houten show similar anomalies as the location of DB. Therefore, weather station De Bilt is representative for the landscape between the urban areas of Utrecht, De Bilt, Zeist and Houten. On the northern side of Utrecht anomalies can still be detected at a large distance from Utrecht. The heat advection has on average an influence of 0.05 K more than 5 km away from the city. Southeast of Utrecht the anomaly is slightly larger than for DB, which is due to a larger urban extension as compared to DB. Note that the current city centre of Utrecht was also present in R1900. The shape of this city centre can be observed in Figure 2.5 as an area with a relatively small anomaly.

Table 2.6: Statistical analysis of the MRF model results for all 14 episodes. The winter episodes have affix 1 and the summer episodes have affix 2. Day and night are divided by sunrise and sunset. (Student *t*-test has been corrected for autocorrelation).

Statistics DB	Mean UITE (K)	No. of hours. N	Student <i>t</i> -test	P value	Wilcoxon signed (\hat{z})	P value	Freq. of occurrence
1. Dec 1999 (W1)	0.293	169	5.79	0.00	-9.94	0.000	28.8%
Day	0.434	56	8.91	0.00	-6.51	0.000	
Night	0.223	113	3.95	0.00	-7.47	0.000	
2. Dec 2000 (SW1)	0.257	169	3.29	0.00	-8.10	0.000	6.3%
Day	0.458	56	5.52	0.00	-6.41	0.000	
Night	0.157	113	1.87	0.06	-4.84	0.000	
3. Jan 2000 (NW1)	0.238	169	2.43	0.01	-5.64	0.000	7.9%
Day	0.487	62	7.78	0.00	-6.24	0.000	
Night	0.093	107	0.72	0.47	-1.96	0.050	
4. Dec 2004 (HM1)	0.089	169	2.15	0.03	-4.72	0.000	17.2%
Day	0.151	56	2.82	0.00	-5.03	0.000	
Night	0.058	113	1.02	0.31	-2.45	0.014	
5. Feb 2005 (N1)	0.189	169	2.41	0.01	-5.09	0.000	13.4%
Day	0.248	72	2.34	0.02	-5.07	0.000	
Night	0.145	97	1.47	0.14	-3.22	0.001	
6. Feb 2003 (E1)	0.100	169	2.46	0.01	-3.97	0.000	15.4%
Day	0.106	70	2.90	0.00	-2.78	0.005	
Night	0.095	99	1.51	0.13	-2.86	0.001	
7. Oct 2000 (S1)	0.004	169	0.07	0.94	-3.30	0.001	8.0%
Day	-0.015	70	-0.22	0.82	-0.64	0.525	
Night	0.018	99	0.19	0.85	-3.73	0.000	
8. June 2004 (W2)	0.314	169	4.59	0.00	-7.04	0.000	25.0%
Day	0.210	119	5.82	0.00	-5.85	0.000	
Night	0.561	50	3.23	0.00	-3.59	0.000	
9. Apr 2003 (SW2)	0.271	169	4.49	0.00	-8.33	0.000	3.8%
Day	0.159	103	4.54	0.00	-6.71	0.000	
Night	0.446	66	3.58	0.00	-5.12	0.000	
10. Sep 2001 (NW2)	0.455	169	7.10	0.00	-9.35	0.000	9.0%
Day	0.322	93	4.22	0.00	-5.80	0.000	
Night	0.617	76	7.40	0.00	-7.17	0.000	
11. Jul 2001 (HM2)	0.245	169	4.15	0.00	-6.91	0.000	16.0%
Day	0.107	112	2.77	0.00	-4.79	0.000	
Night	0.515	57	4.06	0.00	-4.71	0.000	
12. June 2000 (N2)	0.254	169	4.65	0.00	-6.55	0.000	18.4%
Day	0.194	119	3.94	0.00	-4.73	0.000	
Night	0.398	50	2.67	0.01	-4.11	0.000	
13. Apr 2002 (E2)	0.136	169	3.37	0.00	-6.25	0.000	15.5%
Day	0.084	87	2.36	0.02	-2.54	0.011	
Night	0.192	82	2.89	0.00	-5.49	0.000	
14. May 2001 (S2)	0.206	169	1.69	0.09	-5.38	0.000	8.6%
Day	0.161	106	1.05	0.29	-5.05	0.000	
Night	0.283	63	2.54	0.01	-2.70	0.000	

2.4.2 Diurnal evaluation of urban heat advection

For the summer months, we expect the largest UHI (and consequently the largest UITE) in the evening, due to the heat capacity of urban fabric (Oke, 1982). In the night the UITE gradually decreases, until sunrise, when a comparatively faster heating of the rural surroundings cancels the UHI. The episodes with prevailing winds from De Bilt and Utrecht, i.e. June (W2), April (SW2) and May (S2), follow such an evolution. May (S2) is depicted in Figure 2.6. May (S2) is an exception in showing a negative UITE at night. The UITE at weather station De Bilt peaks in the evening, and starts developing more than 1 hour before sunset, and reaches its maximum at 21 UTC. This corresponds to the timing of the maximum UHI found for cities in other studies (Oke, 1982; Unger et al., 2001). During daytime, the signal in the UITE is relatively small but relatively constant i.e. 0.2 K.

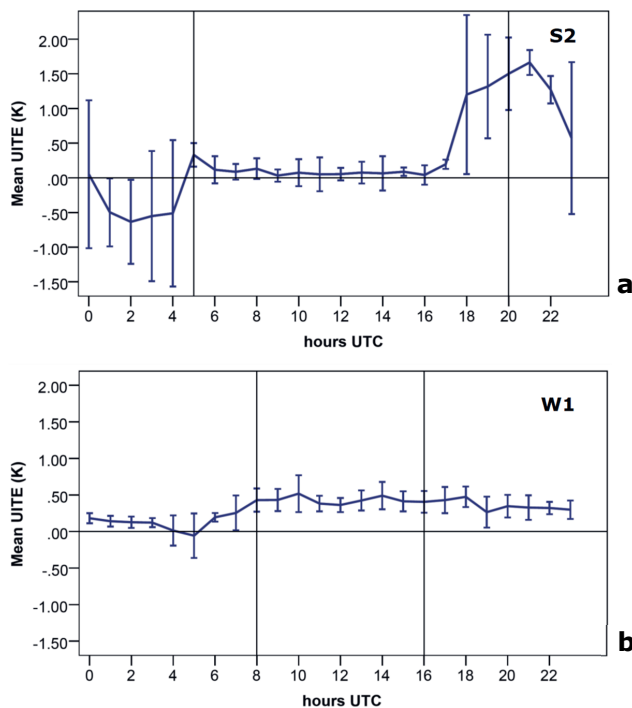


Figure 2.6: a) Diurnal evolution of UITE for the May 2001 case (S2) and b) December 1999 (W1) for wind directions from De Bilt (0° – 40°) and Utrecht (210° – 300°). The vertical lines at 5 UTC, 20 UTC (S2), 8 UTC and 16 UTC (W1) mark sunrise and sunset. The error bars display a 0.9 confidence interval.

The winter episodes show a different diurnal evolution of UITE, i.e. the urban heat advection is clearly higher during daytime and the evening than at night. A good illustration is December 1999 (W1) (Figure 2.6). Differences in energy balances due to solar radiation are of relatively smaller importance in winter than one would anticipate. As such, the differences in AH during the day can largely explain the observed differences in diurnal evolution of UITE. During daytime, more AH is released by traffic and more fuel is used for building heating. The UITE is still present after 22 UTC, when AH consumption is diminished (Figure 2.6), which can be attributed to the large heat capacity of cities.

Because of the windy conditions in the December (W1) case, the ABL in domain 4 is close to neutral in the night. This suggests that AH is approximately mixed in a similar way during day and night. Therefore, the larger contribution of AH during daytime results in a corresponding by higher UITE. The relative importance of AH is confirmed by a sensitivity analysis for the December 1999 (W1) case (not shown). Without AH, December 1999 shows practically no UITE (0.01 K). In the winter the subsequent UITE for downstream areas of cities appeared to be a little larger than that for the summer episodes. Hence, AH is a large contributor to the UITE in winter. For the city of Utrecht itself the mean UHI does not differ substantially between summer and winter. Modelling studies such as Ichinose et al. (1999), Khan and Simpson (2001), Narumi et al. (2009) and Quah and Roth (2012), confirm that AH can have a substantial impact on the surface fluxes and resulting UHI. In addition, model studies (e.g. Ichinose et al., 1999; Aoyagi et al., 2012) and observational analysis (e.g. Klysik, 1996; Simmonds & Keay, 1997) noticed that AH has an impact on UITE in the winter season. Despite the larger AH fluxes, this is related to relatively stable atmospheric conditions in winter (Aoyagi et al., 2012).

2.4.3 Differences in UITE between circulation types

In this section, we quantify the UITE for the weather station De Bilt for each circulation type (Table 2.6). In addition, a Student's *t*-test and the Wilcoxon signed \tilde{z} -test are utilized to determine the significance of the urbanization effect. In addition, to evaluate whether WRF reproduces the downwind heat advection, the UITE is determined per wind direction for each weather episode in Figure 2.7. Most episodes show significantly higher temperatures for R2000 than for R1900, as noted in the mean UITE (Table 2.6). Exceptions are the southerly circulations in October 2000 (S1) and May 2001 (S2). For October (S1) this small UITE is explained by the wind direction that was most from the south and southeast, and then comes from a rural area (Figure 2.7). For case S2 in May especially winds from a northeasterly direction coming from De Bilt are observed. Despite the fact that the average UITE for May (S2) is close to the yearly average UITE (0.206 K), the R2000 run is not significantly warmer than R1900, which is caused by relatively large variations in nighttime temperatures and a high autocorrelation of the time series. It is remarkable that the easterly flows of April 2002 (E2) and February 2003 (E1) also show significantly higher temperatures for R2000. For February (E1) this small UITE is largely explained by the presence of Zeist. For April (E2) partly urban heat is advected from De Bilt, but the winds from the forests north east of weather station De Bilt still have a small UITE of 0.09 K that cannot be explained.

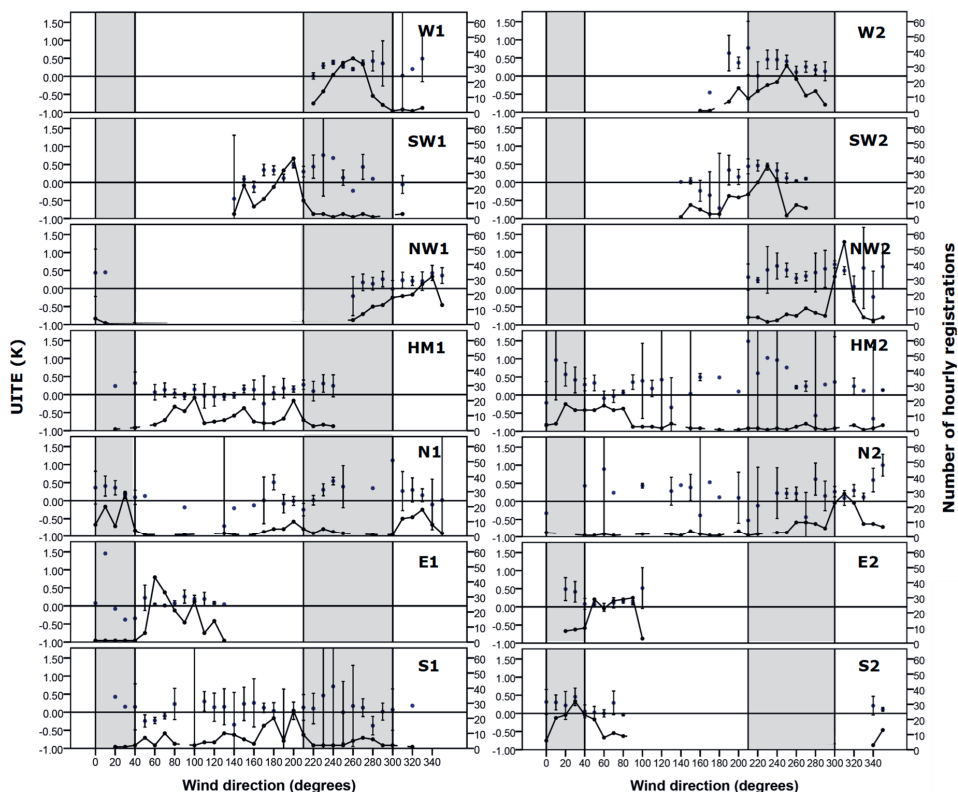


Figure 2.7: Modelled UITE for the 7 weather episodes in winter (left panel, affix 1) and in summer (right panel, affix 2) as function of the modelled wind direction at DB. The shaded areas between the lines are the wind directions where De Bilt (0° – 40°) and Utrecht are located (210° – 300°). The error bars display a 0.9 confidence interval. The black line indicates the number of hours of the wind direction.

To investigate the distribution of the hourly UITE values, one can study by how much the mean UITE values are affected by skewness of the hourly UITE values. Figure 2.8 shows that UITE values are approximately normally distributed for most of the episodes. Results for the circulations with relatively small urbanization upwind, such as the southerly and easterly circulations, do not show a normal distribution (Figure 2.8). Most hourly values are around 0 K or slightly above. A relatively small number of hours with few winds from urban areas cause the large tails at the righthand side. The other episodes, with more urban heat advection, more closely approach a normal distribution. Also, these runs show that the winds are not always directed from the city, but the few winds from rural areas are not disturbing the approximate normal distribution because they have on average no UITE-signal.

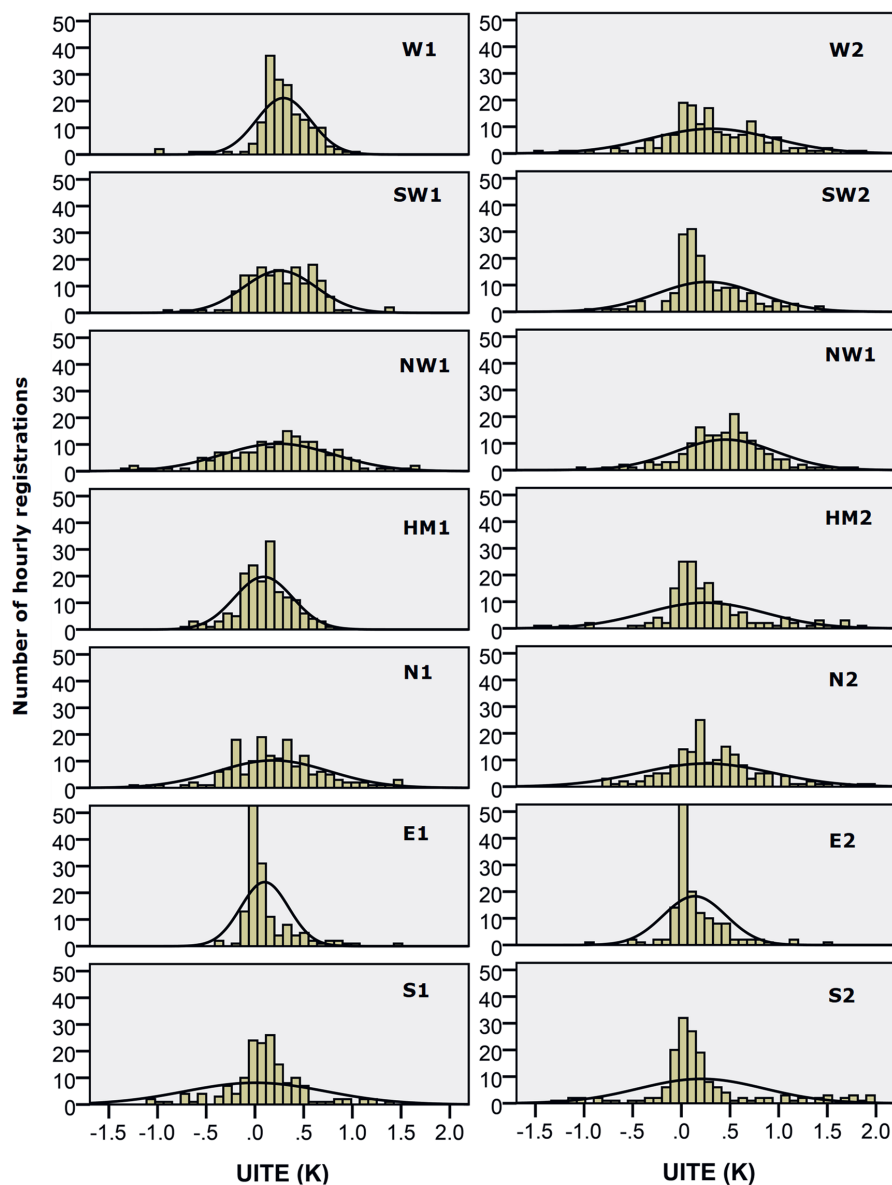


Figure 2.8: Histogram of UITE (K) for the 7 weather episodes for winter (left panel, affix 1) and the 7 episodes in summer (right panel, affix 2). The black line presents the normal distribution fit.

2.4.4 Dependence on wind direction

To evaluate the modelling results it is tempting to analyse whether the largest modelled UITE indeed originates from urban areas. Wind directions from De Bilt and Utrecht predominantly give a significant UITE for a sufficient number of wind direction registrations (Figure 2.9). Good examples of UITE from Utrecht are the circulations in December 1999 (W1), June 2004 (W2), April 2003 (SW2) and September 2001 (NW2). Winds from De Bilt give higher temperatures for February 2005 (N1), July 2001 (HM2) and May 2001 (S2). Sometimes a small UITE is simulated outside

the urban boundaries, as in December 2000 (SW1) for southerly winds and February 2003 (E1) for east-southeasterly wind. However, often this is still related to other urban areas as the outskirts De Uithof and Houten (180° – 210°) and Zeist (90° – 130°). The northwest wind sector (320° – 350°) shows a clear UITE signal because of a fetch over southwest De Bilt, simulated in September 2001 (NW) and June 2000 (N2). Overall, the heat contamination in weather station De Bilt originates equally from the small town of De Bilt and the city of Utrecht.

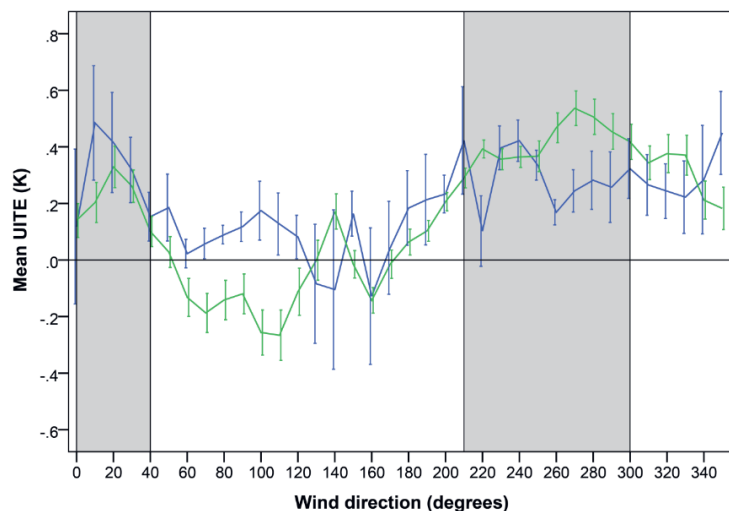


Figure 2.9: UITE (K) as function of wind direction. The blue line represents the case averaged UITE from model simulations. The green line represents the differences in temperature between observations of weather station De Bilt and observations of weather station Herwijnen in the period 2009–2011. The shaded areas between the lines are the wind directions where De Bilt (0° – 40°) and Utrecht (210° – 300°). The error bars display a 0.9 confidence interval.

Similar to B03 we compare the T_2 observations of weather station De Bilt with a nearby located rural weather station, i.e. Herwijnen. In contrast to B03, we use a more recent time span of the De Bilt's temperature record. DB has been moved in 2008 to a more open and representative location (Brandsma, 2011). Therefore, we compare our model results with observations of three consecutive years from 2009 till 2011 (Figure 2.9). The temperature measured at the new site is however on average 0.15 K warmer than at the old location (Brandsma, 2004). The old site was sheltered by nearby vegetation which resulted in lower nighttime temperatures. Assuming that temperatures at the old and new site were equal over hundred years, this implies that the centennial trend caused by urbanization effects becomes 0.25 K for the new operational site (Brandsma, 2004), based on the intercomparison study of DB and SB (B03). This result is clearly more consistent with the findings of our modelling study ($0.22 \text{ K} \pm 0.06$).

In this wind direction analysis (Figure 2.9), weather station Herwijnen is chosen as a rural station instead of weather station Soesterberg (as in B03), because the latter has been terminated in 2008. An advantage of Herwijnen is that it is uniformly rural, without cities located close to the station. Also, both weather station De Bilt and Herwijnen are located at similar distances from the coast, and thus experience the same degree of continentality. An updated analysis on the urbanization effects of DB with 30-year climate data up to 2020 is presented in the Perspectives (Section 6.2).

Averaged over the time span 2009–2011 we clearly find higher temperatures for wind directions between (210° – 300°) and (0° – 40°) from observations of DB compared to observations of Herwijnen (Figure 2.9). These wind directions coincide with city Utrecht and town De Bilt, being upstream for DB. Based on observations, the wind directions from these cities give an approximate UITE of 0.4 K. The dip at 260° can again be explained by the location of the city of Utrecht in R1900. The deviation between the observations of Herwijnen and De Bilt between 270° – 300° is not fully understood. Here, the observations indicate a larger urban heat advection from the northern part of Utrecht than the model does.

For the summer season the model simulations underrepresent the frequency of occurrence of wind directions from the south-east (120° – 145°) and the south (170° – 180°). In these directions relatively minor urban areas are located. In addition, this underrepresentation by WRF hardly affects the UITE estimate of the summer season. If the UITE estimates from these wind directions are weighted based on the observed wind direction frequency, the summer averaged UITE differs less than 0.01 K, compared to an estimate based on GWT frequencies. During the winter, model results show a good representation in the south and south-east directions and also the other wind directions show no considerable underestimation.

Surprisingly, the comparison with measurements of Herwijnen also shows a strong UITE in the directions 310° – 340° . Possibly this effect has a different cause than heat advection from cities since there are no urban areas nearby in these directions. The simulated substantial UITE for 320° – 340° can be partly attributed to the resolution. In reality the urban cell NW of weather station De Bilt consists of a large fraction of green.

2.4.5 Comparison against observational evidence

Finally, we compare our modelling results with observational evidence, and we bring our results in a larger scale context. For the estimation of the yearly averaged UITE, the fourteen simulated episodes represent $\sim 97\%$ of the GWT's. Thereby, these GWT simulations have been run both in summer and in winter season. In contrast to VW08, substantially more simulations are utilized to achieve an annual averaged UITE. On the other hand, a GWT is a class of more Grosswetterlagen that can be mutually diverse in wind direction and weather (Werner and Gerstengarbe, 2010). Thus some particular Grosswetterlagen are not examined in the simulations.

In addition, we note that in the current study we did not account for urbanization in the region beyond Utrecht, i.e. in model domains 1–3. Particularly in the western part of the country, cities like Rotterdam, The Hague, and Leiden have spatially expanded as well. Although it is difficult to estimate this contribution more precisely, this signal will add to the local contribution in UITE for DB. We estimate this effect around ~ 0.02 K, based on UITE values at locations at similar distances from Utrecht as the approximate distances between the western cities and Utrecht. Nevertheless, the currently reported UITE values can be considered as lower boundary values concerning this aspect. Conversely, we see that the urban plume can persist for long distances downstream in the simulations sometimes. At 17 km distance north of the border of Utrecht an averaged UITE of 0.10 K is simulated in the predominant southerly circulation in the December 1999 (SW) case.

Comparing the UITE results of weather stations De Bilt and Uccle (near Brussels), VW08 estimated an UITE of 0.8 K for weather station Uccle, which is much larger than the UITE found from our analysis of 0.22 K. However, their estimate is only based on 57% of the GWT's. Another difference between the stations Uccle and De Bilt is related to the fact that Brussels is a larger city

than Utrecht. In addition, Uccle is surrounded by urban areas in all wind directions and the distance to the urban area is smaller than for DB, namely 200 m. Although we notice a lower UITE in this study, the UITE is statistically more significant than in VW08. This is partly because the internal variation in UITE was much lower for DB than for Uccle and this research simulated significantly more cases.

Next, we aim to estimate the relative contribution of UITE on the centennial temperature trend for DB. van der Schrier et al. (2011) observed a 1.3 K temperature increase for weather station De Bilt during the 20th century. In addition, van Oldenborgh and van Ulden (2003) found that 0.2 K temperature increase can be related to a change in large scale flow pattern towards more (south)westerly winds. Thus, the centennial temperature trend independent of wind direction changes amounts to 1.1 K. In combination with our UITE estimate of 0.22 K, we can conclude that urbanization is responsible for about 20% of the estimated temperature trend at weather station De Bilt.

It is also interesting to note that the difference between the trend of the homogenized series of weather station De Bilt and the CNT trend is smaller than our UITE estimate, i.e. 0.15 K (van Ulden et al., 2009). This is plausible since the CNT-stations other than De Bilt face much less urbanization, but a background urban contamination apparently cannot be neglected as is suggested by the difference with the CNT trend. Also weather station Soesterberg, which serves as rural reference station in the comparison study of B03, was most likely affected. Soesterberg is located 7 km east-north east of weather stations De Bilt and falls within the smallest domain and showed a simulated UITE of 0.08 K. This estimate is probably an underestimation since cities as Amersfoort (6.6 km east of SB) are located in domain 3 and are therefore not represented in the model simulations. At a larger scale Lim et al, (2005) simulated for densely built grids (5° x 5°) covering the Netherlands a 0.6 K larger centennial trend than the trend for agricultural land grids.

2.5 Conclusions

This study quantifies the Urbanization Induced Temperature Effect (UITE) of Utrecht and suburbs on weather station De Bilt (the Netherlands), which is located east of Utrecht. This station has one of the longest observational records worldwide (since 1901). Fourteen 7-day cases with different large-scale flow patterns have been hindcasted with the meso-scale model WRF for both the land use of 1900 and 2000, equally distributed over winter and summer.

It appears that both in summer and in winter UITE is substantial when the flow is directed from the cities. In winter, this is mainly caused by anthropogenic heat emission. By upscaling the large-scale circulation frequencies (Grosswettertypes) a yearly averaged UITE is constructed which amounts to 0.22 ± 0.06 K for the 20th century. This is substantially more than earlier estimates from comparison of field observations (0.10 ± 0.06 K) as reported by B03. This remarkable difference calls for further investigation.

We would like to remark that the current modelling approach must be seen as a first attempt with the currently available computer capacity. This allows for adequate modelling of flows with downwind heat advection, but finer scale details such as the urban breeze (as in Hidalgo et al., 2008) are less likely reproduced. However, the use of a spatially finer resolution would violate assumptions made in the parameterisations for turbulent transport. This so-called “grey zone problem” (Wyngaard, 2004) currently prevents us from using a higher resolution than 500 m. Although downwind advection is probably the dominant mechanism, we recommend to repeat the current

study in the future if more computer resources and adequate parameterizations are available to investigate the impact of these flows on the finer scale.

Finally, we recommend to investigate the impact of urbanization on UITE for wide areas around cities, in order to determine whether a background UITE occurs. This applies especially to densely built countries.

Acknowledgements

We thank the Royal Netherlands Meteorological Institute (KNMI) and ECMWF for providing the necessary data for our research. Moreover, we thank T. Brandsma and G. van der Schrier (KNMI) for their explanations regarding the displacement of the weather station and CNT trend. Discussions with K. van Weverberg (Catholic University of Leuven, Belgium), S. Basu (North Carolina State University, USA), and our colleagues R.J. Ronda and L. Kroon have been appreciated. N.E. Theeuwes acknowledges funding by the NWO project CESAR within the Sustainable accessibility of the Randstad program. GJS acknowledges funding from the NWO E-science project “Summer in the City” (file number 027.012.103). Finally, we acknowledge two anonymous reviewers for their valuable comments and suggestions.

Chapter 3

Fine-scale urban data assimilation and weather reanalysis for Amsterdam

Abstract

Ongoing urbanization highlights the need for a better understanding and a high-resolution documentation of the urban climate. In this study, we combine rural observations by WMO surface stations, weather radar data and urban crowd-sourced observations with very fine scale modelling efforts for Amsterdam (the Netherlands). As model we use the Weather Research and Forecasting (WRF) mesoscale model with 3D variational data assimilation at a 100-m resolution in the innermost model domain. In order to enable the assimilation of observations within the urban canopy, we develop a scheme to reduce the urban temperature biases by adjusting the urban fabric temperatures. The scheme is tested against independent urban observations for the summer month of July 2014 and specifically for a hot period and an extreme precipitation event therein. We find data assimilation reduces biases in temperature, wind speed and specific humidity. Within the city the most significant improvement is the reduction of negative temperature biases during clear nights, which implies a better prediction of the urban heat island (UHI). Concerning precipitation, the fractional skill score improves step by step when assimilating additional observations, while the largest impact is seen from assimilation of weather radar observations.

This chapter is to be submitted:

Koopmans, S., van Haren, R., Theeuwes, N.E., Ronda, R.J., Uijlenhoet, R., Holtslag, A.A.M., Steeneveld, G.J. (2021), The set-up and evaluation of fine-scale data assimilation for the urban climate of Amsterdam. *Quart. J. Roy Meteorol. Soc.*

3.1 Introduction

Today's weather and climate models are progressing towards ever finer spatiotemporal scales, which is closely related to the enhanced computational capabilities that have become available. Recently a global grid spacing of 1 km was employed for numerical weather prediction (NWP) models (Wedi et al., 2020). While moving to these high resolutions, the representation of cities in NWP models becomes crucial. The complex structures of cities, made up of buildings, streets and vegetation of variable sizes and shapes, require a different modelling approach than the usually more homogeneous rural surroundings. In mesoscale atmospheric models (resolution: 0.5–2 km), urban canopy-layer schemes are primarily used to model the radiation and energy balance of the urban surfaces in the modelling domain (Masson, 2000; Kusaka et al., 2001; Martilli et al., 2002; Chen et al., 2011). Most of these parameterisations take into account effects of shading, radiation trapping, drag and anthropogenic heat emissions. In spite of evidence that the models perform well on a case-by-case basis (Miao et al., 2009; Salamanca et al., 2011), most models still show large biases in the representation of the energy balance and have a large spread without “proper tuning” (Grimmond et al., 2010; Loridan et al., 2010). Therefore, steps are still required to improve meteorological forecasting and hindcasting of the urban environment.

Improved model performance can be achieved by advancing the physics of the model and/or steering the model using observations, e.g. by applying data assimilation. The purpose of data assimilation is to accurately describe the state of the atmosphere using observations and model results. By using data assimilation, the model fields and observational fields are compared and the model is steered in the direction of the observations based on the weighted uncertainties of both observations and model output. Various studies have shown the benefits of data assimilation for the improvement of mesoscale weather forecasts (e.g. Xiao & Sun, 2007; Huang et al., 2009; Dee et al., 2011; Adam et al., 2016). Data assimilation is especially useful in hind- and forecasting extreme precipitation, as there is rapid error growth at the convective scale, which is a well-known challenge for atmospheric models (Sun et al., 2014). Data assimilation techniques have also been applied in meteorological reanalysis data sets, like Era-Interim and its successor Era-5 (Dee et al., 2011; Hersbach et al., 2020). Reanalysis data consists of a complete and coherent collection of meteorological gridded data, which is the best-known atmospheric state computed from the model and observations. Era-Interim and Era-5 are commonly used in climate research and have many applications in renewable energy, e.g. siting of favourable areas of wind (Kalverla et al., 2019) and solar power plants (Boilley & Wald, 2015; Lorenz & Barstad, 2016).

Current generation reanalysis products lack accuracy on the relatively fine sub-kilometre urban scales. These fine scales are crucial to account for the variability of the urban morphology, which directly affects meteorological processes and accordingly improves forecasts of routine weather variables, e.g. air temperature (Ching et al., 2009; Ronda et al., 2017). For the fine urban scale, specific studies reporting on data assimilation in the urban canopy or urban boundary layers are absent. In this paper we explore whether data assimilation techniques have the potential to improve the representation of urban weather characteristics in an NWP system. This includes a novel approach to nudge modelled urban canopy temperatures with quality-controlled crowd-sourced observations and independent verification against professionally installed urban weather stations.

In this study, we perform a hindcast for July 2014 for Amsterdam (the Netherlands) at a high resolution of 100 m nested in coarser resolution surrounding domains. The hindcast benefits from high-resolution (urban) land-use maps in combination with a dense spatial network of crowd-

sourced and professionally installed weather stations. In addition, Amsterdam's complex spatial structure, with a network of canals and its proximity to large water bodies (i.e. the North Sea and Marker Lake), makes Amsterdam an excellent test site for model improvement. The month of July 2014 has been chosen as test case, because it accommodates a couple of days with intense convective precipitation and a relatively warm, dry period, which are both critical conditions for water management and for human thermal comfort in cities. This work builds upon the study by Ronda et al. (2017), which developed urban weather forecasts for Amsterdam at the same high-resolution grid spacing, but without data assimilation. They found a well-reproduced spatial variation of the urban temperature distribution, though a cold bias of 1–2 K, which is a good motivation to explore whether data assimilation can assist to reduce this cold bias. The future goal is to create a reanalysis dataset of 15 years focused on the urban surroundings in order to investigate the urban climatology, based on the evaluation of this study.

This chapter is organised as follows. Section 3.2 presents the modelling set-up, a description of the assimilation approach for the urban canopy, the observations used for data assimilation and model verification. Section 3.3 presents the modelling results and Section 3.4 summarizes discussion and conclusions.

3.2 Methods

3.2.1 Model set-up

This study uses the Weather Research and Forecasting (WRF) model version 3.7.1 (Skamarock et al., 2005; Powers et al., 2017). WRF is a non-hydrostatic numerical model allowing for nesting to step-by-step represent large-scale circulation towards micro-scale transport (Chen et al., 2011). We built upon the study by Ronda et al. (2017) and use four one-way nested computational domains with gradually increasing resolutions (12.5 km, 2.5 km, 500 m, 100 m and respectively, see Figure 3.1 a-b). As initial and boundary conditions the ECMWF reanalysis data (ERA-Interim) is used. At the innermost domain at 100-m resolution, parks and ponds, and runways at Schiphol airport become visible and consequently have their specific impact in the model simulation. The basic WRF configuration is according to the urban weather forecasts of Ronda et al. (2017). This set-up includes 72 vertical eta-levels, makes use of the NOAH land surface model (Ek et al., 2003). The Grell-Freitas cumulus scheme (Grell & Freitas, 2014) is applied in the outer domain (12.5 km resolution). As Planetary Boundary Layer Scheme, YSU is used for the three coarsest domains (Hong et al., 2006). The inner domain turbulence is partly resolved and partly modelled with the Smagorinsky first-order closure scheme. Compared to the set-up of Ronda et al. (2017) our innermost domain has been enlarged such that Schiphol Airport is included (Figure 3.1). In addition, various data assimilation techniques were applied using the WRFDA module (Barker et al., 2012) which will be described in Section 3.2.2.

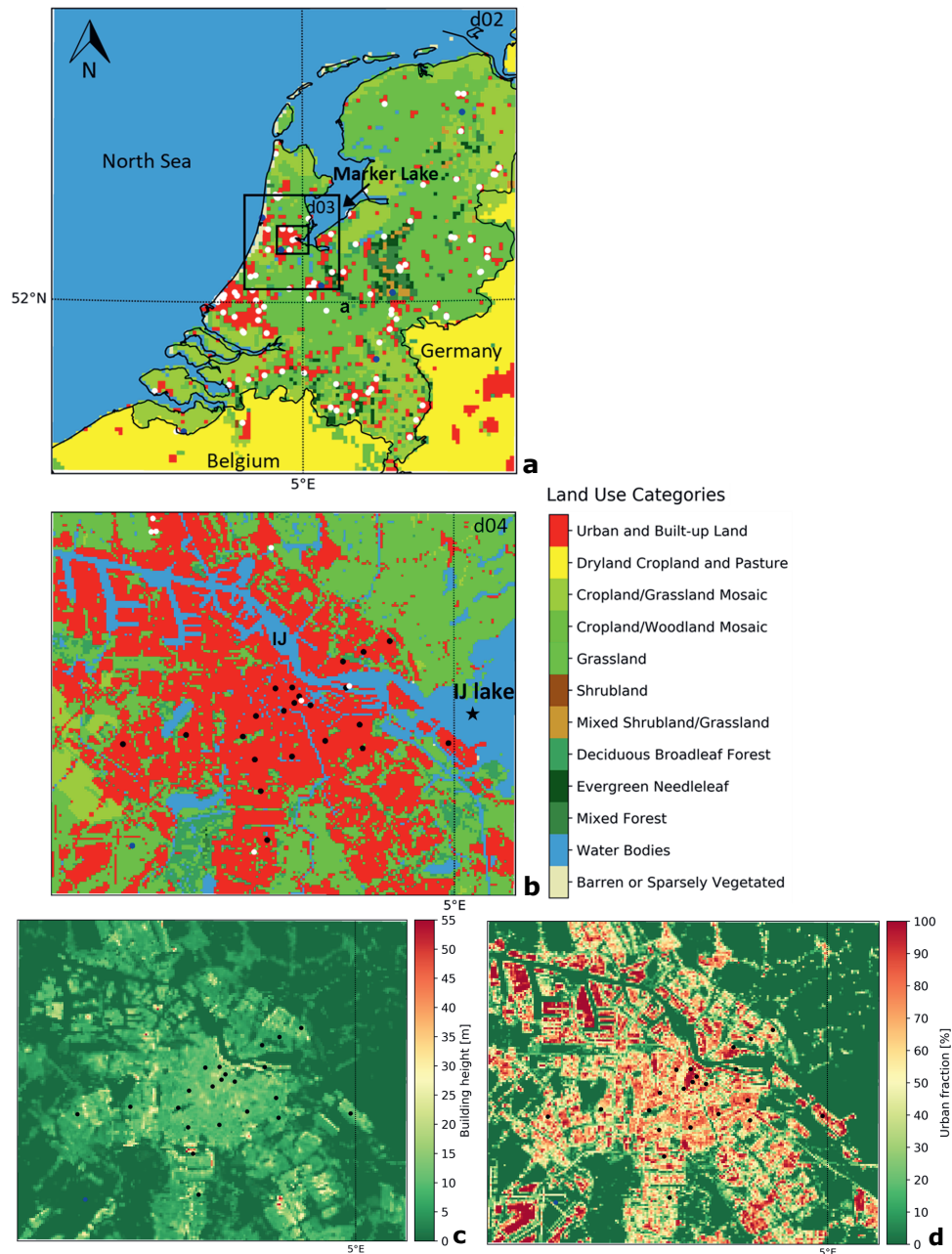


Figure 3.1: a) Land use map of the Dutch model domain (domain 2 with domains 3 and 4 nested). The black rectangles represent the four nested domains (100 – 500 – 2500 – 12500 m). The white dots indicate the 79 personal weather stations and the blue points indicate the 7 WMO stations Schiphol (WMO code: 6240), Wijk aan Zee (WMO code: 6257), De Bilt (WMO code: 6260), Deelen (WMO code: 6275), Eelde (WMO code: 6280), Westdorpe (WMO code: 6319) and Volkel (WMO code: 6375) used for the model evaluation. b) Land use map of the inner model domain (domain 4) with 22 independent AAMS urban weather stations used for the evaluation. The black star is an excluded station. The personal weather stations are indicated with white dots. c and d) Mean building height and urban (built) fraction.

As the urban scheme within WRF, we use the Single-Layer Urban Canopy Model (SLUCM) of (Kusaka et al., 2001). The most relevant input parameters are listed in Table 3.1. The physical properties of buildings, which include albedo, thermal conductivity, and thickness of roads, walls and roofs, are uniform for all buildings in Amsterdam. These values are determined by calculating averages from typical housing types in different construction year intervals (Agentschap NL, 2011) (De Waag, 2021). The calculated albedo values were checked and marginally adjusted (less than 0.01) with albedo calculations from remote sensing bands from the Landsat satellite (USGS, 2021) (Liang, 2001). Other building properties, such as mean -, area weighted - and standard deviation building height, are grid cell specific adopted from Ronda et al. (2017) using the NUDAPT approach (National Urban Data and Access Portal Tool) (Ching et al., 2009) (Figure 3.1c). Together with other grid cell specific geomorphological statistics, such as frontal area index and plan area fraction, neighbourhood-specific energy balance calculations can be made for the urban canyon, leading to a more accurate representation of meteorological variables in the urban area (Zhang et al., 2020). For completeness, the urban fraction has been displayed (Figure 3.1d) to demonstrate the urban density differences in the study area.

Following Monaghan et al. (2014), the value of the ‘Akanda’-parameter, was modified from default 1.29 (Kanda et al., 2007) to 0.4 (Table 3.1). This parameter affects the ratio of the roughness length for heat and the roughness length of momentum to enhance sensible heat exchange between urban canopy and atmosphere aloft. To grasp how sensitive such a change is, tuning this Akanda-parameter with the mentioned difference has a similar effect on RMSE performance of net radiation and sensible heat flux as albedo changes of roof and wall with 0.09 and 0.15 respectively (Loridan et al., 2010). For the anthropogenic heat flux (Table 3.1) we account for energy consumption, gas consumption (CBS, 2018a), traffic scaled for Amsterdam population density (Klok et al., 2010), and metabolic rate estimates from (Sailor & Lu, 2004).

Table 3.1: Used configurations in urban canopy model SLUCM (Kusaka et al., 2001).

TS_Scheme	4-layer model
CH_Scheme	2 (Narita scheme for the convective heat transfer coefficients within urban canopies)
Akanda (exchange variable)	0.4 Monaghan et al. (2014), parameter introduced by Kanda et al. (2007)
Thickness roof layers	0.23 m
Thickness of building wall	0.179 m
Thermal conductivity of road	$0.4 \text{ Js}^{-1}\text{K}^{-1}$
Thermal conductivity of wall	$0.4004 \text{ Js}^{-1}\text{K}^{-1}$
Thermal conductivity of roof	$0.48 \text{ Js}^{-1}\text{K}^{-1}$
Heat capacity of road	1.4 MJK^{-1}
Heat capacity of wall	1.3 MJK^{-1}
Heat capacity of roof	1.65 MJK^{-1}
Surface albedo of road	0.2
Surface albedo of wall	0.2
Surface albedo of roof	0.175
Roughness length for momentum over ground (road) and roof	0.01 m
Roughness length for momentum over wall	0.0001 m
Maximum anthropogenic heat flux	38.5 Wm^{-2} (average 21.4 Wm^{-2})
Hourly weights of maximum Anthropogenic heat flux, starting from 0 to > 23 UTC	{ 0.16 0.13 0.08 0.07 0.08 0.26 0.67 0.99 0.89 0.79 0.74 0.73 0.75 0.76 0.82 0.9 1.0 0.95 0.68 0.61 0.53 0.35 0.21 0.18 }

3.2.2 Data assimilation

Data assimilation aims to describe the state of the atmosphere by steering model fields in the direction of observations in a statistical manner by limiting a cost function, and accounting for the uncertainties in the model results and observations (Barker et al., 2012). The observations used for data assimilation and for the independent evaluation of the model performance consist of five types:

1. Observations from WMO-certified SYNOP stations in the Netherlands, Germany and the UK;
2. Volume radar data from the C-band Doppler weather radar as operated by KNMI (Royal Netherlands Meteorological Institute) in the Netherlands (Beekhuis & Holleman, 2008);
3. Data from personal weather stations available from the Wunderground database (Wunderground, 2021);
4. Observations from the Amsterdam Atmospheric Monitoring Supersite (AAMS) which are solely used for verification (Ronda et al., 2017);
5. Rain gauge-adjusted radar data (Overeem et al., 2009), which is solely used for precipitation verification.

In the research set-up, three types of data assimilation have been sequentially applied in four simulations. Between brackets the abbreviated experiment names are given, used as reference in the next sections:

- No data assimilation (NO-DA)
- WMO stations data assimilation (WMO-DA)
- WMO stations data assimilation + radar data assimilation (RADAR-DA)
- WMO stations data assimilation + radar data assimilation + urban nudging using personal weather stations (URBAN-DA)

The observations from the WMO-certified stations and volume radar data are assimilated with the WRF module WRFDA 3.8.1. using variational data assimilation. This is presented in a flowchart (Figure 3.2) where the two-hourly WRFDA update cycle is shown left, and the internal WRFDA data assimilation iteration cycles shown right. An improved estimate (analysis) is made from a first-guess background model forecast and its respective error variances and the observations and predefined errors (Figure 3.2 internal WRFDA cycle, right). Thereafter this data assimilation is cycled until the final analysis has sufficiently converged, with a maximum of two (outer loop) x 200 (inner loop) iterations. A second outer-loop iteration accounts for nonlinear effects and includes more observations in the data assimilation process (Rizvi et al., 2008; Barker et al., 2012). The variational data assimilation uses a prescribed cost function to minimize the errors for both observations and the background forecast of the model. The background forecast of the model is determined by estimating the variance at one time step by comparing two overlapping 24-hour forecasts with 12 hour shifted lead times, also known as the NMC-method (Parrish & Derber, 1992). So, more specifically, forecast 1 starting at day 1 at 0 UTC and forecast 2 starting at day 1 at 12 UTC are compared at day 2 at 0 UTC, both on the largest domain 1 and leaps of 12 hours. At last, the lateral boundaries and the lower boundaries, such as soil moisture / temperature and sea surface temperatures are updated from ERA-interim every 6 hours. These update cycle of the lower boundaries is important to retain the model boundaries to realistic reanalysis values throughout the monthly run and will be crucial to maintain consistency in the 15-year reanalysis later on.

From the WMO observations we assimilate 2-m temperature and air pressure. Wind has not been assimilated, since pressure gradients are well-correlated with wind speed. Also surface humidity has not been assimilated, because it showed no improved skill in the data assimilation for this case (July 2014). The liquid water in the atmosphere can be adjusted via the radar data assimilation, in case of precipitation in the model or radar observations.

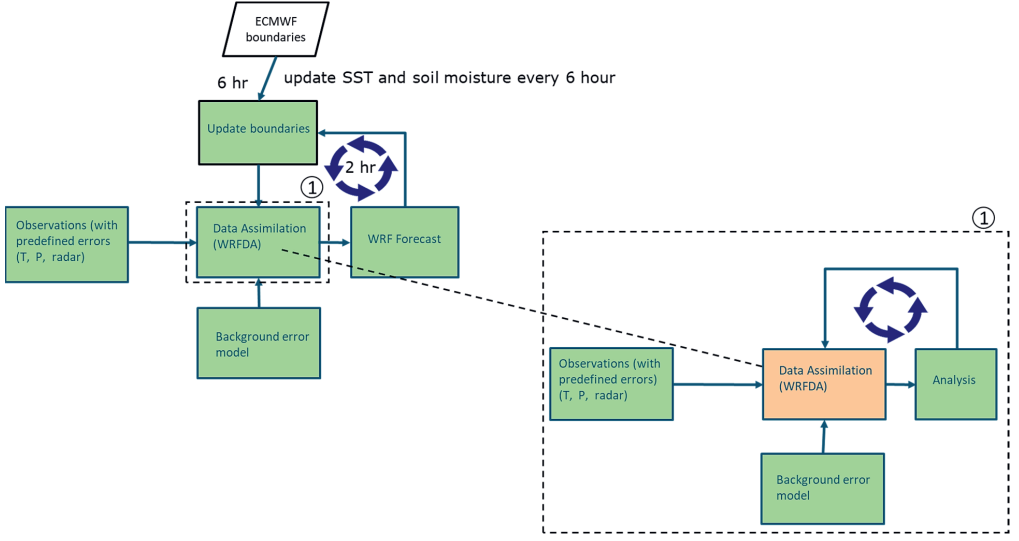


Figure 3.2: Flowchart of WRF update cycle (left) and the internal WRFDA model cycles (right).

For the radar data assimilation, we used the C-band Doppler weather radar located in De Bilt (52.099°N 5.176°E). As product, both radial (wind) velocity and reflectivities were used. Data from the lowest elevation angle (0.3°) was discarded, since this elevation contained a disproportional amount of clutter related to nearby buildings. From the remaining elevations, an average variance of 2 dBZ was calculated for the reflectivity employing the parameters of the volume scanning (Beekhuis & Holleman, 2008) and the method of Chumchean et al. (2003), see Equation 3.1. The variance of the radial velocity was supplied with the radar product.

$$\sigma_Z^2 = 0.13 \frac{R}{P} \quad (3.1)$$

σ_Z^2 = reflectivity measurement error variance (dB²)

R = observation range from the radar (km)

P = number of pulses per range bin.

Finally, the reflectivities and radial wind velocities are interpolated to model resolutions. The heights and locations of the C-band doppler radar observations have been calculated with the WRADLIB module (Heistermann et al., 2013). This module converts the data from a polar to a Cartesian representation and takes refraction into account.

In WRFDA different options exist for radar data assimilation, i.e. directly assimilating reflectivity or first converting to rainwater mixing ratios before data assimilation is applied. The latter is known as the indirect method and was used in Wang et al. (2013). This method has the advantage that the specific humidity remains more realistic in the whole atmosphere including better 2-m dew point temperatures. We adopt the method of Wang et al. (2013) as it has the most constraints for specific humidity in the atmosphere, which should also lead to a better representation of clouds. For details about this method, we refer to Wang et al. (2013).

Referring to data assimilation of observations taken in urban areas, we notice that the canopy scheme SLUCM does not interact well with WRFDA. This is because WRFDA needs control

variables among which pressure and temperature on model levels. These model levels starting from ~50 m are present above the urban canopy and therefore not part of SLUCM. The latter is crucial, because the control variables should be in balance with energy fluxes from the urban fabric i.e. roads and walls. Therefore, we propose a new method that “nudges” urban canopy temperatures within the canopy scheme, through adjustments in the wall and road temperatures of the scheme (see subsection ‘Nudging urban temperatures’ here in 3.2.2). To do so, a temperature bias must first be determined in the city by using personal weather stations (see subsection ‘Model bias correction with personal weather stations’ below in 3.2.2). The personal weather stations are not used to correct other meteorological variables as wind. Wind is not used for data assimilation for the urban areas, since the spatial and time representativeness at one given moment of wind measurements of weather hobbyists is too limited (Droste et al., 2020).

Model bias correction with personal weather stations

The estimation of the temperature bias differs between personal weather stations and WMO weather stations. Where WMO stations are sited according to well-defined standards and obtain a high degree of spatial representativeness, this is less obvious for personal weather stations in built-up areas (Bell et al., 2013). The urban environment is very heterogeneous on a local scale resulting in microclimates (Heusinkveld et al., 2014), and therefore single urban weather station records show little spatial correlation. This is confirmed by the inter- and intra local climate zone variability of a large number of personal weather stations in Berlin (Fenner et al., 2017). Local characteristics, such as north or south facing gardens and the difference between paved and a lawn show large variability in diurnal cycles of the UHI effect (Oke, 2006). The uniform signal of quality-controlled personal weather stations has been extracted by using a statistical model dependent on the weather at that time. This statistical model excludes specific weather station variability and intends to remove the cold biases in the urban area Ronda et al. (2017). The urban canopy temperatures are calculated with a revised SLUCM scheme of (Theeuwes et al., 2014), which applies the stability correction between the first model level (~50 m) and the 2-m level instead of between the first model level and the roughness length of heat.

This is not yet a representative urban temperature for the whole urban grid cell, which consists of a vegetation fraction (e.g. green backyards, parks). As in Ronda et al. (2017), urban grid cells in WRF consist of a paved urban canopy fraction (buildings and streets) and a separate vegetated fraction. Energy fluxes and air temperature are separately calculated for the urban tile in SLUCM and for the vegetated tile. A combined area-weighted urban-vegetation temperature, indicated by urban fraction, is calculated and is considered as a representative 2-m temperature for urban grid cells. Consequently this 2-m temperature is used in the statistical model.

The statistical model consists of a linear regression based on modelled weather variables to explain the difference between crowd-sourced temperature observations and modelled 2-m temperatures. The corresponding fit is shown in Equation 3.2 and is determined every 2 hours on domain 2 covering the Netherlands and downscaled to the other domains. This equation is then applied to all urban grid cells. The estimated ΔT_c is used to correct the model bias, and this is further described in the next subsection ‘Nudging urban temperatures’. Thus, the statistical fit reads as:

$$\Delta T_c = \alpha * L \downarrow + \beta * U + \gamma \quad (3.2)$$

ΔT_c = difference in urban temperature between model and personal weather stations from the statistical regression model (°C)

$L \downarrow$ = WRF modelled surface downward longwave radiation (Wm^{-2})

U = WRF modelled 10-m wind speed (ms^{-1})

α , β and γ = regression coefficients

It turns out that the biases (obs - model) were greatest in clear sky nights. Thus, personal weather stations facing cloudy conditions show generally smaller biases. As such, the incoming longwave radiation is a suitable variable to correct the model temperature state. Also, wind is an important factor, as a high wind speed mixes the air and therefore usually reduces the modelled UHI. On the contrary, urban characteristics like urban fraction and aspect ratio play no significant role in the statistical model. The aspect ratio is taken into account in the implementation of the temperature nudging in the urban canopy model (see next subsection ‘Nudging urban temperatures’). The longwave radiation and wind variable are retrieved from the model at the location of the personal weather stations.

The quality control of personal weather observations contains a number of steps. First, some personal weather station brands do not have proper radiation shields and are excluded beforehand at daytime (Bell et al., 2015). During daytime only Davis Vantage stations were used, since we are confident in their relatively small radiation error. The remaining stations can still report unreliable values due to effects of wrong placement or malfunctions. The number of crowdsourced personal weather stations and the long period of time makes it unfeasible to inspect, inquiry or trace these stations and determine if they meet proper placement criteria. Therefore, additional criteria have been applied to select acceptable stations for the statistical model:

- The observed temperature should not deviate from the model by more than 5 °C
- After the previous selection, a median is determined from the observed values of the remaining personal weather stations
- The remaining personal weather stations are discarded if their values deviate from the median $\pm 2 * \text{standard deviation}$
- Depending on the number of remaining observations:
 - o Equation 3.2 is fitted when there are enough observations, which has been set at >5
 - o For 3 or 4 observations, the median is recalculated
 - o With less than 3 observations, the number is too small to statistically correct the model
- In case the fitted statistical model is not significant ($p\text{-value} > 0.1$), the median is used to nudge the model.

Note that Meier et al. (2017) used a less strict $3 * \text{standard deviation}$ as threshold for omitting personal weather stations. However, the employed number of stations (Berlin) was substantially larger in their study than available for Amsterdam. The temperatures resulting from the urban data assimilation are verified against 22 independent urban weather stations (AAMS stations) within domain 4. The station on a small island in the IJ lake was excluded (see black star in Figure 3.1b), because it is non-urban and shows an atypical diminished diurnal cycle above the water surface

compared to land stations. The temperature sensors of the AAMS stations are shielded (Decagon VP-3) and ventilated and mounted at 4 m on lantern posts (de Vos et al., 2020).

Nudging urban temperatures

The correction, ΔT_c , is applied in the urban canopy model SLUCM via a nudging approach and serves as forcing for the model bias correction. This ΔT_c engages within SLUCM's original canopy temperature on the level of the roughness length of heat rather than the revised 2-m canyon temperature of Theeuwes et al. (2014). This choice is described after the explanation of the nudging concept.

We note that the nudged canopy temperatures cannot preserve the effect of nudging until the next data assimilation cycle, because no change in heat storage in the canopy is realized. Therefore, we adjust the urban fabric temperatures in such a way that it is consistent with ΔT_c as derived from Equation 3.2. This includes both walls and roads, which have a large heat storage. Accordingly, altering the temperature of the urban fabric is also more effective in altering energy fluxes which are fed back to the atmospheric model levels. Hence, the ΔT_c is redistributed to temperature corrections of the wall and road layers, while maintaining the physical formulation of the resistance scheme in Kusaka et al. (2001) (see Appendix). Thereby, the average diurnal temperature amplitude (difference maximum and minimum daily temperature) in each layer of urban fabric determines the proportion of the temperature correction applied. SLUCM consists of four road and wall layers. Smaller amplitudes belonging to deeper layers receive a smaller temperature correction and vice versa. So, urban fabric layers at the surface respond faster to temperature changes than the deeper layers imposed by the nudging approach. Hence, these often-raised temperatures for wall and road surfaces increase the aimed urban canopy temperature and the air temperature of the first model level ~50 m above SLUCM, via an increased sensible heat flux. The average diurnal cycle amplitudes are determined for all urban grid cells in the 4-day warm period of July 2014. Subsequently, amplitude factors are derived for the inner layers denoting the diurnal cycle amplitude relative to the largest diurnal cycle amplitude on the wall and road surfaces (Table 3.2).

Thus before changes can be applied to the four wall and road layers, ΔT_c is translated to a difference in wall surface and road surface temperatures $\Delta T_{w,g}$ (the suffix g standing for ground is used to be consistent with variable names in WRF). This has been calculated with Equation 3.3, which is based on the SLUCM resistance equations of Kusaka et al. (2001), and the complete derivation can be found in the Appendix. The temperature increments for wall and road layers are calculated by multiplying the $\Delta T_{w,g}$ with the accompanying amplitude factors (see Equation 3.6 and Table 3.2). In addition, in accordance with the amplitude determination for walls and roads, the soil temperatures are also adjusted for the vegetated fraction of urban cells. This is because personal weather stations temperatures are often measured in green backyards, which is not part of the paved urban canyon.

$$\Delta T_{w,g} = \Delta T_c \left(1 + \frac{w}{(2h + w)} \frac{C_{ah}}{C_w} \right) \quad (3.3)$$

$$C_{ah} = \frac{\kappa u_*}{\psi_h} \quad (3.4)$$

$$C_w = C_g = \begin{cases} 7.51 U_c^{0.78} & (U_c > 5 \text{ ms}^{-1}) \\ 6.15 + 4.18 U_c & (U_c \leq 5 \text{ ms}^{-1}) \end{cases} \text{ (Kusaka et al., 2001)} \quad (3.5)$$

ΔT_c = difference urban temperature between model and personal weather stations from the statistical regression model (predicted variable) ($^{\circ}\text{C}$)

$\Delta T_{w,g,s}$ = wall and road surface temperature and soil temperature ($^{\circ}\text{C}$)

h = wall height (m)

w = road width (m)

κ = karman constant = 0.4

u_* = friction velocity (ms^{-1})

ψ_h = Monin Obukhov stability term (-)

$C_{w,g}$ = heat transfer coefficient from wall and road to the canopy (ms^{-1})

C_{ah} = heat transfer coefficient from the canyon to the overlying atmosphere (ms^{-1})

U_c = urban canopy wind speed (ms^{-1})

$$\Delta T_{\text{layer}_{w,g,s}} = \Delta T_{w,g,s} * \text{amp}_{w,g,s} \quad (3.6)$$

Table 3.2: Diurnal cycle amplitude of temperature for wall (-), road and soil layers relative to the diurnal cycle amplitude of the skin (surface) temperature. Wall layers consists of four equally divided layers of 0.0448 m thickness. Road and soil layers increase with depth, 0.05 m, 0.25 m, 0.50 m, 0.75 m.

	Layer 1	Layer 2	Layer 3	Layer 4
Wall (amp_w)	0.709	0.503	0.357	0.253
Road (amp_g)	0.734	0.157	0.007	
Soil (amp_s)	0.499	0.015		

The magnitude of $\Delta T_{w,g}$ in Equation 3.3 depends on the heat exchange between the urban fabric and urban canopy, and the heat exchange between urban canopy and first model layer on top, which is dependent on wind speed and stability, see Equation 3.4 and 3.5. Thus, more unstable conditions allow for larger adjustments to road and wall layers with changing ΔT_c . The street width to building height ratio plays a significant role. In narrow urban canyons, the total heat exchange decreases between the urban fabric and the overlying atmosphere (first model level at ~ 50 m), and this leads to smaller adjustments to road and wall layers with the same ΔT_c . An example of a temperature adjustment of the outer wall is given in Figure 3.3. Here it is visible that the denser centre of Amsterdam has a smaller adjustment, because of a larger aspect ratio.

We chose to apply ΔT_c in Equation 3.3 on the level of the roughness length, because the newly defined 2-m canopy temperature by Theeuwes et al. (2014) is an output variable and not implemented in the iterative energy flux calculations within SLUCM. Adjusting the heart of the SLUCM code cause easily instabilities. As original canopy temperatures are located closer to walls and roads, it acts more as an effective skin temperature. Therefore, adjustments to roads and walls $\Delta T_{w,g}$ is smaller with the current method than when ΔT_c was applied on the 2-m level (the 2-m level is further away from the road and therefore leads to smaller heat transfer coefficient ratio $\frac{C_{ah}}{C_w}$ in Equation 3.3). Thus, the magnitude of the model correction, resulting from the adjustments of walls and roads is generally on the safe side, which is also a benefit since the nudging relies strongly to observations.

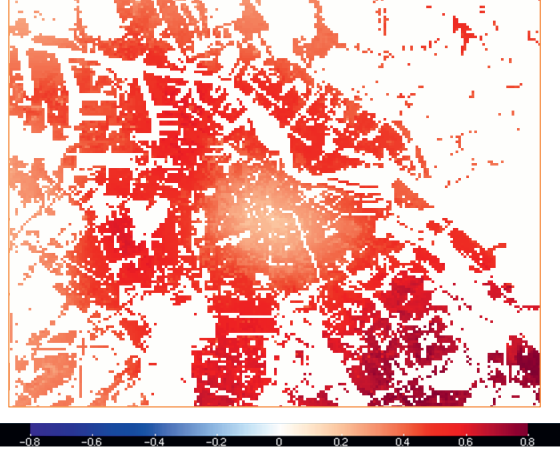


Figure 3.3: Example of outer wall temperature correction ΔT_w (in °C) due to the nudging approach on the evening of 2 July 2014 at 22 UTC.

3.2.3 Model evaluation methods

Different verification methods are applied to evaluate the performance of consecutive data assimilation steps. We use the bias and the root mean squared error to evaluate the model performance for air and dew point temperature, wind speed, and sea-level pressure. This evaluation is performed for seven selected WMO stations spread across the country (Figure 3.1a). All these stations provide observations suitable to apply in the data assimilation and are also used for model verification 1 and 2 hours after the data assimilation cycling. This time delay is considered sufficient to avoid serious dependence between cycling and verification. Nonetheless, for the verification of urban air temperatures, we make use of independent weather stations.

$$FSS = \frac{1}{N_{days}} \sum_{i=1}^{N_{days}} FSS(d) \quad (3.7)$$

$$FSS(d) = 1 - \frac{\sum_{i=1}^{N_x} \sum_{j=1}^{N_y} [O(d)_{i,j} - M(d)_{i,j}]^2}{\sum_{i=1}^{N_x} \sum_{j=1}^{N_y} O(d)_{i,j}^2 + \sum_{i=1}^{N_x} \sum_{j=1}^{N_y} M(d)_{i,j}^2} \quad (3.8)$$

$O(d)_{i,j}$ = observed fraction precipitation grid cells above threshold value over window i,j

$M(d)_{i,j}$ = model fraction precipitation grid cells above threshold value over window i,j

To verify the spatial representation of precipitation, the Fractional Skill Score (FSS) was calculated for daily accumulated precipitation of the consecutive data assimilation runs for domain 2 that covers the Netherlands. The FSS is a neighbourhood-based verification method to evaluate the spatial accuracy of precipitation (Roberts & Lean, 2008) and has been applied in real case verification studies (Ebert, 2009; Mittermaier et al., 2013; Skok & Roberts, 2016; Imhoff et al., 2020; Khain et al., 2020). In order to do so, the gauge-adjusted radar data (Overeem et al., 2009) have been transformed with an average weighted interpolation scheme (Met Office, 2018) to match the model resolution. The FSS calculates the skill of precipitation forecasts by comparing fractions of precipitation over a threshold in a certain spatial window between model and observations, see Equation 3.7 and 3.8. This window is moved in the horizontal and vertical direction over the entire

domain, and the FSS is determined as the spatial average. A FSS of 1 indicates perfect skill and 0 no skill. Evaluating fractions determined over a window has the advantage that the location differences of showers are not double-penalized.

A 90th percentile threshold has been chosen to evaluate the spatial accuracy of extreme precipitation (Skok & Roberts, 2016), and an average threshold to evaluate the spatial accuracy in general. Since evaluating spatial accuracy is the aim of FSS, the model and observation fractions are unbiased (Mittermaier et al., 2013). Hence, threshold values are separately determined for the model and observations. For the 90th percentile, this means that precipitation fractions comprise both 10% of domain 2 for model and observations. Correcting for bias is important, because a substantial bias would deteriorate the FSS and positive biases have larger impacts than negative biases because of the $M(d)_{i,j}^2$ in the denominator of Equation 3.8. The window or neighbourhood size is 50 km and, thus, consists of 20 x 20 cells with a resolution of 2.5 km according to domain 2. This window size is small enough for forecast purposes (Roberts & Lean, 2008).

3.3 Results

3.3.1 Model evaluation

In the model evaluation we first present monthly time series of the nearby KNMI weather station Schiphol Airport (WMO code 6240) (Figure 3.4), and statistics of pre-selected other WMO stations spread across the country (Figure 3.5). The diurnal cycles of air temperatures in the NO-DA run and WMO-DA run are well represented for most days. However, WMO-DA is able to remove or substantially reduce cold biases at clear nights, clearly visible on 13 and 29 July 2014. In NO-DA the maximum hourly cold bias amounts 3.5 °C on 13 July 2014 (virtually disappears in WMO-DA), and is reduced from 5.3 °C to 2.6 °C on 29 July 2014. Also maximum temperatures are better modelled in the WMO-DA run looking at biases, e.g. 11 July (2.5 °C to 1.0 °C), 16 July (3.2 °C to 0.8 °C), 27 July (3.3 °C to 0 °C) and 29 July (3.3 °C to 0.1 °C). On the other hand, the 9 July and 21 July are clear examples of cases which are both too warm in NO-DA and WMO-DA during daytime, which is related to a surplus of solar radiation.

Note that for solar downwelling radiation at the surface, no data assimilation was applied. Over the whole month the cloud cover is underestimated in the NO-DA and WMO-DA run, resulting in an overestimation of solar downwelling radiation. In addition, both WRF simulations have a surplus of surface solar radiation on clear days. The modelled surface pressure corresponds reasonably well for the model runs and observations, especially in timing and for high-pressure situations. Some low-pressure system occurrences remain too deep in the WMO-DA run. The WMO-DA run partly restores this around 21 July and 27 July 2014. The largest hourly deviations on these days reduced from 6.7 hPa to 3.4 hPa and from 3.2 hPa to 1.4 hPa respectively. The modelling system is unable to resolve the minimum pressure on 9 July (recall the deviations in solar radiation and temperature). Both WRF simulations have difficulties to correctly represent precipitation events, especially high-intensity precipitation. The model runs are in generally drier than the observations, with the largest deviation for NO-DA. Comparing precipitation at a point is not very representative due to spatial variability of convective precipitation, therefore we will perform a spatial analysis in Section 3.3.3.

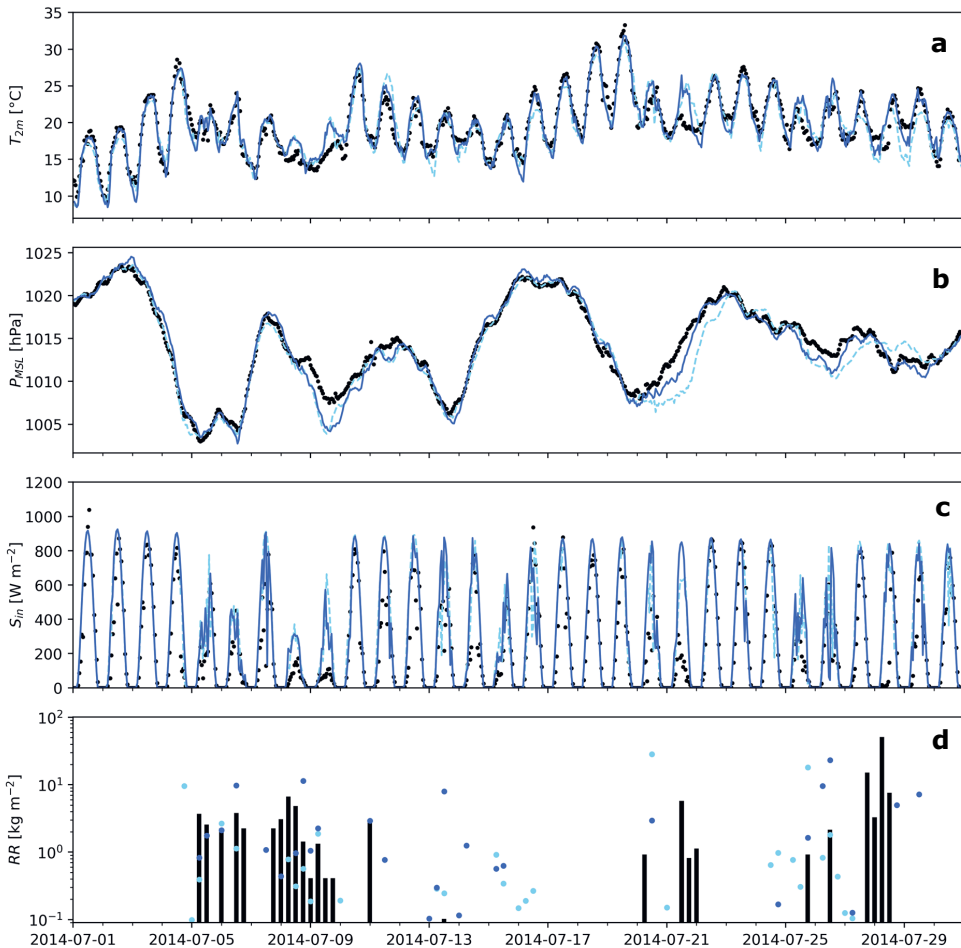


Figure 3.4: Times series of modelled and observed (a) 2-m temperature, (b) mean sea-level pressure further referred to as SLP, (c) downwelling solar radiation, and (d) precipitation at Schiphol airport weather station (52.301°N, 4.774°E, WMO code 6240) for July 2014. The black dots and bars indicate the observations, the dark blue solid lines and dots the WMO-DA run and the light blue dashed lines and dots the NO-DA run.

The statistics plots (Figure 3.5) show significantly lower root mean squared error (RMSE) for the WMO-DA run compared to the base NO-DA run for the rural WMO stations. Also the bias is overall smaller for the WMO-DA simulation, although this is less pronounced. The sea level pressure (SLP) and wind (FF) show smaller biases, 44 and 49% respectively in WMO-DA. For the dew point temperature a small positive bias (~ 0.3 °C) was introduced, but this is accompanied with a lower RMSE. The RADAR-DA run has only small changes compared to the WMO-DA run. RADAR-DA adjusts clouds and humidity on different model levels, which has a slightly negative effect on the RMSE of the dew point temperature (and indirectly on SLP). The bias, on the other hand, is improved for the dew point temperature and the air temperature. Straightforwardly, the URBAN-DA mimics the RADAR-DA, since the additional nudging in the urban canopy has no substantial impact on the rural station outside.

Noting the significant differences between simulations and observations (paired Student t -test, $\alpha = 0.05$), the RMSE is slightly larger for dew point temperature (TD) and wind speed (U). The RMSE for air temperature is also smaller (just significant for URBAN-DA and just not significant for RADAR-DA). The URBAN-DA should not have a substantial effect on the evaluated variables on the rural stations, which is confirmed by the large similarities of RADAR-DA and URBAN-DA.

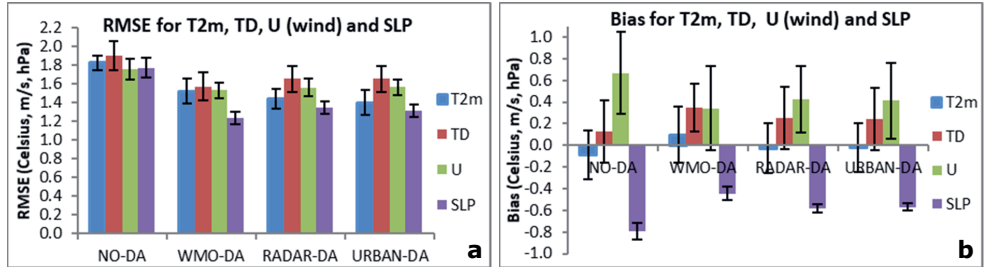


Figure 3.5: RMSE a) and Bias b) of 2-m temperature (T2m), dew point temperature (Td), wind speed (U) and sea level pressure (SLP), for the data assimilation model runs at seven WMO stations (see Figure 3.1a). The analysis is done on an hourly interval between 3 July (2 days spin up) and 29 July 2014. The bars indicate the standard deviation.

3.3.2 Heat wave case

The nudging of urban air temperatures (URBAN-DA) has also been evaluated for a warm episode between 16 July and 20 July 2014. Urban air temperatures are underestimated by WRF in clear nights for the simulations without urban nudging (NO-DA). Nudging crowdsourced weather data increases the nocturnal temperatures and decreases the bias with respect to independent urban observations (Figure 3.6a). In addition, the simulated hours in the warm period are closer to the 1 : 1 line in Figure 3.6b. With additional urban data assimilation (URBAN-DA) the bias decreases from -0.9°C to -0.2°C and the RMSE decreases from 1.5°C to 1.0°C . During daytime only small adjustments in urban air temperature are made by the nudging process, since the atmospheric boundary layer is well-mixed. The underestimation in maximum temperature is reduced to less than 1°C in URBAN-DA for all four days. The WMO-DA effectively reduce the cold bias in urban areas during daytime (Figure 3.6a), which means the cold bias is not caused by urban-specific processes. WMO-DA strongly reduces the cold bias for Schiphol (Figure 3.4a) and other stations during the warm period and affects urban areas via interpolated model fields. In addition, during daytime urban model temperatures in WMO-DA correlate better with rural WMO temperature observations compared to the night, because of day-time enhanced turbulent mixing and predominant temperature advection from the countryside.

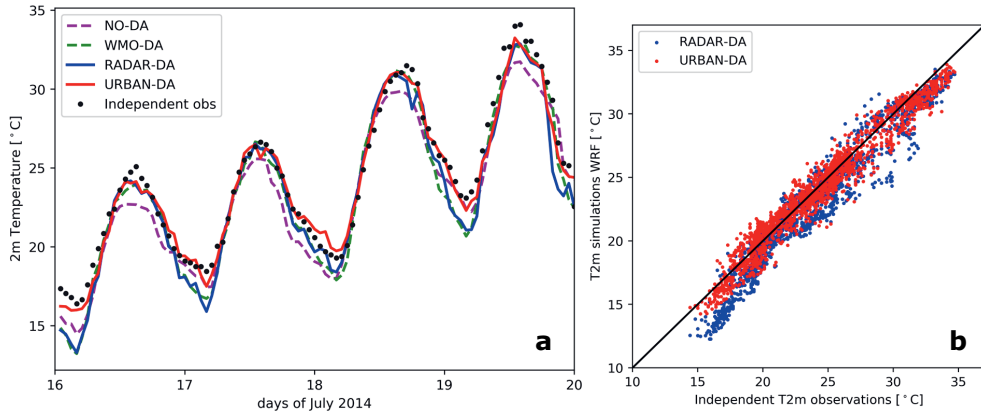


Figure 3.6: a) Time series of median 2-m air temperature of all model runs with consecutive data assimilation at observation grid points and median observations from independent AAMS urban weather stations in Amsterdam for the warm period from 16–20 July 2014. b) Scatter plot of modelled RADAR-DA and URBAN-DA, and observed 2-m air temperature from 16–20 July 2014.

Supplementary to the time series results, contour plots are shown for Amsterdam after urban nudging to provide a spatial overview (Figure 3.7). The minimum temperatures are clearly higher for the densely built areas of Amsterdam for July 2014. These areas are either largely paved or have a small sky-view factor. The fine resolution allows runways at Schiphol Airport to be distinguished as warmer areas. The canals and the large water body, the IJ, can be distinguished as cooler places than the adjacent urban areas. The parks and rural parts adjacent to the city are relatively cool and are only slightly warmer than the rural areas further away (~ 0.3 °C). Therefore, it can be stated that (intra)-urban heat advection does not play a substantial role for modelled minimum temperatures and corresponding results apply for average temperatures in the model context at this grid spacing. In the average monthly urban temperatures, temperature differences between cities and the rural counterparts are smaller, due to the lower daytime UHI. Water surfaces are relatively cool at daytime. Maximum temperatures, lastly (not shown), are only 0.5–1.0 °C warmer for urban areas compared to the rural environment.

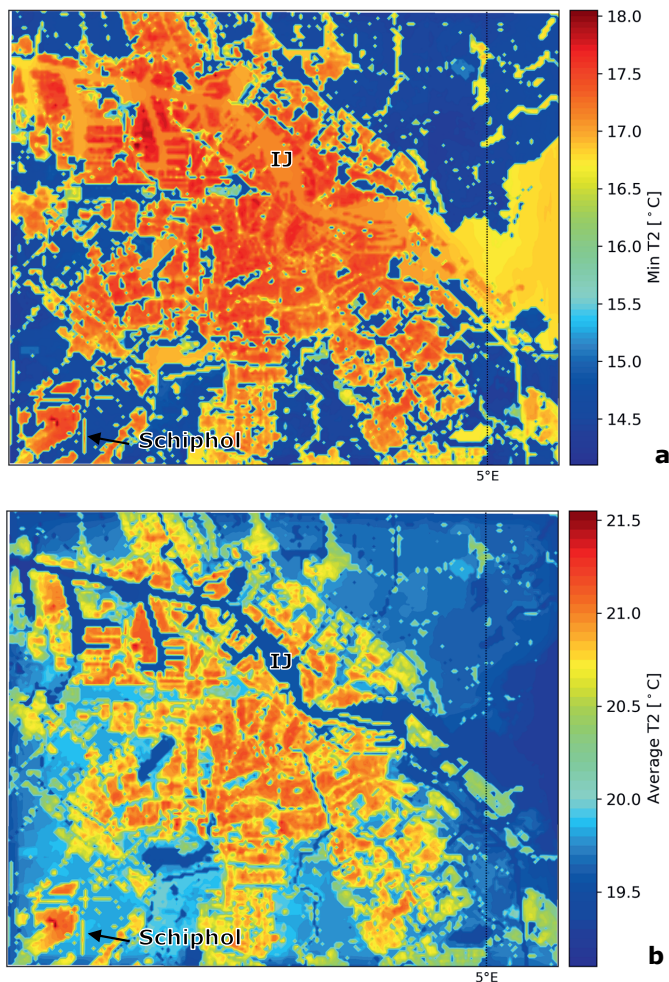


Figure 3.7: a) Daily minimum temperature and, b) Monthly mean modelled 2-m air temperature (URBAN-DA) on hourly intervals for 3–31 July 2014.

3.3.3 Extreme precipitation

In order to evaluate the modelled extreme precipitation for each of the data assimilation steps, 28 July 2014 is selected as an example of extreme precipitation over Amsterdam, which resulted in precipitation sums over 100 mm in 24 hours with flooding in parts of the city (Figure 3.8). The synoptic pattern is characterised by little background flow at 850 hPa, and hence the development of showers is strongly bound to a local circulation influenced by land–sea interactions and the diurnal cycle. Below we evaluate the NO-DA, WMO-DA and RADAR-DA run (Figure 3.8), and describe their differences using time series and a skill score designed for precipitation (Figure 3.9).

In the NO-DA run, a high-pressure area arises above the North Sea counteracting the warm moist air masses on land. This leads to a weak northerly flow over the Netherlands transporting relatively cool and dry air which suppresses deep convection. In addition, the air flow is

diffluent, which is associated descending air motions. The WMO-DA run is able to create a convergence zone, which in the moist unstable air leads to heavy showers. This is related to a better representation in surface pressure (Figure 3.4). The maximum daily precipitation amounts (127 mm) are close to those using the radar estimates (116 mm) (Figure 3.8). Unfortunately, the location of this convergence zone and extreme rainfall is ~ 150 km to the south of what was observed by the radar. In the afternoon the gauge-adjusted radar product has the largest precipitation intensities in the east of the country. WMO-DA is able to generate convective precipitation in this area, although this convective precipitation is more widespread and dispersed with lower intensities. The development of storms in the east seen in the gauge-adjusted radar is also not present in WMO-DA either.

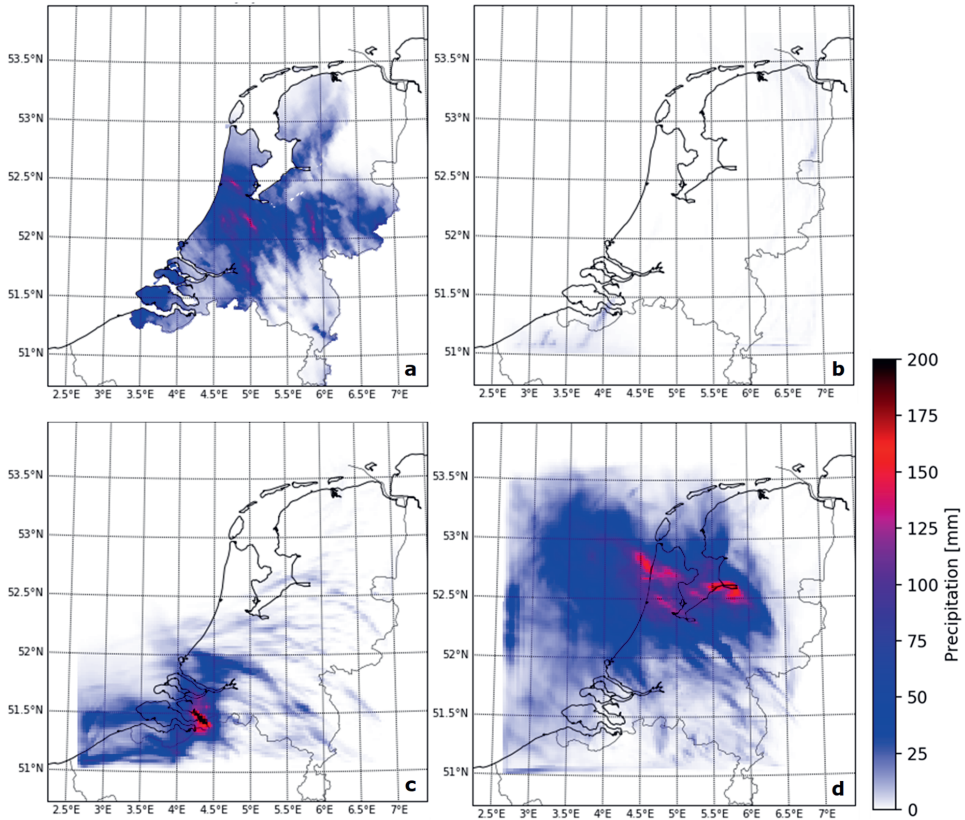


Figure 3.8: Cumulative daily precipitation on 28 July 0 UTC – 29 July 0 UTC for NO-DA (b), WMO-DA (c) and RADAR-DA (d) and radar observations (a), for domain 2. The rain observations represent the rain gauge-adjusted radar data.

The RADAR-DA run is able to simulate the heavy convective precipitation at the approximate location compared to the gauge adjusted radar. With the assimilated convective precipitation, the model is able to create the convergence zone in the middle of the country. Therefore, 28 July 2014 shows a clearly improved performance utilizing radar data assimilation. Until 28 July 2014 13 UTC the radar run resembles the gauge-adjusted radar data. The northwest-southeast oriented convergence line is well represented by the RADAR-DA run (and URBAN-DA). Thereafter, the most active precipitation in the convergence line will remain in the northwest in the radar run,

while the gauge-adjusted radar data shows activation in the east of the country on this convergence line. At the end of the afternoon the location of convective precipitation diverges between RADAR-DA and the gauge-adjusted radar. The convergence line itself is still present in the RADAR-DA run (and URBAN-DA run). On other days with convective precipitation, the improvement of consecutive data assimilation steps is less distinct.

The performance of multiple precipitation days is reflected in the FSS (Figure 3.9a), and daily accumulated precipitation (Figure 3.9b). The FSS shows better scores for average daily precipitation and extreme precipitation (90th percentile) with each additional data source used for assimilation, although the differences are small (Figure 3.9a), and there is a large spread among individual days. In the Discussion section (3.4) we further examine which FSS value should be considered as useful predicting value. Figure 3.9b presents the daily averaged precipitation sums for the Netherlands domain. On average, the runs without radar data assimilation (NO-DA and WMO-DA) produce too little precipitation. For most days those runs resemble each other, except for the last decade of July, including the July 28th. Occasionally WMO-DA has a substantial impact on the simulated precipitation fields leading to better precipitation sums. RADAR-DA and URBAN-DA, on the contrary, overestimate the precipitation and differ extensively from the runs without data assimilation. From July 24th onwards, the runs with radar data assimilation (RADAR-DA and URBAN-DA) resemble the gauge-adjusted radar much more closely than the runs without (NO-DA and WMO-DA). In the other rainy periods, the magnitude of the biases is similar but reversed between these runs (7–12 July), or the radar data assimilation runs show separately an overestimation of precipitation (20–21 July). The URBAN-DA simulation is very similar to the RADAR-DA run regarding precipitation, since urban data assimilation only marginally impacts urban temperatures at daytime, which therefore has a small impact on the development of convective precipitation.

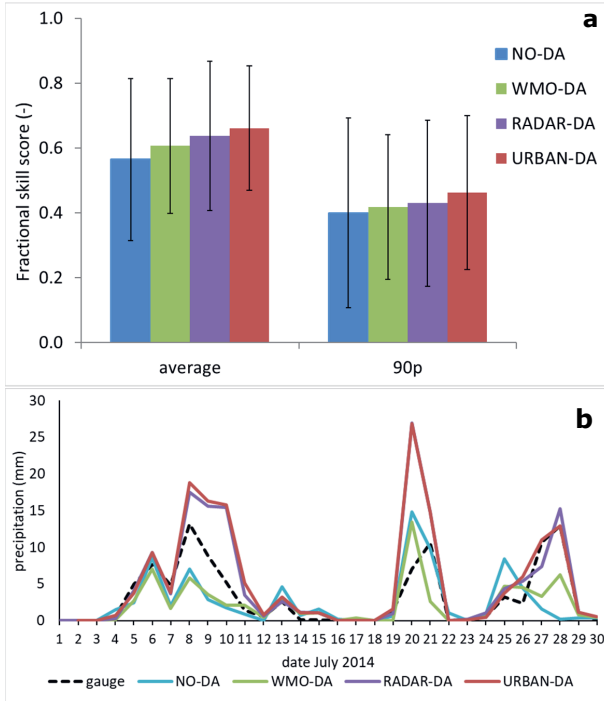


Figure 3.9: a) Average fractional skill scores for the consecutive data assimilation runs for days with precipitation for domain 2. The bars indicate the standard deviation of average FSS and 90th percentile (90p) FSS of the different days. b) Daily precipitation sums for the consecutive data assimilation runs and gauge adjusted radar as reference for domain 2. Precipitation outside the land surfaces of the Netherlands are excluded in the model simulations according to the gauge adjusted radar data in Figure 3.8a.

3.4 Discussion

3.4.1 Urban data assimilation.

The inclusion of observations from personal weather stations in reanalysis products is new and challenging. As such there have been attempts to include citizen observations in operational forecasts via data assimilation (4D-Var). For example, the meteorological services in Norway (MET Norway) have introduced citizen weather observations in the postprocessing of their forecasts (Nipen et al., 2020). A Kalman filtering approach has been applied to spatially interpolate innovations (difference between observation and model just before the data assimilation cycling) by the observation to form a gridded truth. A remarkable similarity between Kalman filtering and the urban nudging presented in the current work is that the so-called innovation at a station is less or not spread across meteorological features such as fronts. In our fit, wind and clouds generally cause smaller innovations as the UHI is suppressed during such conditions; and Kalman filtering can determine the lack of correlation of innovations across such features in the gridded truth, preventing single innovations at one observing station affecting areas with different weather. Computational 4D-Var data assimilation requires linear approximations used in a tangent linear model (Courtier et al., 1994). In a complex urban boundary layer this linear model error evolution holds for districts with high aspect ratios like downtown Hong Kong, while other urban geometries exhibit such linear model error evolution to a lesser extent, leading to lower accuracy (Ngan & Lo,

2017). Lastly, the data assimilation of personal weather station observations in operational forecasts is investigated by several European National weather institutes as the Danish – and Finnish Meteorological Institute and the Deutscher WetterDienst (Hintz et al., 2019).

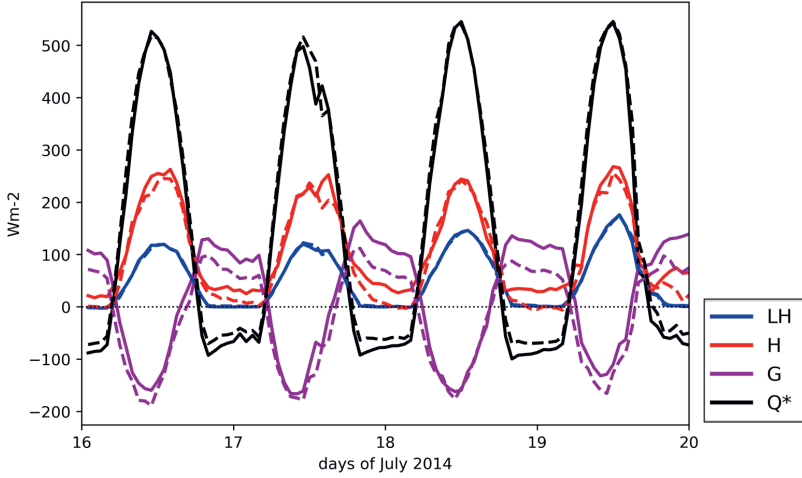


Figure 3.10: Modelled energy balance for URBAN-DA (full line) and RADAR-DA (dashed line) for the average of the AAMS urban stations locations, for the 4-day warm period (corresponding Figure 3.6). H denotes sensible heat flux, LH denotes latent heat flux, G denotes storage heat flux, and Q^* denotes the net radiation.

Here, we illustrate the impact of the urban nudging technique on the modelled surface energy balance during the 4-day warm period (Figure 3.10). The net radiation is calculated as the sum of the modelled energy fluxes. The energy fluxes are typically associated with an urban surface, best seen in the storage heat flux. The maximum storage heat flux in the morning amounts to 150 Wm^{-2} , while the soil heat flux for a rural grassland area typically amounts to 30 Wm^{-2} (Cleugh & Oke, 1986).

For URBAN-DA it appears that increasing the temperature of wall, road and soil layers leads to an increased release of stored heat and an increase in the sensible heat flux, which is most pronounced at night (Figure 3.10). On clear nights in the warm period the sensible heat flux typically is 30 Wm^{-2} larger for URBAN-DA compared to RADAR-DA. The storage heat flux is $\sim 50\%$ larger. The difference can be explained by the increased skin temperature and an associated increase in outgoing longwave radiation. During the day, the difference in energy balance between URBAN-DA and RADAR-DA is smaller. At solar noon around 47% of the net radiation is used for sensible heat flux (RADAR-DA 46% and URBAN-DA 48%). This H/Q^* ratio is close to the urban sites of Basel $\sim 51\%$, (Christen & Vogt, 2004) and lies within the range of 75th percentile July energy fluxes of downtown London (Kotthaus & Grimmond, 2014). In a high-rise district of Marseille the H/Q^* ratios are around 60%, (Grimmond et al., 2004), which matches the denser urban sites of Amsterdam with low green fraction (48-61% for RADAR-DA and 51-64% for URBAN-DA). On the other hand, Kato et al. (2007) shows for the city of Nagoya considerably lower H/Q^* ratios, which is related to low sky-view factors and related obstruction of solar radiation of tall buildings.

The storage heat flux consists of 29% and 25% of the net radiation (G/Q^*) for RADAR-DA and URBAN-DA at solar noon. These results correspond with the observed storage heat flux for the urban districts of Basel (Christen & Vogt, 2004). The maximum G/Q^* ratio is modelled in

the morning at 7–8 UTC and amounts to 41% for RADAR-DA and 37% for URBAN-DA and these values are in the range of the different urban districts of Basel (Christen & Vogt, 2004), and is close to different cities in North America (Grimmond & Oke, 1999). Thus, this means that in general the energy partitioning in the urban area is in agreement with typical values in the literature both for URBAN-DA and RADAR-DA.

3.4.2 Radar data assimilation

The runs without radar data assimilation appear to have too little precipitation. It is worthwhile to also review the Era-Interim dataset, which has been used as boundary condition. The near-surface conditions of temperature and humidity are captured well relative to their resolution, since there are enough high-quality observations available for the reanalysis. However, the relative and specific humidity is likely too low for the layers between 925 hPa and 775 hPa, due to a known dry bias of radiosonde observations (Vaisala RS90/92) used in the Era-Interim (Simmons et al., 2010). The dry bias is confirmed by comparing these type of radiosonde measurements with reference satellite-based measurement systems (GPSRO and GCOS) (Ladstädter et al., 2015). This dry bias has likely a reduced effect on shower development and precipitation rates. At screen level (~ 1.5 m), the NO-DA run does not reveal a dry bias looking to the dew point temperature verification (Figure 3.5), which is in accordance with Era-Interim showing no structural bias in humidity near the surface (Simmons et al., 2010). So, among other processes (e.g. data assimilation of weather stations), too dry model levels higher up are not forcing a reduction of the humidity near the surface.

Large differences in FSS are observed between individual days displayed in the large standard deviations in Figure 3.9 (0.19 – 0.25 for average precipitation and higher for the 90th percentile). On many days there is not a clear signal that the model sufficiently adopts the location of precipitation observed by the radar. We suppose the model often has a non-supportive atmosphere for shower development. In that case, eventually adopted radar signals of showers die down quickly, so that they are not perceived in the model run. That non-supportive atmosphere is substantiated with the radiosonde-related dry biases (Ladstädter et al., 2015). In addition, the related convection of the showers should be assimilated (via radial wind velocity) in an early stage of development (Bachmann et al., 2019), which is not commonplace every day.

The FSS deviates between 0 (no skill) and 1 (perfect skill). To put the score in a perspective, a random forecast FSS_{random} equates the fraction of threshold exceedances (10% threshold exceedances is a FSS_{random} of 0.1). The average FSS_{random} is 0.31 and the 90th percentile (90-p) FSS_{random} is 0.10 for days with precipitation in July 2014. Achieving this benchmark is a very minimal performance. Consulting literature (Roberts & Lean, 2008; Skok, 2015) suggests FSS should be at least >0.5 to be useful, which is the case for our model results. Moreover, Roberts and Lean (2008) proposed to use $FSS_{uniform}$ as skill parameter, which is defined as $FSS_{uniform} = 0.5 + f/2$. Herein f is the fraction threshold exceedances for radar observations. The $FSS_{uniform}$ is 0.66 for the average FSS and 0.55 for the 90-p FSS. According to Figure 3.9, the criterium is just met for the average FSS (0.66) and not met for the 90-p FSS (0.46). In addition, Skok, (2015) obtained the FSS_{useful} , which is an analytical solution corresponding a rain band which is displaced half the size of neighbourhood size. Although Skok (2015) obtained an objective benchmark, the FSS_{useful} is less interpretable in situations with multiple rain areas (see e.g. 28 July, Figure 3.8a) that is less than the neighbourhood length apart, which also occur in our study. In addition, rain bands might be interrupted, since lighter precipitation patches within the rainband may not exceed the threshold. This especially applies for the 90th percentile results.

3.5 Conclusion

In this study, we investigate how WRF simulations can be improved by applying consecutive data assimilation steps (WRF 3D-Var) and nudging techniques for the urban environment of Amsterdam at a 100-m grid spacing. Assimilated observations consist of WMO synoptic weather observations, volume radar data and urban weather observations recorded by personal weather stations. Specific for the urban canopy, a novel approach has been developed to nudge temperatures with quality-controlled personal weather observations. Hindcasts are presented for July 2014 for Amsterdam, which inhibits both a warm dry period as days with extreme precipitation. We have demonstrated that data assimilation of 2-m air temperature, dew point temperature and pressure from WMO stations largely improve the background fields. The assimilation of weather radar observations shows a slightly better performance in the location of precipitation fields. In addition, the data assimilation of personal weather station observations reduces the cold biases at night within the urban canopy and it produces more realistic energy fluxes. The findings and best practices will be used to create a 15-year urban reanalysis for Amsterdam, which increases knowledge in urban climatology and enables to trace trends in thermal comfort and extreme precipitation.

Acknowledgements

The authors acknowledge funding from NWO-eScience project 027.014.203 (ERA-urban) and from the AMS Institute (grant VIR16002) for supporting the Amsterdam Atmospheric Monitoring Supersite. The authors also acknowledge the funding from UK EPSRC Data assimilation for the Resilient City (DARE). In addition, funding from NWO grant 864.14.007 was employed for this research.

Appendix

Derivation of wall and road temperature increments

This Appendix presents the derivation of temperature increment of wall and road layers based on differences in modelled–observed urban canopy temperature ΔT_c . Our point of departure is the formulation of the sensible heat flux from walls H_w and H_G roads (Kms^{-1}) in the SLUCM model (Kusaka et al., 2001) and visualised in Figure A3.1.

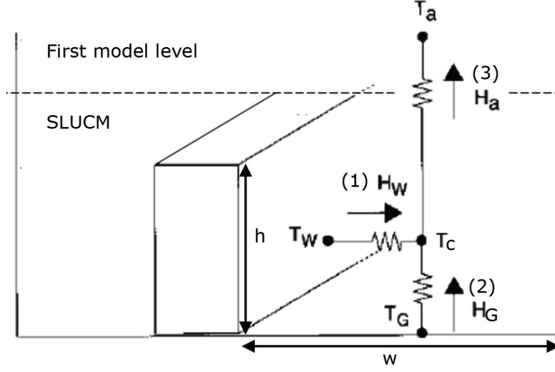


Figure A3.1: Schematic of SLUCM with the relevant energy fluxes adapted for urban nudging. Reused and adapted from Kusaka et al. (2001) with permission.

$$H_w = C_w(T_w - T_c) \quad (\text{A3.1})$$

$$H_G = C_G(T_G - T_c) \quad (\text{A3.2})$$

Herein T_w and T_G are the wall and road temperature (K), T_c the urban canopy temperature (K), and C_G and C_w the heat transfer coefficients (ms^{-1}) that have been parameterized as follows:

$$C_w = C_G \begin{cases} 7.51U_c^{0.78} & (U_c > 5\text{ms}^{-1}) \\ 6.15 + 4.18U_c & (U_c \leq 5\text{ms}^{-1}) \end{cases} \quad (\text{A3.3})$$

Herein U_c is the wind speed at the canopy level of T_c . In addition, the sensible heat exchange through the canyon top towards the overlying atmosphere H_a (Kms^{-1}) is parameterized using classical Monin-Obukhov theory:

$$H_a = \frac{\kappa u_*}{\psi_h}(T_c - T_a) \quad (\text{A3.4})$$

In which κ is the Von Karman constant (-), u_* the surface friction velocity (ms^{-1}), ψ_h the stability correction (-) and T_a the air temperature (K) at the first model layer.

In Figure A3.1, w represents the road width and h the building height (m). Conservation of these energy fluxes (with no storage in the urban canopy) requires that:

$$wH_a = 2hH_w + wH_G \quad (\text{A3.5})$$

The ratio $2h$ for walls compared to w for roads arise, because there are two walls on both sides of one road in an urban canopy.

Inserting Equation A3.1, A3.2, A3.4 in Equation A3.5 results in:

$$w \frac{\kappa u_*}{\psi_h} (T_c - T_a) = 2hC_w(T_w - T_c) + 2hH_w + wC_G(T_G - T_c) \quad (\text{A3.6})$$

Bring T_a in front, because later on we can set changes in T_a to 0 between two data assimilation cycles.

$$w \frac{\kappa u_*}{\psi_h} T_a = w \frac{\kappa u_*}{\psi_h} T_c - 2hC_w T_w + 2hC_w T_c - wC_G T_G + wC_G T_c$$

$$T_a = T_c - \frac{\psi_h 2hC_w T_w}{w\kappa u_*} + \frac{\psi_h 2hC_w T_c}{w\kappa u_*} - \frac{\psi_h wC_G T_G}{w\kappa u_*} + \frac{\psi_h wC_G T_c}{w\kappa u_*}$$

$$T_a = T_c \left(1 + \frac{\psi_h 2hC_w}{w\kappa u_*} + \frac{\psi_h wC_G}{w\kappa u_*} \right) - \frac{\psi_h 2hC_w T_w}{w\kappa u_*} - \frac{\psi_h wC_G T_G}{w\kappa u_*}$$

Write the equation as differences Δ denoting the changes in canopy and wall and road temperatures. Assume $\Delta T_a = 0$, since the first model layer is not part of SLUCM and serves as boundary condition.

$$\frac{\psi_h 2hC_w \Delta T_w}{w\kappa u_*} + \frac{\psi_h wC_G \Delta T_G}{w\kappa u_*} = \Delta T_c \left(1 + \frac{\psi_h 2hC_w}{w\kappa u_*} + \frac{\psi_h wC_G}{w\kappa u_*} \right)$$

$$2hC_w \Delta T_w + wC_G \Delta T_G = \frac{\Delta T_c \left(1 + \frac{\psi_h 2hC_w}{w\kappa u_*} + \frac{\psi_h wC_G}{w\kappa u_*} \right)}{\frac{\psi_h}{w\kappa u_*}} = \Delta T_c \left(\frac{w\kappa u_*}{\psi_h} + 2hC_w + wC_G \right)$$

Subsequently, assume $\Delta T_g = \Delta T_w$ since $C_w = C_G$

$$(2h + w)C_w \Delta T_w = ..$$

$$C_w \Delta T_w = \frac{\Delta T_c \left(\frac{w\kappa u_*}{\psi_h} + 2hC_w + wC_w \right)}{2h + w} = \Delta T_c \frac{w\kappa u_*}{\psi_h(2h + w)} + \frac{\Delta T_c C_w(2h + w)}{(2h + w)}$$

$$C_w \Delta T_w = C_w \Delta T_c \left(1 + \frac{w\kappa u_*}{\psi_h C_w(2h + w)} \right)$$

The final result (A3.7) matches Equation 3.5 of the main paper with the full notation $C_{ah} = \frac{\kappa u_*}{\psi_h}$

$$\Delta T_{w,G} = \Delta T_c \left(1 + \frac{w\kappa u_*}{\psi_h C_w(2h + w)} \right) = \Delta T_c \left(1 + \frac{w}{(2h + w)} \frac{\kappa u_*}{\psi_h C_w} \right) = \Delta T_c \left(1 + \frac{w}{(2h + w)} \frac{C_{ah}}{C_w} \right) \quad (\text{A3.7})$$

Chapter 4

Urban planning strategies on heat stress for current and future climates

Abstract

In the Netherlands, there will be an urgent need for additional housing by the year 2040, which mainly has to be realized within the existing built environment rather than in the spatial extension of cities. In this data-driven study, we investigated the effects of different urban planning strategies on heat stress for the current climate and future climate scenarios (year 2050) for the urban agglomeration of The Hague. Heat stress is here expressed as the number of days exceeding minimum temperatures of 20 °C in a year. Thereto, we applied a diagnostic equation to determine the daily maximum urban heat island based on routine meteorological observations and straightforward urban morphological properties including the sky-view factor and the vegetation fraction. Moreover, we utilized the Royal Netherlands Meteorological Institute's (KNMI) climate scenarios to transform present-day meteorological hourly time series into the future time series. The urban planning strategies differ in replacing low- and mid-rise buildings with high-rise buildings (which reduces the sky-view factor), and constructing buildings on green areas (which reduces the vegetation fraction). We found that, in most cases, the vegetation fraction is a more critical parameter than the sky-view factor to minimize the extra heat stress incurred when densifying the neighbourhood. This means that an urban planning strategy consisting of high-rise buildings and preserved green areas is often the best solution. Still, climate change will have a larger impact on heat stress for the year 2050 than the imposed urban densification.

This chapter is based on:

Koopmans, S., Ronda, R. J., Steeneveld, G. J., Holtslag, A. A. M., & Klein Tank, A. M. G. (2018). Quantifying the effect of different urban planning strategies on heat stress for current and future climates in the agglomeration of The Hague (The Netherlands), *Atmosphere*, 9(9), 353. doi:10.3390/atmos9090353

4.1 Introduction

Climate change is expected to affect society substantially in terms of increased temperatures and precipitation, as well as more frequent weather extremes (IPCC, 2013; IPCC, 2014a). Sophisticated climate-change projections were carried out for many countries including the Netherlands. However, these projections mostly focus on rural areas, while policy makers are also interested in how they can make future cities more heat resilient. The Netherlands has the challenge of realizing one million new houses by the year 2040, which mainly need to be created within the existing built environment. This study aims to clarify how climate change evolves in Dutch cities, and which urban morphological factors need to be modified in order to reduce heat stress.

Temperatures in cities are typically significantly higher for most of the day compared to their rural surroundings (Oke, 1982). The heat stress due to these higher temperatures has a significant impact on health (Clarke, 1971; Basu & Samet, 2002). These elevated urban temperatures are known as the urban heat island (UHI), which is defined as the difference in 2-m air temperatures between a city and the surrounding countryside. Many factors contribute to a warmer urban environment. In general, the radiation balance of a city is altered due to its complex canyon structure, which results in a relatively small albedo, and thus, a large energy gain for the urban surface (Aida, 1982). Furthermore, the energy balance of urban areas is different from rural areas due to the lower sky-view factor (Oke, 1982; Holmer, 1992), enhanced impervious surfaces (initiating a higher sensible heat flux at the expense of the latent heat flux), and anthropogenic heat release (Allen et al., 2011). Because of the relatively large heat conductivity and thermal capacity of the urban fabric, cities can store more heat during the daytime than rural environments. This energy is released after sunset creating the largest UHI in the evening or onset of the night. The elevated temperatures in urban areas affect human health and are a significant contributor to the excess mortality observed during heat waves (Clarke, 1971; Basu & Samet, 2002). High nighttime temperatures have adverse effects on human health by preventing an adequate recovery from daytime heat and by inducing sleep deprivation (Fischer & Schär, 2010). The best-known examples for western Europe were the high number of excess deaths in France during the heat waves of 2003 and 2006 (Fouillet et al., 2006; Joe et al., 2016). In the Netherlands, the number of excess deaths was estimated to be between 1400 and 2200 in the summer of 2003 (Garssen et al., 2005).

The UHI is difficult to quantify directly with observations since the availability of long-term climatologic observational data in cities is limited. This is because official weather stations are preferably located in open rural or natural areas with the aim of obtaining a substantial spatial representativeness (WMO, 2014). Consequently, long-term climatological observations to monitor urban heat are rarely available for cities. Other observational sources from urban areas such as amateur weather station data or field campaign data generally do not cover long periods, and the data often represent only small areas due to the high variability in temperature within the urban area setting (Steenveld et al., 2011a; Brandsma & Wolters, 2012). To overcome this lack of observations, the UHI is often modelled using sophisticated atmospheric mesoscale models coupled to an urban canopy (Kusaka et al., 2001; Chen et al., 2011; Salamanca et al., 2011; Ronda et al., 2017). However, those models require large amounts of initial urban morphological data, which are often inaccurate and sometimes not available (Theeuwes et al., 2017). Another approach is to measure the UHI with remote sensing techniques (Roth et al., 1989; Yuan & Bauer, 2007). However, correlations between remote sensing derived surface temperatures and air temperatures are weak, due to the absence of advection and flux divergence in the air volume (Roth et al., 1989). In addition, the intervals of the revisiting times restrict a dynamical analysis of UHIs (Yuan & Bauer, 2007).

As an alternative approach, in this study, we diagnosed the daily maximum UHI by applying an empirical formula designed by Theeuwes et al. (2017). With this approach, we calculated urban minimum temperatures and compared them with rural minimum temperatures. The data needed in this equation consist of routine meteorological observations and morphological city characteristics. A novel concept is the application of this equation to determine the UHI for current and future climates in an urban agglomeration. As a testbed, we computed the UHI for the agglomeration of The Hague in the Netherlands (Figure 4.1). Previous research shows that cities of varying size in a maritime climate such as the Netherlands may experience severe heat stress (Steenneveld et al., 2011a). This also holds for near-coastal cities like Rotterdam where nocturnal UHIs are up to 7 °C during clear heat-wave days (Heusinkveld et al., 2014). Molenaar et al. (2016) estimated that the number of hours of experienced heat stress, here defined as the hours with physiologically equivalent temperatures above 23 °C, will double from the current average of about 250 hours per year to slightly more than 500 hours per year under the warmest KNMI (Royal Netherlands Meteorological Institute) climate scenario.

Also a novel concept, we investigated the impact of construction plans on the magnitude of the UHI. In the future, the Dutch government will face the challenge of building an additional one million residences before the year 2040 (EIB, 2015). A substantial part of this new construction has to be developed within existing urban areas. This means that the population density will increase, which will apply pressure to the heat resiliency of cities. For instance, Steenneveld et al. (2011a) found a good correlation between the higher percentiles of UHI and population densities for Dutch cities of various sizes. Within the current research, we investigated the effect of different urban planning strategies on heat stress for current and future climate scenarios by creating heat maps with a resolution of 100 m. The urban planning strategies refer to the redevelopment and the construction of additional residences within the urban neighbourhoods. The construction differs between high-rise buildings and low- and mid-rise buildings. The choice has consequences for the urban morphological characteristics of an urban area, as vegetation fractions and sky-view factors are important parameters in determining the UHI. The aim of this study was to estimate urban nighttime temperatures for current and future climate in order to obtain measures which reduce the UHI.

This chapter is organized as follows: Section 4.2 summarizes the modelling approach and introduces the climate scenarios and urban planning strategies we explored. Section 4.3 presents the results we obtained. Finally, in Sections 4.4 and 4.5, we reflect on our modelling approach and outcomes, and we draw conclusions.

4.2 Methods

This section presents the followed research methodology, the utilized KNMI climate scenarios, and the study area.

4.2.1 Study area

The Ministry of Infrastructure and Environment of the Netherlands was interested in the consequences of climate change and additional housing on heat stress in cities. The Hague was chosen, because it is located in a large urbanized area where there is a great demand for housing (EIB, 2015). The study area (referring to rectangle in Figure 4.1a) includes the cities of The Hague, Delft, and Zoetermeer, as well as the green agricultural areas that surround these cities. These cities have 532,561, 102,253, and 124,695 inhabitants, respectively (CBS, 2018b), spread over 98.12, 24.06, and

37.06 km², respectively. Other cities were included in our study to allow for a reliable verification and to enable a robust statistical relationship between residence density and urban morphological characteristics (see Section 4.2.2). Taking into account the population of the smaller villages and hamlets, the agglomeration of The Hague accommodates about one million inhabitants. It is one of the most densely populated regions in the Netherlands. The study area has a population density of 1270 inhabitants per km² (CBS, 2018c).

The climatological conditions of these regions are characterized by the vicinity of the North Sea. The prevailing wind direction is from the southwest. The temperature distribution is rather mild with maximum and minimum temperatures of 21 °C and 16 °C in August. In January, the daily maximum and minimum temperatures amount to 6 °C and 3 °C. The yearly precipitation measures 666 mm, with the largest monthly precipitation in November.

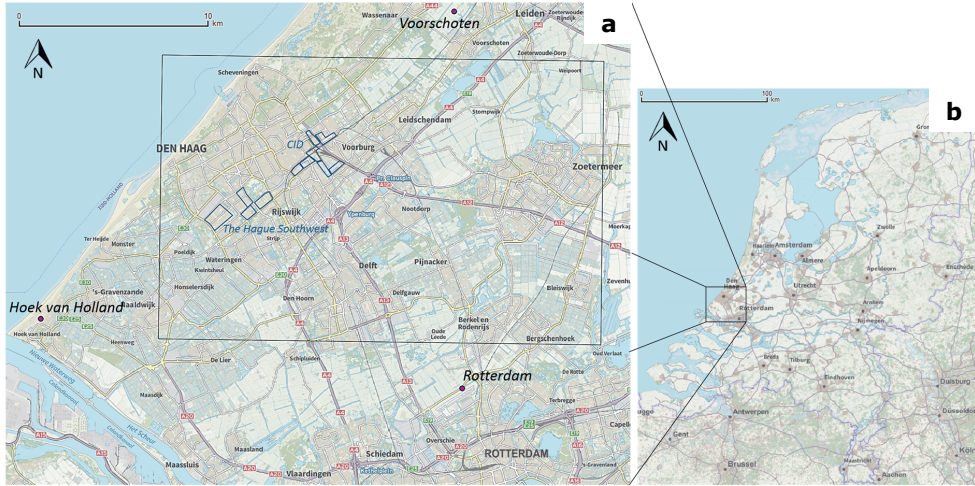


Figure 4.1: a) The agglomeration of The Hague and b) an overview map of the Netherlands (OpenTopo, 2018). The black rectangle in panel A indicates the study area for which the heat map was calculated. The three WMO stations are indicated in italics (Voorschoten, Hoek van Holland, and Rotterdam). Rotterdam acts as a rural reference station. The blue shapes in The Hague (Den Haag) represent the urban districts, Central Innovation District (CID), and The Hague Southwest, for which different urban planning strategies were evaluated for heat stress.

4.2.2 Diagnostic equation to compute minimum temperatures in cities

Urban heat islands and urban temperatures can be estimated looking at the combined effects of weather conditions and urban morphological characteristics. From these factors, a daily maximum urban heat island (UHI_{max}) can be estimated using a diagnostic equation created by Theeuwes et al. (2017), henceforth referred as T17 (Equation 4.1).

$$UHI_{max} = \left(2 - SVF - f_{veg} \right)^4 \sqrt[4]{\frac{S^{\downarrow} * (T_{max} - T_{min})^3}{U}} \quad (4.1)$$

urban morphology meteorology

This equation was validated using observational data from 14 cities across northwestern Europe that vary in size. The equation appears to be robust. The UHI_{max} expresses the maximum

temperature difference between urban and rural environments on a given day in Equation (4.1). SVF denotes the sky-view factor and f_{veg} denotes the vegetation fraction of the urban area. S_d denotes the mean downward shortwave radiation (Kms^{-1}), DTR denotes the diurnal temperature range (K), and U denotes the mean wind speed (ms^{-1}) measured at a rural station nearby the city. The average measurement period for each of the meteorological parameters can be found in T17. The heat maps are computed on grid cells with a resolution of 100 m. The SVF and vegetation fraction were determined using a source area of 500 by 500 meters around the grid cell, which was designated to a 100-m resolution. The SVF originates from a 5-m resolution dataset (KNMI, 2018), derived from a digital elevation model based on airborne lidar measurements from aircraft measurements made in 2008 (AHN, 2012). Upscaling from a 5-m to a 500-m resolution was performed by taking the median of street level SVF data points. The vegetation fraction dataset originates from a normalized difference vegetation index map (NDVI) (Attema et al., 2015).

The spatial contrast of the UHI_{max} across the city is a good measure to estimate which parts of the city suffer more from heat stress. Nevertheless, when climate change is incorporated, the UHI_{max} is not an adequate measure of heat stress anymore since climate change is heating up the world regardless of whether an area is classified as rural or urban. Therefore, it is useful to make an evaluation based on the absolute values of urban temperatures, such as minimum temperatures (Tn_{city}), which can be calculated as follows:

$$Tn_{city} = Tn_{rural} + UHI_{max} \times 0.46 \quad (4.2)$$

When minimum temperatures are observed at the rural reference station, the UHI is typically substantially smaller than the UHI_{max} . On a typical cloudless day, the minimum rural temperature increases by 46% of the UHI_{max} (Oke, 1982). This fraction of the UHI_{max} is also known as the UHI_{TMIN} . The WMO station in Rotterdam acts as a rural reference station (provides Tn_{rural} in Equation 4.2) (Figure 4.1a). Measurements from other nearby WMO stations were discarded, because they were located too close to the sea (Hoek van Holland) or were recently relocated (Voor-schoten). In order to compute climatologies, we used the data from 15 summer half years (1 April – 30 September) covering the years 2002 to 2016 from the WMO station Rotterdam. Finally, we present heat maps showing the average number of nights per year that exceed the minimum temperature of 20 °C. This metric is consistent with ongoing climate adaption policies in the Netherlands (CAS, 2020). These nights are often referred to as tropical nights. The heat maps were generated with the QGIS software (QGIS, 2018).

4.2.3 Future climate scenarios

For future climate scenarios, the meteorological time series from the rural station Rotterdam during the period 2002–2016 were transformed into the projected climate of 2050. The Netherlands weather services (KNMI) developed four different scenarios to depict how the climate may evolve, namely the G_L , G_H , W_L , and W_H scenarios. The scenarios differ in the estimated global temperature rise (G or W) and the degree of change in air circulation patterns (L and H suffix), all of which are schematically represented in Figure 4.2.

These climate scenarios are based on the Intergovernmental Panel on Climate Change (IPCC) global climate model calculations, on global climate model EC-Earth results, and on a downscaling step within the regional climate model, Racmo (Klein Tank et al., 2015). All four scenarios have an equal chance of occurrence. As indicated in Figure 4.2, the scenarios differ in the degree of change in air circulation patterns and the global temperature rise. The differences in

global temperature rise are due to different projections of greenhouse gas emissions adopted from the emission scenarios from the IPCC. The scenarios G_L and G_H match the lower end of the emission reduction scenarios (RCP4.5 and RCP6), and the scenarios W_L and W_H match the high-emission scenario (RCP8.5) which does not include specific climate mitigation (Riahi et al., 2011; Cubasch et al., 2013). Within all of the model simulations, a distinction can be made between models showing a large and small precipitation response (van den Hurk et al., 2014). Simulations with a large precipitation response foresee wet humid winters and dry summers, and are assigned to H-scenarios. The change in precipitation response is linked to circulation change, and H-scenarios show more frequent westerly circulation in the winter and domination of high pressure in the summer. In the summer, this means an increase in solar radiation and more easterly winds, which implies higher temperatures. This weather type also favours urban heat islands.

The scenarios provide monthly temperature increments for daily percentiles (KNMI, 2015). These increments were relative to the climate period of 1981–2010. There is already a climate signal in the time series (2002–2016) compared to this climate period, and this bias was subtracted from the results. Using the procedure of Molenaar et al. (2016), these increments were interpolated for all of the days in a month. In this study, the transformation was performed on hourly values, because the time frame in which minimum temperatures were determined differs from the standard, i.e., from 8 UTC to 8 UTC the next day. After the creation of a future hourly time series, a proper minimum temperature can be derived. As such, we use

$$T^f(h) = T^c(h) + \Delta T(d) + \Delta HTD(h) - \overline{\Delta HTD(h)} \quad (4.3)$$

where

$$\Delta HTD(h) = \frac{(T^c(h) - T_{min}^c)}{(T_{max}^c - T_{min}^c)} \times \Delta DTR \quad (4.4)$$

The symbols are defined by the following:

$T^c(h)$ = hourly temperature current climate

T_{min}^c = minimum daily temperature, 8 a.m. UTC to 8 a.m. UTC the next day

T_{max}^c = maximum daily temperature, 8 a.m. UTC to 8 a.m. UTC the next day

$T^f(h)$ = hourly temperature for future climate

$\Delta T(d)$ = daily temperature increment to future climate

ΔDTR = change in average diurnal temperature range to future climate

$\Delta HTD(h)$ = hourly temperature deviation

$\overline{\Delta HTD(h)}$ = 24-hour average bias of hourly temperature deviation

For a transformation to hourly values, the daily temperature increments, $\Delta T(d)$, were added to individual hours (see Equation 4.3). This increment, $\Delta T(d)$, was the outcome of the procedure of Molenaar et al. (2016). A novel aspect is that the change in diurnal temperature range, ΔDTR , between the future and current climate was also taken into account (Equations 4.3 and 4.4). With Equation 4.3, a new dataset of minimum temperatures for 2050 can be directly calculated using the hourly temperature dataset of $T^f(h)$. The $\overline{\Delta HTD(h)}$ is subtracted in Equation 4.4 to conserve an average increase of $\Delta T(d)$ over 24 hours.

The UHI_{max} from Equation 4.1 also changes in a future climate. The scenarios generally show an increase in global radiation and generally show a decrease in DTR , which influences the UHI_{max} . On the contrary, however, the H-scenarios (G_H and W_H) show a small increase in DTR for the warmest months of July and August. In all climate scenarios, these months show an increase in global radiation from 2% in the G_L scenario to 7% in the W_H scenario, as well as a change in DTR between -3% in the G_L scenario and 2% in the W_H scenario. For the transformation in global radiation, we followed the method of Bakker (2015). The climate scenarios provided only monthly changes in global radiation. In our study, the change in radiation was distributed over all days without exceeding the maximum realistic daily radiation sum, which was set at 75% of the radiation at the top of the atmosphere (Bakker, 2015). Changes in wind speed were not considered, because they fell within the natural variation range (Klein Tank et al., 2015). Used transformation values for temperature percentiles DTR , solar irradiation can be found for July in Table A.5.6 in the Appendix of Chapter 5.

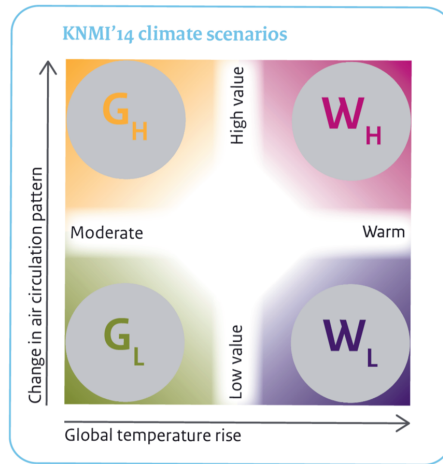


Figure 4.2: Four scenarios were used to calculate future heat stress. They differ in global temperature rise and change in air circulation pattern. Reproduced with permission from KNMI, Brochure KNMI'14 climate scenarios, 2015 (Klein Tank et al., 2015).

4.2.4 Urban planning strategies

The impact of the redevelopment and the construction of additional residences was evaluated for two urban districts. One district was a residential area consisting of low- and mid-rise buildings located in the southwestern part of The Hague, referred to as “The Hague Southwest” (Figure 4.3a). The other district was located near the centre of The Hague and mainly consisted of a relatively old business area and newer high-rise commercial buildings. This area is scheduled for redevelopment and is referred to as the Central Innovation District (CID) (Figure 4.3b). The densification of this district is much larger than that of The Hague Southwest, because of the larger building assignment.

The building assignments of the districts could either be achieved by building on currently green spaces or by replacing the existing low- and mid-rise buildings with high-rise buildings. This will either reduce the vegetation fraction or raise the SVF , which will consequently increase the UHI_{max} . This choice and the alternative of building residences in surrounding green corridors were examined using five distinct urban planning strategies shown in Table 4.1.

Table 4.1: Five urban planning strategies that complete the building assignments for The Hague Southwest and the Central Innovation District (CID). The enumeration starts with B, in accordance with the panels in Figures 4.8 and 4.10. Panel A in these figures represents the current housing.

The Hague Southwest	CID (Central Innovation District)
B. Build on green corridors around the urban neighbourhoods with low- and mid-rise buildings.	B. Construct high-rise buildings whereby green spaces are preserved as much as possible.
C. Construct low- and mid-rise buildings on green spaces within the urban neighbourhoods.	C. Construct high-rise buildings whereby the vegetation fraction is increased.
D. Construct high-rise buildings within the urban neighbourhoods to preserve existing green spaces.	

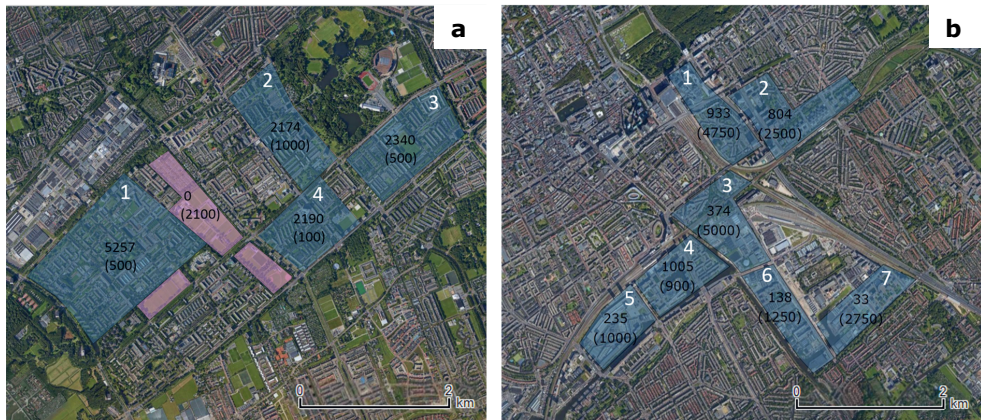


Figure 4.3: a) Theoretical building assignment for districts of The Hague Southwest, and b) the CID. The building assignment is indicated for different neighbourhoods within brackets, and the number above the brackets indicates the current number of residences in the neighbourhood. The pink areas in panel A indicate green corridors which were built using strategy C. The white numbers label the different neighbourhoods.

In this study, the building assignment was expressed as a change in the *SVF* and/or vegetation fraction in order to estimate the changes in the UHI (see Equation 4.1). Hence, as a first step, we had to determine the numerical relationship among the density of the residences (CBS, 2018c), the *SVF*, and the vegetation fraction (f_{veg}) for the current building volume of the agglomeration of The Hague. This is expressed as

$$\begin{aligned} \text{Residences per km}^2 \\ = -213(\pm 19)SVF - 200(\pm 30)f_{veg} + 1.85(\pm 0.04)(SVF \times f_{veg}) + 22687 \quad (4.5) \end{aligned}$$

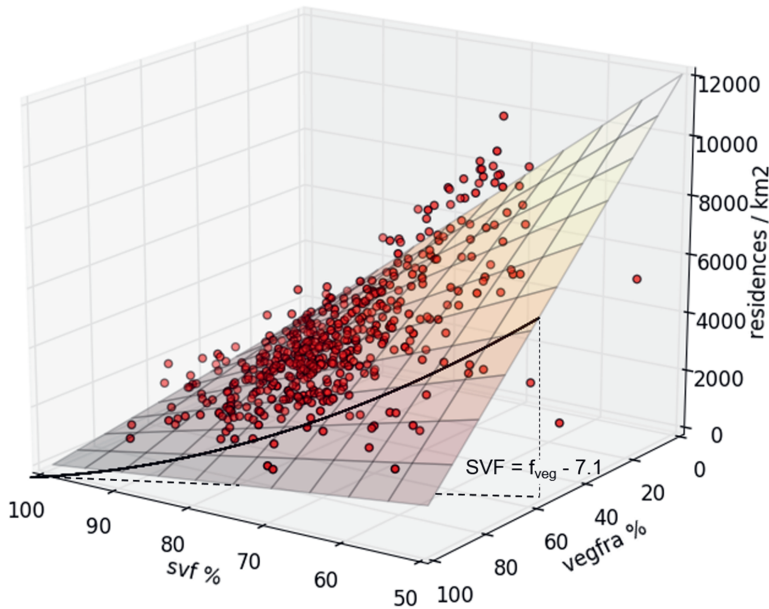


Figure 4.4: Empirical relationship among the density of the residences (CBS, 2018c), the sky-view factor (SVF), and the vegetation fraction for the agglomeration of The Hague presented on a three-dimensional (3D) surface ($R^2 = 0.64$). Areas with more than one-third non-residential buildings were removed from the analysis. Areas with a population density below 750 per km^2 were also removed. The black line and the black dotted line indicate the equilibrium between the slopes of the vegetation fraction and the SVF. The grid resolution used is 500 m.

Figure 4.4 shows the empirical relationship among the density of the residences, the SVF, and the f_{veg} in a three-dimensional (3D) plot. Herein, the SVF and the f_{veg} are denoted in percentages. The ranges used for this relationship vary between 52–99% and 11–93% for the SVF and the f_{veg} respectively. For the CID, it was necessary to extrapolate to a minimum SVF of 22% and a vegetation fraction of 5% to meet the requirements of the high density of residences. Note that the population density does not currently occur in the agglomeration of The Hague. The UHI_{max} equation (Equation 4.1), however, was tested for highly urbanized areas (Theeuwes et al., 2017); thus, it can deal with the planned densification for the CID. The values used for the SVF, the f_{veg} , and the density of residences for the five urban planning strategies can be found in Table A4.1 and A4.2 in the Appendix.

4.3 Results

4.3.1 Model validation for the agglomeration of The Hague

The diagnostic equation for the UHI applied here (Equation 4.1) was designed and tested using observational data from cities of variable sizes in northwestern Europe (Theeuwes et al., 2017). It was crucial to verify the results presented here with personal weather stations in the agglomeration of The Hague. First, minimum temperatures are a different metric from the maximum UHI used for verification by T17. Second, the retrieval and integration of morphological data and meteorological data were slightly different compared with the procedure of T17. Finally, spatial differences may occur because the area is bordered by the coast, where seasonality in sea-surface temperatures and the presence of a sea breeze may play a role.

A quality assessment of crowdsourced weather data is indispensable, because weather stations may have issues and are not always properly installed (Bell et al., 2015; Meier et al., 2017). For the verification, we used data from personal weather stations in the agglomeration of The Hague, and data were also obtained from the Weather Underground platform. We selected only Davis Vantage Pro and Oregon scientific stations, since they show small biases in the night (Bell et al., 2015). This added up to nine stations in total. The time series from these stations comprised two years of data (2015–2016) restricted by the summer period (April–October). Minimum temperatures were discarded if more than two hourly values were missing (as in the analysis by Hopkinson et al. (2011). After evaluating this constraint, the minimum availability was 48% and the average availability was 78% for a single personal weather station.

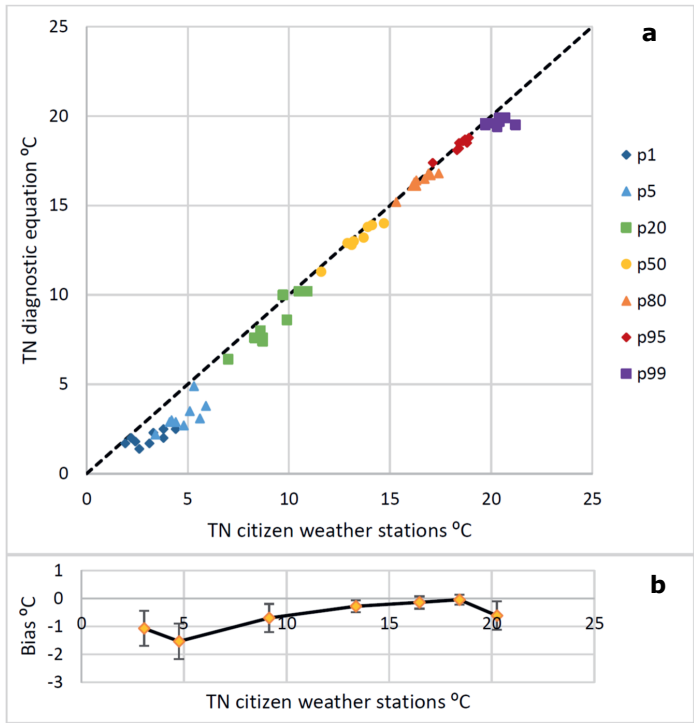


Figure 4.5: a) Quantile–quantile plot for modelled and observed (Davis and Oregon personal weather stations) nighttime minimum temperatures for the years 2015–2016. b) The bias between the data from these personal weather stations and the diagnostic equation are presented as a function of temperature. Error bars indicate the standard deviation.

The personal weather stations and the diagnostic equation were compared in a quantile–quantile plot in Figure 4.5a, and the bias and standard deviation of the stations grouped by percentile are shown in Figure 4.5b. Only the lower percentiles with low minimum temperatures had a substantial cold bias. It is expected that the lack of anthropogenic heat led to the underestimation in the diagnostic equation (Equation 4.1). During cold weather in the spring, the anthropogenic heat source is larger than in the summer due to heating of buildings (CBS, 2018a). Furthermore, in the lowest and highest percentile, there seemed to be more variance in minimum temperatures of the personal weather stations than in the modelled minimum temperatures of the diagnostic equation. The other percentiles showed good agreement between the model and the observations, with only slight cold biases, and supported the reliability of the equation.

4.3.2 Heat stress for current and future climate in 2050

As a starting point, a heat map of the current climate was constructed for The Hague (Figure 4.6). Note that this heat map covered a smaller area than the study area displayed in Figure 4.1. In the current climate, tropical nights are not common. On average, rural areas experience 1.25 tropical nights per year, while the urbanized parts of The Hague face 3.5 to a maximum 4.5 tropical nights per year.

Note that, in rural areas, the number of tropical nights was distributed quite uniformly over the 15 years. During 20% of the years, there were no tropical nights and the warmest year in the series. The year 2006, on the other hand, had three tropical nights. The tropical nights typically occurred when weather conditions were governed by a warm humid cyclonic southerly flow with an upper level trough west of the European continent and approaching fronts, sometimes referred to as a Spanish plume (Hamid, 2012). These situations are unstable with high chances of thunderstorm and squall lines bringing in colder air masses; therefore, such situations do usually not last long. These situations prevent rural areas from developing a cool stable boundary layer at night. Urban areas may experience tropical nights particularly during relatively long warm episodes or heat waves, which is more often accompanied by an anticyclonic weather type. For the year 2006, a maximum of 14 tropical nights occurred in the centre of The Hague. Six tropical nights occurred within a period of eight days. Note that a warm summer like 2006 is not unlikely in the current climate. The return time of such a summer is estimated at eight years (KNMI, 2006).

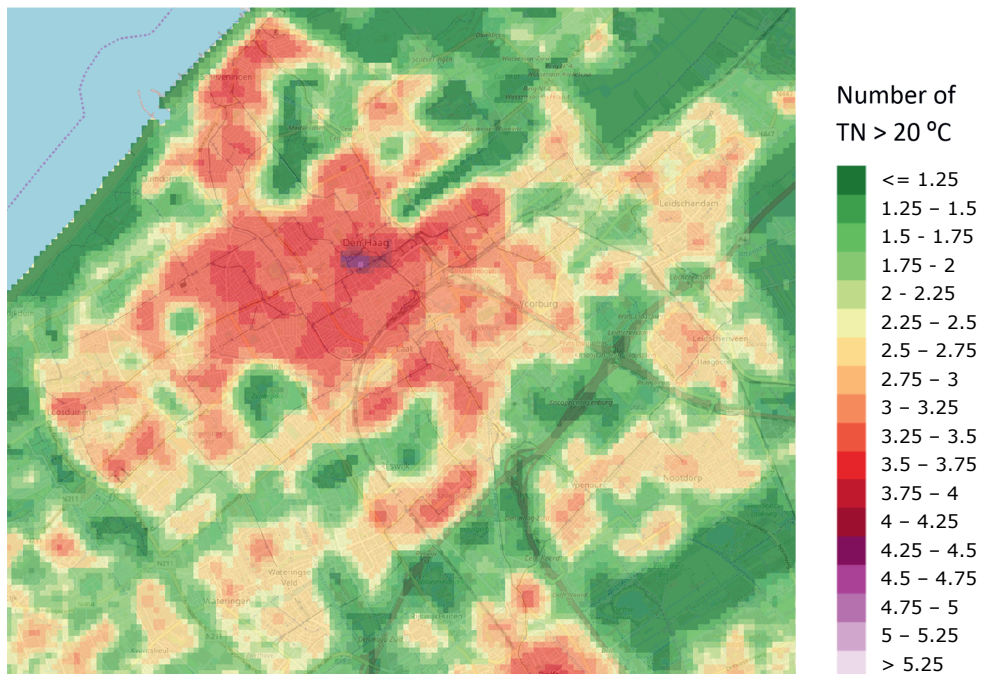


Figure 4.6: Modelled average number of nights per year above 20 °C for the current climate (2002–2016) for The Hague.

Concerning the climate in 2050, we foresee that the number of tropical nights will increase substantially. Depending on the scenario, rural areas may experience 2.1–5.8 tropical nights per year, and the centre of The Hague may experience 6.5–16 tropical nights per year (Figure 4.7). For

the city, this means a three- to fourfold increase in tropical nights for the warmest W_H scenario compared to the current climate. The observed warm year 2006 would fall in between the W_L and the W_H scenarios for an average year around 2050. The transformed year 2006 would lead to 15 tropical nights in rural areas and up to 32 tropical nights in the centre of The Hague for the W_H scenario.

The absolute difference in tropical nights between rural and urban areas increases in the warmer scenarios, because more prevalent weather conditions will enable more tropical nights in cities in a warmer climate. Minimum temperatures simulated in cities of around 18 °C in the current climate will exceed 20 °C in the W_H scenario, and those nights will occur much more frequently than the tropical nights of today. Interestingly, the average UHI is likely to decrease a little for urban tropical nights in the future, because the more prevalent weather conditions are less related to strong UHIs. In any case, there will be very little change in the number of tropical nights for all future climate scenarios (less than 3%). This is elaborated in the discussion.

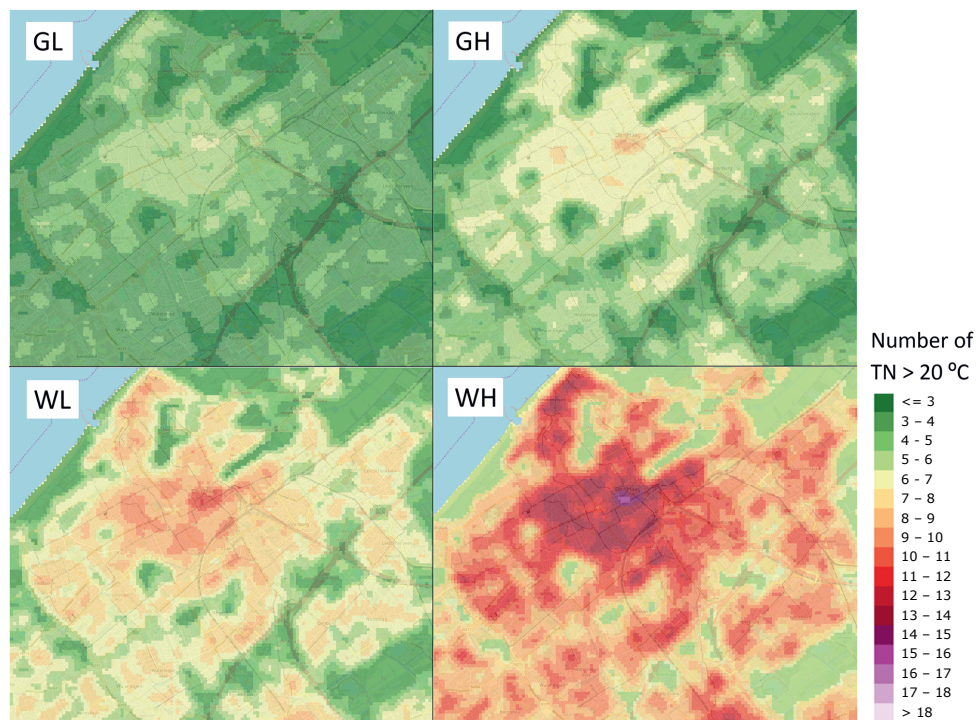


Figure 4.7: Modelled average number of nights per year above 20 °C for the four KNMI'14 climate scenarios representing the year 2050.

4.3.3 Urban planning strategies for The Hague Southwest

For the urban district, The Hague Southwest, three urban planning strategies (abbreviated to strategies) were examined, and the impact on the number of tropical nights and UHI_{max} was evaluated. The current climate does not indicate clear absolute differences in tropical nights between urban areas, due to the scarcity of these nights in low- and mid-rise urban areas. Therefore, the different strategies were shown for the future W_H scenario only. The additional heat stress (measured in number of tropical nights per year) will be mostly scattered over the urban district in the strategy

where new residences will be built on the currently green corridors around the neighbourhoods (Figure 4.8A,B).

The other strategies concentrate the heat stress particularly within the neighbourhoods. The largest increase in the number of tropical nights takes place in neighbourhood 2, which has the highest density of residences with the largest building assignment (Figure 4.3). For the hottest place in this district, the average number of tropical nights per year will increase from 3.1 to 3.5 in the current climate (not shown), and from 11 to 13 nights in the W_H scenario shown in Figure 4.8C,D (the mildest G_L scenario shows an increase from 4.7 to 5.4–5.5 tropical nights per year). Thus, the maximum expected numbers of tropical nights for this neighbourhood in strategy C and strategy D are very similar. However, strategy C (construct low- and mid-rise buildings) shows larger patterns of these maxima than strategy D (construct high-rise buildings to preserve green spaces). Strategy C is moderately warmer than strategy D for the entire urban district, especially in neighbourhood 2. This is best seen in the continuous scale of the 95th percentile of UHI_{max} in Figure 4.9 for the current climate. The maximum increase in the 95th percentile of UHI_{max} is 1.2 °C for strategy C and 0.8 °C for strategy D, and remains nearly constant for the future scenarios. Note that these relative differences in the scenarios are also reflected in the expected minimum temperatures. In summary, the realization of high-rise buildings to preserve existing green spaces appears to be a better strategy than constructing low- and mid-rise buildings on existing green spaces for The Hague Southwest.

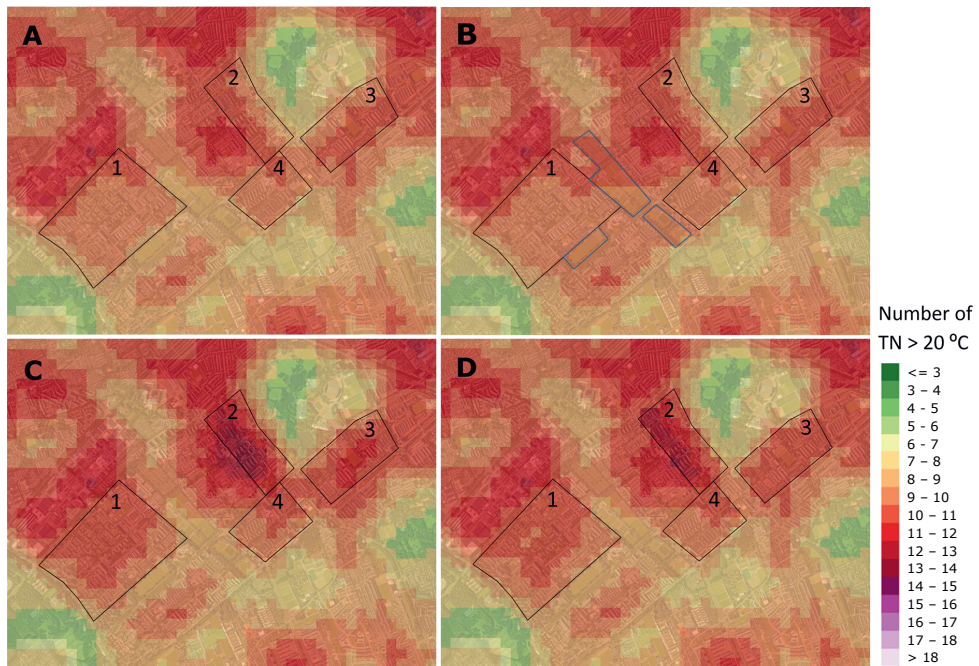


Figure 4.8: Modelled number of tropical nights per year for the W_H climate scenario in 2050 for The Hague Southwest for: (A) current housing, (B) building on green corridors around the neighbourhoods with low- and mid-rise buildings, (C) constructing low- and mid-rise buildings on green spaces within the urban neighbourhoods, and (D) constructing high-rise buildings within the urban neighbourhoods to preserve existing green spaces.

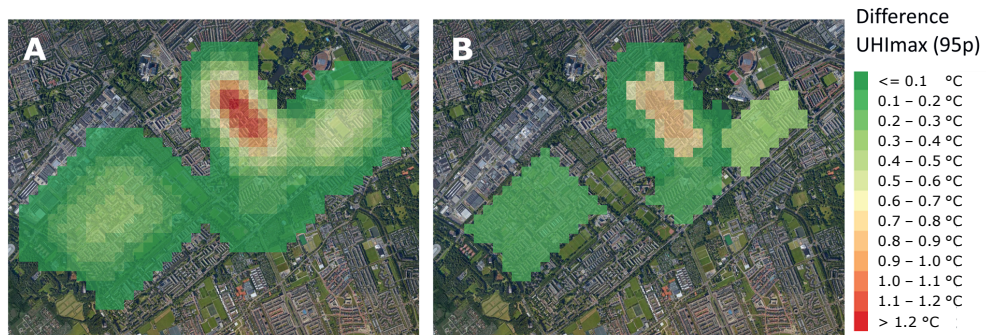


Figure 4.9: Difference in the modelled 95th percentile of UHI_{max} between (A) strategy C (constructing low- and mid-rise buildings) and (B) strategy D (constructing high-rise buildings). Both are compared with the current housing for the current climate.

4.3.4 Urban Planning Strategies for the CID

For the CID (Central Innovation District), we looked at the frequency of tropical nights and UHI_{max} to examine the effects of the urban planning strategies (Figures 4.10 and 4.11). In contrast to The Hague Southwest, the effect of the urban planning strategies is larger for the current climate, and therefore, is presented in Figure 4.10. The most urbanized neighbourhoods 1 and 3 show the largest increase in tropical nights in both strategies, from 3.5 tropical nights per year up to more than five tropical nights per year in the current climate. The future climate scenarios foresee 8–15 tropical nights per year in the G_L and W_H scenarios, respectively. When compared to the district, The Hague Southwest, it is not clear which strategy is best. However, differences between the two strategies for the 95th percentile in UHI_{max} reveal that the strategy where green spaces are preserved most (strategy C) is the best choice (Figure 4.11). The neighbourhoods 1, 2, 3, and 7 show mixed results, which is due to the small sizes of the areas. If the neighbourhoods were larger, then strategy C would result more clearly in less heat stress. In the Appendix the other climate scenarios are displayed for the urban planning strategies for CID and The Hague Southwest, the number of tropical nights for the warmest year 2006, and monthly transformation tables for temperature, DTR and global radiation from the current climate to the future climate in 2050.

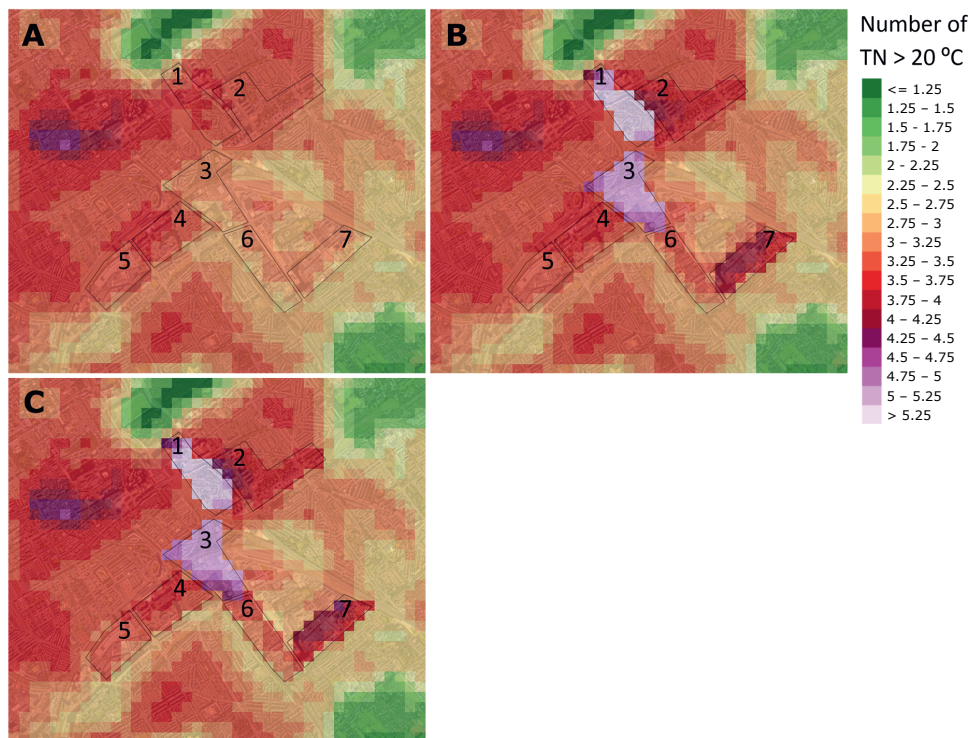


Figure 4.10: Modelled number of nights above 20 °C per year for the CID in the current climate for (A) current housing, (B) constructing high-rise buildings whereby green spaces are preserved as much as possible, and (C) constructing high-rise buildings whereby the vegetation fraction is increased.

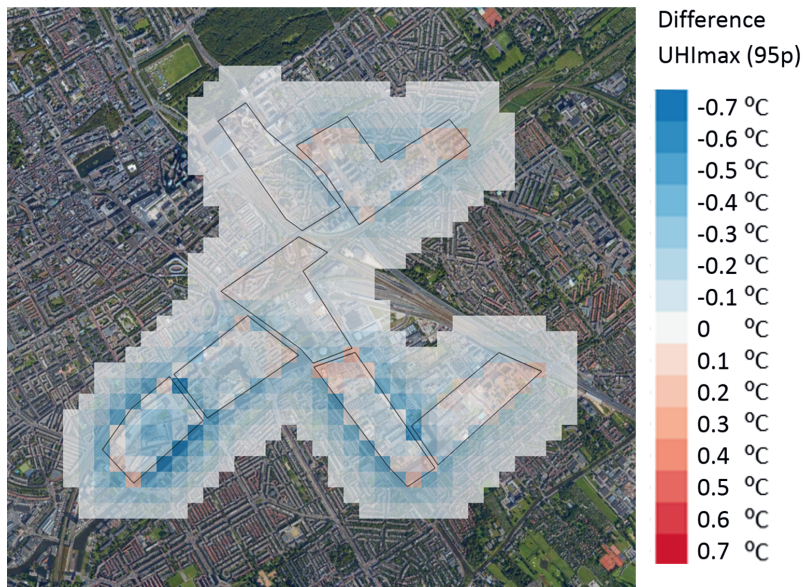


Figure 4.11: Difference in the modelled 95th percentile of the UHI_{max} between strategy B and strategy C for the W_H climate scenario.

4.4 Discussion

4.4.1 Thresholds in urban planning strategies

In this paper, we studied the effects of different urban planning strategies on heat stress for current and future climates in the agglomeration of The Hague. It appears that preserving green spaces was clearly the best urban planning strategy in order to avoid heat stress for The Hague Southwest. The difference between the strategies for the CID was much smaller. An explanation for this difference appears when examining the statistical relationship among the density of residences, the SVF , and the vegetation fraction (Equation 4.5). The larger the slope or partial derivative is in Equation 4.5, the more residences could be built per a certain decrease in SVF or decrease in vegetation fraction. Thus, the effectiveness of the strategy depends on the specific urban conditions. The vast majority of the data points in Figure 4.4 are positioned above the black line, which means that more residences could be built per percentage point decrease in the SVF than per percentage point decrease in the vegetation fraction. Note that a percentage point decrease in the SVF has the same effect on UHI_{max} as a percentage point decrease in the vegetation fraction (Equation 4.1). This means that, for the majority of neighbourhoods, a decrease in the SVF due to high-rise buildings causes less heat stress than building low- and mid-rise buildings on green spaces.

$$SVF = f_{veg} - 7.1 \quad (4.6)$$

The threshold which determines the favourable strategy can be derived from Equation 4.5 and is denoted in Equation 4.6. It is also represented as the dotted black line at the bottom of Figure 4.4. Note that this relationship is specific for The Hague agglomeration and might alter slightly for other urban areas, even in the similar climates of other countries in northwestern Europe.

This threshold indicates that reducing the SVF by constructing high-rise buildings is a better measure, unless the SVF is considerably low and the vegetation fraction is high. This is relatively rare for the agglomeration of The Hague. The differences in effectiveness between the strategies can be attributed to the cross product in Equation 4.5, which appeared to be significant. The density of residences can be imagined roughly as a product of urban fraction (inverse of vegetation fraction) and height of the buildings (more or less correlated with the inverse of SVF). Two intermediate values in this product result in a substantial larger density of residences rather than a low and a high value for equal levels of heat stress.

4.4.2 Applicability and limitations of the UHI diagnostic equation

Spatial variation in UHI_{max} and nighttime minimum temperatures within cities were investigated several times using multi-year observation data in cities. Montavez et al. (2000) found that the urbanization of Granada in Spain resulted in increased nighttime minimum temperatures predominantly in the city centre. Eliasson (1996) concluded that urban–park temperature differences were on the same order of magnitude as urban–rural temperature differences, which corresponds to large parks in The Hague. Heusinkveld et al. (2014) found that spatial differences in vegetation cover are paramount in determining the spatial variation in UHI, and the correlation coefficients were best for an upwind fetch area of 700 m. In the current study, the wind direction was not taken into account, and therefore, a smaller area of 500 by 500 m was an appropriate choice. When considering SVF , an aerial mean is used to relate the SVF to UHI to incorporate advection effects on air temperature, which was performed in studies such as those by Goh and Chang (1999) and Unger (2004). Similar to our study, Unger (2004) extracted the SVF on a scale of 500 by 500 m.

The verification of two years of crowdsourced city temperature data reveals that the diagnostic method used in this study does not indicate substantial biases in minimum temperatures in urban areas. This supports the use of the current diagnostic equation. Although the diagnostic equation is a physically meaningful equation with conservation of fundamental dimensions, not all potentially important contributing factors were taken into account. One can think of contributing factors such as anthropogenic heat, albedo, thermal admittance, which is related to the heat storage of buildings, distance to open water from a city's edge, and a vertical temperature gradient, as a measure for stability at the rural reference station. The latter two appeared to have less significance (Theeuwes et al., 2017). Caution is advised when applying the method to places that have large anthropogenic heat production like industrial areas or highly densely populated areas. Industrial areas were not sampled in the validation of T17. Anthropogenic heat can be included into the equation by adding it to the incoming solar radiation, or it can be added as a separate variable. When added to the incoming solar radiation, it has no substantial influence, apart from the cautioned areas with large anthropogenic heat production. Since the proximity to open water is not considered in the equation, the urban areas close to the sea have larger uncertainties for our study area. Open water is difficult to implement in a time-invariant UHI_{max} equation, because the effect is strongly dependent on the season (Theeuwes et al., 2013). For albedo and thermal admittance, it is a challenge to retrieve reliable area-wide data on building properties. Albedo data can be straightforwardly retrieved from satellite observations, although a top view would over-represent roof albedo, which is less decisive on the street level than wall and street albedo (Hamdi & Schayes, 2008).

A conversion factor of 0.46 was used to estimate the UHI_{TMIN} from the UHI_{max} (see Equation 4.2). The ratio between UHI_{max} and UHI_{TMIN} (conversion factor) is probably not fixed for all the percentiles, as demonstrated in a crowdsourced data study conducted in the Netherlands (Steenekveld et al., 2011a), and for city weather stations in Rotterdam (Heusinkveld et al., 2014). The last study reported UHI_{max} to UHI_{TMIN} ratios in the range of 0.63–0.87 for the 95th percentile. However, it might be a safe choice to have a conservative conversion factor, since the rural reference station Rotterdam is affected by UHI mainly due to advection from Rotterdam and the airport itself (Heusinkveld et al., 2014). Spatially, the conversion factor may change between areas with dominant narrow or wide street canyons (Theeuwes et al., 2014).

4.4.3 Climate change projections on heat stress

As demonstrated in Figure 4.7, the projected climate change could have a large to huge effect on heat stress levels. Regional climate models for Europe show similar outcomes. The high consistency in worsening health indices seem alarming for Europe (Fischer & Schär, 2010). Gasparrini et al. (2017) and Huynen and Martens (2015) found an increase in heat-related excess mortality for future climate scenarios. For the Netherlands, the population-attributable fraction of mortality is estimated to increase by 44–119%, depending on the KNMI'14 climate scenarios (Huynen & Martens, 2015). Furthermore, mortality increases when heat waves are combined with air pollution (Analitis et al., 2014). Air pollution also increases with higher temperatures, due to the associated higher chemical reaction rates and elevated emissions of biogenic ozone precursors (Athanassiadou et al., 2010). Nevertheless, the direct effect of elevated temperatures during heat waves seems to primarily be the effect of excess mortality (Basu & Samet, 2002; Analitis et al., 2014).

Specific to the number of tropical nights, Fischer and Schär (2010) showed a three- to fourfold increase in the number of tropical nights for France and Central Europe between 1961–1991 and 2021–2050. For downtown Paris, an increase from six to 35 tropical nights per year was

estimated between current and future climate (A1B scenario 2071–2099) (Lemonsu et al., 2013). Apart from the different methodology used, these results are in line with our findings.

4.4.4 Comparison of urban heat island and climate scenario contributions on heat stress

Urban heat islands, as well as the projections of the climate scenarios for 2050, show significantly raised temperatures compared to rural areas in the current climate (see Figure 4.7). More specifically, rural areas in the W_L and W_H scenarios showed approximately the same number of tropical nights for the centre of The Hague in the current climate. Nevertheless, climate change appears to create more significant heat stress than the imposed urbanization by the applied building assignments. This applies especially to The Hague Southwest. The neighbourhoods 1 and 3 in the CID have large building assignments, and the increase in the number of tropical nights falls within the single climate-change effect of the G_L and G_H scenarios. In particular, the higher minimum temperatures showed a large increase in the climate scenarios. For the 5% warmest nights, an increase in night minima of 0.7 °C is foreseen for the G_L scenario, and up to 2.2 °C for the W_H scenario (1.2 °C and 2.7 °C compared to the reference climate period of 1981–2010). This climate-change effect is about the same for rural and urban areas, which is discussed in the next paragraph. In contrast, the impact of urban planning strategies is smaller, but still relevant. The largest relative temperature differences among the urban planning strategies were found in The Hague Southwest. The preserving green strategy led to a 42% lower increase in UHI_{max} in the 95th percentile than the building on green spaces strategy, i.e., 0.33 °C and 0.57 °C, respectively. For the CID, the building assignment was much larger, and the increased vegetation fraction strategy noted an increase of 1.09 °C compared to 1.36 °C for the preserving green strategy (difference of 20%). Tropical nights in urban areas were generally related to a lower UHI_{max} percentile, which corresponds to a lower UHI_{max} and consequently, the numbers increased by 25%.

The climate change effect is nearly the same for rural and urban areas since the UHI will be very similar in the future climate. In the diagnostic equation for UHI_{max} (Equation 4.1), this is represented by an offset between a projected decrease in DTR and a projected increase in incoming shortwave radiation, except for the W_L scenario. This scenario shows the largest decrease in DTR with an unchanged amount of sunshine. However, this results in a minor reduction in UHI by 2–3%. In July and August, the UHI slightly increased (2–3%) for the H-scenarios, according to the increase in DTR . Most other studies confirmed the small or non-significant average UHI changes for mid-latitude cities in western Europe for the future climate (McCarthy et al., 2010; Grossman-Clarke et al., 2014). There are climate models even hinting at a decrease in UHI_{max} and UHI_{TMIN} due to larger projected precipitation deficits and associated drier soils in the summer time (Lemonsu et al., 2013; Hamdi et al., 2014). In such situations, rural temperatures increase, because less energy is used for evapotranspiration. Hamdi et al. (2014) found that, for a coupled urban and regional climate model, the higher percentiles of UHI_{TMIN} could decrease by 1 °C. For our study area, the effect of soil dryness does not play a substantial role in the UHI, because the land is below sea level and ground water levels are controlled.

4.5 Conclusions

In this study, we investigated the effect of additional housing in constructed zones on heat stress, worked out using different urban planning strategies for the current and future climates for the city of The Hague (the Netherlands). The heat stress is expressed based on the frequency of tropical nights, where minimum temperatures are above 20 °C, and on the 95th percentile of the maximum daily urban heat island, UHI_{max} . The proposed additional housing was added near the city centre

and in a residential area in The Hague. The urban planning strategies were applied in delineated urban neighbourhoods and differed in replacing low- and mid-rise buildings with high-rise buildings, or constructing buildings on vegetated areas. The temperature projection was computed using a validated diagnostic equation which combined weather data and urban morphological characteristics. The vegetation fraction appeared to be a more critical parameter than the sky-view factor, which was reduced by the tall buildings for the vast majority of urban configurations. This means that the combination of mid-rise and high-rise buildings with a preservation of vegetated areas was the best strategy. There is, however, an empirically determined optimum between vegetation fraction and sky-view factor. The most favourable green strategy mitigated the heat stress by 42% and 20% for the two urban districts tested.

In general, climate change will cause a larger increase in heat stress than the extra heat stress caused by the imposed urbanization. Only the largest imposed building assignments could compete with the colder climate scenarios. The most urbanized area of the city has on average 4.5 tropical nights per year. For this area, we found a range of 6.5–16 tropical nights per year for the coldest and warmest climate scenarios. For the warmest summer in the data series (year 2006), the number of tropical nights would increase from 14 in the current climate to 32 in the warmest climate scenario. The results were verified with a selection of high-quality personal weather stations. The model results were in good agreement with observations and showed only a slight cold bias. The prescribed method based on a diagnostic equation is a fast and efficient way of determining climatologies in minimum temperatures, and it is directly applicable for other cities across northwestern Europe.

Supplementary Materials reference

The following are available online at <http://www.mdpi.com/2073-4433/9/9/353/s1>, Figure S1: Modelled number of tropical nights per year for the year 2006, Figure S2: Modelled number of tropical nights per year for year 2006 transformed to the four KNMI'14 scenarios, Figure S3: Modelled average number of nights per year above 20 °C for The Hague Southwest for the current climate, Figure S4: Modelled average number of nights per year above 20 °C for The Hague Southwest for the G_L climate scenario, Figure S5: Modelled average number of nights per year above 20 °C for The Hague Southwest for the G_H climate scenario, Figure S6: Modelled average number of nights per year above 20 °C for The Hague Southwest for the W_L climate scenario, Figure S7: Modelled number of nights above 20 °C per year for the CID for the G_L climate scenario, Figure S8: Modelled number of nights above 20 °C per year for the CID for the G_H climate scenario, Figure S9: Modelled number of nights above 20 °C per year for the CID for the W_H climate scenario, Table S1: Transformation table G_L climate scenario from current climate to future climate in 2050, Table S2: Transformation table G_H climate scenario from current climate to future climate in 2050, Table S3: Transformation table W_L climate scenario from current climate to future climate in 2050, Table S4: Transformation table W_H scenario from current climate to future climate in 2050.

Acknowledgements

The authors acknowledge feedback from Jan Willem Notenboom, Raymond Sluiter (KNMI Datalab), Rien Bout and Nieske Bisschop (Ministry of Infrastructure and Environment), Erik de Haan (Province of South Holland), and Arno Lammers (Municipality of The Hague). In addition, the authors acknowledge Andrea Pagani (KNMI Datalab) for the provision and feedback of the sky-view factor data. The authors acknowledge Weather Underground® for making the weather data

available, which were used for verification, and acknowledge the weather enthusiasts for sharing their data to the platform of Weather Underground[®]. We acknowledge Robin Palmer for language editing.

Appendix

Here, the values for the sky-view factor SVF and the vegetation fraction f_{veg} are presented, which were used for the urban planning strategies shown in Table A4.1 and Table A4.2. According to strategies C and D, only one characteristic, the SVF or, was changed. The green corridor in strategy B has the urban characteristics of neighbourhood 1, which allows it to meet the criteria of the building assignment.

For the CID strategy C, both the SVF and the f_{veg} were changed for neighbourhoods which became heavily urbanized in order to maintain realistic values. For instance, neighbourhood 1 has urban characteristics similar to downtown Paris in strategy C (Theeuwes et al., 2017).

Table A4.1: Values used for the SVF and f_{veg} for urban planning strategies in The Hague Southwest. In addition, the density of residences is indicated. Neighbourhoods are displayed in Figure 4.3.

Southwest	A. Current situation			B. Building green corridors			C. Building low-/mid-rise			D. Preserve existing green Spaces		
Neighbourhood	Res/km ²	f_{veg}	SVF	Res/km ²	f_{veg}	SVF	Res/km ²	f_{veg}	SVF	Res/km ²	f_{veg}	SVF
1	5344	0.51	0.73	5344	0.51	0.73	5852	0.43	0.73	5852	0.51	0.69
2	5606	0.49	0.72	5606	0.49	0.72	8185	0.11	0.72	8185	0.39	0.58
3	5305	0.48	0.70	5305	0.48	0.70	6439	0.32	0.70	6439	0.48	0.61
4	6703	0.51	0.72	6703	0.51	0.72	7009	0.47	0.72	7009	0.51	0.69
5	0	n/a	n/a	5344	0.73	0.51	0	n/a	n/a	0	n/a	n/a

Table A4.2: Values used for the SVF and f_{veg} for the urban planning strategies in urban district CID. In addition, the residence density is indicated. Neighbourhoods are displayed in Figure 4.3.

CID	A. Current situation		B. Green spaces preserved			C. Increased vegetation fraction		
Neighbourhood	f_{veg}	SVF	Res/km ²	f_{veg}	SVF	Res/km ²	f_{veg}	SVF
1	0.20	0.71	17010	0.05	0.23	17010	0.06	0.22
2	0.30	0.66	9811	0.13	0.55	9811	0.26	0.47
3	0.21	0.87	15643	0.06	0.29	15643	0.10	0.26
4	0.21	0.67	7706	0.17	0.64	7706	0.35	0.54
5	0.08	0.80	5805	0.08	0.77	5805	0.47	0.60
6	0.15	0.86	5907	0.15	0.74	5907	0.46	0.60
7	0.19	0.82	11919	0.09	0.46	11919	0.19	0.39

Chapter 5

Mapping thermal comfort on a 1-m scale with meteorological and geographical tools

Abstract

In the Netherlands, municipalities and other sub-national governments have to conduct climate stress tests to examine the societal impact of heat load by citizens. So far, these parties have been hindered by the abundance of contrasting urban heat maps produced with different metrics and methods by different agencies. To unify the stress tests, we present a methodology for a standardized urban heat map at 1-m spatial resolution by selecting the Physiological Equivalent Temperature (PET) as metric for heat stress. First, we present an empirical regression model for PET, based on a variety of weather data and street configurations in the human thermal energy balance model Rayman. Thereafter, this empirical PET model is evaluated for the midsized town Wageningen (the Netherlands). Meteorological observations taken at a nearby reference site and straightforward geographical data have been used as model input. Also, established methods were applied and elaborated to account for the urban heat island effect and wind speed reduction in the city. The presented method is validated against bike traverse observations of PET. Wind speed is the most challenging feature to map, due to its unsteady and local behaviour in cities. As a result, an afternoon averaged PET heat map is demonstrated as standard for an extreme heat day (1:1000 summer half year days), and a cumulative exceedance PET heat map for a representative year. Furthermore, a heat map is projected for 2050 according a warm climate change scenario.

This chapter is based on:

Koopmans, S., Heusinkveld, B. G., & Steeneveld, G. J. (2020). A standardized Physical Equivalent Temperature urban heat map at 1-m spatial resolution to facilitate climate stress tests in the Netherlands, *Building and Environment*, **181**, 106984. <https://doi.org/10.1016/j.build-env.2020.106984>

5.1 Introduction

Climate change and the urbanization urges authorities to investigate whether climate adaptation measures should be taken (IPCC, 2014a), via so called climate stress tests in the Netherlands. A climate stress test assesses bottlenecks and vulnerabilities in the physical and socio-economic infrastructure in case of flooding, drought and ultimately also heat stress. This study focuses on heat stress by developing high-resolution (1 m) heat maps that indicate the hot spots, which aims to help decision makers to plan their climate adaptation and infrastructural measures. So far, many different urban heat maps circulate right now indicating different heat metrics, which may confuse stakeholders of municipalities and subnational governments. These metrics may vary from remote sensing based surface temperatures (van der Hoeven & Wandl, 2015), urban heat islands (UHIs) based on air temperature (Atlas Natuurlijk Kapitaal, 2020), to the number of tropical nights (nights with minimum temperatures above 20 °C) (CAS, 2020). To unify the heat maps the Dutch Ministry of Infrastructure asked a broad consortium to select one heat metric, and to develop a recipe to create an accompanying heat map.

Heat waves are projected to become more severe and have longer durations in Europe (Fischer & Schär, 2010). The higher temperatures more often lead to thermal discomfort and heat stress with adverse effects on human health and labour productivity (Pogačar et al., 2018). Under high-risk groups like elderly and people with cardiovascular diseases, higher mortality rates have been observed in recent severe heat waves in Europe in 2003 and 2006 (Fouillet et al., 2006; D'Ippoliti et al., 2010) and the number of heat related deaths are projected to increase in the climate scenarios (Huynen & Martens, 2015; Gasparrini et al., 2017). Most people suffer from heat stress in cities, which also result in higher mortality rates (Clarke, 1971; Basu & Samet, 2002; Grize et al., 2005). This is related to higher air temperatures relative to their rural counterparts which is known as the UHI. Higher temperatures are induced by the urban morphological characteristics (Holmer, 1992) and reduced evaporation by impervious surfaces (Oke, 1982). Due to the relatively high heat capacity of the urban fabric, higher temperatures are especially observed in evenings and early nights.

Air temperatures, however, do explain only a small part how humans experience heat. More important is to include factors which affect the heat release of the human body. These factors include the wind speed, which provides ventilation and ameliorates heat stress, humidity which determines how efficient humans can release heat by transpiration and radiation load, which has the largest contribution from solar radiation. One of the thermal comfort indexes accounting for these factors is the Physiological Equivalent Temperature (PET) (Höppe, 1999). PET classes have previously been constructed to define different grades of thermal perception (Matzarakis et al., 2009). In case of low wind speed and low insolation due to cloudiness, the air temperature is close to the PET. In sunlit calm conditions during summer, the PET can exceed the air temperature by 20 °C.

Compared to an open rural environment, the urban PET increase is expected to exceed the air temperature increase (Heusinkveld et al., 2014; Klemm et al., 2015), due to relatively low wind speeds induced by a high surface roughness and multiple reflections of solar radiation from buildings. Wind speed and incoming radiation vary on a very small scale in cities. Therefore, heat maps are calculated at a 1-m resolution to reveal small-scale hotspots to offer decision makers insight in the vulnerable locations in their urban environment, and are an indispensable tool needed for climate stress tests.

A novelty of the presented heat maps is the combination of different state-of-the-art empirical meteorological models and GIS-based tools at 1-m resolution, which is subsequently tested against in situ observations in the urban environment. Applying empirical models avoids expensive high-resolution numerical simulations, but it allows for relatively easy to implement routines. For instance, urban air temperatures and wind speed can be estimated with routine weather observations and information about land use and geometries of buildings and trees (Matzarakis et al., 2010; Theeuwes et al., 2017). Heat maps are demonstrated for the town of Wageningen in the Netherlands for a representative hot day afternoon and an average summer half year (April–September). In addition, an outlook is given by creating a heat map for the warmest climate scenario in 2050 (Klein Tank et al., 2015). Wageningen serves as a testbed since traverse meteorological measurements were available for a validation.

This Chapter is organized as follows: Section 5.2 summarizes the model approach of the heat map, Section 5.3 presents the results and validation, and in Section 5.4 and 5.5 we discuss and conclude our outcomes and modelling approach. A complete step-by-step recipe is attached in the Appendix.

5.2 Methods

Here, we present the description of the empirical PET model which determines the important components that the heat map consist of in Section 5.2.2. Thereafter in Section 5.2.3 the calculation of these components is described in distinct steps, including the required geographical information datasets. Finally, we present the methodology to create a heat map according a future climate scenario and the methodology for the validation of traverse measurements.

5.2.1 Large town Wageningen as testbed

Wageningen is a large town with 39,673 inhabitants (2020) in the middle of the Netherlands (CBS, 2019) (see Figure 5.1). The town is located at the edge of a shallow valley in the west and the slightly sloping nature area Veluwe in the east. On the south, Wageningen is bordered by the river Rhine. The built-up area of the town contains about $2.5 \times 2.5 \text{ km}^2$.

Figure 5.1 indicates two important reference weather stations that will be used in this study. Wageningen University's weather station The Veenkampen (Figure 5.1a) was used for the initial development of the recipe and verification of the standardized heat map. Since this weather station is located only 3 km from where the traverse measurements have been taken, we expect minimal errors in the heat map. To facilitate the development of future heat maps for other urban areas in the Netherlands, we advise to use nearby representative KNMI weather stations, which are easily accessible and equally formatted. All presented heat maps for Wageningen are driven by the closest representative KNMI station, which is KNMI station Herwijnen (WMO code 06356) Notwithstanding, it is noticed that the Veenkampen station meet the WMO requirements and it is located in an open rural area.

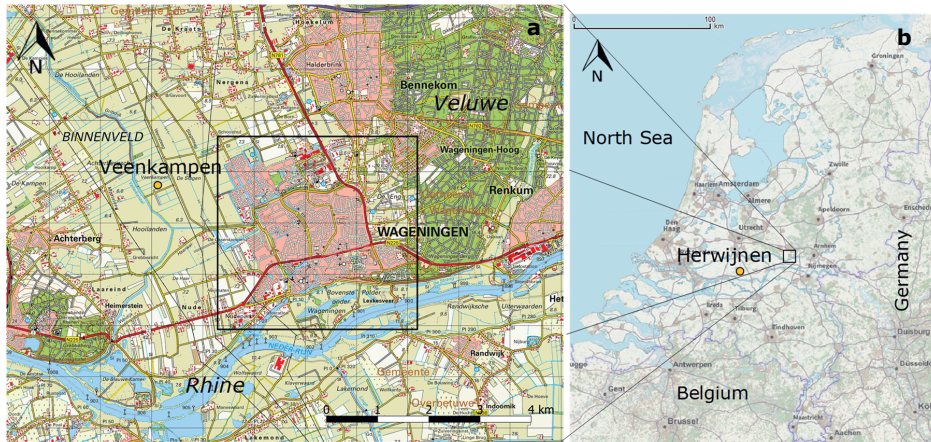


Figure 5.1: a) The surroundings of the town Wageningen, and b) an overview map of the Netherlands. The black rectangle in panel a indicates the size of the calculated heat map. In panel a, the weather station De Veenkampen (51.981°N, 5.620°E) is indicated and in panel b the reference station Herwijnen (51.859°N, 5.146°E) is indicated.

5.2.2 The empirical PET model

Humans experience heat by registering the skin temperature and the blood temperature in the brains. The human body temperature is, apart from the meteorological conditions, also influenced by the internal heat production, sweat rate and clothing. These are personal and will vary substantially between the human activity outside (Fanger, 1973), and is climate zone dependent (Cohen, et al., 2013). However, for policy making, it is important to use a standardized person, to fairly compare outside thermal conditions. For PET, this standardized person is male, 35 years old, 1.75 m, 75 kg, a clothing factor of 0.9 clo and he has a metabolic rate belonging to walking with 4 km h⁻¹ (VDI, 1998). PET classes were constructed to define different grades of thermal perception (Matzarakis et al., 2009). A PET above 29 °C indicates moderate heat stress in a temperate climate as western and central Europe. The PET limit of 29 °C marks the point that the majority of persons feel uncomfortable regarding heat stress (Fanger, 1973; Matzarakis et al., 1999).

The PET was computed by a human body energy balance model (Matzarakis et al., 2010), which accounts for the regulatory physiological processes of the human body and the meteorological parameters influencing the fluxes. Especially radiation, is very complex since it varies in three directions. We distinguish between direct radiation from the unobstructed sun, and diffuse radiation when scattered by clouds, and multiple reflections from buildings. At the moment it is computationally impossible to calculate on a 1-m grid accurately the radiation components for a whole city. Therefore, we used the 3D energy model Rayman to simulate the PET for three summer periods (April–September) for 10 typical Dutch street configurations (Matzarakis et al., 2010), consisting of equal height terraced houses on both sides of the road (Figure 5.2). The street configurations are east west and vary in canyon width resulting in sky-view factor *SVF* ranging 0.05 to 1 both for natural surface and impervious road surface.

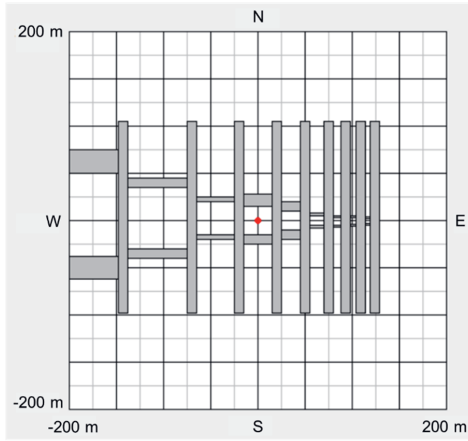


Figure 5.2: Representation of street configurations (grey bars) in human energy model Rayman. All walls are 10 m high and their albedo is 0.3. The resulting S_{VF} varied in successively steps from: 1.0, 0.809, 0.740, 0.620, 0.525, 0.373, 0.205, 0.152, 0.108 and 0.05.

Air temperature, solar irradiation, thermal radiation and wind speed were used as meteorological input, as observed at the nearby weather station De Veenkampen. Only hours with PET values exceeding 20 °C were used as meteorological input to target for heat stress situations. The Rayman results were used to train an empirical PET model, based on regression techniques and meteorological and geographical data as input variables. In fact, two regression models have been developed, one for sunlit conditions and one for shadowed and nighttime conditions.

For sunlit conditions the resulting PET equation denotes:

$$PET_{sun} = -13.26 + 1.25T_a + 0.011Q_s - 3.37 \ln(u_{1.2}) + 0.078T_w + 0.0055Q_s \ln(u_{1.2}) + 5.56 \sin(\varphi) - 0.0103Q_s \ln(u_{1.2}) \sin(\varphi) + 0.546B_b + 1.94S_{vf} \quad (5.1)$$

And for shadow and nighttime conditions:

$$PET_{shade,night} = -12.14 + 1.25T_a - 1.47 \ln(u_{1.2}) + 0.060T_w + 0.015S_{vf} Q_d + 0.0060(1 - S_{vf})\sigma(T_a + 273.15)^4 \quad (5.2)$$

Herein T_a denotes the 2-m air temperature (°C), Q_s is the solar irradiation (Wm^{-2}), $u_{1.2}$ is the wind speed at 1.2-m height (ms^{-1}), T_w the wet-bulb temperature, σ the Stefan Boltzmann constant ($5.67 \cdot 10^{-8} \text{Wm}^{-2} \text{K}^{-1}$), φ is the solar elevation angle (degrees), B_b is the Bowen ratio (ratio between sensible and latent heat flux), S_{vf} is the sky-view factor and Q_d the diffuse radiation (Wm^{-2}). For impervious urban surfaces a typical value of $B_b=3$ was used and for well-evaporating vegetation B_b was set to 0.4 (Oke, 1987). The used Bowen ratio is applicable for grass vegetation that can evaporate well (Bowen ratio for potential evaporation is about 0.3 (Oke, 1982), and this can be found at many times in deltas with relatively stable water tables in the western part of the Netherlands. The wind speed and air temperature are different for urban areas compared to the open rural reference station due to the differences in roughness and the UHI effect which methods are described in the next section (5.2.3).

5.2.3 Mapping

The PET model of Equation 5.1 and 5.2 allows one to compute a heat map for the surroundings of the rural reference station mainly intended for urban areas but not limited to urban areas only. Hence, geographical or meteorological data must be processed to estimate the different components of these equations, which is presented in the flow chart in Figure 5.3 and Table 5.1. In case of the air temperature and wind speed, meteorological and geographical data must be combined. We discuss the estimation of the components governing the PET mapping, i.e. air temperature and humidity effects, wind speed, and shade effects by buildings and trees.

Table 5.1: Overview of used data sources for calculating the heat map. The resolution used for the calculation steps is 1 m. The resolution of the source data is shown in brackets. The exact links can be found in Table A5.1 in the Appendix.

Map	Resolution (m or h)	Flow-chart	Source	Open data?
Land use	1 (vector data)	D1	Buildings and Water map: OpenStreetMap via www.Geofabrik.de Vegetation: www.pdok.nl	Yes
Aerial photo (RGBI)	1 (0.25)	D2	www.pdok.nl	Yes
Rural reference station, KNMI or Wageningen Univ.	1	D3	www.knmi.nl www.met.wur.nl/veenkampen/data	Yes
Lidar based height map	1 (0.5)	D4	www.ahn.nl	Yes
Tree register	1 (vector data)	D5	www.boomregister.nl	No
Sky-view factor map	1	D6	www.knmi.nl	Yes

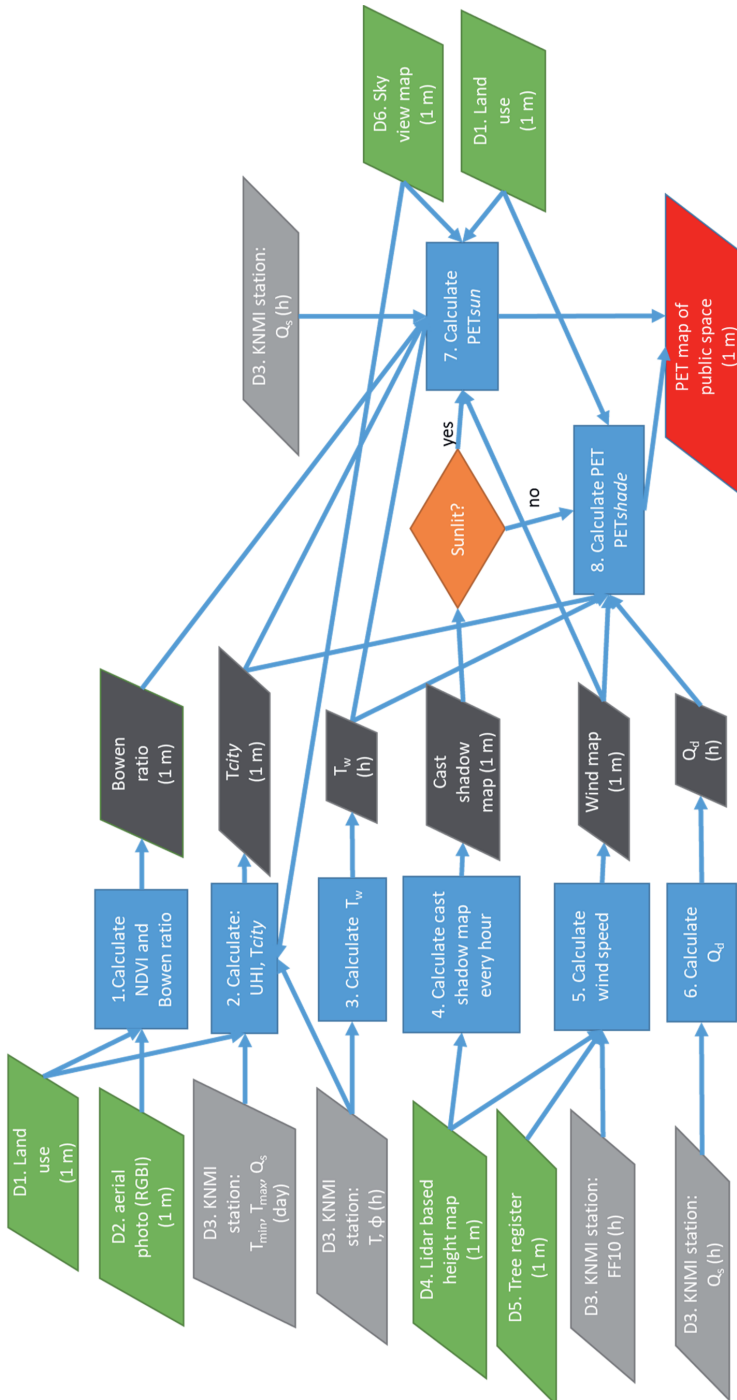


Figure 5.3: Flow chart of the data sources (D), subdivided in maps (green) and temporal weather data (grey). The intermediate products are indicated in dark grey and actions are indicated in blue rectangles. The end product in this flow chart is the PET map (red).

Air temperature and wet-bulb temperature

The UHI depends on meteorological conditions and the density of the urban environment. Typical weather leading to high UHI are low wind speeds and sunny conditions. The daily maximum UHI (UHI_{max}) can be estimated by a diagnostic equation, which includes geographical - (left) and meteorological factors (right) (Theeuwes et al., 2017):

$$UHI_{max} = (2 - SVF - f_{veg}) \sqrt[4]{\frac{S^{\downarrow} * (T_{max} - T_{min})^3}{U}} \quad (5.3)$$

Herein SVF and f_{veg} are the spatially averaged sky-view factor, and vegetation fraction respectively with a certain source area (see Figure 5.4). The meteorological term contains S^{\downarrow} , mean downward shortwave radiation (in Kms^{-1}) (kinematic units), $T_{max} - T_{min}$, the maximum and minimum temperature ($^{\circ}C$) representing the diurnal temperature range and U the mean wind speed (ms^{-1}), all measured at the rural reference station. T_{max} and T_{min} are determined between 8 UTC current day – 7 UTC next day (10 – 9 h local time) to represent the cooling potential outside the city (Unger et al., 2001; Theeuwes et al., 2017). The mean wind speed was also determined over this period. The mean downward shortwave radiation is determined over the current day. The maximum UHI occurs about four hours after sunset for calm clear days. For the other hours, the UHI_{max} is diminished by a correction factor that varies between -0.02 and 1 in the diurnal cycle Equation 5.4, Tables A5.3 and A5.4 in the Appendix).

$$T_a[h] = T_{refstation} + UHI_{max} * diurnal_{cycle}[h] \quad (5.4)$$

The diurnal cycle is inspired by a characteristic curve of UHI by Oke (1982). This curve was defined for one particular day length. For other day lengths the curves were adjusted considering that the minimum UHI occurs about 4 hours after sunrise (Theeuwes et al., 2015).

The derivation of Equation 5.3 implicitly considered that the remaining fraction of f_{veg} is built-up area (Theeuwes et al., 2017). Apart from the morphological effects described by the SVF , this built-up area is on average warmer due to the larger partitioning of sensible heat flux compared to the latent heat flux and has a temporal shift due the heat storage. The presence of water surfaces complicates the application of this equation. On the one hand, water bodies have a high heat capacity like built-up area (Steenekveld et al., 2014), but on the other hand do evaporate and have higher latent heat fluxes and consequently lower sensible heat fluxes averaged over the day. To enable the applicability of the straightforward equations, water surfaces are treated as built-up area at night, and as vegetation at daytime. This temperature pattern is observed for a weather station in the harbour of Rotterdam (Heusinkveld et al., 2014).

The SVF and f_{veg} were averaged for a source area of 500 x 1100 m (Figure 5.4), which corresponds to the correlation of land use and urban temperature as found in Heusinkveld et al. (2014). The source area is oriented towards the wind direction. In case of low wind speeds ($< 1.5 ms^{-1}$) a square-shaped source area of 700 x 700 m is used around the calculated grid cell. Since SVF and f_{veg} are averaged over a large source area, the output resolution was set to 25 m to reduce computational costs.

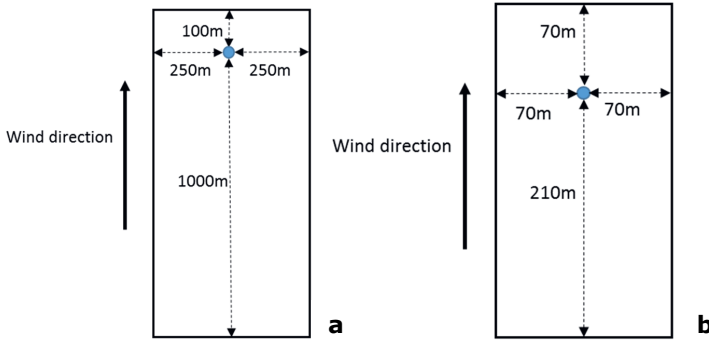


Figure 5.4: a) Source area for which the average sky-view factor and vegetation fraction is calculated on a resolution of 25 m. b) Source area for the calculation of frontal area density and building and tree heights which serves as input for wind speed computations.

To assign the f_{veg} two maps are created, one for daytime and one for nighttime, due to the special role of water surfaces. The vegetation fraction per grid resolution is determined using NDVI < 0.16 in the aerial photography. However, cropland might not be classified as vegetation fraction then, especially when it is bare at the time of data collection. Cropland, even if it is bare, will not store the amount of heat as built up area does. Therefore, cropland is assigned as vegetation fraction in the computation of air temperature (Table A5.1 D1 bgt_begroeidterreindeel in the Appendix).

For the SVF (either 1-m resolution for PET equation as 25-m resolution for T_a), water surfaces and buildings need to be excluded. A SVF cannot be identified for water bodies, which is a limitation of the underlying lidar technology (Worstell, et al., 2014). To estimate T_a , the SVF under trees and other vegetated surfaces has been excluded. The effect of reduced SVF in an urban canyon (mainly consisting of impervious road and pavements) has a more enhanced UHI effect than the reduced SVF in parks by trees, due to the storage difference between buildings and trees. Ignoring the SVF from green surfaces cancels a large part of this uncertainty. Subsequently, the mean SVF is computed over the source area. In case the vast majority is filtered out, then the SVF is set to 1 corresponding the rural reference case. The specific rules are presented in the Appendix B2.

The wet-bulb temperature was calculated according to (Stull, 2011):

$$T_w = T_a \operatorname{atan}(0.151977(\phi + 8.313659)^{0.5}) + \operatorname{atan}(T_a + \phi) - \operatorname{atan}(\phi - 1.676331) + 0.00391838\phi^{\left(\frac{3}{2}\right)} \operatorname{atan}(0.023101\phi) - 4.686035 \quad (5.5)$$

Herein T_a denotes the air temperature and ϕ the relative humidity, both measured at the rural reference station. So, a constant T_w is applied everywhere including the city. The relatively small coefficients of T_w in Equation 5.1 (6% compared to T_a), justifies this pragmatic approach, instead of calculating T_w for every urban grid cell with urban temperature. Besides, the relative humidity is generally lower in urban areas (Landsberg & Maisel, 1972; Hage, 1975), which counteracts the slight rise on T_w due to higher urban air temperatures.

Wind speed

According to WMO guidelines reference weather stations were sited in open terrain with a low surface roughness (WMO, 2014). The surface roughness is substantially higher at other locations in the heat map in the vicinity of buildings and trees which coincides with lower wind speeds. A translation of the wind speed was made from the open reference station to locations with a higher surface roughness. First, we computed the mesowind at the blending height (60 m) from the wind and surface roughness of the weather station (roughness length $z_0 = 0.03$ m) using a logarithmic wind profile in neutral conditions. The blending height is where the wind flow is supposed to be homogenous and thus independent of z_0 . According to field experiments performed by MacDonald (2000), the wind speed is translated to 1.2 m in the urban canopy and representative for an averaged wind speed at neighbourhood scale. Above the roughness layer the wind profile is semi-logarithmic, whereas the wind profile is exponential within the urban canopy. A stepwise approach with equations is presented in the Appendix B5).

For the MacDonald method, the frontal area density of buildings is an important indicator of wind reductions in urban areas. The frontal areas were determined by deriving the perpendicular surfaces towards the wind direction (see Appendix Figure A5.3 for a visual representation). The source area for the frontal area density is 280 x 140 m aligned in the wind direction (Figure 5.4b).

Here we added the implementation of frontal area density of trees to compute a total frontal area density in Equation 5.6, because trees also slow down the wind in real urban situations. The frontal area density for trees is represented as if it was a rectangular shape (frontal view) which holds for ordinary buildings. The wind-oriented crown area consists of 55% of a rectangle λ surface, based on an ellipse shaped crown stretching 2/3 of the total height. Together with a small roughness reducing effect of porosity (0.9), the coefficient for trees 0.3 is half as large as the coefficient for buildings (0.6) (Equation 5.6). The offset 0.015 is used to account for a small saturation effect. Larger frontal areas have higher chances that buildings and trees stand in each other's wind shadow.

$$\lambda_{tot} = 0.6\lambda_{buildings} + 0.3\lambda_{trees} + 0.015 \quad (5.6)$$

The coefficients in Equation 5.6 do not add up to 1, which is because often a part of the trees lies in the wind shade of adjacent buildings.

Sun and shadow

Exposure to direct sunshine is a prerequisite for high PET values. Sunlit locations can be determined by a cast shadow map. This cast shadow map can be created with the lidar based height map (AHN) and the UMEP GIS tool (Lindberg et al., 2018). This GIS tool can calculate cast shadows at all solar elevation angles during the day and season. Unfortunately cast shadows cannot be determined at the surface under the tree crown. Therefore, the area below trees is designated as shadow if trees are higher than 2 m. This last prerequisite of 2 m is introduced to enable entering solar rays at the edge of the trees. In reality the foliage is partially transparent to solar radiation, so that PET values are slightly underestimated under trees. However, the priority is to distinguish the hot spots in the heat map which is never found under trees during daytime.

The empirical PET equation in 5.2.1 require the solar irradiation (Q_s) and the diffuse radiation (Q_d). The Q_d is calculated from Q_s as measured at the rural reference station, with a solar elevation angle (ϕ) that depends on the time of the day and the date:

$$\frac{Q_d}{Q_s} = \begin{cases} 1, & \text{if } \tau_a < 0.3, \\ 1.6 - 2\tau_a, & \text{if } 0.3 < \tau_a < 0.7, \\ 0.2, & \text{if } \tau_a > 0.7. \end{cases} \quad (5.7)$$

herein the atmospheric transmissivity (τ_a) is estimated as (de Rooy & Holtslag, 1998):

$$\tau_a = \frac{Q_s}{1367 \sin(\varphi)} \quad (5.8)$$

The solar irradiation from the reference station is a sum of the past hour. To estimate the amount of radiation for the entire hour, the radiation for the coming hour and the past hour is averaged.

5.2.4 Climate scenarios

The recipe for the heat maps can also be utilized for climate projections. KNMI developed four scenarios for 2050 to depict how the climate may evolve (Klein Tank et al., 2015). These scenarios are derived from global climate model computations of the IPCC, global climate model EC-Earth results and on a downscaling step within a regional climate model. These model results are grouped in a scenario with a low - or high global temperature rise, and small or large change in circulation pattern. For each scenario, KNMI provides numerical values for temperature, relative humidity and radiation shifts, allowing conversion of meteorological time series from the current to a future climate (KNMI, 2015). In this study we transformed the time series to the so called W_H scenario of 2050, which represents a high global temperature rise (W). The suffix “H” denotes a change in air circulation pattern, which envisages more high pressure dominance in summer resulting in drier, sunnier summers with an increase of easterlies. Daily maximum -, minimum - and average temperatures are transformed to the W_H scenario of 2050 and interpolated to hourly temperature values according Chapter 4, which further elaborates on Molenaar et al. (2016).

We use a new hourly based transformation of radiation, which elaborates on the transformation of daily solar irradiation by Bakker (2015). In the W_H scenario, an increase in monthly radiation is expected due to a decrease in cloudiness in the summer months. It is important that already clear-sky sunny days will not receive extra radiation, since radiation is an important term in the PET. Therefore, the Angot radiation is determined on an hourly basis (Allen et al., 1998), and multiplied with a daily averaged transmission factor of the atmosphere as used in the Angstrom equation. For individual hours, a daily averaged transmission factor does not hold. At noon, the sun ray path through the atmosphere is shorter than just after sunrise and before sunrise. To estimate this difference, we created a series of measured ratio of solar irradiation / Angot radiation for the different hours for 15 summer half years. Per hour we created a 95th percentile. For the Netherlands this percentile represents days with unobstructed sunshine. Hours that receive this amount of radiation or more in current climate, cannot receive extra radiation in a future climate. For hours below the 95th percentile the projected radiation increase is applied with an upper limit of the 95th percentile. So, this procedure ensures a realistic transformation of radiation on an hourly basis and this is summarized in the conditional equations below (Equation 5.9). The values of the percentiles to calculate $Q^a(h)$ is presented in the Appendix B9, based on the climatology of reference weather station Herwijnen.

$$Q^f(h) = \begin{cases} Q^c(h), & \text{if } Q^c(h) > Q^a(h) \\ Q^a(h), & \text{if } Q^c(h) * \Delta Q(m) > Q^a(h) \\ Q^c(h) * \Delta Q(m), & \text{else} \end{cases} \quad (5.9)$$

$Q^c(h)$ = hourly Q_s current climate

$Q^f(h)$ = hourly Q_s future climate

$Q^a(h)$ = Angot radiation corrected for 95th percentile of observed hourly Q_s

$\Delta Q(m)$ = monthly Q_s increment to future climate

5.2.5 Traverse measurements with cargo bicycle

The heat map has been validated against mobile observations consisting of all meteorological quantities that affect the human energy balance. The mobile measuring set-up consists of a cargo bicycle that is equipped with shortwave and thermal radiation sensors, ventilated air temperature and humidity sensors and an ultrasonic anemometer, see Heusinkveld et al. (2010). The measurement consists of a pre-programmed route, extending 6 km through urban areas. The route has been designed such that they sample as much as possible contrasting neighbourhoods, such as neighbourhoods with terraced houses, multi-storey apartments and a forested quarter with detached houses. The wind observations have been corrected for the bicycle speed by means of wheel speed and GPS speed measurements. Since the sensors have a certain inertia, observations should be averaged over a stretch of 20 m. Besides, the radiation sensors are separated on both sides of the driver to prevent measuring the driver himself, which means it is not possible to measure exactly on the square meter. However, variables such as temperature and wind speed also vary greatly over time, which means that validation of a heat map is only useful after spatial averaging. The model results are averaged over a stretch of 20 m, and 10 m in width. Curves and (near) stand stills for intersections have not been sampled. Curves have more uncertainty in wind speed estimates and source areas. Also, locations where the building stock dataset (documented in 2010) strongly differs from the real building stock at the moment of the observations (in 2013), have been eliminated to ensure a proper comparison.

5.3 Results

5.3.1 Validation

In the validation section the empirical model is compared with thermal energy model Rayman and the model results are validated with cargo bike observations. We find a sound agreement between the empirical model and Rayman (Figure 5.5). The deviations for the sunlit empirical model show a little more spread, with a RMSE of 0.74 °C compared to an RMSE of 0.36 °C for shadowed empirical model.

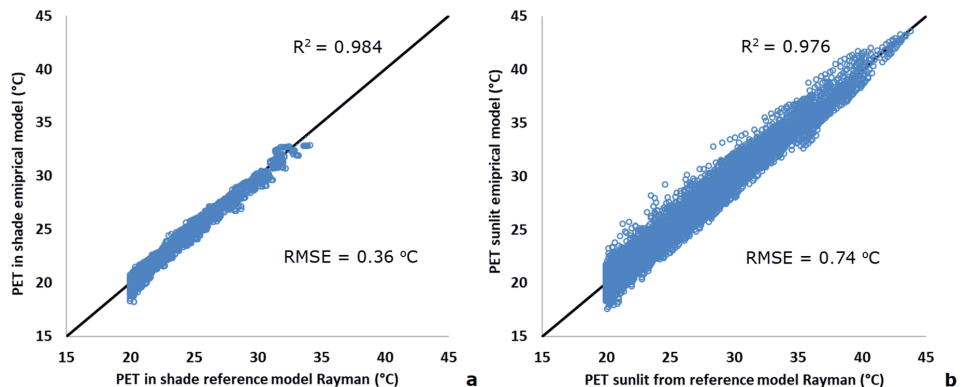


Figure 5.5: Comparison between results of the empirical PET model and the reference output from human thermal energy model Rayman for a) sunlit conditions and b) shadowed conditions.

The validation with observations and corresponding heat map is presented for 2 August 2013, which was a clear-sky hot summer day for which traverse measurements were available. The maximum temperature recorded at the rural site was 34.2 °C, and the afternoon background 10-m wind was 3 Bft (5 ms⁻¹). This day is comparable in temperature with the 1:1000 heat day presented in the next section.



Figure 5.6: a) Heat maps of modelled PET and b) observed PET on August 2nd 2013 12 UTC (14 h local time).

Figure 5.6 and 5.7 present respectively the modelled and observed PET and the difference between the modelled and observed PET for 12 UTC for urban areas. The relatively cool areas in the forested quarter in the northeast are well represented (white circle Figure 5.7). In the city itself deviations in PET are larger, consisting of mainly positive biases. Figure 5.8 shows the correlation between modelled and observed PET, especially in the higher PET percentiles with relatively small

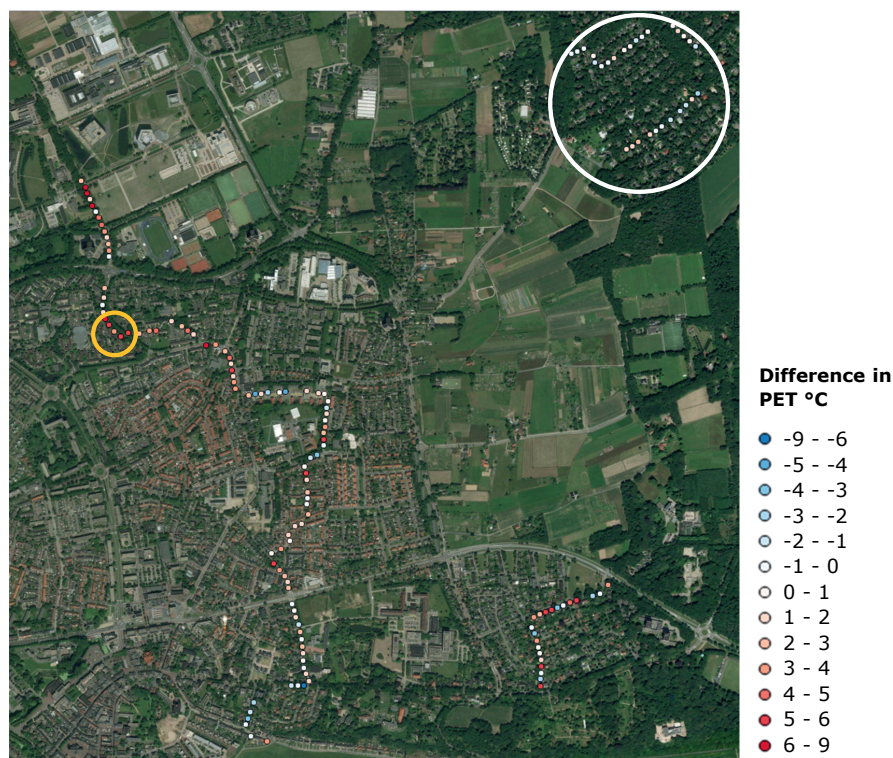


Figure 5.7: Difference between modelled and observed PET on August 2nd 2013 12 UTC, (14 h local time). The white circle indicates the forested quarter which is simulated well. The orange circle indicates a place with a positive PET bias induced by an overestimation of modelled radiation.

standard deviations. In the lower and mid percentile groups (0.2 - 0.6) the differences are larger with a positive bias (median) that correspond to shadowed or partially shadowed locations. Most of these sampled locations have trees providing shade and the differences are directly linked to differences in observed and modelled radiation. Substantial differences occur in the real tree crown providing shadow and the tree crowns used in the model. PET differences between neighbouring shadow and sunlit data points are ≈ 13 °C in the city and this can have a significant effect in the sampled source area. E.g. in the orange circle (Figure 5.7) positive PET biases are caused by an overestimation of sunlit data points in the middle of the road. In the method, we used a 2-m object height threshold (lidar based) to remove edges of trees and defoliated trees. This operation leads to an overestimation in modelled radiation here and on average for the whole route. However, although PET biases are much smaller by renouncing this operation this leads to too low radiation averages near trees and a larger bias corrected RMSE. Besides, we note that there is a general uncertainty in the transmissivity of radiation of trees, especially in the diffuse component for foliated trees (Konarska et al., 2014). During droughts there is a larger risk of defoliation by insect defoliators and pests (Rouault et al., 2006), which logically increase the transmissivity of radiation. In general, the variation of multiple reflections between buildings, street surface differing in albedo and trees in different configurations cannot be covered in its full complexity. The PET equation can resolve a part, based on the street configurations in the training dataset.

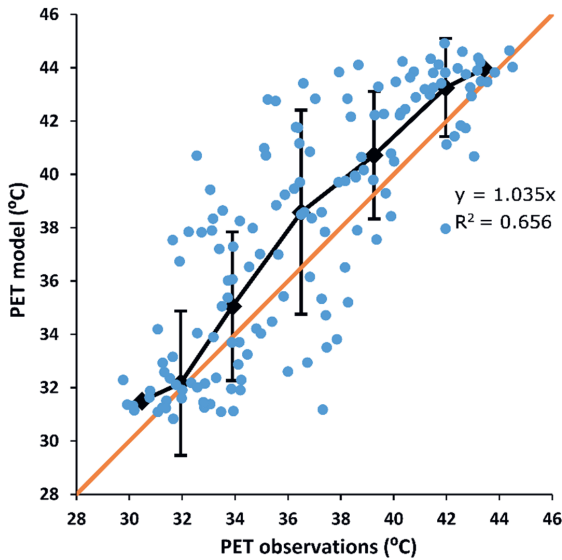


Figure 5.8: Scatter plot of observed and modelled PET samples on August 2nd 2013 at 12 UTC in Wageningen (blue dots). The black line and points indicate the percentile groups of the PET bike with bars indicating the standard deviation of PET differences between model and observation. The borders of the PET percentile groups are 0.05, 0.2, 0.4, 0.6, 0.8, 0.95. The lowest and highest percentile group <0.05 and >0.95 did not show a standard deviation, because the amount of data is limited compared to the other percentile groups. The orange line indicates the 1:1 line.

In Wageningen the average modelled wind speed corresponds well with the observations (bias amounts to 0.18 ms^{-1}). The spatial wind variation of the cargo bike and model does not match so well. From the observation side, uncertainties in wind speed arise through wind modifications by traffic and in lesser extent stream flow by the cargo bike and driver itself. More important, the wind speed is variable at short time scales because of daytime turbulence, and higher or lower wind observed wind speed may not always reflect the general wind speed at certain locations. From the model side, the urban wind is discussed in Section 5.4. Wind speed differences are about three times less important in explaining the PET deviations than radiation differences. Finally, the modelled urban air temperature resembles the measured air temperature. The spatial differences in urban temperature are small at this time step, because the UHI is small in afternoon.

5.3.2 PET heat map for daytime

For the standardized PET map, we selected 1 July 2015, which is the 1:1000 heat day for WMO reference station Herwijnen (38 km southwest of Wageningen, Figure 5.1b) for the period April–September. This corresponds to a 1 in 5.5 chance for the current climate. Also this day had continuous clear-sky weather with slightly more wind in afternoon, 3–4 Bft at the reference station. The afternoon average PET heat maps are shown in Figure 5.9 for the current climate and for the future climate (KNMI'14 W_H scenario 2050).

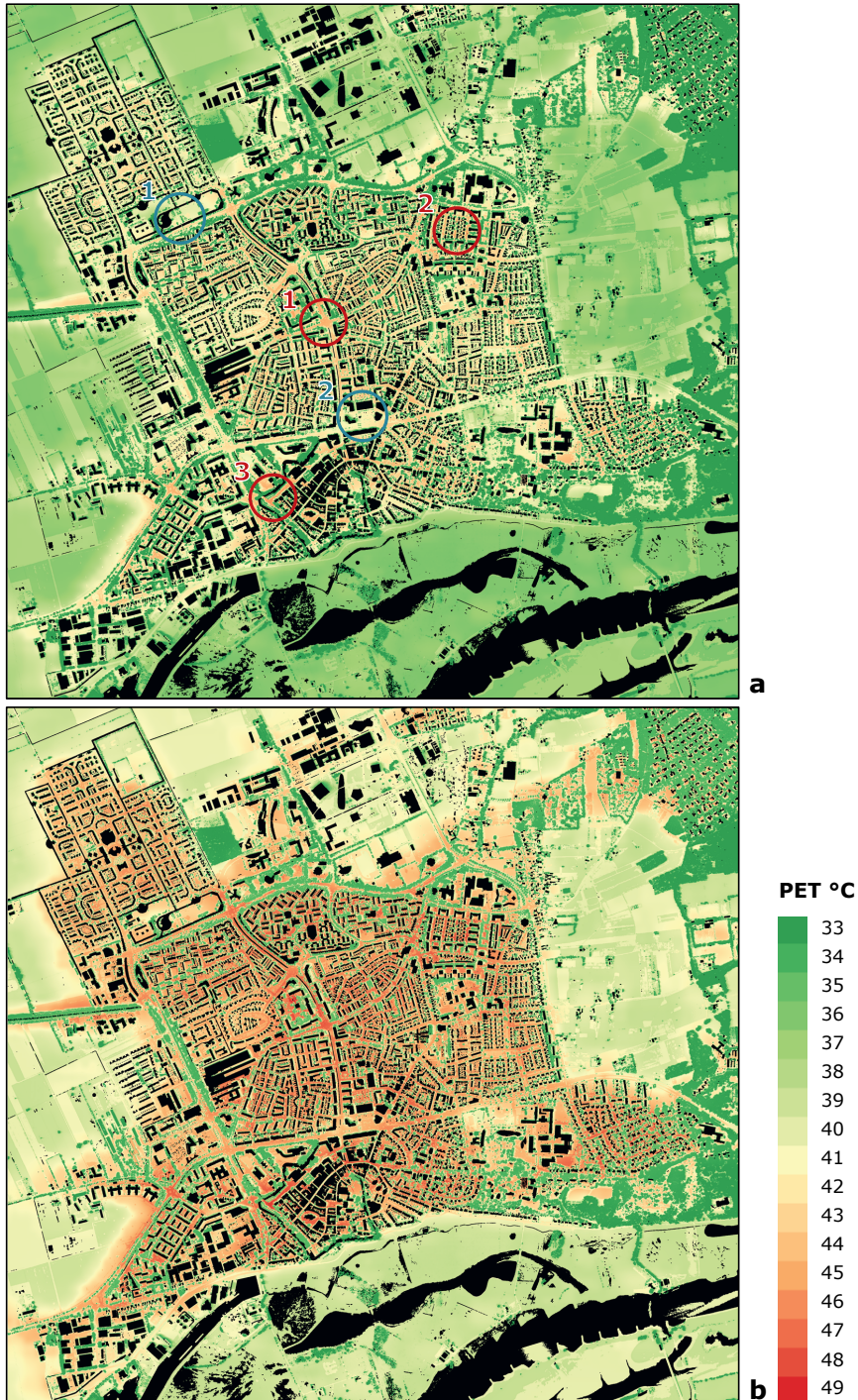


Figure 5.9: Heat map showing mean PET for July 1st 2015, during 10–16 UTC (12–18 h local time) driven with the meteorology of the Herwijnen reference station. (a) current climate, (b) future climate 2050, translation to the WH climate scenario. Red circles indicate hot spots and the blue circle a cool spot.

Hot spots with $44\text{ }^{\circ}\text{C} < \text{PET} < 46\text{ }^{\circ}\text{C}$ are found on locations facing many hours of sun during afternoon and where the wind is reduced due to large frontal area densities of buildings. Examples of such locations are relatively open spaces like squares and non-vegetated roundabouts (red circle 1 in Figure 5.9a). Less open spaces as street canyons with middle-rise buildings, and downwind the urban centre with a large area of buildings and narrow streets are also hot spots (see red circles 2 and 3 in Figure 5.9a). The coolest spaces at daytime are the locations under the trees in the shadow. Other relatively cool spaces that are sunlit are open places with much ventilation such as open parks (blue circle 1). Remarkably, also a crossing leeward of an impervious bus station is relatively cool (blue circle 2). Upwind there are only few buildings that aligned as such that the wind is not obstructed much.

The increase in PET in the W_H scenario amounts to $2.8\text{ }^{\circ}\text{C}$ all over the map and can be almost entirely attributed to the change in background air temperature, so changes in urban–rural differences and changes in shade–sun differences are negligible (Figure 5.9b). In other words, the magnitude of UHI is virtually unchanged in this scenario. The increase of sun duration is expected in the summer months for the W_H scenario and therefore solar irradiation increases on average. However, the selected day was already sunny and significant increases in solar irradiation are therefore not possible. the W_H scenario is slightly drier in the summer months by adding the monthly numerical values. However, the lower relative humidity in the W_H scenario has a negligible effect on PET ($0.04\text{ }^{\circ}\text{C}$).

5.3.3 PET exceedance map

From a climatological perspective it is interesting to examine an entire summer season of spatial PET differences. As climate stress tests should be focussed on heat stress, we may count the number of hourly exceedances of a PET threshold where most persons feel dissatisfied regarding heat stress, i.e. $29\text{ }^{\circ}\text{C}$. A PET exceedance map is robust since it is not influenced by day-specific weather. In the Netherlands warm episodes can originate from different circulation types (Kyselý, 2008), varying from weak winds from a central European high, or a stronger circulation of warm air from the south or east. To cover both mechanisms the accumulation of heat load over a whole summer is more representative than for a selected day. An analogous approach is used for moderating air quality in the European Union, whereby daily contaminant concentration exceedances are counted above a threshold value (EU-Commission, 2008). For contaminants, there is also a limit indicating the number of days per year this threshold value may be exceeded, which is not regulated for heat stress.

The exceedance maps show the number of hours the PET exceeded ($\text{PET} > 29\text{ }^{\circ}\text{C}$) for the current climate and translated into the future climate (Figure 5.10). The summer half year of 2013 has a climatological average temperature and average heat production (accumulation average daily temperatures above $18\text{ }^{\circ}\text{C}$) and is therefore representative as example.

Figure 5.10a shows that in the town, the PET criterion was exceeded by ≈ 160 hours per year in the rural countryside up to 430 hours in wind sheltered and unshaded locations places. For the W_H scenario, an increase of 80–110 PET exceedance hours is expected for predominantly unshaded places. Locations with a relatively high shade and / or windy locations show a smaller increase i.e. up to a 30-hour increase under trees.



Figure 5.10: Modelled number of hourly PET exceedances above 29 °C in 2013 for the current climate (a) and the W_H climate scenario (b) with the meteorology of the Herwijnen reference station.

5.4 Discussion and recommendations

5.4.1 Urban climate maps

Here we discuss heat maps developed with various models of contrasting complexity and grid spacings from 5 m to 500 m and compare these with our heat map. First, the urban heat maps are discussed which are based on general urban classifications and/or predominantly analytical or statistical geo-information models for landscaping a wind. Second, the heat maps based on complex numerical simulations are evaluated.

In the field of urban planning a popular method to distinguish distinct local climates is the use of climatopes (Scherer et al., 1999). Climatopes are urban classifications based on common climatic geographical aspects. Examples include the Thermal Environmental Map of Tokyo, (TMG, 2005) and urban climatic maps for Hong Kong and Arnhem (UCMAPS) (Ren et al., 2012; Ng, 2012). The Thermal Environmental map of Tokyo distinguishes different thermal classes on 500-m resolution based on urban density and anthropogenic heat, apart for residential and commercial areas (TMG, 2005; Ren et al., 2011). Although this map may be intuitive and clear to urban planners, they miss spatial detail and lacks heat stress criteria which is provided by our heat map.

The urban climatic map of Hong Kong contains more spatial detail and is also based on the PET estimated with continuous urban morphology data, green spaces and wind (Ren et al., 2011; Ng, 2012). However, the map does not visualise PET but an urban classification scale. In contrast to our heat map, they did not take into account sun and cast shadow effects, which apparently is important for fine grid PET calculations. Another widely used methodology are the Local Climate Zone (LCZ) based on a scale of 250 m and larger. The LCZ differs from climatopes by leaving out local topography and local climatology factors (Stewart & Oke, 2012), i.e. it will not represent wind ventilation paths. They are based on universally recognized built forms and land cover types and may serve well as basis for heat maps scaled up from neighbourhood observations (Alexander & Mills, 2014), and numerical model heat maps (Bassett et al., 2016; Ching et al., 2018). Verdonck et al. (2018) carried out both numerical simulations and an observational assessment on LCZ classes and found quite overlapping normalized temperature ranges. Alternatively, Shi et al. (2016) interpolated urban observations with different geographical mapping methods into an urban climate map and noted a RMSE for PET of 2.0–2.3 °C for Hong Kong. This compares well with the found RMSE in our study.

The finer scale heatmaps from numerical simulations which use a grid resolution between 100 m and 1 km (Bohnenstengel et al., 2011; Heaviside et al., 2015; Ronda et al., 2017; Hoffmann et al., 2018), cannot capture the energy and wind flow of individual buildings and therefore it needs to parameterize. For urban parameters as building height and frontal area index the determination for a grid is comparable as calculated by the source areas in our study (Bohnenstengel et al., 2011; Ronda et al., 2017). Although the offered detail is not so large for a heat map, the simulated temperatures were within an accuracy range of 1–2 °C for Bohnenstengel et al. (2011). Ronda et al. (2017) evaluated urban fine-scale forecasting for lead times up to 48 hours. Mean absolute errors from independent air temperature observations were quite low in the first 24 hours, with 1.5 °C at daytime and 1 °C at nighttime. Relatively small-scale models with grid spacings of ~5 m apply computational fluid dynamics, which implies that individual buildings with accompanying wind flow and energy exchanges could be resolved. Ashie and Kondo (2011) performed a heat map for whole Tokyo with an RMSE of 1.1 °C. However, it should be noted that they used a steady state calculation since the size of the domain is huge. Although numerical models might perform slightly

better than the analytical and statistical geo-models including ours, the applicability of the latter is larger to other areas. Moreover, the calculations of climate adaptation measures in the urban climate map is much faster for geo-models. Finally, it was demonstrated for our climate map that it is possible to calculate a climatology for a year, which is impossible for numerical models with a fine resolution for a city domain.

5.4.2 Urban wind

Wind speed strongly affects the PET, because it determines largely how efficient the human body can transfer heat to the atmosphere (Höppe, 1999). Especially in situations with low wind speed, the PET is relatively sensitive to the wind speed as this can be observed in the logarithmic terms in the PET equation. So, the uncertainties in wind speed lead to a larger deviation in PET at low wind speeds.

Pedestrian wind speeds have also been derived with urban morphology by Johansson et al. (2016), who found good statistical scores based upwind fetch distances to closest buildings and downwind *SVF*. A downside is that trees are not implemented and that the set-up and validation is done against another model instead of independent observations. The role of trees on the wind speed in urban canyons has been investigated by several studies (Heisler, 1990; Huang et al., 1990; Salim et al., 2015; Kent et al., 2017; Zhang et al., 2018). Huang et al. (1990) produced a straightforward regression equation translating open field wind velocities to urban site wind velocities by conducting one total canopy (planar surface) density from buildings and trees data from Heisler (1990).

In addition, Kent et al. (2017) earlier adopted vegetation frontal area densities in the morphometric method of MacDonald et al. (1998) to calculate urban canopy wind. They expand the method by recalculating the z_0 and using separate drag coefficients for trees and based on porosity estimations of Guan et al. (2003). The relative contribution of trees in the frontal area density is similar (45%) to our estimations, holding the same dimensions of trees. Alternatively, Kent et al. (2017) add the frontal area densities of trees to an unaltered definition of frontal areas for buildings. On the contrary, we reduced the contribution of buildings by a factor 0.6 (Equation 5.6), so our frontal area densities are smaller which correlates with less wind reduction.

With small-scale computational fluid dynamics models, wind speeds can be properly modelled around individual buildings and trees on a 1-m scale resolving turbulence (Salim et al., 2015). However, the domain size is limited since the method is computationally intensive. Salim et al. (2015) simulated a wind field for a domain size of 2 by 2 km² on 1-m scale for the city centre of Hamburg. A large city as Tokyo (33 x 33 km²) has been simulated on 5-m resolution. Another advantage of the GIS-based tools approach in our study is that it allows for quicker computation of modifications in an urban area like greening or implementation of extra trees.

In the current approach, the source area for wind including the frontal area density is 280 x 140 m, aligned in the wind direction (Figure 5.4b). Ching et al. (2009) used 1 km² as resolution for frontal area density in NUDAPT, which is a database with an urban morphology statistic set-up for meteorological models. Wong and Nichol (2013) and Burian et al. (2002) used a smaller source area of 100 m. Although Wong and Nichol (2013) finds a good correlation of 0.57 for modelled and observed windspeed in Hong Kong, we think 100 m is too small to estimate the wind speed. Firstly, local wind behaviour, like channel flow can be resolved partly with our approach and corner accelerations are not possible. Second, winds at higher levels, such as at the top of the roughness layer are affected by roughness elements further upstream (Grimmond et al.,

1998). The top of the roughness layer varies within urban morphologies differing in density and building height. Kent et al. (2017) used this weighted source area approach for determination of roughness variables to calculate λ for a climatology of Swindon UK. Applied to Wageningen (similar urban density), our stationary source area covers 80% of the weighted source area, which corresponds well. Note that a larger source area for Wageningen would give excessive weight to obstacles further away.

5.4.3 Outlook and recommendations

Development and disclosure of reliable monitoring data regarding urban heat stress is of primary importance in order to better describe the influence of land use and urban morphology factors. Also fixed stations which measure the required components of the PET are indispensable. Validation with these stations may provide clarity about the skill of the PET heat maps, by comparing uncertainties due to temporal variations of wind humidity and temperature (Shi et al., 2016). Geographical improvements in the heat map consists of applying thermal properties of the urban fabric including albedo, a more sophisticated approach incorporating water surfaces, and anthropogenic heat sources.

Starting with anthropogenic heat, this may be included in the UHI formula by adding it to the solar irradiation. Although it implies that not all terms on the meteorological of the formula is measured at a rural site anymore, physically urban specific energy fluxes can be applied here. Note, that the UHI equation is in the end a diagnostic regression formula between two dimensionless groups in a dimensional analysis. For most cities in western Europe (where the equation has been tested) anthropogenic heat plays a minor role on hot summer days, compared to solar irradiation determining the UHI. For dense high-rise districts as the city of London and central Tokyo reporting summer daily averages over 100 Wm^{-2} (Ichinose et al., 1999; Iamarino et al., 2012), anthropogenic heat becomes more significant. For comparison warm sunny days denote typically $300\text{--}350 \text{ Wm}^{-2}$ for mid-latitudes.

The albedo determines the fraction of solar radiation that is absorbed by a surface. For urban areas this determines also how much energy is stored in the urban fabric and relates directly to UHIs. Increasing urban fabric albedo by 0.2 can result in a daily peak reduction of 0.65°C for a clear summer day based on validated model simulations for Basel, Switzerland (Hamdi & Schayes, 2008). In Equation 5.3 the albedo can be included as an absorption coefficient in front of the solar irradiation term.

However, Equation 5.3 will not account for direct effects of adjustments of albedo on air temperature at daytime, since at daytime the diurnal factor is small. It is more complicated to incorporate these effects in a practical formula. Different albedos lead also to different partition of incoming shortwave radiation reflected by walls and streets. Therefore, it is recommended to re-train the PET model with the human energy model Rayman for various albedos. For both albedo and anthropogenic heat, it is advised to re-evaluate the underlying regression of the UHI equation and coefficients might be added to the meteorological variables. Furthermore, we like to address that soil moisture availability is important to consider. Dry episodes will reduce the cooling effects of vegetation by limiting evapotranspiration. It is recommended to apply higher Bowen ratios if soil moisture is limited. This is common for drier climates and sandy soils that is known to be unable to retain water well. In our study the soil moisture availability was quite high and relatively stable, because parts of Wageningen are a seepage area and water levels are managed in detail.

Finally, we discuss the empirical PET equation and the thermal thresholds. In other climate zones thermal perceptions may vary, due to the adaptation to a warmer or colder climate (Cohen et al., 2013). Also, the metabolic rates of equal activities vary and therefore the corresponding PET is different. The moderate heat stress limit in Taiwan is 5 °C higher compared to that of western and central Europe (Lin & Matzarakis, 2008). Besides it is important to retrain the PET model with representative climate data in other climate zones.

5.5 Conclusions

In this paper, we present a recipe for a 1-m resolution heat map representing the Physiological Equivalent Temperature (PET) at pedestrian height for current and future climate. As testbed the mid-sized town of Wageningen (the Netherlands) has been chosen since traverse observations are available for this town. The heat map is developed in two stages. First, we derive an empirical PET model based on Rayman model simulations for a representative set of street configurations and through the summer season. Second, this empirical model is applied for a city using geographical information. Herein, established methods for estimating urban air temperatures and street-level winds are combined in an empirical PET model.

Subsequently, one heat map is derived for a warm clear-sky summer afternoon which represents a 1:1000 heat day. By aggregating the PET load for the entire afternoon, the map represents an average heat load and justifies the hourly sun and shadow differences. The maximum PET in the afternoon amounts to 46 °C for calm sun exposed locations. In the KNMI W_H climate scenario for 2050 the PET is projected to increase quite uniformly with 2.8 °C. In addition, climatological heat doses are calculated by counting exceedances of PET values above 29 °C. For a representative year the maximum exceedances develop from 430 hours to 530 hours per year in the W_H scenarios. Within a city, the amount of exceedance hours is threefold that of the open rural environment. From a verification with cargo bike weather observations, radiation differences lead to largest uncertainties in PET, due to uncertainties in the size and transmissivity of tree crowns.

With this recipe for heat maps we intend to promote risk dialogues within municipalities and relevant boards. A logical next step is the development of a national PET heat map based on the developed recipe. Further progress can be made by including albedo, anthropogenic heat and a more sophisticated inclusion of water surfaces.

Acknowledgements

GJS acknowledges funding from the Netherlands Organization for Scientific Research (NWO) VIDI Grant 'The Windy City' (file no. 864.14.007). Moreover, we acknowledge funding from the Ministry of Infrastructure and Water management. We thank Ton de Nijs (RIVM) for his feedback and leading the Dutch program for developing a standard stress test, and we thank all other contributors. In particular we thank Reinder Ronda (KNMI/WUR) for the initial discussions in setting up the framework of the different steps. In addition, we acknowledge all other users (students, stakeholders) for their feedback and questions, while they conduct the recipe. Finally, we thank prof. Andreas Matzarakis (DWD) for fruitful discussion in the design phase of our PET map.

Appendix

This document is a concise but complete step-by step recipe including all operations to create the PET heat map. It starts with two tables listing the input data sources and calculation steps (Table A5.1; Table A5.2). Thereafter, the operations are separately described in the sections B1-8. The numbers refer to the flow chart numbers in Figure 5.3. In B9, it is explained how meteorological data can be transformed to future climate scenarios. Lastly, B10 contains a list of symbols.

Table A5.1: Overview of used data sources for calculating the heat map. The resolution used for the calculation steps is 1 m.

Map	Resolution (m or h)	Flow chart	Source	Open data?
Land use	1 (vector data)	D1	Buildings OpenStreetMap via Geofabrik: http://download.geofabrik.de/europe/netherlands.html/netherlands-latest-free.shp.zip Vegetation PDOK (bgt): https://mijn.pdok.nl/nl/producten/pdok-downloads/download-basisregistratie-groot-schalige-topografie(bgt_begroeidterreindeel) Water OpenStreetMap via Geofabrik: http://download.geofabrik.de/europe/netherlands.html/netherlands-latest-free.shp.zip (gis.osm_water_a_free.shp)	Yes
Aerial photo (RGBI)	1 (0.25)	D2	PDOK: Within the PDOK plugin in QGIS the following maps are retrieved: Luchtfoto 2016 Ortho 25 cm RGB Luchtfoto 2016 Infrarood 25 cm	Yes
Rural reference station, KNMI or WUR	1	D3	KNMI: https://www.knmi.nl/nederland-nu/klimatologie/uurgegevens WUR: www.met.wur.nl/veenkampen/data	Yes
Lidar based height map	1 (0.5)	D4	www.ahn.nl (original source) map sheets: https://www.pdok.nl/viewerwebmap object height: http://geodata.nationaalgeoregister.nl/ahn2/atom/ahn2_05m_ruw.xml ground level: http://geodata.nationaalgeoregister.nl/ahn2/atom/ahn2_05m_int.xml	Yes
Tree register	1 (vector data)	D5	www.boomregister.nl	No
Sky-view factor map	1	D6	KNMI: ftp://data.knmi.nl/download/sky_view_factor_netherlands/1.0/noversion/2007/01/01/	Yes

Table A5.2: Overview of calculation steps, and its locations in the flow chart. The description of the operation steps is described in the sections B+(flow chart number). The air temperature and wind speed map are interpolated from 25 and 35 m to 1 m, respectively, before the PET calculations are performed.

Operation	Resolution (m)	Flow-chart	Operations and sections in Appendix.
Vegetation per pixel and Bowen ratio per pixel	1	1	Vegetation pixel as $(I-R)/(I+R) > 0.16$ I= infrared value R=red value Bowen ratio =3 in city and 0.4 for water and vegetation. (well evaporating)
T_{city} , (T_a in city), UHI, vegetation fraction and average sky-view factor	1 (25)	2	Sec B2
Wet bulb temperature T_w	-	3	As function of T_a and ϕ , see B3
Cast shadow map	1	4	Calculate cast shadow map for 1 h intervals with the lidar based height map (for the entire year 2013 a 2-hour interval is used for practical reasons). Per month decade new cast shadow calculations should be made.
Wind speed	1 (35)	5	Translating wind from reference station to mesowind at 60-m height and then translating to street level via method MacDonald (see B5).
Diffuse irradiation	-	6	Sec B6
PET in the sun	1	7	Sec B7
PET in the shadow and night	1	8	Sec B8

B1. NDVI and Bowen ratio

$$PET_{sun} = -13.26 + 1.25T_a + 0.011Q_s - 3.37 \ln(u_{1.2}) + 0.078T_w + 0.0055Q_s \ln(u_{1.2}) + 5.56 \sin(\varphi) - 0.0103Q_s \ln(u_{1.2}) \sin(\varphi) + 0.546B_b + 1.94S_{vf} \quad (A5.1)$$

The B_b Bowen ratio indicates the ratio between sensible heat flux and latent heat flux. For urban surfaces a typical value of 3 was used and well evaporating vegetation and water was set to 0.4. The NDVI threshold of 0.16 determines if a model data point is designated as vegetation pixel with corresponding Bowen ratio (Table A5.2).

B2. Urban air temperature

$$PET_{sun} = -13.26 + 1.25T_a + 0.011Q_s - 3.37 \ln(u_{1.2}) + 0.078T_w + 0.0055Q_s \ln(u_{1.2}) + 5.56 \sin(\varphi) - 0.0103Q_s \ln(u_{1.2}) \sin(\varphi) + 0.546B_b + 1.94S_{vf}$$

$$PET_{shade,night} = -12.14 + 1.25T_a - 1.47 \ln(u_{1.2}) + 0.060T_w + 0.015S_{vf} Q_d + 0.0060(S_{vf})\sigma(T_a + 273.15)^4 \quad (A5.2)$$

The UHI magnitude is related to meteorological conditions and the density of the urban environment, e.g. the UHI is strongest under low wind speed and sunny conditions. The daily maximum UHI (UHI_{max}) can be estimated by a diagnostic equation which includes geographical - (left) and meteorological factors (right) (Theeuwes et al., 2017):

$$UHI_{max} = (2 - SVF - f_{veg})^4 \sqrt{\frac{S^\downarrow * (T_{max} - T_{min})^3}{U}} \quad (A5.3)$$

Herein SVF and f_{veg} are the spatially averaged sky-view factor, and vegetation fraction respectively. The size of the source areas that should be averaged over can be found in Figure A5.1. The meteorological part of the equation consists of S^\downarrow , mean downward shortwave radiation (in Kms^{-1}) (kinematic units), $T_{max} - T_{min}$, the maximum and minimum temperature (K) representing the diurnal temperature range and U the mean wind speed (ms^{-1}), all measured at the rural reference station. The maximum UHI occurs about 4 hours after sunset (Oke, 1982; Unger et al., 2001). For the other hours, the UHI_{max} is diminished by a correction factor that varies between -0.02 and 1 in the diurnal cycle (Equation A5.4, Table A5.3 and A5.4). The maximum and minimum temperature are determined in the period 8 UTC current day – 7 UTC (10 – 9 h local time) next day to obtain the cooling potential outside the city (Theeuwes et al., 2017). The mean wind speed was also determined over this period. The mean downward shortwave radiation is determined over the current day.

$$T_a[h] = T_{refstation} + UHI_{max} * diurnal_{cycle}[h] \quad (A5.4)$$

The diurnal cycle is inspired by a characteristic curve of UHI by Oke (1982). This curve was defined for one particular day length. For other day lengths the curves were adjusted considering that the minimum UHI occurs about 4 hours after sunrise (Theeuwes et al., 2015). In the derivation of Equation A5.3, it was implicitly considered that the remaining fraction of f_{veg} is built-up area (Theeuwes et al., 2017). Apart from the morphological effects described by the SVF this built-up area is on average warmer due to the larger partitioning of sensible heat flux compared to the latent heat flux and has a temporal shift due the heat storage. The presence of water surfaces complicates the application of this equation. On the one hand, they have a high heat capacity like built-up area (Steenekveld et al., 2014), but on the other hand do evaporate and have higher latent heat fluxes and consequently lower sensible heat fluxes averaged over the day. To enable the applicability of the straightforward equations, water surfaces are treated as built-up area at night, and as vegetation at daytime (Table A5.1 D1).

The SVF and f_{veg} were averaged using a source area of 500 x 1100 m (Figure A5.1), which corresponds to the correlation of land use and urban temperature as found in Heusinkveld et al. (2014). The source area is oriented towards the wind direction. In case of low wind speeds ($< 1.5 ms^{-1}$) a square shaped source area of 700 x 700 m is used around the calculated grid cell. Since the vegetation fraction and sky-view factor was averaged over a large source area, the output resolution was set to 35 m to reduce computational costs.

To assign the f_{veg} two maps are created, one for daytime and one for nighttime, due to the special role of water surfaces. The vegetation fraction per grid resolution is determined using NDVI > 0.16 in the aerial photography. However, cropland might not be classified as vegetation fraction then, especially when it is bare at the time of data collection. Cropland, even if it is bare, will not store the amount of heat as built up area does. Therefore, cropland is assigned as vegetation fraction in the computation of air temperature. This can be determined with `bgt_begroeidterreindeel`, in Table A5.1 D1.

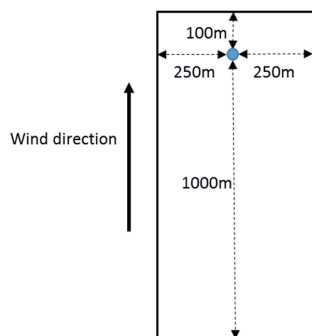


Figure A5.1: Source area for which the average sky-view factor and vegetation fraction is calculated on a resolution of 25 m.

For the *SVF* (either 1-m resolution for PET-equation as 25-m resolution for T_a), water surfaces and buildings need to be excluded. A *SVF* cannot be identified for water bodies, which is a limitation of the underlying lidar technology (Worstell et al., 2014). Specific for determining the air temperature, the *SVF* under trees and other vegetated surfaces ($\text{NDVI} > 0.16$ and $\text{bgt_be-groeidterreindeel}$ Table A5.1 D1) has been excluded (set as no data). The effect of reduced *SVF* in an urban canyon (mainly consisting of impervious road and pavements) has a more enhanced UHI effect than the reduced *SVF* in parks by trees, due to the storage difference between buildings and trees. By removing the *SVF* from green surfaces a large part of this uncertainty has been removed. As an intermediate step the average is calculated for a 25-m grid size to reduce computational costs and it gives smoother results at city borders (which relates to the filtering out of large areas). Here applies, that if more than 90% has no data in the 25-m tile, the whole 25-m tile is set as no data. This is important because otherwise a few *SVF* points have an unrealistic weight in the total *SVF* calculation over the whole source area.

Subsequently, the average *SVF* is computed over the source area based on this 25-m grid *SVF*. If the remaining area for a location is 10% of the source area or less, a *SVF* of 1 is assigned because this small part cannot be considered representative. If the area is more than 20% of the source area, the sky-view factor is straightforwardly determined by the average of the non-filtered points. If the area is between 10 and 20% of the source area, then the *SVF* is linearized between $\text{SVF} = 1$ and the average *SVF* for all non-filtered points. Finally, the *SVF* at the 25-m grid is interpolated back to a 1-m grid.

B2.1 Look-up tables

The corrections on the UHI_{max} depend on the time of sunrise and sunset.

Table A5.3: Sunrise and sunset times

Period	Sunrise / sunset (in hours UTC)
1 April – 12 April	5/18
13 April – 19 April	5/19
20 April – 19 May	4/19
20 May – 25 May	4/20
26 May – 10 July	3/20
11 July – 30 July	4/20
31 July – 21 August	4/19
22 August – 30 August	5/19
31 August – 24 September	5/18
25 September – 27 September	5/17
28 September – 30 September	6/17

Table A5.4: UHI-factors during the hours of the day (vertically) for different sunrise and sunset times (horizontally) (in hours UTC).

Sunrise / sunset	6/17	5/17	5/18	5/19	4/19	4/20	3/20
UTC 0	0.748	0.728	0.807	0.910	0.900	1.000	1.000
1	0.667	0.640	0.704	0.780	0.757	0.888	0.866
2	0.602	0.573	0.617	0.675	0.710	0.728	0.690
3	0.525	0.490	0.533	0.590	0.543	0.609	0.560
4	0.449	0.355	0.435	0.490	0.413	0.490	0.380
5	0.281	0.150	0.227	0.320	0.150	0.256	0.107
6	0.127	0.078	0.095	0.120	0.057	0.079	0.015
7	0.063	0.025	0.032	0.040	0.000	0.007	-0.020
8	0.019	-0.013	-0.009	-0.005	-0.020	-0.020	-0.007
9	-0.015	-0.020	-0.020	-0.020	-0.005	-0.006	0.007
10	-0.020	-0.001	-0.003	-0.004	0.013	0.010	0.029
11	0.000	0.025	0.020	0.016	0.037	0.033	0.050
12	0.030	0.056	0.048	0.042	0.063	0.056	0.074
13	0.065	0.090	0.080	0.071	0.090	0.082	0.108
14	0.117	0.165	0.136	0.111	0.150	0.128	0.161
15	0.205	0.270	0.215	0.176	0.222	0.184	0.228
16	0.335	0.413	0.325	0.270	0.318	0.270	0.312
17	0.532	0.600	0.485	0.386	0.450	0.366	0.424
18	0.747	0.803	0.662	0.546	0.600	0.506	0.556
19	0.906	0.920	0.849	0.716	0.762	0.651	0.695
20	0.975	0.978	0.932	0.877	0.890	0.803	0.838
21	1.000	1.000	0.979	0.941	0.950	0.901	0.911
22	0.931	0.925	1.000	0.981	0.982	0.958	0.964
23	0.849	0.830	0.918	1.000	1.000	0.983	0.984

B3. Wet bulb temperature

$$PET_{sun} = -13.26 + 1.25T_a + 0.011Q_s - 3.37 \ln(u_{1.2}) + \mathbf{0.078}T_w + 0.0055Q_s \ln(u_{1.2}) + 5.56 \sin(\varphi) - 0.0103Q_s \ln(u_{1.2}) \sin(\varphi) + 0.546B_b + 1.94S_{vf}$$

$$PET_{shade,night} = -12.14 + 1.25T_a - 1.47 \ln(u_{1.2}) + \mathbf{0.060}T_w + 0.015S_{vf} Q_d + 0.0060(S_{vf})\sigma(T_a + 273.15)^4$$

The wet-bulb temperature was calculated according to (Stull, 2011):

$$T_w = T_a \operatorname{atan}(0.151977(\phi + 8.313659)^{0.5}) + \operatorname{atan}(T_a + \phi) - \operatorname{atan}(\phi - 1.676331) + 0.00391838\phi^{(\frac{3}{2})} \operatorname{atan}(0.023101\phi) - 4.686035 \quad (\text{A5.5})$$

Herein T_a denotes the air temperature and ϕ denotes the relative humidity. The wet bulb temperature was computed once for the rural reference station and used everywhere including the city. The relatively small coefficients of T_w in Equation A5.1 (6% compared to T_a), justifies this more practical approach, instead of calculating T_w for every urban grid cell with urban temperature. Besides, the relative humidity is generally lower in urban areas (Landsberg et al., 1972; Hage, 1975), which counteracts the slight rise on wet-bulb temperatures due to higher urban temperatures.

B4. Cast shadow map

$$PET_{sun} = -13.26 + 1.25T_a + 0.011Q_s - 3.37 \ln(u_{1.2}) + 0.078T_w + 0.0055Q_s \ln(u_{1.2}) + \mathbf{5.56} \sin(\varphi) - \mathbf{0.0103}Q_s \ln(u_{1.2}) \sin(\varphi) + 0.546B_b + 1.94S_{vf}$$

$$PET_{shade,night} = -12.14 + 1.25T_a - 1.47 \ln(u_{1.2}) + 0.060T_w + 0.015S_{vf} Q_d + 0.0060(S_{vf})\sigma(T_a + 273.15)^4$$

Exposure to direct sunshine is a prerequisite for high PET values. Sunlit locations can be determined by a cast shadow map. This cast shadow map can be created with the lidar based height map (AHN) and the UMEP GIS tool (Lindberg et al., 2018). This GIS tool can calculate cast shadows at all sun angles during the day and season. Unfortunately cast shadows cannot be determined at the surface under the tree crown. Therefore, the area below trees is designated as shadow if trees are higher than 2 m. This last prerequisite of 2 m is introduced to enable entering solar rays at the edge of the trees. In reality the foliage is partially transparent to solar radiation, so that PET values are slightly underestimated under trees. However, the priority is to distinguish the hot spots in the heat map which is never found under trees during daytime.

B5. Wind speed

$$PET_{sun} = -13.26 + 1.25T_a + 0.011Q_s - \mathbf{3.37} \ln(u_{1.2}) + 0.078T_w + \mathbf{0.0055}Q_s \ln(u_{1.2}) + 5.56 \sin(\varphi) - 0.0103Q_s \ln(u_{1.2}) \sin(\varphi) + 0.546B_b + 1.94S_{vf}$$

$$PET_{shade,night} = -12.14 + 1.25T_a - \mathbf{1.47} \ln(u_{1.2}) + 0.060T_w + 0.015S_{vf} Q_d + 0.0060(S_{vf})\sigma(T_a + 273.15)^4$$

According to WMO guidelines reference weather stations were sited in an open terrain with a low surface roughness WMO (2014). The surface roughness is substantially higher at other locations in the heat map in the vicinity of buildings and trees which coincides with lower wind speeds. A translation of the wind speed was made from the open reference station to locations with a

higher surface roughness. First, we computed the mesowind at the blending height (60 m) from the wind and surface roughness of the weather station ($z_0 = 0.03$ m) using a logarithmic wind profile in neutral conditions. This is the height where the wind flow is supposed to be homogeneous and thus independent of the surface roughness. According to field experiments performed by MacDonald (2000), the wind speed is translated to 1.2 m in the urban canopy. The wind profile in and near the urban canopy is more complex and non-logarithmic. The procedure is demonstrated in the following steps:

1. Take a 1 ms^{-1} normalized wind speed at a height of 10 m as the starting point (u_{10}) representative for open terrain (including reference station) in order to create a wind reduction field. In the end (step 15), all calculated wind speeds in the wind reduction field can then be used as a multiplication factor for the real wind time series at 10 m.
2. Translate wind to 60-m height.

$$u_{60} = 1.3084 u_{10} \quad (\text{A5.6})$$

3. Determine the average obstacle height for buildings and trees. The height of the buildings can be determined from the lidar based height map (object height - ground level). Note that we had to fill the raw object height data, because for water no heights can be determined for the lidar methodology. (a search distance of 100 m was sufficient for Wageningen). The height of trees can be determined with the information from the tree register. In case of unavailability it can be determined with a lidar based height map and own derived trees derived with NDVI.
4. Project the building - and tree height separately on a 1-m grid as shown in Figure A5.3. Buildings with an average height below 2 m are excluded. (this is rare for Wageningen). Determine with the source areas (280 x 140 m) (Figure A5.2) the average obstacle heights of buildings and trees. For low wind speeds under 1.5 ms^{-1} a squared source area (175 x 175 m) is used, for which the calculation point is centred.

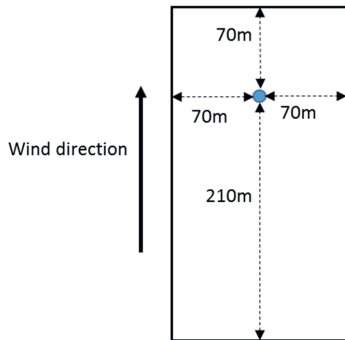


Figure A5.2: Source area for the calculation of frontal area density of building and tree heights which serves as input for wind speed computations.

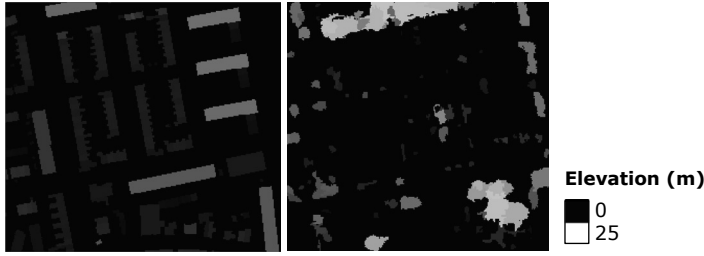


Figure A5.3: Elevation grid of buildings (left) and trees (right) for a neighbourhood in Wageningen relative to ground level.

5. Determine tree and building average obstacle height H (weighted to surface area).
6. Derive the frontal areas (perpendicular surfaces) towards the wind direction within the source area for trees and buildings separately. Determine the frontal area density for buildings and trees (total frontal area / source area).
7. Determine the frontal area density λ (-) in the wind direction (total frontal area / source area) for trees and buildings with the equation below. Trees have a smaller frontal surface density because of the shape and porosity.

$$\lambda_{tot} = 0.6\lambda_{buildings} + 0.3\lambda_{trees} + 0.015 \quad (\text{A.5.7})$$

8. Calculate the weighted average height of trees and buildings, with 4 m as lower limit.
9. With the calculated weighted average height and frontal surface density the variables d , z_w , z_0 and parameters A and B can be derived (see Table A5.5).

Table A5.5: According to MacDonald (2000): d is the zero-plane displacement, z_w is the top of the roughness layer, z_0 is the roughness length and A and B are the parameters for interpolation of the wind profile.

Array type	λ_{cor}	d/H	z_w/H	z_0/H	A/H	B
squared	0.05 (< 0.08)	0.066	2	0.048	-0.35	0.56
„	0.11 (0.08 to 0.135)	0.26	2.5	0.071	-0.35	0.50
„	0.16 (0.135 to 0.18)	0.32	2.7	0.084	-0.34	0.48
„	0.20 (0.18 to 0.265)	0.42	1.5	0.08	-0.56	0.66
„	0.33 (≥ 0.265)	0.57	1.2	0.077	-0.85	0.92

10. With sufficient frontal surface area $0.6\lambda_{buildings} + 0.3\lambda_{trees} > \frac{25 \text{ (m}^2\text{)}}{\text{surface area (m}^2\text{)}}$ (A5.8)

$$11. \text{ Calculate } u_{zw} = u_{60} \frac{\ln\left(\frac{z_w - d}{z_0}\right)}{\ln\left(\frac{60 - d}{z_0}\right)} \quad (\text{A5.9})$$

$$12. \text{ Calculate } u^* = 0.4 \frac{u_{60}}{\ln\left(\frac{60 - d}{z_0}\right)} \quad (\text{A5.10})$$

$$13. \text{ Calculate } u_H = \frac{-u^*}{B} \ln\left(\frac{A + Bz_w}{A + BH}\right) + u_{zw} \quad (\text{A5.11})$$

$$14. \text{ Calculate } u_{1.2} = u_H \exp\left(9.6\lambda\left(\frac{1.2}{H} - 1\right)\right) \quad (\text{A5.12})$$

With a smaller frontal surface area, the MacDonald method no longer applies, and the wind can be translated directly to 1.2 m based on the logarithmic wind profile above grass.

$$u_{1.2} = 0.6350 u_{10} \quad (\text{A5.13})$$

15. Recall that the $u_{1.2}$ is a wind reduction compared to a reference wind of 1 ms^{-1} at 10 m (u_{10}). To obtain the urban wind speed at a specific time, the wind reduction is multiplied with the 10-m wind (FF_{10}) of the reference station. The maximum wind reduction appeared to be too strong for Wageningen through verification. Therefore, the final urban wind speed has been scaled:

$$\text{scaled } u_{1.2} = FF_{10}((u_{1.2} - 0.0796)0.9175 + 0.1254) \quad (\text{A5.14})$$

The minimum $u_{1.2}$ (wind reduction) observed was 0.0796 and the maximum wind reduction is 0.6350. After scaling the minimum wind reduction becomes 0.1254 while the maximum wind reduction remains 0.6350. The scaled $u_{1.2}$ is used in the PET calculation in B7 and B8.

16. The wind in the heat maps is calculated with a spatial interval of 35 m in north-south and west-east directions. This means the source areas are shifted in steps of 35 m accordingly.
17. For the heat map area, a smooth wind field is created at 1-m resolution with cubic interpolation.

B6. Diffuse irradiation and solar elevation angle

$$PET_{sun} = -13.26 + 1.25T_a + \mathbf{0.011}Q_s - 3.37 \ln(u_{1.2}) + 0.078T_w + \mathbf{0.0055}Q_s \ln(u_{1.2}) + 5.56 \sin(\varphi) - \mathbf{0.0103}Q_s \ln(u_{1.2}) \sin(\varphi) + 0.546B_b + 1.94S_{vf}$$

$$PET_{shade,night} = -12.14 + 1.25T_a - 1.47 \ln(u_{1.2}) + 0.060T_w + \mathbf{0.015}S_{vf} Q_d + 0.0060(S_{vf})\sigma(T_a + 273.15)^4$$

In the empirical PET equation (Equation A5.1) the solar irradiation (Q_s) and the diffuse irradiation (Q_d) are used. The diffuse irradiation (Q_d) is calculated from the solar irradiation (Q_s) as measured at the KNMI rural weather station, with a solar elevation angle (φ) that depends on the time of the day and the date.

$$\frac{Q_d}{Q_s} = \begin{cases} 1, & \tau_a < 0.3, \\ 1.6 - 2\tau_a, & 0.3 < \tau_a < 0.7, \\ 0.2, & \tau_a > 0.7. \end{cases} \quad (\text{A5.15})$$

herein the atmospheric transmissivity (τ_a) is estimated as (de Rooy & Holtslag, 1998):

$$\tau_a = \frac{Q_s}{1367 \sin(\varphi)} \quad (\text{A5.16})$$

The solar irradiation from the KNMI station is a sum of the past hour. To estimate the amount of radiation for the entire hour, the radiation for the coming hour and the past hour is averaged.

The solar elevation angle is retrieved from the nearby weather station Veenkampen. We recognize that the majority of WMO stations does not provide solar elevation angles when calculating a heat map for another city. In that case it is recommended to calculate the solar elevation

angle on an hourly basis. Python packages as pysolar or the equations in Allen et al. (1998) can be used to determine the solar elevation angle.

B7. Calculate PETsun

$$PET_{sun} = -13.26 + 1.25T_a + 0.011Q_s - 3.37 \ln(u_{1.2}) + 0.078T_w + 0.0055Q_s \ln(u_{1.2}) + 5.56 \sin(\varphi) - 0.0103Q_s \ln(u_{1.2}) \sin(\varphi) + 0.546B_b + 1.94S_{vf}$$

B8. Calculate PETshade and night

$$PET_{shade,night} = -12.14 + 1.25T_a - 1.47 \ln(u_{1.2}) + 0.060T_w + 0.015S_{vf} Q_d + 0.0060(S_{vf})\sigma(T_a + 273.15)^4$$

B9. Climate scenarios

Table A5.6: Transformation table W_H scenario from current climate to future climate in 2050 (KNMI, 2015). The percentage change for solar irradiation and RH are in absolute percentage points.

	Temperature percentiles (°C)					(°C)	%	%
	1	5	50	95	99	DTR	solar irradiation	RH
April	3.2	2.5	2	1.7	1.9	-0.44	-2.8	0.2
May	2.3	2.1	1.7	1.8	2	-0.48	-0.6	-0.3
June	2	1.9	2	2.5	2.7	-0.09	4	-1.5
July	1.9	2	2.2	3	3.3	0.13	6.6	-2.5
August	2.2	2.1	2.3	3.1	3.5	0.21	7.1	-2.7
September	2.6	2.3	2.1	2.6	2.9	-0.03	3.1	-1.7

A future temperature series is transformed as follows (KNMI, 2015): The scenarios provide monthly temperature increments for daily percentiles. These increments were relative to the climate period of 1981–2010. There is already a climate signal in the time series (2002–2016) compared to this climate period, and this bias was subtracted from the results. Using the procedure of Molenaar et al. (2016), these increments were interpolated for all of the days in a month. In this study, the transformation was performed on hourly values (likewise as in Chapter 4), because the time frame in which minimum temperatures were determined differs from the standard, i.e. from 8 UTC current day – 7 UTC (10 – 9 h local time) the next day. The corresponding transformation equations are Equation 4.3 and 4.4 in Chapter 4.

In the transformation of solar irradiation, the *percQ* indicates the 95th percentiles $Q_s/Angot(h)$ for every hour. In the morning and evening the values are smaller than at noon, which is due to the different length of sun ray paths in the atmosphere.

$$Q^a(h) = percQ(h) * Angot(h) \quad (A5.17)$$

$$percQ = [1,1,1,1,1,0.031,1.01,0.841,0.903,0.946,0.975,0.992,1.002,1.001,0.991,0.979,0.956,0.923,0.881,0.897,0.984,1,1,1,1]$$

$Q^a(h)$ = Angot radiation corrected for 95th percentile of observed hourly Q_s .

$Angot(h)$ = maximum hourly Q_s based on $0.75 * \text{radiation at top of the atmosphere}$.

$percQ(h)$ = 95 percentile of $Q_s/Angot(h)$ for every hour

Lastly, the relative humidity has been straightforwardly transformed by applying the monthly numerical values (Table A5.6) (KNMI, 2015).

B10. List of symbols

Symbol	Description	Unit
A	Parameter for interpolation wind profile	-
B	Parameter for interpolation wind profile	-
B_b	Bowen ratio (sensible heat flux / latent heat flux)	-
d	Zero-plane displacement	m
FF_{10}	10-m wind at reference station	ms^{-1}
f_{veg}	Vegetation fraction	-
ϕ	Solar elevation angle	$^{\circ}$
$\lambda_{\text{buildings}}$	Frontal area density for buildings	-
λ_{tot}	Frontal area	-
λ_{trees}	Frontal area density for trees	-
H	Building height	m
I	Infrared value of aerial photo (RGBI)	-
PET	Physiological Equivalent Temperature	$^{\circ}\text{C}$
ϕ	Relative humidity at reference station	%
Q_d	Diffuse irradiation (shortwave)	Wm^{-2}
Q_s	Solar irradiation at reference station	Wm^{-2}
R	Red value of aerial photo (RGBI)	-
σ	Stefan Boltzmann constant	$\text{Wm}^{-2}\text{K}^{-4}$
S^{\downarrow}	Daily average solar irradiation (in kinematic units)	Kms^{-1}
SVF	Sky-view factor	-
τ_a	Transmissivity	-
T_a	Air temperature	$^{\circ}\text{C}$
T_{gem}	Daily average air temperature	$^{\circ}\text{C}$
T_{max}	Daily average maximum temperature	$^{\circ}\text{C}$
T_{min}	Daily average minimum temperature	$^{\circ}\text{C}$
$T_{\text{refstation}}$	Air temperature at reference station	$^{\circ}\text{C}$
T_w	Wet-bulb temperature	$^{\circ}\text{C}$
U	Daily average wind speed at reference station	ms^{-1}
$u_{1.2}$	Wind reduction at 1.2 m relative to $u_{10} = 1 \text{ ms}^{-1}$	ms^{-1}
u_{10}	Reference normalized wind of 1 ms^{-1} representative for open terrain	ms^{-1}
u_{60}	Wind at 60-m height (relative to $u_{10} = 1 \text{ ms}^{-1}$), mesowind	ms^{-1}
UHI	Urban Heat Island	$^{\circ}\text{C}$
UHI_{max}	Daily maximum urban heat island	$^{\circ}\text{C}$
u^*	Friction velocity	ms^{-1}
u_H	Wind speed at roof height	ms^{-1}
z_0	(Surface) Roughness length	m
z_w	Top of the roughness layer	m

Chapter 6

Perspectives

The previous chapters of the thesis have dealt with the research questions as formulated in Chapter 1. The previous chapters also discussed some aspects where research methods could be improved, or applications could be scaled up in space and time. This chapter presents a number of possible future research lines that can build upon the thesis research. These comprises the upscaling of the data assimilation approach in Chapter 3 to a 15-year urban reanalysis product, an extended estimate of the impact of urbanization on the temperature record in De Bilt from Chapter 2, and an illustration of high resolution urban weather modelling for city planning and climate adaptation interventions in the city of Breda (the Netherlands).

6.1 First results of a 15-year reanalysis for Amsterdam

In Chapter 3, a modelling and data assimilation approach for the city of Amsterdam was introduced for the summer of 2014. Here we discuss the results of a 15-year reanalysis dataset for Amsterdam. This product has been developed using the same set-up but then extended for a continuous series for the years 2002-2016. Herein the WRF model was run with two hourly cycles of data assimilation including the assimilation of urban weather stations and output is stored at a resolution of 167 m. As such this approach develops a product with the best estimated state of the atmosphere over the city for 15 years. Exploration of this dataset offers the opportunity to allow for answering research questions that was not possible before since due to lack of coherent city-covering data.

Here we show the modelled UHI intensity over all months to document and explore the seasonal dependence of the UHI climatology, both for the 2-m temperature (UHI_{T2m}) and the surface skin temperature (UHI_{TSK}). Earlier a study by (Zhou et al., 2013) observed hysteresis-like behaviour when monthly averaged UHI were plotted against the monthly mean rural temperatures for cities across Europe. Subsequently, we analyse whether this hysteresis-like behaviour is also present within our reanalysis dataset for the 2002-2016 period. Indeed, a hysteresis-like clockwise curve was found for the annual cycle of UHI_{T2m} , UHI_{TSK} and for daily maxima (Figure 6.1 a-b). This hysteresis effect is most prominent for UHI_{TSK} (Figure 6.1b), and is clearly separated by the standard error for all months on both sides of the curve. The found hysteresis-like curve does have similarities with the observed surface skin temperature curves for different European cities (Zhou et al., 2013). A plausible explanation for the hysteresis-shaped curve is the correlation with global radiation for both UHI_{T2m} and UHI_{TSK} . Global radiation peaks around solstice in June, while the peak in average temperatures appear more than a month later. However, remarkably June shows lower UHI than May and July. In addition, September has a second peak in UH for which no clear explanation could be found yet.

The monthly means of the daytime UHI (12 UTC), on the other hand, are much lower than for the diurnal maximum UHIs (Figure 6.11 c-d). For the 2-m temperature (Figure 6.1c) hardly any UHI is perceived, and for TSK, UHI is about 40% of maximum UHI. Especially the spring season displays a relatively low daytime UHI, and no clear hysteresis curve is obtained. Zhou et al. (2013), in contrast, found daytime UHI hysteresis-like curves for observed surface skin temperature at daytime based on satellite data for different European cities. In accordance to our findings, a modelling and observational study for London found less clear hysteresis curves, with winter and summer UHI intensities much less far apart to each other for London (Zhou et al., 2016). As a comparison with observations of nearby city Rotterdam, a clearer hysteresis-like UHI curve is found based on 4-year midnight UHI values for 2-m temperature (Droste et al., 2015).

The shapes of the hysteresis-like curves may differ between cities with a relatively dry summer season and cities with high water availability in summer (Manoli et al., 2020), based on a coarse-grained model of surface skin UHI coupled with a water balance model. With a high water availability for evapotranspiration the rural background remains cooler and UHI peaks in phase with maximum solar radiation. For cities with a dry summer season, the UHI is much lower and peaks earlier in spring, and the UHI can even be negative in summer and autumn due to the oasis effect of urban irrigation. The hysteresis-like cycle can also be determined for long-term temperature trends for stations facing urbanization with the largest trend around June (Chrysanthou et al., 2014).

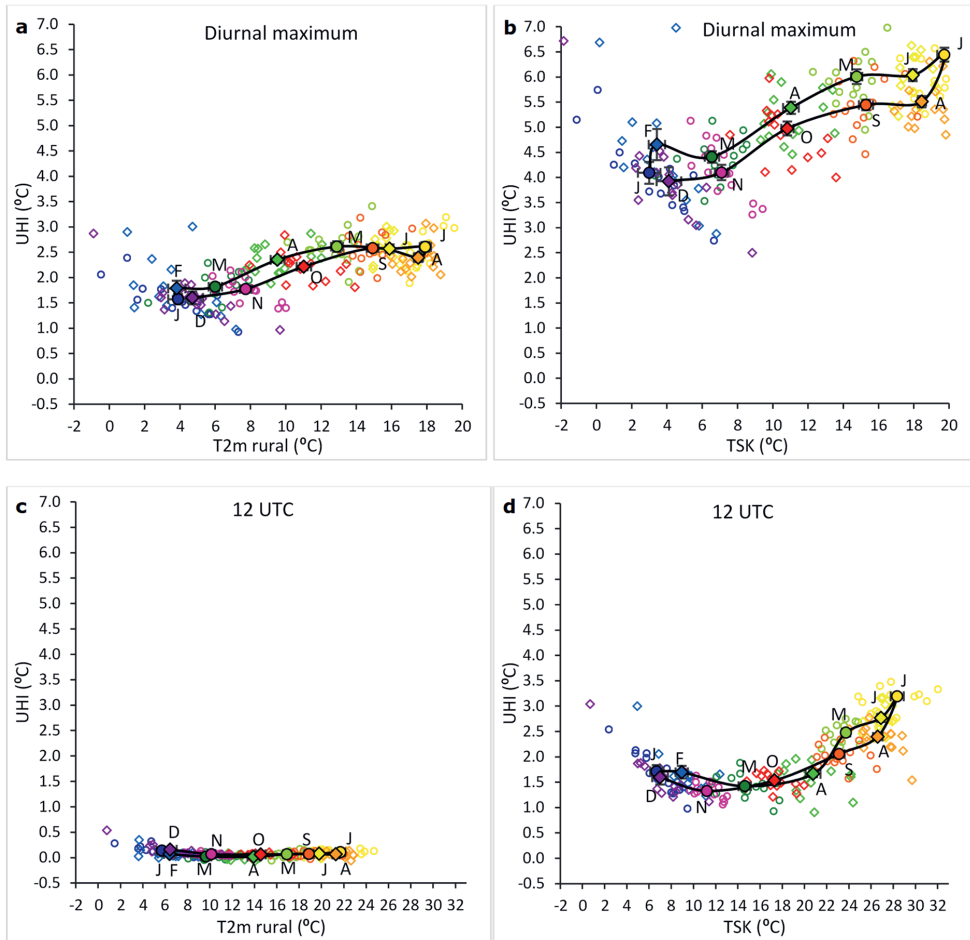


Figure 6.1: Seasonal characteristics of the modelled UHI of Amsterdam (all urban cells domain 3 minus rural reference) based on 15 years of model reanalysis data. The rural reference consists of the average temperature from the rural grid cells at least 1 grid cell separated from urban and water grid cells. (a-b) denote the monthly averages of daily maximum UHI for 2-m air temperature and surface skin temperature respectively. (c-d) denote monthly averages of the UHI at 12 UTC for 2-m air temperature and surface skin temperature. The bars of the mean monthly UHIs indicate the standard error and the letters indicate the first character of the months (January–December). The colours and shapes of the monthly averaged UHI's on the curve matches the points representing the individual months in the period 2002-2016.

The urban climate of the 15-year reanalysis can also be largely described by isothermal plots showing the diurnal cycle and seasonal variation (Figure 6.2). Here model results at the location of three weather stations in the Amsterdam Atmospheric Monitoring Supersite (Ronda et al., 2017) are displayed in order from high density to low density (a, b and c). Clearly the sunrise and sunset can be observed by the sharp transition of the relatively high UHI in the night and diminished UHI at daytime throughout the seasons. The mid-rise district (b) has the strongest UHI, even slightly higher than the high-rise district (a). In general, the daily maximum UHIs are modelled in the hour after sunset, which is a few hours earlier than adopted from (Oke, 1982). Maximum UHI amounts 2.4 °C for the mid-rise district, 2.3 °C for the high-rise district and 2.0 °C for the low-rise district. This may be partly explained by the fact that this station is located in the central part of Amsterdam,

and thus winds from urban areas in all wind directions. The green fractions of this mid-rise site and high-rise site are comparable.

In the morning a clear minimum UHI is simulated in the summer months, which is even slightly negative for the high-rise and low-rise cases ($-0.2\text{ }^{\circ}\text{C}$). These so called urban cool islands are studied by Bohnenstengel et al. (2011), Theeuwes et al. (2015), Yang et al. (2017), and arise due to higher rural surface heating rates induced by urban–rural boundary-layer height differences around sunrise and differences in the storage flux. In addition, urban cool islands appear when urban surfaces are substantially more shaded for high aspect ratios (Johansson, 2006). In the winter this phenomenon is not visible in the model, since the global radiation forcing is smaller and anthropogenic heat is more significant. Diurnal anthropogenic heat cycles may cause enhanced warming around the rush hours. This seems especially visible in the morning for the three stations. In the morning the heat is spread over a relatively shallow stable boundary layer. The negative UHI in the winter months in the night cannot be logically explained. For final conclusions about urban temperatures, more in-depth research is needed, to relate surface fluxes to simulated urban temperatures.

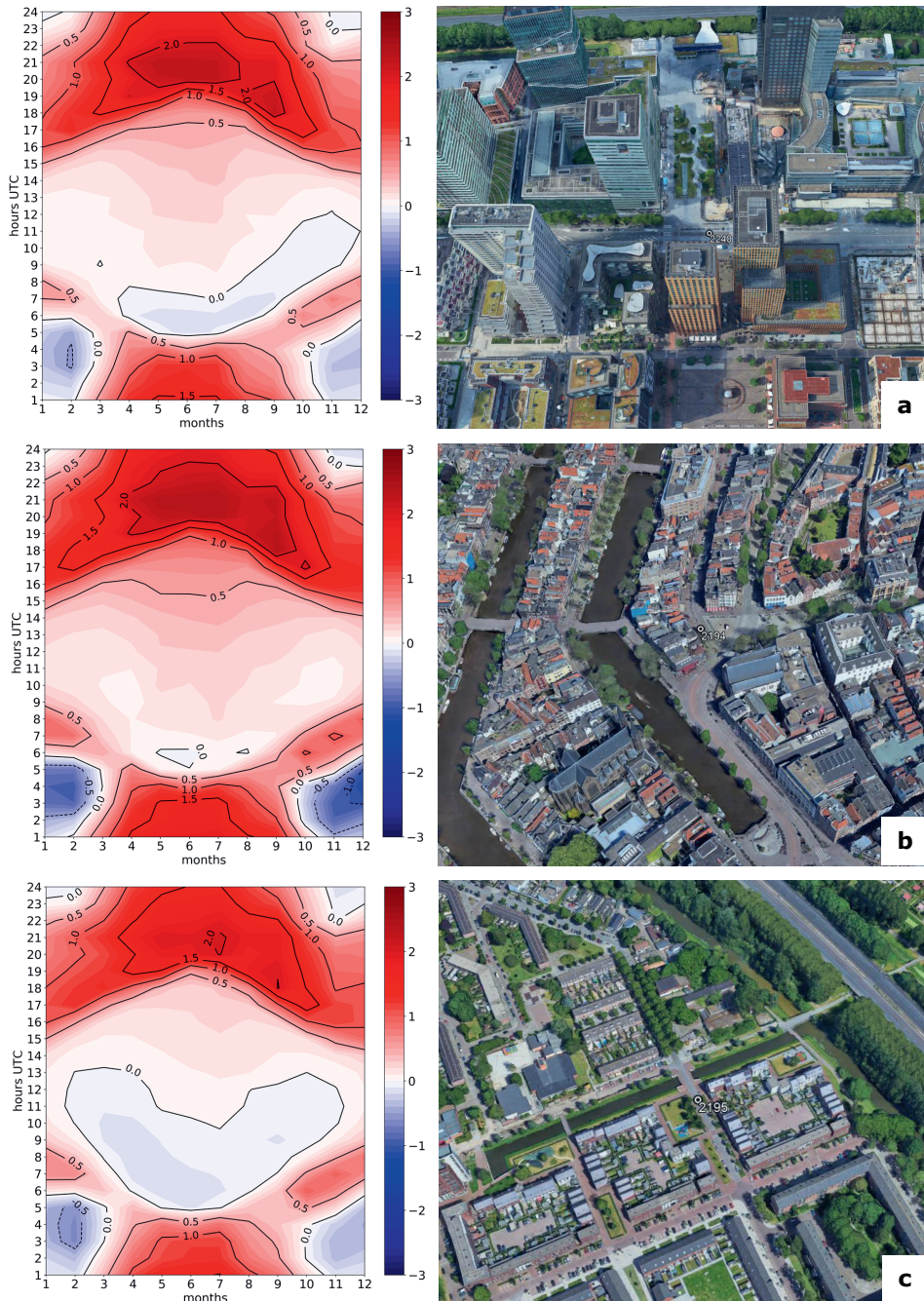


Figure 6.2: Isothermic plot of the 15-year climatology UHI based on 2-m temperatures for 2002-2016 showing daily and seasonal variation for three stations in Amsterdam (left). a) is high-rise district, b) compact mid-rise, and c) compact low-rise. This correspond with the local climate zones (LCZ) 1, 2 and 3 respectively, as defined by (Stewart & Oke, 2012). The rural reference consists of the average temperature from the rural grid cells at least 1 grid cell separated from urban and water grid cells. Right: location and surrounding is displayed by satellite images from LANDSAT provided by Google Earth®.

6.2 Urbanization effects on the surrounding

Chapter 2 revealed the influence the urbanization of Utrecht on the temperature record of the main Dutch weather station De Bilt. In this section, we update the analysis of urban heat advection for this weather station using recent rural reference observations of Herwijnen and Cabauw in the time frame between 1991 and 2020.

In Chapter 2 we found that the air temperature recorded in De Bilt was significantly higher for cases with wind directions from the nearby city Utrecht, compared to nearby rural weather station Herwijnen (Figure 2.9 in Chapter 2). As an alternative to this previous observational analysis, the influence of the urbanization can be visualised with a temperature difference isopleth in Figure 6.3a by distinguishing seasonal effects (per month) and diurnal cycle. This is similar to the isopleth for the urban stations in Amsterdam in the previous section (6.1), with the difference that De Bilt weather station is located outside the city. In addition, we selected wind directions coming from Utrecht (210° until 290°) as observed in De Bilt. As such the temperature difference is directly related to urban heat advection and is referred as UITE (Urban Induced Temperature Effect). In the summer half year a clear diurnal maximum in UITE can be distinguished in the evening ranging from 0.9 °C in June and September to 1.3 °C in April. Around solar noon, temperature differences disappear. The time of the minimum UITE is around 4 hours later than typically can be expected as minimum UHI for urban stations (Oke, 1982). Though, differences in diurnal cycles of UITE might be partially explained by the fact that Herwijnen (WMO: 06356) is located 12 km more inland than De Bilt and has a little less marine influences and as such a larger diurnal amplitude in air temperature can be explained.

As alternative to Herwijnen, another station that can be used as a reference is Cabauw (WMO:06348), which is also located in an open rural area on clay soil (25 km southwest of De Bilt) and is located 8 km closer to the sea. The UITE is also here clearly visible in nighttime (Figure 6.3b). However, at daytime De Bilt remains warmer, especially during the summer months. A seasonal shift is observed, as the temperature difference between De Bilt and Cabauw is larger in spring than early autumn (September and October). The surface roughness of the surrounding of De Bilt is lower due to urbanization and nearby forest on a moraine. The accompanied reduced wind speeds might “block” maritime influences to a small degree. Furthermore, urban heat islands are expected to be small in autumn, since the global radiation is relatively low and anthropogenic heat is yet relatively unimportant. November and December show higher UITE throughout the day, which might be largely explained by higher anthropogenic heat consumption compared to September/October (see model estimates in Chapter 2 Table 2.3).

Urban environments can modify the wind field at regional scale, and sometimes create their own circulation (Lemonsu & Masson, 2002; Hidalgo et al., 2008). A clear urban breeze, defined as convergence together with even opposing wind directions, as demonstrated in Hidalgo et al. (2008) is not reproduced in the simulations and unlikely to occur. However, the WRF simulations of the various weather regimes (Grosswetterlagen) described in Chapter 2 show remarkable changes in wind directions between the years 2000 and 1900. The frequency of winds originating from the city centre of Utrecht have been reduced and have been enhanced just outside the borders of the city. The wind tends to avoid the relatively rough city surfaces at the city border, and is deflected around the city. Altering wind flows by urban land use has been also found in WRF simulations for Birmingham and London (Bohnenstengel et al., 2011; Bassett et al., 2017). Concerning the model study of urban heat advection in Chapter 2, a side note should be given that the model grid resolution of 500 m is relatively coarse to obtain robust and realistic wind directions. In addition, the

observed wind roses for De Bilt and reference stations Herwijnen and Cabauw does not show differences in wind directions through time or any signs of wind deflection around Utrecht that can be explained by the relatively rough city surface.

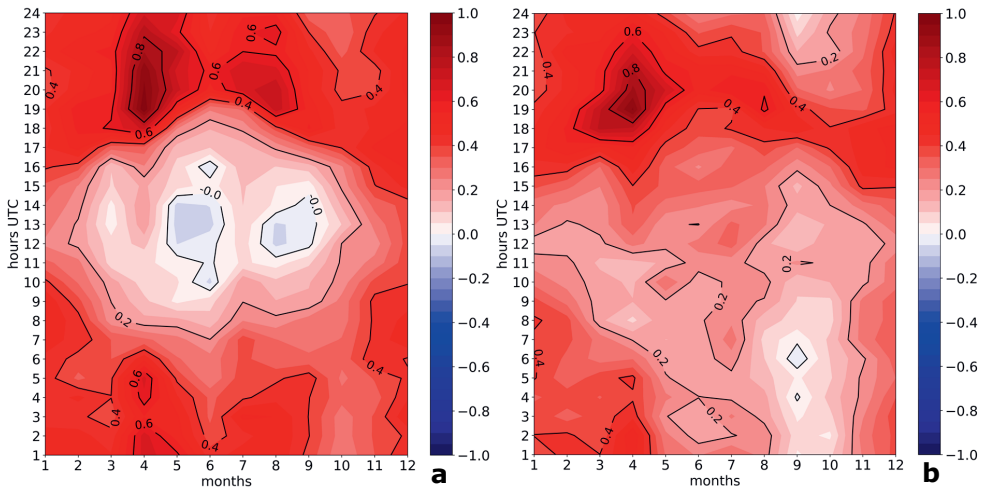


Figure 6.3: Isothermic plots of climatological temperature differences (period 1991–2020) showing seasonal and diurnal variations, between weather station De Bilt (WMO: 06280) and rural reference stations Herwijnen (WMO: 06356) (a), and Cabauw (WMO: 06348) (b). Winds originating from Utrecht are selected at weather station De Bilt.

Other model studies as by Heaviside et al. (2015) report 2.5 °C higher air temperatures downwind compared to upwind urban areas for Birmingham. This is largely explained by urban heat advection and less by local geographical effects. In that study likewise a mesoscale WRF simulation was performed. Urban heat advection was determined with a decomposition method where simulated temperatures were split in a local temperature and advection part. Bassett et al. (2016) used this decomposition method to separate the UHI advection term for observation sites in and around Birmingham. Maximum urban heat advection was found to be 1.2 °C in clear summer nights with moderate winds (2–3 ms⁻¹). This corresponds with a found peak urban heat advection for De Bilt at moderate wind speeds (2.2–3.9 ms⁻¹), in the study of Brandsma et al. (2013). In this study, observations of De Bilt were compared to observations from the former nearby station Soesterberg (WMO:6265) during the period (1993–2000). Station Soesterberg has been closed in 2008. In Figure 6.4, maximum UHI has been recalculated for De Bilt versus Herwijnen in the period (1991–2020), split into summer and winter half year and day and night. In all panels the maximum UHI is found at the 2 ms⁻¹ class. In winter, the optimum tends to be closer to 3 ms⁻¹ compared to the summer, and UHIs are relatively high above 3 ms⁻¹ compared to summer conditions. A plausible explanation for the higher optimum in winter is the shallower (and more often stable) boundary layer. Urban heat is therefore mixed away less effectively with increasing wind. On the other hand, low wind speeds (1 ms⁻¹) transport less urban heat as the urban heat has more time to be mixed with the overlying atmosphere. At night, the UHI advection is smaller at low wind speeds because of more expected frequent formations of so-called urban plume present above a stable nocturnal rural boundary layer (Oke, 1982; Cosgrove & Berkelhammer, 2018). This has been found in temperature profile observations using helicopters (Clarke, 1969). So, this means the largest portion of urban heat is missed at screen level in clear nights and strong surface cooling, as mixing is suppressed in the stable nocturnal boundary layer. Furthermore, at low wind speeds the

footprint of surface fluxes is smaller, analytically derived by Schuepp et al. (1990) and simulated by Bassett et al. (2016). This implies that for weather station De Bilt surface characteristics of the rural area just next to this weather station is of more importance than at a further distance for the observed temperature. Finally, the diurnal differences in maximum UHI between summer and winter in Figure 6.4 can be explained by stronger nocturnal UHI in summer due to more stored heat by larger radiation inputs, and more constant anthropogenic heat forcings in winter.

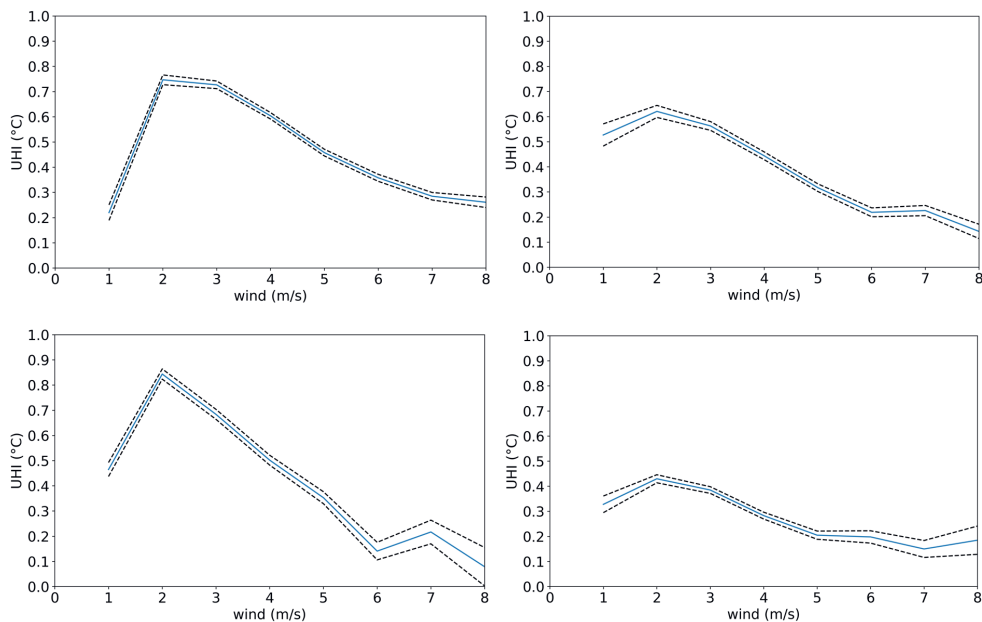


Figure 6.4: UITE based on hourly temperature difference of WMO station De Bilt (6240) and WMO station Herwijnen (6356) in the period 1991–2020. The dashed lines indicate the standard error. Top panels: summer half year, bottom panels: winter half year, left panels: night, right panels: day. The wind speed groups are based on wind measurements of De Bilt. Hours where the wind speed at Herwijnen deviates 2 ms^{-1} or more are discarded.

6.3 Refined urban heat modelling

This section discusses a range of contrasting modelling techniques and evaluates their role and performance in urban meteorology studies. Herein we distinguish between GIS-based approaches as in Chapter 4–5, microscale simulations with a RANS model like ENVI-met (Bruse & Fleer, 1998) and simulations of the urban environment using numerical weather prediction models. These contrasting modelling approaches serve different purposes. The GIS-based approach serves consultancies with limited computing effort, preserves a relatively high spatial urban detail in combination with a large model domain size based on empirical relations. With the RANS (Reynolds Averaged Navier-Stokes) approach more spatiotemporal urban details can be simulated with physical modelling at the expense of high computational costs. Finally, compared to the RANS approach, NWP models can model longer periods for larger model domains and includes the larger synoptical scale. Although they have a coarser resolution, they are designed to simulate sophisticated estimates of the urban surface energy balance and urban weather/climate (e.g. WRF).

Wind in urban areas is a challenge to simulate across all scales, i.e. from the scale where turbulence is largely resolved (~ 1 m) to the mesoscale used in more practical studies, in which weather for relatively large cities is simulated for longer periods. In addition, it is interesting to look closely at comparisons between PET (Physiological Equivalent Temperature) on these small scales and the empirical GIS-modelling approach in Chapter 5. To demonstrate the differences between these approaches, we focus on the urban centre of Breda, the Netherlands (Figure 6.5). Here an applied study has been conducted with the ENVI-met microscale model to invest in cool adaptation measurements in the city centre along a restructured river. ENVI-met is a RANS model and is able to simulate complex wind flows around buildings and trees on a grid spacing down to 1 m. Furthermore, it can simulate radiation and energy budgets in the complex urban canopy (reflection and emission buildings and trees). The wind, humidity and the radiation effects on the human body can be translated in an accurate thermal comfort index PET. Figure 6.5 depicts a comparison of the PET urban heat map according to the recipe in Chapter 5 and the ENVI-met simulation for Breda again for the relatively warm day of 1 July 2015. Figure 6.5a displays an average PET from 12 to 18 h local time (LT), and Figure 6.5b shows the result of an ENVI-met simulation for 14 h LT. As a consequence, the peak values of PET as simulated with ENVI-met are somewhat higher at 14 h LT than in the GIS-based PET map. Also, afternoon averages have more smoothed transitions of PET between sunlit and partly shadowed areas. The ENVI-met method shows clearly a higher spatial variability in PET due to advanced variation in wind speed at relatively short distances. Local wind shadows cannot be reproduced in the PET heat map, which leads to PET maxima exceeding 55°C . While the ENVI-met model solves the RANS equations and wind for individual grid cells, the GIS-based PET heat map uses a wind speed estimate derived from the frontal area densities of buildings and trees over a larger source area (280×140 m or 175×175 m). Another difference is that the GIS-based heat map uses minimum thresholds for wind speed (i.e. 0.5 ms^{-1}). However, we find a high correlation in PET between both methods for the vast area along the river including sun/shadow differences.

Looking at the model results, we find a strong cooling of 0.5 – 1.3°C for the 2-m temperature and $\sim 10^\circ\text{C}$ PET in the shade of trees in the ENVI-met simulation of Breda, as compared to adjacent sunlit places. This is explained by the absence of direct sun radiation and evapotranspiration. The modelled air temperature reduction fits in the lower ends of the observational study (0.7 – 5.7°C) (Jiao et al., 2017). Also, an ENVI-met study for Montreal shows some larger tree cooling effects than in our study, $\sim 2^\circ\text{C}$, which may be partially explained by a larger intervention area where the trees are introduced (Wang & Akbari, 2016). The modelled reduction in PET in ENVI-met corresponds well with the conclusions from a high-resolution modelling study that used the PALM-4U LES model (Geletić et al., 2021). They used a similar thermal comfort index UTCI instead. Differences between LES-models as PALM-4U, and RANS models as ENVI-met is the parameterization of small grid turbulence of RANS and resolved turbulence for LES. Geletić et al. (2021) shows stronger vortexes arise when walls are heated on one-side of the road. (Gromke et al., 2008) discovered that a RANS model tends to have weaker vortexes than wind tunnel experiments in the canyon. This is caused by a too small vertical momentum exchange between the flow above the roofs and the canyon which is related to poorer TKE parameterization of RANS models. Thus, local winds show especially better performance in LES in situations where ground or wall heating is relatively important via the buoyancy flux term in the TKE (Xie et al., 2005; Tominaga & Stathopoulos, 2011).

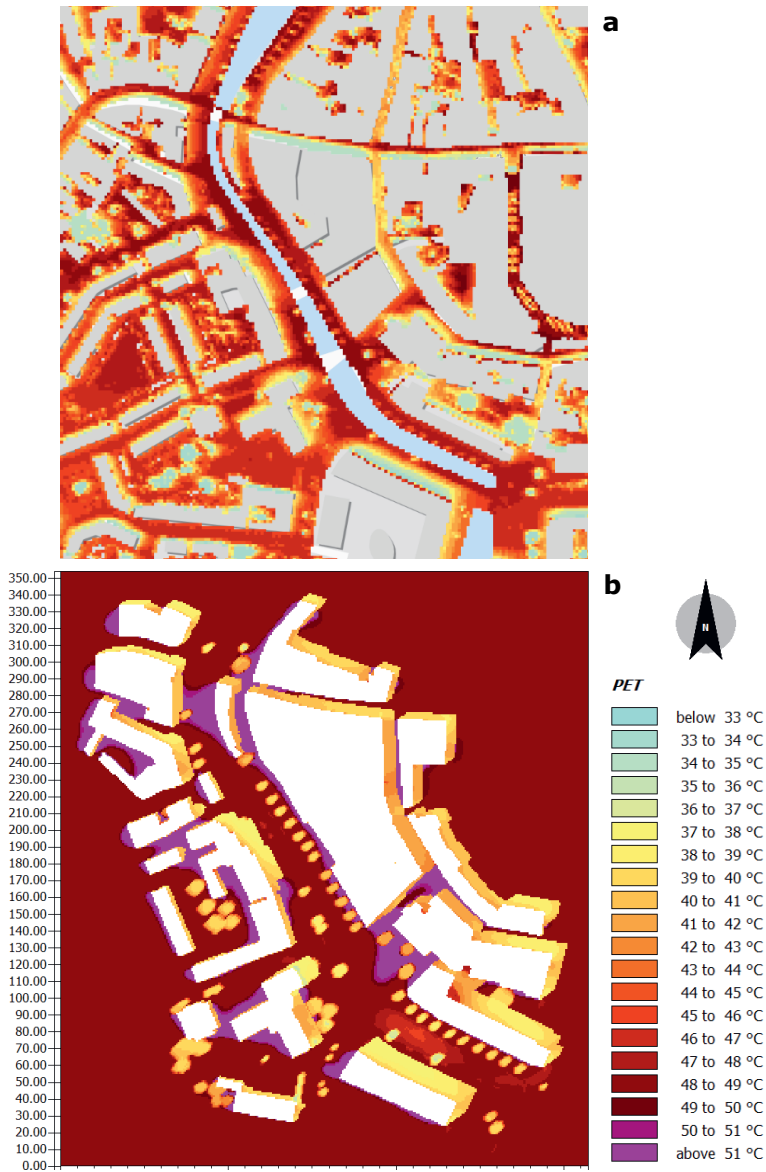


Figure 6.5: a) Comparison between GIS-modelling approach heat map and b) ENVI-met simulation of Breda (the Netherlands) for the heat wave day 1 July 2015. Heat map (top) shows afternoon average 12 h LT – 18 h LT and ENVI-met simulation (down) 16 h LT. The numbers on the left indicate the spatial scale of the model simulation (1-m resolution).

The larger scale NWP models with grid spacings of >100 m cannot represent individual buildings or trees, and urban geographical parameterizations are still necessary. The possibilities to vary urban morphological properties per grid cell has been increased in the last decades for the popular research model WRF. By default, WRF offers three urban categories in its most basic urban canopy model (SLUCM), e.g. low density residential, high density residential, and industrial/commercial (Chen et al., 2011). Each category can have their typical urban canopy parameters

as street width, anthropogenic heat etc. In WUDAPT (World Urban Database And Portal Tool), an initiative to map cities in an urban database (Ching et al., 2018), this has been extended to include 10 Local Climate Zone (LCZ) classes in WRF (Stewart & Oke, 2012), and this shows an improved representation of urban climate variability between neighbourhoods (Brousse et al., 2016).

The latest development to represent urban morphology per grid cell in NWP models like WRF, is the geomorphological approach introduced in NUDAPT (Ching et al., 2009). Herein, urban canopy parameters as building height, frontal area density, plan area fraction etc. derived from individual buildings can be calculated per grid cell, rather than that these are constant per urban class. This results in a larger variety of roughness lengths and displacement heights (Burian et al., 2002), which affects the wind and energy fluxes in the urban area. In a comparative study for Xi'an (China) the NUDAPT approach performed better for dense urban areas and areas with complex and mixed morphology compared to the default three urban categories (Zhang et al., 2020). For Houston, model results for the majority of the studied weather stations showed better performance with the NUDAPT approach compared to the three urban categories (Salamanca et al., 2011).

The sensitivity of the urban morphology becomes larger when a building energy model is coupled to the urban canopy model, as has been done for BEP+BEM model infrastructure. This energy model BEP+BEM (Martilli et al., 2002; Salamanca et al., 2009), allows for a grid specific anthropogenic heat computation, which strongly depends on the urban morphology (Salamanca et al., 2011). Another major advancement of BEP+BEM is that the sink of momentum is spread up to the buildings instead of being limited to the ground (Martilli et al., 2002). Wind speed and directions were relatively well simulated compared to a reference WRF configuration (de la Paz et al., 2016). A promising development in urban canopy modelling is BEP-tree (Krayenhoff et al., 2020). This method enables to include trees in the urban canopy and resolves the mutual energy fluxes between trees and canopy.

In general, trees ameliorate heat stress in dense urban environments by providing shadow and lowers air temperatures by evapotranspiration (Akbari et al., 2001). However, the disadvantage of using trees in climate adaptation is that too many trees can block the wind in the canyon, and the distribution and species matter (Zhang et al., 2018). 3D numerical simulations with a microscale RANS model reveal that the wind reduction of trees extends above the street canyon in open spaces and winds are redirected to tree-free streets (Salim et al., 2015). Per m^2 unit of frontal area trees are not as effective in reducing the wind speed than non-porous objects as buildings. Wind tunnel experiments show that the effective drag coefficient accounting for porosity, the retarding force slowing down air, is typically 50–90% for different foliated tree species compared to that of a building at $3\text{--}4 \text{ ms}^{-1}$ wind speed. This denotes the higher coefficients for dense coniferous species (Rudnecki et al., 2004; Vollsinger et al., 2005). Higher wind speeds decrease the effective (static) drag coefficient, because the frontal area decreases due to the bending of the foliage along the wind. By accounting for the different drag coefficients, the tree species in the wind calculation in the heat map receipt can be improved, i.e. via a weighted tree coefficient in Chapter 5 in Equation 5.6. Thus, for a good thermal comfort on hot days, blocking of the wind by trees should be avoided. However, the cooling effect of trees to the surroundings increases if trees are placed in streets which serve as ventilation paths (Tan et al., 2016). Future research should focus on the assessments of trees in a 3D urban environment modelling for wind speed reduction for different street and tree configurations.

Chapter 7

Summary

The overarching goal of this thesis is to develop methods and models to create better insights in urban weather and climate. The approaches are diverse, ranging from data assimilation of crowdsourced urban weather observations to adjust a complex numerical weather prediction model for the urban environment, to a more scalable practical application of statistical urban morphological and meteorological relations in detailed urban heat maps. The specific goals are twofold: Firstly, to offer a realistic representation of the weather for different urban districts and their near surroundings, for both the current and the future climate. Secondly, to better understand the involved physical processes and to interpret the remaining uncertainties in modelling urban weather and climate.

7.1 Effects of urbanization on a homogenized temperature record

In monitoring climate change long historical records of weather stations are essential. Changes in land-use in their surroundings through time can affect the observed climatological trend. Urbanization around weather stations is a world-wide phenomenon. Chapter 2 focused on research question 1:

Research question 1: What is the influence of urbanization on the climate record of a nearby rural weather station?

Using the Weather Research and Forecasting (WRF) mesoscale model, we estimate the impact of urbanization on the 2-m temperature record of WMO station De Bilt (the Netherlands). This station has a long historical record, but the nearby city of Utrecht and its suburbs expanded during the 20th century. We find this urbanization during the 20th century has resulted in a 100-year temperature trend of 0.22 ± 0.06 K. This is about 20% of the observed 20th century climate trend at WMO station De Bilt. This has been done by comparing WRF mesoscale model simulations for the land-use conditions for the years 1900 and 2000. Episodes of 14 different weather regimes were run to cover a 97% climatology taking account their frequency distribution. In addition, we find that the temperature trend is quite insensitive to the selected boundary-layer scheme in the model.

7.2 Fine-scale urban data assimilation and weather reanalysis for Amsterdam

As a succession of the urbanization effects on the rural surroundings in Chapter 2, Chapter 3 focuses on an improved urban climate model representation for a large city with Amsterdam as a test case. This led to the following research question:

Research question 2: How can we develop modelling techniques to best create and validate an urban reanalysis dataset?

In the urban reanalysis for Amsterdam various observations and model fields are combined to produce a complete and coherent collection of consistent meteorological gridded data. This is achieved through data assimilation, which computes an intermediate atmospheric state based on the weighted uncertainties of model and observations. Here we utilize the WRF mesoscale model with 3D variational data assimilation for July 2014 as a testbed. The data assimilation module is fed with volume radar data and WMO routine weather station data. The assimilation of surface pressure and air temperature of these WMO stations strongly improves the rural background meteorology, which is an important boundary condition for urban areas. The assimilation of volume radar data marginally improves the spatial representation and average biases over the whole Netherlands domain.

The novel part of our approach is the nudging of temperatures of personal weather station data in the city, also known as crowdsourced observations, and this was not included in WRFDA so far. To assimilate effectively urban temperatures a statistical scheme was developed to discard unreliable crowdsourced data, and a statistical fit was created based on genuine personal weather station observation-model differences and explanatory weather variables. For urban areas WRF provides a surface scheme, which calculates the typical energy and radiation fluxes in the urban canopy. Heat storage in the urban fabric is a major contribution to the Urban Heat Island (UHI) effect. Therefore, to effectively nudge urban model temperatures with personal weather sta-

tion data, we adjust the urban fabric, which includes walls and roads. A model evaluation with independent urban observations reveals this urban nudging technique reduces the temperature biases, especially the cold bias seen at night.

7.3 Urban planning strategies on heat stress for current and future climates

In the Netherlands, there is an urgent need for additional housing, i.e. 1 million houses must be built before 2040. A large part of this assignment has to be realized within the existing city borders. The densification of urban areas is expected to raise the UHI and the heat stress load. Therefore, the following research question was studied in Chapter 4:

Research question 3: What is the best approach to densify an urban environment with least effects on urban heat?

High nocturnal temperatures have adverse effects on human health by preventing an adequate recovery from daytime heat. Different urban planning strategies are investigated and evaluated on the impact on the UHI for testbed The Hague, the Netherlands. Thereto, a validated diagnostic equation was applied to estimate the UHI based on routine meteorological observations and straightforward urban morphological properties as sky-view factor and vegetation fraction. Here we choose to use the diurnal minimum air temperature as metric to quantify urban heat. The urban planning strategies have in common that a fixed amount of population was housed in urban districts. The urban planning strategy differs in replacing low- and mid-rise buildings with high-rise buildings and, construction of low-rise buildings on neighbouring green areas. The first strategy causes higher sky-view factors and the second strategy is at the dispense of cooling green. We find that, in most cases, the vegetation fraction is a more critical parameter than the sky-view factor to minimize the extra heat stress incurred when densifying a neighbourhood. This means that an urban planning strategy consisting of high-rise buildings and preserved green areas is often the optimal solution. In addition, meteorological observations are transformed according to four different KNMI climate scenarios in 2050. The impact of climate change on the urban thermal load using these climate scenarios is clearly larger than the imposed urban densification.

7.4 Mapping thermal comfort on a 1-m scale with meteorological and geographical tools

In order to quantify outdoor human thermal comfort differences on a 1-m scale, the evaluation with just air temperature is not sufficient to describe heat stress in an urban heat map. Heat stress is also influenced by other meteorological factors, like exposure to solar radiation and wind speed. The societal assignment is that municipalities and other sub-national governments in the Netherlands have to conduct so called climate stress tests to examine impact of heat stress of citizens. With an urban heat map and a corresponding manual, we want to offer users the possibility to distinguish between hot and cool places. The following research questions were answered in Chapter 5:

Research question 4: What meteorological and geographical inputs are needed to create a high-resolution urban heat map for city planning purposes and climate stress tests?

Research question 5: Is a heat map based on empirical meteorological and geographical relations sufficiently accurate to describe the urban climate?

A suitable index that mimic more closely how people experience heat is the Physiological Equivalent Temperature (PET). The PET includes factors which affect the heat release of the human body, such as radiation load, air temperature, wind and humidity. Humans can release their excess heat by transpiration and ventilation by wind and dry air supports this process. So, a good PET calculation requires good estimates for these meteorological variables in the city. For rural areas these data are available from weather stations. However, for urban areas diagnostic meteorological and geographical models are required. As a testbed, a PET map at 1 m² grid spacing for a mid-sized town Wageningen, the Netherlands is constructed. To calculate urban air temperatures, urban morphological properties as vegetation fraction and sky-view factor are required. The vegetation fraction is extracted from land-use and satellite data. Furthermore, the surface wind is typically reduced in urban areas and can be estimated by frontal density of buildings and trees. Lidar based height maps and tree register data are required as geographical inputs. The concept behind the PET map is an empirical PET model which is trained with 10 street configurations differing in aspect ratio and 15-year climatological data with the advanced 3D energy model Rayman[®]. With a regression technique the PET for Wageningen was estimated based on weather station data and real geographical inputs.

One of the presented heat maps consists of an afternoon averaged PET. The average afternoon heat load justifies and blends the hourly sun and shadow differences and is a good metric to identify hot and cool places. Sun and shadow differences can be accurately determined with the used 1-m resolution, and the resulting PET differences are therefore a useful and a step forward in mapping urban heat. However, verifications against traverse bike measurements reveal the largest uncertainties arise from radiation differences due to the size and transmissivity of tree crowns.

References

- Adachi, S. A., Kimura, F., Kusaka, H., Inoue, T., & Ueda, H. (2012). Comparison of the Impact of Global Climate Changes and Urbanization on Summertime Future Climate in the Tokyo Metropolitan Area. *Journal of Applied Meteorology and Climatology*, **51**(8), 1441-1454. doi:10.1175/JAMC-D-11-0137.1
- Adam, S., Behrendt, A., Schwitalla, T., Hammann, E., & Wulfmeyer, V. (2016). First assimilation of temperature lidar data into an NWP model: impact on the simulation of the temperature field, inversion strength and PBL depth. *Quarterly Journal of the Royal Meteorological Society*, **142**(700), 2882-2896. doi:https://doi.org/10.1002/qj.2875
- Agentschap NL (2011). Voorbeeldwoningen 2011: Bestaande bouw, Publicatie-nr. 2KPWB1034. <https://www.rvo.nl/sites/default/files/bijlagen/4.%20Brochure%20Voorbeeldwoningen%202011%20bestaande%20bouw.pdf> (in Dutch)
- AHN (2012). Actueel Hoogtebestand Nederland, Version 2. www.ahn.nl, (Accessed 1 April 2018) (in Dutch)
- Aida, M. (1982). Urban albedo as a function of the urban structure — A model experiment. *Boundary-Layer Meteorology*, **23**(4), 405-413. doi:10.1007/BF00116269
- Akbari, H., Pomerantz, M., & Taha, H. (2001). Cool surfaces and shade trees to reduce energy use and improve air quality in urban areas. *Solar Energy*, **70**(3), 295-310. doi:https://doi.org/10.1016/S0038-092X(00)00089-X
- Alexander, P. J., & Mills, G. (2014). Local climate classification and Dublin's urban heat island. *Atmos.*, **5**, 755-774. doi:https://doi.org/10.3390/atmos5040755
- Allen, R. G., Pereira, L. S., Raes, D., & Smith, M. (1998). Crop evapotranspiration: Guidelines for computing crop water requirements - FAO irrigation and drainage paper 56: FAO. UN, Rome. https://www.scsd.org/complexcivil/105CV049053/volume3/172618e_5xAGWAx8.pdf
- Allen, L., Lindberg, F., & Grimmond, C. S. B. (2011). Global to city scale urban anthropogenic heat flux: model and variability. *International Journal of Climatology*, **31**(13), 1990-2005. doi:https://doi.org/10.1002/joc.2210
- Analitis, A., Michelozzi, P., D'Ippoliti, D., de'Donato, F., Menne, B., Matthies, F., . . . Katsouyanni, K. (2014). Effects of Heat Waves on Mortality: Effect Modification and Confounding by Air Pollutants. *Epidemiology*, **25**(1), 15-22. <http://www.jstor.org/stable/24759018>
- Aoyagi, T., Kayaba, N., & Seino, N. (2012). Numerical Simulation of the Surface Air Temperature Change Caused by Increases of Urban Area, Anthropogenic Heat, and Building Aspect Ratio in the Kanto-Koshin Area. *Journal of the Meteorological Society of Japan*. Ser. II, **90B**, 11-31. doi:10.2151/jmsj.2012-B02
- Ashie, Y., & Kono, T. (2011). Urban-scale CFD analysis in support of a climate-sensitive design for the Tokyo Bay area. *Int. J. Climatol.*, **31**(2), 174-188. doi:https://doi.org/10.1002/joc.2226
- Athanassiadou, M., Baker, J., Carruthers, D., Collins, W., Girnary, S., Hassell, D., . . . Witham, C. (2010). An assessment of the impact of climate change on air quality at two UK sites. *Atmospheric Environment*, **44**(15), 1877-1886. doi:https://doi.org/10.1016/j.atmosenv.2010.02.024
- Atlas Natuurlijk Kapitaal (2020). www.atlasnatuurlijkkapitaal.nl/kaarten (Accessed 19 February 2020) (in Dutch)
- Attema, J. J., Heusinkveld, B. G., Ronda, R. J., Steeneveld, G. J., & Holtslag, A. A. M. (2015). Summer in the city: Forecasting and mapping human thermal comfort in urban areas, Paper presented at the IEEE 11th International Conference on e-Science, Munich, Germany. doi:https://doi.org/10.1109/eScience.2015.21.
- Bachmann, K., Keil, C., & Weissmann, M. (2019). Impact of radar data assimilation and orography on predictability of deep convection. *Quarterly Journal of the Royal Meteorological Society*, **145**(718), 117-130. doi:https://doi.org/10.1002/qj.3412

- Bakker, A. (2015). Time Series Transformation Tool Version 3.1. De Bilt, Netherlands, Technical Report. <http://bibliotheek.knmi.nl/knmi/TR/TR349.pdf>
- Balling, R. C., Vose, R. S., & Weber, G. R. (1998). Analysis of long-term European temperature records: 1751-1995. *Climate Research*, **10**(3), 193-200. Retrieved from <https://www.int-res.com/abstracts/cr/v10/n3/p193-200/>
- Barker, D., Huang, X.-Y., Liu, Z., Auligné, T., Zhang, X., Rugg, S., . . . Zhang, X. (2012). The Weather Research and Forecasting Model's Community Variational/Ensemble Data Assimilation System: WRFDA. *Bulletin of the American Meteorological Society*, **93**(6), 831-843. doi:10.1175/bams-d-11-00167.1
- Barthelmie, R. J. (1999). The effects of atmospheric stability on coastal wind climates. *Meteorological Applications*, **6**(1), 39-47. doi:<https://doi.org/10.1017/S1350482799000961>
- Bassett, R., Cai, X.-M., Chapman, L., Heaviside, C., & Thornes, J. E. (2017). Methodology to separate urban from regional heat advection by use of the Weather Research and Forecasting mesoscale model. *Quarterly Journal of the Royal Meteorological Society*, **143**(705), 2016-2024. doi:<https://doi.org/10.1002/qj.3062>
- Bassett, R., Cai, X., Chapman, L., Heaviside, C., Thornes, J. E., Muller, C. L., . . . Warren, E. L. (2016). Observations of urban heat island advection from a high-density monitoring network. *Q. J. R. Meteorol. Soc.*, **142**, 2434-2441. doi:<https://doi.org/10.1002/qj.2836>
- Basu, R., & Samet, J. M. (2002). Relation between Elevated Ambient Temperature and Mortality: A Review of the. *Epidemiol. Rev.*, **24**(2), 190-202. doi:<https://doi.org/10.1093/epirev/mxf007>
- Beekhuis, A., & Holleman, I. (2008). From pulse to product: Highlights of the digital-IF upgrade of the Dutch national radar network. Paper presented at the Proc. Fifth European Conf. of Radar Meteorology and Hydrology, ERAD 5, Helsinki, Finland. <https://www.knmi.nl/kennis-en-datacentrum/publicatie/from-pulse-to-product-highlights-of-the-digital-if-upgrade-of-the-dutch-national-radar-network>
- Bell, S., Cornford, D., & Bastin, L. (2013). The state of automated amateur weather observations. *Weather*, **68**(2), 36-41. doi:<https://doi.org/10.1002/wea.1980>
- Bell, S., Cornford, D., & Bastin, L. (2015). How good are citizen weather stations? Addressing a biased opinion. *Weather*, **70**(3), 75-84. doi:10.1002/wea.2316
- Bergan, T., Thomas, D., Schwartz, E., McKibben, J., & Rusiecki, J. (2015). Sleep deprivation and adverse health effects in United States Coast Guard responders to Hurricanes Katrina and Rita. *Sleep Health*, **1**(4), 268-274. doi:<https://doi.org/10.1016/j.sleh.2015.09.010>
- Berrisford, P., Dee, D. P., Poli, P., Brugge, R., Mark, F., Manuel, F., . . . Adrian, S. (2011). The ERA-Interim archive Version 2.0. Report, Shinfield Park, Reading, UK, <https://www.ecmwf.int/node/8174>
- Bohnenstengel, S. I., Evans, S., Clark, P. A., & Belcher, S. E. (2011). Simulations of the London urban heat island. *Q. J. R. Meteorol. Soc.*, **137**, 1625-1640. doi:<https://doi.org/10.1002/qj.855>
- Boilley, A., & Wald, L. (2015). Comparison between meteorological re-analyses from ERA-Interim and MERRA and measurements of daily solar irradiation at surface. *Renewable Energy*, **75**, 135-143. doi:<https://doi.org/10.1016/j.renene.2014.09.042>
- Brandsma, T. (2010). Warmte-eiland effect van de stad Utrecht. Zenit, 37, 500-504. <https://www.knmi.nl/kennis-en-datacentrum/publicatie/warmte-eilandeffect-van-de-stad-utrecht> (in Dutch)
- Brandsma, T. (2011). Parallel temperature measurements at the KNMI observatory in De Bilt (the Netherlands) May 2003- June 2005. Scientific Report (WR-2011-01), KNMI, De Bilt, the Netherlands, p. 56. <https://www.knmi.nl/kennis-en-datacentrum/publicatie/parallel-air-temperature-measurements-at-the-knmi-observatory-in-de-bilt-the-netherlands-may-2003-june-2005>
- Brandsma, T., Können, G. P., & Wessels, H. R. A. (2003). Empirical estimation of the effect of urban heat advection on the temperature series of De Bilt (The Netherlands). *International Journal of Climatology*, **23**(7), 829-845. doi:<https://doi.org/10.1002/joc.902>

- Brandsma, T., Können, G. P., & Wessels, H. R. A. (2004). Parallel Air Temperature Measurements at the KNMI-terrain in De Bilt (the Netherlands) May 2003–April 2005, Interim Report (KNMI-publication 207), KNMI, De Bilt, The Netherlands. <https://www.knmi.nl/kennis-en-datacentrum/publicatie/parallel-air-temperature-measurements-at-the-knmi-terrain-in-de-bilt-the-netherlands-may-2003-april-2005>
- Brandsma, T., & Wolters, D. (2012). Measurement and Statistical Modeling of the Urban Heat Island of the City of Utrecht (the Netherlands). *Journal of Applied Meteorology and Climatology*, **51**(6), 1046–1060. doi:10.1175/JAMC-D-11-0206.1
- Breedveld, W. (2005). Grote historische atlas Utrecht (2nd ed.). Tilburg, the Netherlands: Uitgeverij Nieuwland.
- Brohan, P., Kennedy, J. J., Harris, I., Tett, S. F. B., & Jones, P. D. (2006). Uncertainty estimates in regional and global observed temperature changes: A new data set from 1850. *Journal of Geophysical Research: Atmospheres*, **111**(D12). doi:<https://doi.org/10.1029/2005JD006548>
- Brousse, O., Martilli, A., Foley, M., Mills, G., & Bechtel, B. (2016). WUDAPT, an efficient land use producing data tool for mesoscale models? Integration of urban LCZ in WRF over Madrid. *Urban Climate*, **17**, 116–134. doi:<https://doi.org/10.1016/j.uclim.2016.04.001>
- Bruse, M., & Fleer, H. (1998). Simulating surface–plant–air interactions inside urban environments with a three dimensional numerical model. *Environmental Modelling & Software*, **13**(3), 373–384. doi:[https://doi.org/10.1016/S1364-8152\(98\)00042-5](https://doi.org/10.1016/S1364-8152(98)00042-5)
- Burian, S. J., Brown, M. J., & Linger, S. P. (2002). Morphological analyses using 3D building databases: Los Angeles, California (LA-UR-02-0781). Los Angeles, California. <https://www.researchgate.net/publication/260286741>
- Buttner, G., Feranec, J., & Jaffrain, G. (2002). CORINE land cover update 2000, technical guidelines, technical guidelines. Copenhagen. http://www.eea.europa.eu/publications/technical_report_2002_89/at_download/file
- CAS (2020). Climate Impact Atlas. <https://www.klimaat-effectatlas.nl/en/> (Accessed 19 February 2020)
- CBS (2001). Statline, www.statline.cbs.nl (Accessed 29 November 2011) (in Dutch)
- CBS (2018a). Aardgas; Aanbod en Verbruik. https://opendata.cbs.nl/statline/portal.html?_la=nl&_catalog=CBS&tableId=00372&_theme=200 (Accessed 7 August 2018) (in Dutch)
- CBS (2018b). Bevolking; Geslacht, Leeftijd, Regio. https://opendata.cbs.nl/statline/portal.html?_la=nl&_catalog=CBS&tableId=03759ned&_theme=299 (Accessed 7 August 2018) (in Dutch)
- CBS (2018c). Kaart van 100 meter bij 100 meter met Statistieken. Retrieved from <https://www.cbs.nl/nl-nl/dossier/nederland-regionaal/geografische%20data/kaart-van-100-meter-bij-100-meter-met-statistieken> (Accessed 7 August 2018) (in Dutch)
- CBS (2019). Regionale kerncijfers Nederland. <https://opendata.cbs.nl/statline/#/CBS/nl/dataset/70072ned/table?ts=1574944489452> (Accessed 20 December 2019) (in Dutch)
- Chapman, S., Watson, J. E. M., Salazar, A., Thatcher, M., & McAlpine, C. A. (2017). The impact of urbanization and climate change on urban temperatures: a systematic review. *Landscape Ecology*, **32**(10), 1921–1935. doi:10.1007/s10980-017-0561-4
- Chen, F., Kusaka, H., Bornstein, R., Ching, J., Grimmond, C. S. B., Grossman-Clarke, S., . . . Zhang, C. (2011). The integrated WRF/urban modelling system: development, evaluation, and applications to urban environmental problems. *International Journal of Climatology*, **31**(2), 273–288. doi:10.1002/joc.2158
- Ching, J., Brown, M., Burian, S., Chen, F., Cionco, R., Hanna, A., . . . Williams, D. (2009). National urban database and access portal tool. *Bull. Am. Meteor. Soc.*, **90**(8), 1157–1168. doi:<https://doi.org/10.1175/2009BAMS2675.1>

- Ching, J., Mills, G., Bechtel, B., See, L., Feddema, J., Wang, X., . . . Theeuwes, N. E. (2018). WUDAPT: An urban weather, climate, and environmental modeling infrastructure for the Anthropocene. *Bull. Am. Meteor. Soc.*, **99**, 1907-1924. doi:<https://doi.org/10.1175/BAMS-D-16-0236.1>
- Choi, G., Collins, D., Ren, G., Trewin, B., Baldi, M., Fukuda, Y., . . . Zhou, Y. (2009). Changes in means and extreme events of temperature and precipitation in the Asia-Pacific Network region, 1955–2007. *International Journal of Climatology*, **29**(13), 1906-1925. doi:10.1002/joc.1979
- Christen, A., Oke, T., Grimmond, S., Steyn, D., & Roth, M. (2013). 35 years of urban climate research at the 'Vancouver-Sunset' flux tower. <https://open.library.ubc.ca/collections/52383/items/1.0103588>
- Christen, A., & Vogt, R. (2004). Energy and radiation balance of a central European city. *International Journal of Climatology*, **24**(11), 1395-1421. doi:<https://doi.org/10.1002/joc.1074>
- Chrysanthou, A., van der Schrier, G., van den Besselaar, E. J. M., Klein Tank, A. M. G., & Brandsma, T. (2014). The effects of urbanization on the rise of the European temperature since 1960. *Geophysical Research Letters*, **41**(21), 7716-7722. doi:<https://doi.org/10.1002/2014GL061154>
- Chumchuan, S., Sharma, A., & Seed, A. (2003). Radar rainfall error variance and its impact on radar rainfall calibration. *Physics and Chemistry of the Earth, Parts A/B/C*, **28**(1), 27-39. doi:[https://doi.org/10.1016/S1474-7065\(03\)00005-6](https://doi.org/10.1016/S1474-7065(03)00005-6)
- Clarke, J. F. (1969). Nocturnal urban boundary layer over Cincinnati, Ohio. *Monthly Weather Review*, **97**(8), 582-589. doi:10.1175/1520-0493(1969)097<0582:NUBLOC>2.3.CO;2
- Clarke, J. F. (1971). Some effects of the urban structure on heat mortality. *Environ. Res.*, **5**(1), 93-104. doi:[https://doi.org/10.1016/0013-9351\(72\)90023-0](https://doi.org/10.1016/0013-9351(72)90023-0)
- Cleugh, H. A., & Oke, T. R. (1986). Suburban–rural energy balance comparisons in summer for Vancouver, B.C. *Boundary-Layer Meteorology*, **36**(4), 351-369. doi:10.1007/BF00118337
- Cohen, P., Potchter, O., & Matzarakis, A. (2013). Human thermal perception of Coastal Mediterranean outdoor urban environments. *Appl. Geogr.*, **37**, 1-10. doi:<https://doi.org/10.1002/joc.1330>
- Cosgrove, A., & Berkelhammer, M. (2018). Downwind footprint of an urban heat island on air and lake temperatures. *npj Climate and Atmospheric Science*, **1**(1), 46. doi:10.1038/s41612-018-0055-3
- Courtier, P., Thépaut, J. N., & Hollingsworth, A. (1994). A strategy for operational implementation of 4D-Var, using an incremental approach. *Quarterly Journal of the Royal Meteorological Society*, **120**(519), 1367-1387. doi:<https://doi.org/10.1002/qj.49712051912>
- Crank, P. J., Sailor, D. J., Ban-Weiss, G., & Taleghani, M. (2018). Evaluating the ENVI-met microscale model for suitability in analysis of targeted urban heat mitigation strategies. *Urban Climate*, **26**, 188-197. doi:<https://doi.org/10.1016/j.uclim.2018.09.002>
- CRED (2020), Disaster Year in Review (2019), CRED Crunch Issue No. 58, Brussels, Belgium, 2020. <https://reliefweb.int/report/world/cred-crunch-newsletter-issue-no-58-april-2020-disaster-2019-year-review> (Accessed 27 May 2021)
- Cubasch, U., Wuebbles, D., Chen, D., Fachini, M. C., Frame, D., Mahowald, N., & Winther, J. G. (2013). Introduction. In *Climate Change 2013: The Physical Science Basis. Contribution of Working Group I to the Fifth Assessment Report of the Intergovernmental Panel on Climate Change*. Cambridge, UK and New York, NY, USA: Cambridge University Press.
- D'Ippoliti, D., Michelozzi, P., Marino, C. *et al.* (2010). The impact of heat waves on mortality in 9 European cities: Results from the Euroheat Project. *Environ. Health*, **9**. doi:<https://doi.org/10.1186/1476-069X-9-37>
- de la Paz, D., Borge, R., & Martilli, A. (2016). Assessment of a high resolution annual WRF-BEP/CMAQ simulation for the urban area of Madrid (Spain). *Atmospheric Environment*, **144**, 282-296. doi:<https://doi.org/10.1016/j.atmosenv.2016.08.082>
- de Rooy, W. C., & Holtslag, A. A. M. (1998). Estimation of surface radiation and energy flux densities from single-level weather data. *J. Appl. Meteorol.*, **38**, 526-540. doi:[https://doi.org/10.1175/1520-0450\(1999\)038<0526:EOSRAE>2.0.CO;2](https://doi.org/10.1175/1520-0450(1999)038<0526:EOSRAE>2.0.CO;2)

- de Vos, L. W., Droste, A. M., Zander, M. J., Overeem, A., Leijnse, H., Heusinkveld, B. G., . . . Uijlenhoet, R. (2020). Hydrometeorological Monitoring Using Opportunistic Sensing Networks in the Amsterdam Metropolitan Area. *Bulletin of the American Meteorological Society*, **101**(2), E167-E185. doi:10.1175/BAMS-D-19-0091.1
- De Waag. (2021). Construction years of buildings. <https://code.waag.org/buildings/#52.3844,4.9171,11> (Accessed 12 February 2021)
- Deardorff, J. W. (1980). Stratocumulus-capped mixed layers derived from a three-dimensional model. *Boundary-Layer Meteorology*, **18**(4), 495-527. doi:10.1007/BF00119502
- Dee, D. P., Uppala, S. M., Simmons, A. J., Berrisford, P., Poli, P., Kobayashi, S., . . . Vitart, F. (2011). The ERA-Interim reanalysis: configuration and performance of the data assimilation system. *Quarterly Journal of the Royal Meteorological Society*, **137**(656), 553-597. doi:10.1002/qj.828
- Douville, H., Colin, J., Krug, E., Cattiaux, J., & Thao, S. (2016). Midlatitude daily summer temperatures reshaped by soil moisture under climate change. *Geophysical Research Letters*, **43**(2), 812-818. doi:10.1002/2015gl066222
- Droste, A. Ronda, R. J., Theeuwes, N. E., Steeneveld, G. J. (2015). Influence of the urban green vegetative fraction on the urban heat island effect across Europe. ICUC9 - 9th International Conference on Urban Climate jointly with 12th Symposium on the Urban Environment. http://www.meteo.fr/icuc9/LongAbstracts/poster_13-9-2111220_a.pdf
- Droste, A. M., Heusinkveld, B. G., Fenner, D., & Steeneveld, G. J. (2020). Assessing the potential and application of crowdsourced urban wind data. *Quarterly Journal of the Royal Meteorological Society*, **146**(731), 2671-2688. doi:10.1002/qj.3811
- Ebert, E. E. (2009). Neighborhood Verification: A Strategy for Rewarding Close Forecasts. *Weather and Forecasting*, **24**(6), 1498-1510. doi:10.1175/2009WAF2222251.1
- EIB (2015). Investeren in Nederland. https://www.eib.nl/pdf/investeren_in_nederland.pdf (Accessed 21 May 2021) (in Dutch)
- Ek, M. B., Mitchell, K. E., Lin, Y., Rogers, E., Grunmann, P., Koren, V., . . . Tarpley, J. D. (2003). Implementation of Noah land surface model advances in the National Centers for Environmental Prediction operational mesoscale Eta model. *Journal of Geophysical Research: Atmospheres*, **108**(D22). doi:https://doi.org/10.1029/2002JD003296
- Eliasson, I. (1996). Urban nocturnal temperatures, street geometry and land use. *Atmospheric Environment*, **30**(3), 379-392. doi:https://doi.org/10.1016/1352-2310(95)00033-X
- EU-Commision (2008). Directive 2008/50/EC of the European Parliament and of the Council of 21 May 2008 on ambient air quality and cleaner air for Europe. *Official J. European Communities*, **152**, 1-44. <https://eur-lex.europa.eu/LexUriServ/LexUriServ.do?uri=OJ:L:2008:152:0001:0044:en:PDF>
- Fall, S., Niyogi, D., Gluhovsky, A., Pielke Sr, R. A., Kalnay, E., & Rochon, G. (2010). Impacts of land use land cover on temperature trends over the continental United States: assessment using the North American Regional Reanalysis. *International Journal of Climatology*, **30**(13), 1980-1993. doi:https://doi.org/10.1002/joc.1996
- Fanger, P. O. (1973). Assessment of man's thermal comfort in practise. *Br. J. Ind. Med.*, **30**, 313-324. doi:http://dx.doi.org/10.1136/oem.30.4.313
- Fenner, D., Meier, F., Bechtel, B., Otto, M., & Scherer, D. (2017). Intra and inter 'local climate zone' variability of air temperature as observed by crowdsourced citizen weather stations in Berlin, Germany. *Meteorologische Zeitschrift*, **26**(5), 525-547. doi:10.1127/metz/2017/0861
- Field, P. R., Brožková, R., Chen, M., Dudhia, J., Lac, C., Hara, T., . . . McTaggart-Cowan, R. (2017). Exploring the convective grey zone with regional simulations of a cold air outbreak. *Quarterly Journal of the Royal Meteorological Society*, **143**(707), 2537-2555. doi:10.1002/qj.3105
- Fischer, E. M., & Schär, C. (2010). Consistent geographical patterns of changes in high-impact European heatwaves. *Nat. Geosci.*, **3**, 398-403. doi:https://doi.org/10.1007/s00484-018-1530-6

- Fischer, P. H., Brunekreef, B., & Lebrete, E. (2004). Air pollution related deaths during the 2003 heat wave in the Netherlands. *Atmospheric Environment*, **38**(8), 1083-1085. doi:https://doi.org/10.1016/j.atmosenv.2003.11.010
- Folland, C. K., Rayner, N. A., Brown, S. J., Smith, T. M., Shen, S. S. P., Parker, D. E., . . . Sexton, D. M. H. (2001). Global temperature change and its uncertainties since 1861. *Geophysical Research Letters*, **28**(13), 2621-2624. doi:https://doi.org/10.1029/2001GL012877
- Fouillet, A., Rey, G., Laurent, F., Pavillon, G., Bellec, S., & Ghihenneuc-Jouyau, C. (2006). Excess mortality related to the August 2003 heat wave in France. *Int. Arch. Occup. Environ.*, **80**, 16-24. doi:https://doi.org/10.1007/s00420-006-0089-4
- Fouillet, A., Rey, G., Laurent, F., Pavillon, G., Bellec, S., Guihenneuc-Jouyau, C., . . . Hémon, D. (2006). Excess mortality related to the August 2003 heat wave in France. *International Archives of Occupational and Environmental Health*, **80**(1), 16-24. doi:10.1007/s00420-006-0089-4
- Fouillet, A., Rey, G., Wagner, V., Laaidi, K., Empereur-Bissonnet, P., Le Tertre, A., . . . Hémon, D. (2008). Has the impact of heat waves on mortality changed in France since the European heat wave of summer 2003? A study of the 2006 heat wave. *International Journal of Epidemiology*, **37**(2), 309-317. doi:10.1093/ije/dym253
- Francis, J. A., & Wu, B. (2020). Why has no new record-minimum Arctic sea-ice extent occurred since September 2012? *Environmental Research Letters*, **15**(11), 114034. doi:10.1088/1748-9326/abc047
- Fröhlich, J., & von Terzi, D. (2008). Hybrid LES/RANS methods for the simulation of turbulent flows. *Progress in Aerospace Sciences*, **44**(5), 349-377. doi:https://doi.org/10.1016/j.paerosci.2008.05.001
- Fujibe, F., Yamazaki, N., Kobayashi, K., & Nakamigawa, H. (2007). Longterm changes of temperature extremes and day-to-day variability in Japan. *Pap. Meteorol. Geophys.*, **58**, 63-72.
- García-Díez, M., Fernández, J., Fita, L., & Yagüe, C. (2013). Seasonal dependence of WRF model biases and sensitivity to PBL schemes over Europe. *Quarterly Journal of the Royal Meteorological Society*, **139**(671), 501-514. doi:https://doi.org/10.1002/qj.1976
- Garssen, J., Harmsen, C., & De Beer, J. (2005). The effect of the summer 2003 heat wave on mortality in the Netherlands. *Eurosurveillance*, **10**(7), 557. doi:https://doi.org/10.2807/esm.10.07.00557-en
- Gasparrini, A., Guo, Y., Sera, F., Vicedo-Cabrera, A. M., Huber, V., Tong, S., et al. (2017). Projections of temperature-related excess mortality under climate change. *Lancet. Planet. Health*, **1**(9), 360-367. doi:https://doi.org/10.1016/S2542-5196(17)30156-0
- Geletić, J., Lehnert, M., Krč, P., Resler, J., & Krayenhoff, E. S. (2021). High-Resolution Modelling of Thermal Exposure during a Hot Spell: A Case Study Using PALM-4U in Prague, Czech Republic. *Atmosphere*, **12**(2). doi:10.3390/atmos12020175
- Goh, K. C., & Chang, C. H. (1999). The relationship between height to width ratios and the heat island intensity at 22:00 h for Singapore. *International Journal of Climatology*, **19**(9), 1011-1023. doi:https://doi.org/10.1002/(SICI)1097-0088(199907)19:9<1011::AID-JOC411>3.0.CO;2-U
- Grell, G. A. (1993). Prognostic Evaluation of Assumptions Used by Cumulus Parameterizations. *Monthly Weather Review*, **121**(3), 764-787. doi:10.1175/1520-0493(1993)121<0764:PEOAUB>2.0.CO;2
- Grell, G. A., & Freitas, S. R. (2014). A scale and aerosol aware stochastic convective parameterization for weather and air quality modeling. *Atmos. Chem. Phys.*, **14**(10), 5233-5250. doi:10.5194/acp-14-5233-2014
- Grimmond, C. S. B., Blackett, M., Best, M. J., Baik, J. J., Belcher, S. E., Beringer, J., . . . Zhang, N. (2011). Initial results from Phase 2 of the international urban energy balance model comparison. *International Journal of Climatology*, **31**(2), 244-272. doi:https://doi.org/10.1002/joc.2227
- Grimmond, C. S. B., King, T. S., Roth, M., & T.R., O. (1998). Aerodynamic roughness of urban areas derived from wind observations. *Boundary-Layer Meteorol.*, **89**(1), 1-24. doi:https://doi.org/10.1023/A:1001525622213

- Grimmond, C. S. B., & Oke, T. R. (1999). Heat Storage in Urban Areas Local-Scale Observations and Evaluation of a Simple Model. *Journal of Applied Meteorology*, **38**(7), 922-940. [https://doi.org/10.1175/1520-0450\(1999\)038<0922:HSIUAL>2.0.CO;2](https://doi.org/10.1175/1520-0450(1999)038<0922:HSIUAL>2.0.CO;2)
- Grimmond, C. S. B., Salmond, J. A., Oke, T. R., Offerle, B., & Lemonsu, A. (2004). Flux and turbulence measurements at a densely built-up site in Marseille: Heat, mass (water and carbon dioxide), and momentum. *Journal of Geophysical Research: Atmospheres*, **109**(D24). doi:<https://doi.org/10.1029/2004JD004936>
- Grimmond, C. S. B., Blackett, M., Best, M. J., Barlow, J., Baik, J. J., Belcher, S. E., . . . Zhang, N. (2010). The International Urban Energy Balance Models Comparison Project: First Results from Phase 1. *Journal of Applied Meteorology and Climatology*, **49**(6), 1268-1292. doi:10.1175/2010JAMC2354.1
- Grize, L., Huss, A., Thommen, O., Schindler, C., & Braun-Fahrländer, C. (2005). Heat wave 2003 and mortality in Switzerland. *Swiss Med. Wkly*, **135**, 200-205.
- Gromke, C., Buccolieri, R., Di Sabatino, S., & Ruck, B. (2008). Dispersion study in a street canyon with tree planting by means of wind tunnel and numerical investigations – Evaluation of CFD data with experimental data. *Atmospheric Environment*, **42**(37), 8640-8650. doi:<https://doi.org/10.1016/j.atmosenv.2008.08.019>
- Grossman-Clarke, S., Schubert, S., & Fenner, D. (2017). Urban effects on summertime air temperature in Germany under climate change. *International Journal of Climatology*, **37**(2), 905-917. doi:<https://doi.org/10.1002/joc.4748>
- Grossman-Clarke, S., Zehnder, J. A., Loridan, T., & Grimmond, C. S. B. (2010). Contribution of Land Use Changes to Near-Surface Air Temperatures during Recent Summer Extreme Heat Events in the Phoenix Metropolitan Area. *Journal of Applied Meteorology and Climatology*, **49**(8), 1649-1664. doi:10.1175/2010JAMC2362.1
- Guan, D., Zhang, Y., & Zhu, T. (2003). A wind-tunnel study of windbreak drag. *Agric For. Meteorol.*, **118**(1-2), 75-84. doi:[https://doi.org/10.1016/S0168-1923\(03\)00069-8](https://doi.org/10.1016/S0168-1923(03)00069-8)
- Hage, K. D. (1975). Urban-rural humidity differences. *J. Appl. Meteorol.*, **14**, 1277-1283. doi:[https://doi.org/10.1175/1520-0450\(1975\)014<1277:URHD>2.0.CO;2](https://doi.org/10.1175/1520-0450(1975)014<1277:URHD>2.0.CO;2)
- Hales, S., Salmond, C., Town, G. I., Kjellstrom, T., & Woodward, A. (2000). Daily mortality in relation to weather and air pollution in Christchurch, New Zealand. *Australian and New Zealand Journal of Public Health*, **24**(1), 89-91. doi:10.1111/j.1467-842X.2000.tb00731.x
- Hamdi, R., & Schayes, G. (2008). Sensitivity study of the urban heat island intensity to urban characteristics. *Int. J. Climatol.*, **28**(7), 973-982. doi:<https://doi.org/10.1002/joc.1598>
- Hamdi, R., van de Vyver, H., De Troch, R., & Termonia, P. (2014). Assessment of three dynamical urban climate downscaling methods: Brussels's future urban heat island under an A1B emission scenario. *International Journal of Climatology*, **34**(4), 978-999. doi:<https://doi.org/10.1002/joc.3734>
- Hamid, K. (2012). Investigation of the passage of a derecho in Belgium. *Atmospheric Research*, **107**, 86-105. doi:<https://doi.org/10.1016/j.atmosres.2011.12.013>
- Hamilton, I. G., Davies, M. I., Steadman, P., Stone, A., Ridley, I., & Evans, S. (2009). The significance of the anthropogenic heat emissions of London's buildings: A comparison against captured shortwave solar radiation. *Building and Environment*, **44**(4), 807-817. doi:<https://doi.org/10.1016/j.buildenv.2008.05.024>
- Hansen, J., & Lebedeff, S. (1987). Global trends of measured surface air temperature. *Journal of Geophysical Research: Atmospheres*, **92**(D11), 13345-13372. doi:<https://doi.org/10.1029/JD092iD11p13345>
- Heaviside, C., Cai, X. M., & Vardoulakis, S. (2015). The effects of horizontal advection on the urban heat island in Birmingham and the West Midlands, United Kingdom during a heatwave. *Q. J. R. Meteorol. Soc.*, **141**, 1429-1441. doi:<https://doi.org/10.1002/qj.2452>
- Heisler, G. M. (1990). Mean wind speed below building height in residential neighborhoods with different tree densities. *ASHRAE Transactions*, **96**(1), 1389-1396. <https://www.fs.usda.gov/treesearch/pubs/37282>

- Heistermann, M., Jacobi, S., & Pfaff, T. (2013). Technical Note: An open source library for processing weather radar data (wradlib). *Hydrol. Earth Syst. Sci.*, **17**(2), 863-871. doi:10.5194/hess-17-863-2013
- Hersbach, H., Bell, B., Berrisford, P., Hirahara, S., Horányi, A., Muñoz-Sabater, J., . . . Thépaut, J.-N. (2020). The ERA5 global reanalysis. *Quarterly Journal of the Royal Meteorological Society*, **146**(730), 1999-2049. doi:10.1002/qj.3803
- Heusinkveld, B. G., Hove, L. W. A., Jacobs, C. M. J., Steeneveld, G. J., Elbers, J. A., Moors, E. J., & Holtslag, A. A. M. (2010). Use of a mobile platform for assessing urban heat stress in Rotterdam. Paper presented at the Proceedings of the 7th Conference on Biometeorology Albert-Ludwigs-University of Freiburg, Freiburg, Germany. <https://library.wur.nl/WebQuery/wurpubs/391825>
- Heusinkveld, B. G., Steeneveld, G. J., van Hove, L.W.A, Jacobs, C. M. J., & Holtslag, A. A. M. (2014). Spatial variability of the Rotterdam urban heat island as influenced by urban land use. *J. Geophys. Res. Atmos.*, **119**(2), 677-692. doi:<https://doi.org/10.1002/2012JD019399>
- Hidalgo, J., Masson, V., & Pigeon, G. (2008). Urban-breeze circulation during the CAPITOUL experiment: numerical simulations. *Meteorology and Atmospheric Physics*, **102**(3), 243-262. doi:10.1007/s00703-008-0345-0
- Hintz, K. S., O'Boyle, K., Dance, S. L., Al-Ali, S., Ansper, I., Blaauboer, D., . . . Yang, X. (2019). Collecting and utilising crowdsourced data for numerical weather prediction: Propositions from the meeting held in Copenhagen, 4-5 December 2018. *Atmospheric Science Letters*, **20**(7), e921. doi:<https://doi.org/10.1002/asl.921>
- Hoeven van der, F., & Wandl, A. (2015). Amsterwarm: Mapping the landuse, health and energy-efficiency implications of the Amsterdam urban heat island. *Building Serv. Eng. Res. Technol.*, **36**(1), 67-88. doi:<https://doi.org/10.1177/0143624414541451>
- Hoffmann, P., Schoetter, R., & Schlünzen, H. (2018). Statistical-dynamical downscaling of the urban heat island in Hamburg. *Meteorol. Z.*, **27**(2), 89-109. doi:<https://doi.org/10.1127/metz/2016/0773>
- Holmer, B. (1992). A simple operative method for determination of sky view factors in complex urban canyons from fisheye photographs. *Meteorol. Z.*, **1**(5), 236-239. doi:<https://doi.org/10.1127/metz/1/1992/236>
- Holtslag, A. A. M., & Boville, B. A. (1993). Local Versus Nonlocal Boundary-Layer Diffusion in a Global Climate Model. *Journal of Climate*, **6**(10), 1825-1842. doi:10.1175/1520-0442(1993)006<1825:LVNBLD>2.0.CO;2
- Holtslag, A. A. M., Svensson, G., Baas, P., Basu, S., Beare, B., Beljaars, A. C. M., . . . van De Wiel, B. J. H. (2013). Stable Atmospheric Boundary Layers and Diurnal Cycles: Challenges for Weather and Climate Models. *Bulletin of the American Meteorological Society*, **94**(11), 1691-1706. doi:10.1175/BAMS-D-11-00187.1
- Holtslag, A. A. M., van Meijgaard, E., & de Rooy, W. C. (1995). A comparison of boundary layer diffusion schemes in unstable conditions over land. *Boundary-Layer Meteorology*, **76**(1), 69-95. doi:10.1007/BF00710891
- Hong, S. Y., Noh, Y., & Dudhia, J. (2006). A New Vertical Diffusion Package with an Explicit Treatment of Entrainment Processes. *Monthly Weather Review*, **134**(9), 2318-2341. doi:10.1175/mwr3199.1
- Honnert, R., Efstathiou, G. A., Beare, R. J., Ito, J., Lock, A., Neggers, R., . . . Zhou, B. (2020). The Atmospheric Boundary Layer and the “Gray Zone” of Turbulence: A Critical Review. *Journal of Geophysical Research: Atmospheres*, **125**(13), e2019JD030317. doi:10.1029/2019jd030317
- Hopkinson, R. F., McKenney, D. W., Milewska, E. J., Hutchinson, M. F., Papadopol, P., & Vincent, L. A. (2011). Impact of Aligning Climatological Day on Gridding Daily Maximum–Minimum Temperature and Precipitation over Canada. *Journal of Applied Meteorology and Climatology*, **50**(8), 1654-1665. doi:10.1175/2011JAMC2684.1
- Höppe, P. (1999). The physiological equivalent temperature - A universal index for the biometeorological assessment of the thermal environment. *Int. J. Biometeorol.*, **43**(2), 71-75. doi:<https://doi.org/10.1007/s004840050118>

- Hu, X.-M., Nielsen-Gammon, J. W., & Zhang, F. (2010). Evaluation of Three Planetary Boundary Layer Schemes in the WRF Model. *Journal of Applied Meteorology and Climatology*, **49**(9), 1831-1844. doi:10.1175/2010JAMC2432.1
- Huang, Y. J., Akbari, H., & Taha, H. (1990). The wind-shielding and shading effects of trees on residential heating and cooling requirements. Paper presented at the ASHRAE proceedings, Atlanta, USA. <https://escholarship.org/uc/item/85g3s8xt>
- Huang, X.-Y., Xiao, Q., Barker, D. M., Zhang, X., Michalakos, J., Huang, W., . . . Kuo, Y.-H. (2009). Four-Dimensional Variational Data Assimilation for WRF: Formulation and Preliminary Results. *Monthly Weather Review*, **137**(1), 299-314. doi:10.1175/2008MWR2577.1
- Huynen, M. T. E., & Martens, P. (2015). Climate change effects on heat- and cold-related mortality in the Netherlands: A scenario-based integrated environmental health impact assessment. *Int. J. Environ. Res. Public Health*, **12**, 13295-13320. doi:<https://doi.org/10.3390/ijerph121013295>
- Iamarino, M., Beevers, S., & Grimmond, C. S. B. (2012). High-resolution (space, time) anthropogenic heat emissions: London 1970–2025. *Int. J. Climatol.*, **32**(11), 1754-1767. doi:<https://doi.org/10.1002/joc.2390>
- Ichinose, T., Shimodozono, K., & Hanaki, K. (1999). Impact of anthropogenic heat on urban climate in Tokyo. *Atmos. Environ.*, **33**(24-25), 3897-3999. doi:[https://doi.org/10.1016/S1352-2310\(99\)00132-6](https://doi.org/10.1016/S1352-2310(99)00132-6)
- Imhoff, R. O., Brauer, C. C., Overeem, A., Weerts, A. H., & Uijlenhoet, R. (2020). Spatial and Temporal Evaluation of Radar Rainfall Nowcasting Techniques on 1,533 Events. *Water Resources Research*, **56**(8), e2019WR026723. doi:<https://doi.org/10.1029/2019WR026723>
- IPCC (2013). Annex I: Atlas of Global and Regional Climate Projections. T. F. Stocker, D. Qin, G.-K. Plattner, M. Tignor, S. K. Allen, J. Boschung, A. Nauels, Y. Xia, V. Bex, & P. M. Midgley (Eds.), In *Climate Change 2013: The Physical Science Basis. Contribution of Working Group I to the Fifth Assessment Report of the Intergovernmental Panel on Climate Change* (pp. 1535). Cambridge, United Kingdom, and New York, NY, USA: Cambridge University Press.
- IPCC (2014a). Impacts, Adaptation, and Vulnerability. Part A: Global and Sectoral Aspects. Contribution of Working Group II to the Fifth Assessment Report of the Intergovernmental Panel on Climate Change. United Kingdom and New York, NY, USA: Cambridge University Press.
- IPCC (2014b). Summary for Policymakers. In O. Edenhofer, R. Pichs-Madruga, Y. Sokona, E. Farahani, S. Kadner, K. Seyboth, A. Adler, I. Baum, S. Brunner, P. Eickmeier, B. Kriemann, J. Savolainen, S. Schlömer, T. Stechow, & J. C. Minx (Eds.), In *Climate Change 2014: Mitigation of Climate Change. Contribution of Working Group III to the Fifth Assessment Report of the Intergovernmental Panel on Climate Change*. Cambridge, United Kingdom and New York, NY, USA: Cambridge University Press.
- Janjić, Z. I. (1996). The surface layer in the NCEP Eta Model. Paper presented at the Proc of the 11th conf. on Num. Wea. Pred., 354-355, Norfolk, VA, USA. (Amer. Meteorol. Soc.)
- Janjić, Z. I. (2001). Nonsingular implementation of the Mellor-Yamada level 2.5 scheme in the NCEP Meso model. NCEP Office Note, 437, 61 pp
- Jiao, M., Zhou, W., Zheng, Z., Wang, J., & Qian, Y. (2017). Patch size of trees affects its cooling effectiveness: A perspective from shading and transpiration processes. *Agricultural and Forest Meteorology*, **247**, 293-299. doi:<https://doi.org/10.1016/j.agrformet.2017.08.013>
- Joe, L., Hoshiko, S., Dobraca, D., Jackson, R., Smorodinsky, S., Smith, D., & Harnly, M. (2016). Mortality during a Large-Scale Heat Wave by Place, Demographic Group, Internal and External Causes of Death, and Building Climate Zone. *International Journal of Environmental Research and Public Health*, **13**(3). doi:10.3390/ijerph13030299
- Johansson, E. (2006). Influence of urban geometry on outdoor thermal comfort in a hot dry climate: A study in Fez, Morocco. *Building and Environment*, **41**(10), 1326-1338. doi:<https://doi.org/10.1016/j.buildenv.2005.05.022>
- Johansson, L., Onomura, S., Lindberg, F., & Seaquist, J. (2016). Towards the modelling of pedestrian wind speed using high-resolution digital surface models and statistical methods. *Theor. Appl. Climatol.*, **124**, 189-203. doi:<https://doi.org/10.1007/s00704-015-1405-2>

- Jones P. D., Raper S. C. B., Bradley R. S., Diaz H. F., Kelly P. M., Wigley T. M. L. (1986a). Northern Hemisphere surface air temperature variations: 1851-1984. *J. Clim. Appl. Meteorol.* **25**, 161-179.
- Jones P. D., Raper S. C. B., Wigley T. M. L. (1986b). Southern Hemisphere surface air temperature variations: 1851-1984. *J. Climate Appl. Meteorol.* **25**, 1213-1230.
- Jones, P. D., Groisman, P. Y., Coughlan, M., Plummer, N., Wang, W. C., & Karl, T. R. (1990). Assessment of urbanization effects in time series of surface air temperature over land. *Nature*, **347**(6289), 169-172. doi:10.1038/347169a0
- Jones, P. D., & Lister, D. H. (2009). The urban heat island in Central London an urban-related warming trends in Central London since 1900. *Weather*, **64**(12), 323-327. doi:10.1002/wea.432
- Kalnay, E., & Cai, M. (2003). Impact of urbanization and land-use change on climate. *Nature*, **423**(6939), 528-531. doi:10.1038/nature01675
- Kalverla, P., Steeneveld, G. J., Ronda, R. J., & Holtslag, A. A. M. (2019). Evaluation of three mainstream numerical weather prediction models with observations from meteorological mast IJmuiden at the North Sea. *Wind Energy*, **22**(1), 34-48. doi:https://doi.org/10.1002/we.2267
- Kanda M. (2007). Progress in Urban Meteorology. *J. Meteorol. Soc. Jpn.* **85B**, 363-383.
- Kanda, M., Kanega, M., Kawai, T., Moriwaki, R., & Sugawara, H. (2007). Roughness Lengths for Momentum and Heat Derived from Outdoor Urban Scale Models. *Journal of Applied Meteorology and Climatology*, **46**(7), 1067-1079. doi:10.1175/jam2500.1
- Karl, T. R., Diaz, H. F., & Kukla, G. (1988). Urbanization: Its Detection and Effect in the United States Climate Record. *Journal of Climate*, **1**(11), 1099-1123. doi:10.1175/1520-0442(1988)001<1099:UIDAEI>2.0.CO;2
- Kato, S., & Yamaguchi, Y. (2007). Estimation of storage heat flux in an urban area using ASTER data. *Remote Sensing of Environment*, **110**(1), 1-17. doi:https://doi.org/10.1016/j.rse.2007.02.011
- Katsouyanni, K., Pantazopoulou, A., Touloumi, G., Tselepidaki, I., Moustiris, K., Asimakopoulos, D., . . . Trichopoulos, D. (1993). Evidence for Interaction between Air Pollution and High Temperature in the Causation of Excess Mortality. *Archives of Environmental Health: An International Journal*, **48**(4), 235-242. doi:10.1080/00039896.1993.9940365
- Kent, C. W., Grimmond, C. S. B., & Gatey, D. (2017). Aerodynamic roughness parameters in cities: Inclusion of vegetation. *J. Wind. Eng. Ind. Aerodyn.*, **169**, 168-176. doi:https://doi.org/10.1016/j.jweia.2017.07.016
- Khain, P., Levi, Y., Shtivelman, A., Vadislavsky, E., Brainin, E., & Stav, N. (2020). Improving the precipitation forecast over the Eastern Mediterranean using a smoothed time-lagged ensemble. *Meteorological Applications*, **27**(1), e1840. doi:https://doi.org/10.1002/met.1840
- Khan, S. M., & Simpson, R. W. (2001). Effect Of A Heat Island On The Meteorology Of A Complex Urban Airshed. *Boundary-Layer Meteorology*, **100**(3), 487-506. doi:10.1023/A:1019284332306
- Kimura, F., & Takahashi, S. (1991). The effects of land-use and anthropogenic heating on the surface temperature in the Tokyo Metropolitan area: A numerical experiment. *Atmospheric Environment. Part B. Urban Atmosphere*, **25**(2), 155-164. doi:https://doi.org/10.1016/0957-1272(91)90050-O
- Klein Tank, A. M. G., Beersma, J., Bessembinder, B., van den Hurk, B., & Lenderink, G. (2015). KNMI'14 Climate Scenarios for the Netherlands; A guide for professionals in climate adaptation. KNMI, De Bilt, the Netherlands, p.34. http://www.klimaatsscenarios.nl/brochures/images/Brochure_KNMI14_EN_2015.pdf (Accessed 13 January 2020)
- Klemm, W., Heusinkveld, B. G., Lenzholzer, S., Jacobs, M. H., & van Hove, L. W. A. (2015). Psychological and physical impact of urban green spaces on outdoor thermal comfort during summertime in The Netherlands. *Build. Environ.*, **66**, 120-128. doi:https://doi.org/10.1016/j.buildenv.2014.05.013

- Klok, L., ten Broeke, H., van Harmelen, T., Verhagen, H., Kok, H., & Zwart, S. (2010). Ruimtelijke verdeling van mogelijke oorzaken van het hitte-eiland effect. TNO Rapport (TNO-034-UT-2010-01229_RPT-MI), p.78. <https://edepot.wur.nl/326309> (in Dutch)
- Klysik, K. (1996). Spatial and seasonal distribution of anthropogenic heat emissions in Lodz, Poland. *Atmospheric Environment*, **30**(20), 3397-3404. doi:[https://doi.org/10.1016/1352-2310\(96\)00043-X](https://doi.org/10.1016/1352-2310(96)00043-X)
- KNMI (2006). Warme en Zonnige Zomer 2006, KNMI <https://www.knmi.nl/over-het-knmi/nieuws/warme-en-zonnige-zomer-2006> (Accessed 20 April 2021)
- KNMI (2013). List of meteorological stations KNMI. <http://www.knmi.nl/klimatologie/metadata/stationslijst.html>. (Accessed 25 June 2013) (in Dutch)
- KNMI (2015). Toelichting Transformatie Tijdreeksen. KNMI, De Bilt, the Netherlands, http://www.klimaatsscenario's.nl/toekomstig_weer/transformatie/Toelichting_TP.pdf (Accessed 20 February 2020) (in Dutch)
- KNMI. (2018). Sky View Factor of the Netherlands. Dataset, https://data.knmi.nl/datasets/sky_view_factor_netherlands/1.0?q=sky+view (Accessed 26 February 2018)
- Knol, W. C., Kramer, H., & Gijsbertse, H. (2004). Historisch Grondgebruik Nederland; een landelijke reconstructie van het grondgebruik rond 1900. Alterra-report 573, Wageningen, the Netherlands.
- Konarska, J., Lindberg, F., Larsson, A., Thorsson, S., & Holmer, B. (2014). Transmissivity of solar radiation through crowns of single urban trees—application for outdoor thermal comfort modelling. *Theor. Appl. Climatol.*, **117**, 363-376. doi:<https://doi.org/10.1007/s00704-013-1000-3>
- Köppen, W., & Geiger, R. (1936). Handbuch der Klimatologie; Das geographische System der Klimate. Borntraeger Science Publishers, 1.
- Kottek, M., Grieser, J., Beck, C., Rudolf, B., & Rubel, F. (2006). World map of the Köppen-Geiger climate classification updated. *Meteorol. Zeitschr.*, **15**(3), 259-263. doi:10.1127/0941-2948/2006/0130
- Kotthaus, S., & Grimmond, C. S. B. (2014). Energy exchange in a dense urban environment – Part I: Temporal variability of long-term observations in central London. *Urban Climate*, **10**, 261-280. doi:<https://doi.org/10.1016/j.uclim.2013.10.002>
- Kramer, M., Heinzeller, D., Hartmann, H., Berg, W. v. d., & Steeneveld, G. J. (2020). Assessment of MPAS variable resolution simulations in the grey-zone of convection against WRF model results and observations. *Climate Dynamics*, **55**(1), 253-276. doi:10.1007/s00382-018-4562-z
- Krayenhoff, E. S., Jiang, T., Christen, A., Martilli, A., Oke, T. R., Bailey, B. N., . . . Crawford, B. R. (2020). A multi-layer urban canopy meteorological model with trees (BEP-Tree): Street tree impacts on pedestrian-level climate. *Urban Climate*, **32**, 100590. doi:<https://doi.org/10.1016/j.uclim.2020.100590>
- Kusaka, H., Kondo, H., Kikegawa, Y., & Kimura, F. (2001). A Simple Single-Layer Urban Canopy Model For Atmospheric Models: Comparison With Multi-Layer And Slab Models. *Boundary-Layer Meteorology*, **101**(3), 329-358. doi:10.1023/A:1019207923078
- Kusaka, H., & Kimura, F. (2004). Thermal Effects of Urban Canyon Structure on the Nocturnal Heat Island: Numerical Experiment Using a Mesoscale Model Coupled with an Urban Canopy Model. *Journal of Applied Meteorology*, **43**(12), 1899-1910. doi:10.1175/JAM2169.1
- Kysely, J. (2008). Influence of the persistence of circulation patterns on warm and cold temperature anomalies in Europe: Analysis over the 20th century. *Glob. Planet. Change*, **62**(1-2), 147-163. doi:<https://doi.org/10.1016/j.gloplacha.2008.01.003>
- Ladstädter, F., Steiner, A. K., Schwärz, M., & Kirchengast, G. (2015). Climate intercomparison of GPS radio occultation, RS90/92 radiosondes and GRUAN from 2002 to 2013. *Atmos. Meas. Tech.*, **8**(4), 1819-1834. doi:10.5194/amt-8-1819-2015
- Landsberg, H. E., & Maisel, T. N. (1972). Micrometeorological observations in an area of urban growth. *Boundary-Layer Meteorol.*, **2**, 365-370. doi:<https://doi.org/10.1007/BF02184776>

- Leduc, M., & Laprise, R. (2009). Regional climate model sensitivity to domain size. *Clim. Dyn.*, **32**, 833–854. doi:DOI 10.1007/s00382-008-0400-z
- Leduc, M., Laprise, R., Morreti-Poisson, M., & Morin, J. P. (2011). Sensitivity to domain size of mid-latitude summer simulations with a regional climate model. *Clim. Dyn.*, **37**, 343–356. doi:DOI 10.1007/s00382-011-1008-2
- Lee, K., Baek, H.-J., & Cho, C. (2013). Analysis of changes in extreme temperatures using quantile regression. *Asia-Pacific J. Atmos. Sci.*, **49**(3), 313–323. doi:DOI:10.1007/s13143-013-0030-1
- Lemonsu, A., Kounkou-Arnaud, R., Desplat, J., Salagnac, J.-L., & Masson, V. (2013). Evolution of the Parisian urban climate under a global changing climate. *Climatic Change*, **116**(3), 679–692. doi:10.1007/s10584-012-0521-6
- Lemonsu, A., & Masson, V. (2002). Simulation of a Summer Urban Breeze Over Paris. *Boundary-Layer Meteorology*, **104**(3), 463–490. doi:10.1023/A:1016509614936
- Letzel, M. O., Krane, M., & Raasch, S. (2008). High resolution urban large-eddy simulation studies from street canyon to neighbourhood scale. *Atmospheric Environment*, **42**(38), 8770–8784. doi:https://doi.org/10.1016/j.atmosenv.2008.08.001
- Liang, S. (2001). Narrowband to broadband conversions of land surface albedo I: Algorithms. *Remote Sensing of Environment*, **76**(2), 213–238. doi:https://doi.org/10.1016/S0034-4257(00)00205-4
- Lim, Y.-K., Cai, M., Kalnay, E., & Zhou, L. (2005). Observational evidence of sensitivity of surface climate changes to land types and urbanization. *Geophysical Research Letters*, **32**(22). doi:https://doi.org/10.1029/2005GL024267
- Lin, T. P., & Matzarakis, A. (2008). Tourism climate and thermal comfort in Sun Moon Lake, Taiwan. *Int. J. Biometeorol.*, **52**, 281–290. doi:https://doi.org/10.1007/s00484-007-0122-7
- Lindberg, F., Grimmond, C. S. B., Gabey, A., Huang, B., Kent, C. W., Sun, T., . . . Zhang, Z. (2018). Urban multi-scale environmental predictor (UMEP): An integrated tool for city-based climate services. *Environ. Modell. Softw.*, **99**, 70–87. doi:https://doi.org/10.1016/j.envsoft.2017.09.020
- Lorenz, R., Stalhandske, Z., & Fischer, E. M. (2019). Detection of a Climate Change Signal in Extreme Heat, Heat Stress, and Cold in Europe From Observations. *Geophysical Research Letters*, **46**(14), 8363–8374. doi:10.1029/2019gl082062
- Lorenz, T., & Barstad, I. (2016). A dynamical downscaling of ERA-Interim in the North Sea using WRF with a 3 km grid—for wind resource applications. *Wind Energy*, **19**(10), 1945–1959. doi:10.1002/we.1961
- Loridan, T., Grimmond, C. S. B., Grossman-Clarke, S., Chen, F., Tewari, M., Manning, K., . . . Best, M. (2010). Trade-offs and responsiveness of the single-layer urban canopy parametrization in WRF: An offline evaluation using the MOSCEM optimization algorithm and field observations. *Quarterly Journal of the Royal Meteorological Society*, **136**(649), 997–1019. doi:https://doi.org/10.1002/qj.614
- MacDonald, R. W. (2000). Modelling the mean velocity profile in the urban canopy layer. *Boundary-Layer Meteorol.*, **97**, 25–45. doi:https://doi.org/10.1023/A:1002785830512
- MacDonald, R. W., Griffiths, R. F., & Hall, D. J. (1998). An improved method for the estimation of surface roughness of obstacle arrays. *Atmos. Environ.*, **32**(11), 1857–1864. doi:https://doi.org/10.1016/S1352-2310(97)00403-2
- Manoli, G., Fatichi, S., Bou-Zeid, E., & Katul, G. G. (2020). Seasonal hysteresis of surface urban heat islands. *Proceedings of the National Academy of Sciences*, **117**(13), 7082. doi:10.1073/pnas.1917554117
- Maronga, B., Banzhaf, S., Burmeister, C., Esch, T., Forkel, R., Fröhlich, D., Fuka, V., Gehrke, K. F., Geletič, J., Giersch, S., Gronemeier, T., Groß, G., Heldens, W., Hellsten, A., Hoffmann, F., Inagaki, A., Kadasch, E., Kanani-Sühring, F., Ketelsen, K., Khan, B. A., Knigge, C., Knoop, H., Krč, P., Kurppa, M., Maamari, H., Matzarakis, A., Mauder, M., Pallasch, M., Pavlik, D., Pfafferoth, J., Resler, J., Rissmann, S., Russo, E., Salim, M., Schrempf, M., Schwenkel, J., Seckmeyer, G., Schubert, S., Sühring, M., von Tils, R., Vollmer, L., Ward, S., Witha, B., Wurps, H., Zeidler, J., & Raasch, S.: Overview of the PALM model system 6.0, *Geosci. Model Dev.*, **13**, 1335–1372, https://doi.org/10.5194/gmd-13-1335-2020, 2020.

- Martilli, A., Clappier, A., & Rotach, M. W. (2002). An Urban Surface Exchange Parameterisation for Mesoscale Models. *Boundary-Layer Meteorology*, **104**(2), 261-304. doi:10.1023/A:1016099921195
- Martinez, G. S., Linares, C., Ayuso, A., Kendrovski, V., Boeckmann, M., & Diaz, J. (2019). Heat-health action plans in Europe: Challenges ahead and how to tackle them. *Environmental Research*, **176**, 108548. doi:https://doi.org/10.1016/j.envres.2019.108548
- Masson, V. (2000). A Physically-Based Scheme For The Urban Energy Budget In Atmospheric Models. *Boundary-Layer Meteorology*, **94**(3), 357-397. doi:10.1023/A:1002463829265
- Matzarakis, A., de Rocco, M., & Najjar, G. (2009). Thermal bioclimate in Strasbourg - the 2003 heat wave. *Theor. Appl. Climatol.*, **98**, 209-220. doi:https://doi.org/10.1007/s00704-009-0102-4
- Matzarakis, A., Mayer, H., & Iziomon, M. G. (1999). Applications of a universal thermal index: physiological equivalent temperature. *Int. J. Biometeorol.*, **43**, 76-84. doi:https://doi.org/10.1007/s004840050119
- Matzarakis, A., Rutz, F., & Mayer, H. (2010). Modelling Radiation fluxes in simple and complex environments – Basics of the RayMan model. *Int. J. Biometeorol.*, **54**, 131-139. doi:https://doi.org/10.1007/s00484-009-0261-0
- McCarthy, M. P., Best, M. J., & Betts, R. A. (2010). Climate change in cities due to global warming and urban effects. *Geophysical Research Letters*, **37**(9). doi:https://doi.org/10.1029/2010GL042845
- Meier, F., Fenner, D., Grassmann, T., Otto, M., & Scherer, D. (2017). Crowdsourcing air temperature from citizen weather stations for urban climate research. *Urban Climate*, **19**, 170-191. doi:https://doi.org/10.1016/j.uclim.2017.01.006
- Met Office (2018). Iris: A Python library for analysing and visualising meteorological and oceanographic data sets. Exeter, Devon. <https://scitools-iris.readthedocs.io/en/stable/> (Accessed 15 February 2021)
- Miao, S., Chen, F., LeMone, M. A., Tewari, M., Li, Q., & Wang, Y. (2009). An Observational and Modeling Study of Characteristics of Urban Heat Island and Boundary Layer Structures in Beijing. *Journal of Applied Meteorology and Climatology*, **48**(3), 484-501. doi:10.1175/2008JAMC1909.1
- Mirzaei, P. A., & Haghighat, F. (2010). Approaches to study Urban Heat Island – Abilities and limitations. *Building and Environment*, **45**(10), 2192-2201. doi:https://doi.org/10.1016/j.buildenv.2010.04.001
- Mittermaier, M., Roberts, N., & Thompson, S. A. (2013). A long-term assessment of precipitation forecast skill using the Fractions Skill Score. *Meteorological Applications*, **20**(2), 176-186. doi:https://doi.org/10.1002/met.296
- Molenaar, R. E., Heusinkveld, B. G., & Steeneveld, G. J. (2016). Projection of rural and urban human thermal comfort. *Int. J. Climatol.*, **36**(4), 1708-1723. doi:https://doi.org/10.1002/joc.4453
- Monaghan, A. J., Hu, L., Brunsell, N. A., Barlage, M., & Wilhelmi, O. V. (2014). Evaluating the impact of urban morphology configurations on the accuracy of urban canopy model temperature simulations with MODIS. *Journal of Geophysical Research: Atmospheres*, **119**(11), 6376-6392. doi:10.1002/2013jd021227
- Montávez, J. P., Rodríguez, A., & Jiménez, J. I. (2000). A study of the Urban Heat Island of Granada. *International Journal of Climatology*, **20**(8), 899-911. doi:https://doi.org/10.1002/1097-0088(20000630)20:8<899::AID-JOC433>3.0.CO;2-I
- Moriwaki, R., & Kanda, M. (2004). Seasonal and Diurnal Fluxes of Radiation, Heat, Water Vapor, and Carbon Dioxide over a Suburban Area. *Journal of Applied Meteorology*, **43**(11), 1700-1710. doi:10.1175/JAM2153.1
- Narumi, D., Kondo, A., & Shimoda, Y. (2009). Effects of anthropogenic heat release upon the urban climate in a Japanese megacity. *Environmental Research*, **109**(4), 421-431. doi:https://doi.org/10.1016/j.envres.2009.02.013
- Ng, E. (2012). Towards planning and practical understanding of the need for meteorological and climatic information in the design of high-density cities: A case-based study of Hong Kong. *Int. J. Climatol.*, **32**, 582 - 598. doi:https://doi.org/10.1002/joc.2292

- Ngan, K., & Lo, K. W. (2017). Linear Error Dynamics for Turbulent Flow in Urban Street Canyons. *Journal of Applied Meteorology and Climatology*, **56**(5), 1195-1208. doi:10.1175/JAMC-D-16-0173.1
- Nipen, T. N., Scierstad, I. A., Lussana, C., Kristiansen, J. r., & Hov, y. (2020). Adopting Citizen Observations in Operational Weather Prediction. *Bulletin of the American Meteorological Society*, **101**(1), E43-E57. doi:10.1175/BAMS-D-18-0237.1
- Oke, T. R. (1973). City size and the urban heat island. *Atmospheric Environment* (1967), **7**(8), 769-779. doi:https://doi.org/10.1016/0004-6981(73)90140-6
- Oke, T. R. (1982). The energetic basis of the urban heat island. *Q. J. R. Meteorol. Soc.*, **108**(455), 1-24. doi:https://doi.org/10.1002/qj.49710845502
- Oke, T. R. (1987). *Boundary Layer Climates*. London: Routledge.
- Oke, T. R. (1988). The urban energy balance. *Progress in Physical Geography: Earth and Environment*, **12**(4), 471-508. doi:10.1177/030913338801200401
- Oke, T. R. (2006). Initial guidance to obtain representative meteorological observations at urban sites. IOM Rep. 81, WMO, Geneva
- Oke, T. R., & McCaughey, J. H. (1983). Suburban–rural energy balance comparisons for Vancouver, B.C.: An extreme case? *Boundary-Layer Meteorology*, **26**(4), 337-354. doi:10.1007/BF00119532
- Oke, T. R., Mills, G., Christen, A., & Voogt, J. A. (2017). *Urban Climates*. Cambridge, UK: Cambridge University Press.
- OpenTopo (2018). Background map. PDOK-Services, Plug-in in QGIS. <http://pdokviewer.pdok.nl> (Accessed 8 May 2018)
- Overeem, A., Buishand, T. A., & Holleman, I. (2009). Extreme rainfall analysis and estimation of depth-duration-frequency curves using weather radar. *Water Resources Research*, **45**(10). doi:https://doi.org/10.1029/2009WR007869
- Parrish, D. F., & Derber, J. C. (1992). The National Meteorological Center's Spectral Statistical-Interpolation Analysis System. *Monthly Weather Review*, **120**(8), 1747-1763. doi:10.1175/1520-0493(1992)120<1747:Tnmcss>2.0.Co;2
- Pino, D., Vilà-Guerau de Arellano, J., Comerón, A., & Rocadenbosch, F. (2004). The boundary layer growth in an urban area. *Science of The Total Environment*, 334-335, 207-213. doi:https://doi.org/10.1016/j.scitotenv.2004.04.039
- Pogačar, T., Casanueva, A., & Kozjek, K. (2018). The effect of hot days on occupational heat stress in the manufacturing industry: implications for workers' well-being and productivity. *Int. J. Biometeorol.*, **62**(7), 1251-1264. doi:https://doi.org/10.1007/s00484-018-1530-6
- Pope, S. (2010). Self-conditioned fields for large-eddy simulations of turbulent flows. *J. Fluid Mech.*, **652**, 139-169. doi:doi:10.1017/S0022112009994174
- Powers, J. G., Klemp, J. B., Skamarock, W. C., Davis, C. A., Dudhia, J., Gill, D. O., . . . Duda, M. G. (2017). The Weather Research and Forecasting Model: Overview, System Efforts, and Future Directions. *Bulletin of the American Meteorological Society*, **98**(8), 1717-1737. doi:10.1175/BAMS-D-15-00308.1
- Pyrgou, A., Hadjinicolaou, P., & Santamouris, M. (2018). Enhanced near-surface ozone under heatwave conditions in a Mediterranean island. *Scientific Reports (Nature Publisher Group)*, **8**, 1-10. doi:http://dx.doi.org/10.1038/s41598-018-27590-z
- QGIS (2018). QGIS Geographic information System. Open Source Geospatial Foundation project. <https://qgis.org/en/site/>
- Quah, A. K. L., & Roth, M. (2012). Diurnal and weekly variation of anthropogenic heat emissions in a tropical city, Singapore. *Atmospheric Environment*, **46**, 92-103. doi:https://doi.org/10.1016/j.atmosenv.2011.10.015
- Ren, C., Ng, E., & Katschnner, L. (2011). Urban climatic map studies: a review. *Int. J. Climatol.*, 2213-2233. doi:https://doi.org/10.1002/joc.2237

- Ren, C., Spit, T., Lenzholzer, S., Yim, H. L. S., Heusinkveld, B. G., van Hove, L. W. A., . . . Katzschner, L. (2012). Urban climate map system for Dutch spatial planning. *Int. J. Appl. Earth Obs.*, **18**, 207-221. doi:<https://doi.org/10.1016/j.jag.2012.01.026>
- Ren, G., Zhou, Y., Chu, Z., Zhou, J., Zhang, A., Guo, J., & Liu, X. (2008). Urbanization Effects on Observed Surface Air Temperature Trends in North China. *Journal of Climate*, **21**(6), 1333-1348. doi:10.1175/2007jcli1348.1
- Riahi, K., Rao, S., Krey, V., Cho, C., Chirkov, V., Fischer, G., . . . Rafaj, P. (2011). RCP 8.5—A scenario of comparatively high greenhouse gas emissions. *Climatic Change*, **109**(1), 33. doi:10.1007/s10584-011-0149-y
- Richardson, H., Basu, S., & Holtslag, A. A. M. (2013). Improving Stable Boundary-Layer Height Estimation Using a Stability-Dependent Critical Bulk Richardson Number. *Boundary-Layer Meteorology*, **148**(1), 93-109. doi:10.1007/s10546-013-9812-3
- Rizvi, S. R. H., Guo, Y. R., Shao, H., Demirtas, M., & Huang, X. Y. (2008). Impact of outer loop for WRF data assimilation system (WRFDA). Paper presented at the WRF Users' Workshop, Boulder, CO, USA. <https://citeseerx.ist.psu.edu/viewdoc/download?doi=10.1.1.522.4799&rep=rep1&type=pdf>
- Roberts, N. M., & Lean, H. W. (2008). Scale-Selective Verification of Rainfall Accumulations from High-Resolution Forecasts of Convective Events. *Monthly Weather Review*, **136**(1), 78-97. doi:10.1175/2007mwr2123.1
- Robine, J.-M., Cheung, S. L. K., Le Roy, S., van Oyen, H., Griffiths, C., Michel, J.-P., & Herrmann, F. R. (2008). Death toll exceeded 70,000 in Europe during the summer of 2003. *Comptes Rendus Biologies*, **331**(2), 171-178. doi:<https://doi.org/10.1016/j.crv.2007.12.001>
- Ronda, R. J., Steeneveld, G. J., Heusinkveld, B. G., Attema, J. J., & Holtslag, A. A. M. (2017). Urban finescale forecasting reveals weather conditions with unprecedented detail. *Bull. Am. Meteor. Soc.*, **98**, 2675-2688. doi:<https://doi.org/10.1175/BAMS-D-16-0297.1>
- Roth, M., Oke, T. R., & Emery, W. J. (1989). Satellite-derived urban heat islands from three coastal cities and the utilization of such data in urban climatology. *International Journal of Remote Sensing*, **10**(11), 1699-1720. doi:10.1080/01431168908904002
- Rouault, G., Candau, J. N., Lieutier, F., Nageleisen, L. M., Martin, J. C., & Warzée, N. (2006). Effects of drought and heat on forest insect populations in relation to the 2003 drought in Western Europe. *Annu. For. Sci.*, **63**, 613-624. doi:<https://doi.org/10.1051/forest:2006044>
- Rudnicki, M., Mitchell, S. J., & Novak, M. D. (2004). Wind tunnel measurements of crown streamlining and drag relationships for three conifer species. *Canadian Journal of Forest Research*, **34**(3), 666-676. doi:10.1139/x03-233
- Sailor, D. J., & Lu, L. (2004). A top-down methodology for developing diurnal and seasonal anthropogenic heating profiles for urban areas. *Atmospheric Environment*, **38**(17), 2737-2748. doi:<https://doi.org/10.1016/j.atmosenv.2004.01.034>
- Salamanca, F. P., Krpo, A., Martilli, A., & Clappier, A. (2009). A new building energy model coupled with an urban canopy parameterization for urban climate simulations—part I. formulation, verification, and sensitivity analysis of the model. *Theoretical and Applied Climatology*, **99**(3), 331. doi:10.1007/s00704-009-0142-9
- Salamanca, F. P., Martilli, A., Tewari, M., & Chen, F. (2011). A Study of the Urban Boundary Layer Using Different Urban Parameterizations and High-Resolution Urban Canopy Parameters with WRF. *Journal of Applied Meteorology and Climatology*, **50**(5), 1107-1128. doi:10.1175/2010JAMC2538.1
- Salcedo Rahola, B., van Oppen, P., & Mulder, K. (2009). Heat in the city; An inventory of knowledge and knowledge deficiencies regarding heat stress in Dutch cities and options for its mitigation. Report (KvR 013/2009). <http://resolver.tudelft.nl/uuid:b0e41aea-7004-4677-b050-14f066d95450>
- Salim, M. H., Schlünzen, K. H., & Grawe, D. (2015). Including trees in the numerical simulations of the wind flow in urban areas: Should we care? *J. Wind. Eng. Ind. Aerodyn.*, **144**, 84-95. doi:<https://doi.org/10.1016/j.jweia.2015.05.004>

- Schaefer, D., & Domroes, M. (2009). Recent climate change in Japan – spatial and temporal characteristics of trends of temperature. *Clim. Past*, **5**(1), 13-19. doi:10.5194/cp-5-13-2009
- Scherer, D., Fehrenbach, U., Beha, H. D., & Parlow, E. (1999). Improved concepts and methods in analysis and evaluation of the urban climate for optimizing urban planning processes. *Atmos. Environ.*, **33**, 4185-4193. doi:https://doi.org/10.1016/S1352-2310(99)00161-2
- Schuepp, P. H., Leclerc, M. Y., MacPherson, J. I., & Desjardins, R. L. (1990). Footprint prediction of scalar fluxes from analytical solutions of the diffusion equation. *Boundary-Layer Meteorology*, **50**(1), 355-373. doi:10.1007/BF00120530
- Shi, Y., Ren, C., Zheng, Y., & Ng, E. (2016). Mapping the urban microclimatic spatial distribution in a sub-tropical high-density urban environment. *Archit. Sci. Rev.*, **59**(5), 370-384. doi:https://doi.org/10.1080/00038628.2015.1105195
- Shin, H. H., & Hong, S.-Y. (2011). Intercomparison of Planetary Boundary-Layer Parametrizations in the WRF Model for a Single Day from CASES-99. *Boundary-Layer Meteorology*, **139**(2), 261-281. doi:10.1007/s10546-010-9583-z
- Shrestha, K. L., Kondo, A., Meada, C., Kaga, A., & Inoue, Y. (2009) Numerical simulation of urban heat island using gridded urban configuration and anthropogenic heat data generated by a simplified method. Paper presented at the Proc. 7th Conf. on Urban Climate, 29 June-3 July 2009. Yokohama, Japan. http://www.ide.titech.ac.jp/~icuc7/extended_abstracts/pdf/384391-1-090515124426-002.pdf
- Shukla, P. R., Skea, J., Slade, R., van Diemen, R., Haughey, E., Malley, J., . . . Portugal Pereira, J. (2019). Technical Summary. In *Climate Change and Land: an IPCC special report on climate change, desertification, land degradation, sustainable land management, food security, and greenhouse gas fluxes in terrestrial ecosystems*. IPCC, Geneva, Switzerland.
- Simmonds, I., & Keay, K. (1997). Weekly cycle of meteorological variations in Melbourne and the role of pollution and anthropogenic heat release. *Atmospheric Environment*, **31**(11), 1589-1603. doi:https://doi.org/10.1016/S1352-2310(96)00344-5
- Simmons, A. J., Willett, K. M., Jones, P. D., Thorne, P. W., & Dee, D. P. (2010). Low-frequency variations in surface atmospheric humidity, temperature, and precipitation: Inferences from reanalyses and monthly gridded observational data sets. *Journal of Geophysical Research: Atmospheres*, **115**(D1). doi:10.1029/2009jd012442
- Skamarock, W. C., Klemp, J. B., Dudhia, J., Gill, D. O., Barker, D. M., Wang, W., & Powers, J. G. (2005). A description of the advanced research wrf version 2. Technical Report, DTIC Document (NCAR/TN-468+STR), University Corporation for Atmospheric Research. doi:https://dx.doi.org/10.5065/D6DZ069T
- Skamarock, W. C., Klemp, J. B., Dudhia, J., Gill, D. O., Barker, D. O., Duda, M. G., . . . Powers, J. G. (2008). A description of the advanced research WRF Version 3. Technical Report (NCAR/TN-475+STR), University Corporation for Atmospheric Research, p.113. doi:https://dx.doi.org/10.5065/D68S4MVH
- Skok, G. (2015). Analysis of Fraction Skill Score properties for a displaced rainband in a rectangular domain. *Meteorological Applications*, **22**(3), 477-484. doi:10.1002/met.1478
- Skok, G., & Roberts, N. (2016). Analysis of Fractions Skill Score properties for random precipitation fields and ECMWF forecasts. *Quarterly Journal of the Royal Meteorological Society*, **142**(700), 2599-2610. doi:https://doi.org/10.1002/qj.2849
- Smith, T. M., Reynolds, R. W., Peterson, T. C., & Lawrimore, J. (2008). Improvements to NOAA's Historical Merged Land–Ocean Surface Temperature Analysis (1880–2006). *Journal of Climate*, **21**(10), 2283-2296. doi:10.1175/2007JCLI2100.1
- Steenefeld, G. J., Mauritsen, T., de Bruijn, E. I. F., Vilà-Guerau de Arellano, J., Svensson, G., & Holtslag, A. A. M. (2008). Evaluation of Limited-Area Models for the Representation of the Diurnal Cycle and Contrasting Nights in CASES-99. *Journal of Applied Meteorology and Climatology*, **47**(3), 869-887. doi:10.1175/2007JAMC1702.1

- Steeneveld, G. J., Koopmans, S., Heusinkveld, B. G., van Hove, L. W. A., & Holtslag, A. A. M. (2011a). Quantifying urban heat island effects and human comfort for cities of variable size and urban morphology in the Netherlands. *Journal of Geophysical Research: Atmospheres*, **116**(D20). doi:https://doi.org/10.1029/2011JD015988
- Steeneveld, G. J., Tol, L. F., Moene, A. F., Hartogensis, O. K., Peters, W., & Holtslag, A. A. M. (2011b). Confronting the WRF and RAMS mesoscale models with innovative observations in the Netherlands: Evaluating the boundary layer heat budget. *Journal of Geophysical Research: Atmospheres*, **116**(D23). doi:https://doi.org/10.1029/2011JD016303
- Steeneveld, G. J., Koopmans, S., & Theeuwes, N. E. (2014). Refreshing the role of open water surfaces on mitigating the maximum urban heat island effect. *Landsc. Urban Plan.*, **121**, 92-96. doi:https://doi.org/10.1080/00038628.2015.1105195
- Stensrud, D. J. (2009). Parameterization schemes: Keys to understanding numerical weather prediction models.: Cambridge Univ. Press.
- Sterk, H. A. M., Steeneveld, G. J., & Holtslag, A. A. M. (2013). The role of snow-surface coupling, radiation, and turbulent mixing in modeling a stable boundary layer over Arctic sea ice. *Journal of Geophysical Research: Atmospheres*, **118**(3), 1199-1217. doi:https://doi.org/10.1002/jgrd.50158
- Stewart, I. D., & Oke, T. R. (2012). Local Climate Zones for Urban Temperature Studies. *Bulletin of the American Meteorological Society*, **93**(12), 1879-1900. doi:10.1175/bams-d-11-00019.1
- Steyn, D. G. (1980). The calculation of view factors from fisheye-lens photographs: Research note. *Atmosphere-Ocean*, **18**(3), 254-258. doi:10.1080/07055900.1980.9649091
- Stocker, T. Dahe Q., Plattner G. K. (eds) (2013). In *Climate Change 2013: Synthesis Report* (Intergovernmental Panel on Climate Change, Cambridge, UK, 2013). Alexander, L., and co-authors, Synthesis Report (for the Fifth Assessment Report of the Intergovernmental Panel on Climate Change), Cambridge Univ. Press, Cambridge, p. 23.
- Stull, R. (2011). Wet-bulb temperature from relative humidity and air temperature. *J. Appl. Meteorol. Clim.*, **50**, 2267-2269. doi:https://doi.org/10.1175/JAMC-D-11-0143.1
- Sun, J., Xue, M., Wilson, J. W., Zawadzki, I., Ballard, S. P., Onvlee-Hooimeyer, J., . . . Pinto, J. (2014). Use of NWP for Nowcasting Convective Precipitation: Recent Progress and Challenges. *Bulletin of the American Meteorological Society*, **95**(3), 409-426. doi:10.1175/BAMS-D-11-00263.1
- Tan, Z., Lau, K. K.-L., & Ng, E. (2016). Urban tree design approaches for mitigating daytime urban heat island effects in a high-density urban environment. *Energy and Buildings*, **114**, 265-274. doi:https://doi.org/10.1016/j.enbuild.2015.06.031
- Tang, Q., Leng, G., & Groisman, P. Y. (2012). European Hot Summers Associated with a Reduction of Cloudiness. *Journal of Climate*, **25**(10), 3637-3644. doi:10.1175/jcli-d-12-00040.1
- Theeuwes, N. E., Solceroová, A., & Steeneveld, G. J. (2013). Modeling the influence of open water surfaces on the summertime temperature and thermal comfort in the city. *Journal of Geophysical Research: Atmospheres*, **118**(16), 8881-8896. doi:https://doi.org/10.1002/jgrd.50704
- Theeuwes, N. E., Steeneveld, G. J., Ronda, R. J., Heusinkveld, B. G., van Hove, L. W. A., & Holtslag, A. A. M. (2014). Seasonal dependence of the urban heat island on the street canyon aspect ratio. *Quarterly Journal of the Royal Meteorological Society*, **140**(684), 2197-2210. doi:https://doi.org/10.1002/qj.2289
- Theeuwes, N. E., Steeneveld, G. J., Ronda, R. J., & Holtslag, A. A. M. (2017). A diagnostic equation for the daily maximum urban heat island effect for cities in Northwestern Europe. *Int. J. Climatol.* **37**(1), 443-454. doi:https://doi.org/10.1002/joc.4717
- Theeuwes, N. E., Steeneveld, G. J., Ronda, R. J., Rotach, M. W., & Holtslag, A. A. M. (2015). Cool city mornings by urban heat. *Environmental Research Letters*, **10**(11), 114022. doi:10.1088/1748-9326/10/11/114022
- TMG (2005). Guidelines for heat island control measures. Bureau of the environment, Tokyo metropolitan Government.

- https://www.kankyo.metro.tokyo.lg.jp/en/about_us/videos_documents/documents_1.files/heat_island.pdf (Accessed 5 May 2020)
- Tominaga, Y., & Stathopoulos, T. (2011). CFD modeling of pollution dispersion in a street canyon: Comparison between LES and RANS. *Journal of Wind Engineering and Industrial Aerodynamics*, **99**(4), 340-348. doi:<https://doi.org/10.1016/j.jweia.2010.12.005>
- Toparlar, Y., Blocken, B., Maiheu, B., & van Heijst, G. J. F. (2017). A review on the CFD analysis of urban microclimate. *Renewable and Sustainable Energy Reviews*, **80**, 1613-1640. doi:<https://doi.org/10.1016/j.rser.2017.05.248>
- Trenberth K. E., Jones P. D., Ambenje P., Bojariu R., Easterling D., Klein Tank, A., Parker D., Rahimzadeh F., Renwick J. A., Rusticucci M., Soden B., Zhai P. 2007. Observations: Surface and Atmospheric ClimateChange. In *Climate Change 2007: The Physical Science Basis*. Contribution of Working Group I to the Fourth Assessment Report of the Intergovernmental Panel on Climate Change, Solomon S, Qin D. ,Manning M., Chen Z., Marquis M., Averyt K.B., Tignor M., Miller H.L. (eds). Cambridge University Press: Cambridge, UK and New York, NY.
- Troen, I. B., & Mahrt, L. (1986). A simple model of the atmospheric boundary layer; sensitivity to surface evaporation. *Boundary-Layer Meteorology*, **37**(1), 129-148. doi:10.1007/BF00122760
- Unger, J. (2004). Intra-urban relationship between surface geometry and urban heat island: review and new approach. *Climate Research*, **27**(3), 253-264. <https://www.int-res.com/abstracts/cr/v27/n3/p253-264/>
- Unger, J., Sümeghy, Z., Gulyás, Á., Botlyán, Z., & Mucsi, L. (2001). Land-use and meteorological aspects of the urban heat island. *Meteorol. Appl.*, **8**, 189-194. doi:<https://doi.org/10.1017/S1350482701002067>
- United Nations (2019). World urbanization prospects: The 2018 revision. Report, Department of Economic and Social Affairs, Population Division, New York. <https://population.un.org/wup/Publications/Files/WUP2018-Report.pdf>
- USGS (2021). Landsat 8 imagery. <https://glovis.usgs.gov/app> (Accessed 12 February 2021)
- van den Hurk, B., Siegmund, P., & Klein Tank, A. (eds) (2014). KNMI'14: Climate Change Scenarios for the 21st Century—A Netherlands Perspective; Royal Netherlands Meteorological Institute (KNMI). Report (KNMI WR 2014-01), De Bilt, The Netherlands. <http://bibliotheek.knmi.nl/knmipubWR/WR2014-01.pdf>
- van der Meulen, J. P., & Brandsma, T. (2008). Thermometer screen intercomparison in De Bilt (The Netherlands), Part I: Understanding the weather-dependent temperature differences). *International Journal of Climatology*, **28**(3), 371-387. doi:<https://doi.org/10.1002/joc.1531>
- van der Schrier, G., van den Besselaar, E. J. M., Klein Tank, A. M. G., & Verver, G. (2013). Monitoring European average temperature based on the E-OBS gridded data set. *Journal of Geophysical Research: Atmospheres*, **118**(11), 5120-5135. doi:<https://doi.org/10.1002/jgrd.50444>
- van der Schrier, G., van Ulden, A., & van Oldenborgh, G. J. (2011). The construction of a Central Netherlands temperature. *Clim. Past*, **7**(2), 527-542. doi:10.5194/cp-7-527-2011
- van Oldenborgh, G. J., Drijfhout, S., van Ulden, A., Haarsma, R., Sterl, A., Severijns, C., . . . Dijkstra, H. (2009). Western Europe is warming much faster than expected. *Clim. Past*, **5**(1), 1-12. doi:10.5194/cp-5-1-2009
- van Oldenborgh, G. J., & van Ulden, A. A. D. (2003). On the relationship between global warming, local warming in the Netherlands and changes in circulation in the 20th century. *International Journal of Climatology*, **23**(14), 1711-1724. doi:<https://doi.org/10.1002/joc.966>
- van Ulden, A., van Oldenborgh, G. J., & van der Schrier, G. (2009). The construction of a central Netherlands temperature. Scientific report, KNMI (WR 2009-03), De Bilt, the Netherlands, p.15. <https://www.knmi.nl/kennis-en-datacentrum/publicatie/the-construction-of-a-central-netherlands-temperature>

- van Weverberg, K., De Ridder, K., & van Rompaey, A. (2008). Modeling the Contribution of the Brussels Heat Island to a Long Temperature Time Series. *Journal of Applied Meteorology and Climatology*, **47**(4), 976-990. doi:10.1175/2007JAMC1482.1
- Vautard, R., van Aalst, M., Boucher, O., Drouin, A., Haustein, K., Kreienkamp, F., . . . Wehner, M. (2020). Human contribution to the record-breaking June and July 2019 heatwaves in Western Europe. *Environmental Research Letters*, **15**(9), 094077. doi:10.1088/1748-9326/aba3d4
- VDI (1998). Methods for the human biometeorological evaluation of climate and air quality for the urban and regional planning, Part 1: Climate. VDI Guideline 3797. Part 2. Beuth. Berlin.
- Verdonck, M. L., Demuzere, M., Hooyberghs, H., Beck, C., Cyrus, J., Schneider, A., . . . van Coillie, F. (2018). The potential of local climate zones maps as a heat stress assessment tool, supported by simulated air temperature data. *Landscape Urban Plan.*, **178**, 183-197. doi:https://doi.org/10.1016/j.landurbplan.2018.06.004
- Visser, H. (2005). The significance of climate change in the Netherlands. Report (RIVM report 550002007/2005), RIVM, Bilthoven, the Netherlands. <https://www.pbl.nl/sites/default/files/downloads/550002007.pdf>
- Vollsinger, S., Mitchell, S. J., Byrne, K. E., Novak, M. D., & Rudnicki, M. (2005). Wind tunnel measurements of crown streamlining and drag relationships for several hardwood species. *Canadian Journal of Forest Research*, **35**(5), 1238-1249. doi:10.1139/x05-051
- Wang, H., Sun, J., Fan, S., & Huang, X.-Y. (2013). Indirect Assimilation of Radar Reflectivity with WRF 3D-Var and Its Impact on Prediction of Four Summertime Convective Events. *Journal of Applied Meteorology and Climatology*, **52**(4), 889-902. doi:10.1175/jamc-d-12-0120.1
- Wang, Y., & Akbari, H. (2016). The effects of street tree planting on Urban Heat Island mitigation in Montreal. *Sustainable Cities and Society*, **27**, 122-128. doi:https://doi.org/10.1016/j.scs.2016.04.013
- Warner, T. T., Peterson, R. A., & Treadon, R. E. (1997). A Tutorial on Lateral Boundary Conditions as a Basic and Potentially Serious Limitation to Regional Numerical Weather Prediction. *Bulletin of the American Meteorological Society*, **78**(11), 2599-2618. doi:10.1175/1520-0477(1997)078<2599:ATOLBC>2.0.CO;2
- Wedi, N. P., Polichtchouk, I., Dueben, P., Anantharaj, V. G., Bauer, P., Boussetta, S., . . . Vitart, F. (2020). A Baseline for Global Weather and Climate Simulations at 1 km Resolution. *Journal of Advances in Modeling Earth Systems*, **12**(11), e2020MS002192. doi:https://doi.org/10.1029/2020MS002192
- Werner, P., & Gerstengarbe, F. (2010). Katalog der Grosswetterlagen Europas. Report (PIK-report 119), Potsdam, Germany. <http://www.pik-potsdam.de/research/publications/pikreports/.files/pr119.pdf>
- WHO (2008). Heat-health action plans, guidance. Matthies, F., Bickler, G., Cardenosa, M., Hales, S. (eds). Copenhagen, Denmark, p.45. https://www.euro.who.int/__data/assets/pdf_file/0006/95919/E91347.pdf (Accessed 23 May 2021)
- Wieberdink, G. L. (1989). Historische atlas Utrecht: chromotopografische kaart des Rijks, 1:25.000: Robas, Landsmeer, the Netherlands (in Dutch)
- Wilks, D. S. (2006). Statistical Methods in the Atmospheric Sciences (2nd ed.): Academic Press.
- Willmott, C. J. (1982). Some Comments on the Evaluation of Model Performance. *Bulletin of the American Meteorological Society*, **63**(11), 1309-1313. doi:10.1175/1520-0477(1982)063<1309:SCOTEO>2.0.CO;2
- WMO (2014). Guide to Meteorological Instruments and Methods of Observation. 2014 edition WMO-No. 8. https://library.wmo.int/doc_num.php?explnum_id=4147 (Accessed 12 March 2020)
- Wong, M. S., & Nichol, J. E. (2013). Spatial variability of frontal area index and its relationship with urban heat island intensity. *Int. J. of Remote Sensing*, **34**(3), 885-896. doi:https://doi.org/10.1080/01431161.2012.714509
- Worstell, B. B., Poppenga, S., Evans, G. A., & Prince, S. (2014). Lidar point density analysis: implications for identifying water bodies. Scientific Investigations Report (2014-5191), U.S. Geological Survey, p.19. Reston, Virginia. <http://dx.doi.org/10.3133/sir20145191>

- Wunderground (2021). Wundermap. <https://www.wunderground.com/wundermap> (Accessed 12 February 2021)
- Wyngaard, J. C. (2004). Toward Numerical Modeling in the “Terra Incognita”. *Journal of the Atmospheric Sciences*, **61**(14), 1816-1826. doi:10.1175/1520-0469(2004)061<1816:TNMITT>2.0.CO;2
- Xiao, Q., & Sun, J. (2007). Multiple-Radar Data Assimilation and Short-Range Quantitative Precipitation Forecasting of a Squall Line Observed during IHOP_2002. *Monthly Weather Review*, **135**(10), 3381-3404. doi:10.1175/MWR3471.1
- Xie, X., Huang, Z., Wang, J., & Xie, Z. (2005). The impact of solar radiation and street layout on pollutant dispersion in street canyon. *Building and Environment*, **40**(2), 201-212. doi:<https://doi.org/10.1016/j.buildenv.2004.07.013>
- Xue, M., Droegemeier, K. K., & Wong, V. (2000). The Advanced Regional Prediction System (ARPS) – A multi-scale nonhydrostatic atmospheric simulation and prediction model. Part I: Model dynamics and verification. *Meteorology and Atmospheric Physics*, **75**(3), 161-193. doi:10.1007/s007030070003
- Yan, Z., Jones, P. D., Davies, T. D., Moberg, A., Bergström, H., Camuffo, D., . . . Yang, C. (2002). Trends of Extreme Temperatures in Europe and China Based on Daily Observations. In: D. Camuffo & P. Jones (Eds.), *Improved Understanding of Past Climatic Variability from Early Daily European Instrumental Sources* (pp. 355-392). Dordrecht: Springer Netherlands. Doi:10.1007/978-94-010-0371-1_13
- Yan, Z., Li, Z., li, Q., & Jones, P. (2010). Effects of site change and urbanisation in the Beijing temperature series 1977–2006. *International Journal of Climatology*, **30**(8), 1226-1234. doi:10.1002/joc.1971
- Yang, X., Li, Y., Luo, Z., & Chan, P. W. (2017). The urban cool island phenomenon in a high-rise high-density city and its mechanisms. *International Journal of Climatology*, **37**(2), 890-904. doi:<https://doi.org/10.1002/joc.4747>
- Yuan, F., & Bauer, M. E. (2007). Comparison of impervious surface area and normalized difference vegetation index as indicators of surface urban heat island effects in Landsat imagery. *Remote Sensing of Environment*, **106**(3), 375-386. doi:<https://doi.org/10.1016/j.rse.2006.09.003>
- Zander, K. K., Botzen, W. J. W., Oppermann, E., Kjellstrom, T., & Garnett, S. T. (2015). Heat stress causes substantial labour productivity loss in Australia. *Nature Climate Change*, **5**(7), 647-651. doi:10.1038/nclimate2623
- Zanobetti, A., & Schwartz, J. (2008). Temperature and mortality in nine US cities. *Epidemiology (Cambridge, Mass.)*, **19**(4), 563-570. doi:10.1097/EDE.0b013e31816d652d
- Zhang, L., Zhan, Q., & Lan, Y. (2018). Effects of the tree distribution and species on outdoor environment conditions in a hot summer and cold winter zone: A case study in Wuhan residential quarters. *Build. Environ.*, **130**, 27-39. doi:<https://doi.org/10.1016/j.buildenv.2017.12.014>
- Zhang, X., Steeneveld, G. J., Zhou, D., Ronda, R. J., Duan, C., Koopmans, S., & Holtslag, A. A. M. (2020). Modelling urban meteorology with increasing refinements for the complex morphology of a typical Chinese city (Xi'an). *Building and Environment*, **182**, 107109. doi:<https://doi.org/10.1016/j.buildenv.2020.107109>
- Zhou, B., Lauwaet, D., Hooyberghs, H., De Ridder, K., Kropp, J. P., & Rybski, D. (2016). Assessing Seasonality in the Surface Urban Heat Island of London. *Journal of Applied Meteorology and Climatology*, **55**(3), 493-505. doi:10.1175/JAMC-D-15-0041.1
- Zhou, B., Rybski, D., & Kropp, J. P. (2013). On the statistics of urban heat island intensity. *Geophysical Research Letters*, **40**(20), 5486-5491. doi:<https://doi.org/10.1002/2013GL057320>
- Zhou, Y., Li, D., & Li, X. (2019). The Effects of Surface Heterogeneity Scale on the Flux Imbalance under Free Convection. *Journal of Geophysical Research: Atmospheres*, **124**(15), 8424-8448. doi:10.1029/2018jd029550

Authorship Statement

- AK = (Prof.) A.M.G (Albert) Klein Tank (KNMI/ WUR / Met Office Hadley Centre (current affiliation))
- BHe = (Dr) B.G. (Bert) Heusinkveld (WUR)
- BHo = (Prof.) A.A.M (Bert) Holtslag (WUR)
- GS = (Dr) G.J. (Gert-Jan) Steeneveld (WUR)
- NT = (Dr) N. (Natalie) Theeuwes (WUR / KNMI (current affiliation))
- RH = (Dr) R. (Ronald) van Haren (SURFSARA/ RWS (current affiliation))
- RR = (Dr) R.J. (Reinder) Ronda (KNMI / WUR (current affiliation))
- RU = (Prof.) R. (Remko) Uijlenhoet (WUR / TU Delft (current affiliation))
- SK = (PhD candidate) S. (Sytske) Koopmans (WUR)

Chapters 1, 6 and 7 have been solely written by SK, with the inclusion of comments of GS and BHo.

The model set-up and model analysis and of Chapter 2 was performed by SK with input of GS and NT. The article was drafted by SK and revised by GS, NT, and BHo, and approved by all authors. SK and GS answered and revised the comments in the peer review process.

The applicants of the project proposal of Chapter 3 consisted of GS, RR and BHo and GS shaped the experimental set-up. NT, SK and RH did the research set-up. RH developed the modelling infrastructure and monitored the simulations. NT and SK did the analysis. NT wrote the initial outline and SK finished the writing of the drafted chapter. The chapter was revised by GS, NT, RH, RU and BHo, and approved by all authors.

The research plan of Chapter 4 has been shaped by GS and AK and further elaborated including SK and RR. The geographical data was retrieved by SK and RR. The model set-up, computations and analysis was conducted by SK. The article was drafted by SK and revised by RR, AK, GS and BHo.

The research plan of Chapter 5 was shaped by BHe, SK and GS (and many others including RR which have been acknowledged). The geographical data was retrieved by SK. The model was set up by SK and BHe. The validation data was provided by BHe and the verification was executed by SK. The analysis was performed by SK. The article was drafted by SK and revised by BHe and GS, and approved by all authors.

Dankwoord / Acknowledgements

De afgelopen vier en een half jaar heb ik met veel plezier onderzoek mogen doen aan stadsklimaat op de Meteorologie en Luchtkwaliteit vakgroep. Ik kijk tevreden terug op het promotietraject. Op het moment dat het wat moeilijker werd toen we massaal moesten thuiswerken, was ik gelukkig op het punt dat verreweg het meeste onderzoek achter me lag. Ik heb daarna de tijd genomen om te schrijven en vertrouwen gehad dat het proefschrift er zou komen.

Allereerst wil ik Gert-Jan bedanken. In eerste instantie was de looptijd van mijn aanstelling nog niet voldoende voor een promotietraject. We maakten een plan en konden nieuwe projecten aantrekken, zodat een promotie mogelijk werd. Je hebt altijd veel vertrouwen in mij gehad, en dat waardeer ik. Daarnaast stond je altijd voor me klaar, heb je me goed geholpen met het schrijfsproces en waardeer ik de inhoudelijke discussies.

Daarnaast wil ik Bert Holtslag ook bedanken voor de tijd op de vakgroep die hij mij heeft geboden om te kunnen promoveren. Bedankt voor het meedenken en de nuttige bijdragen in het ERA-urban project, en natuurlijk jouw feedback aan de synthese van het proefschrift. Ik ben je dankbaar voor het helpen van prioriteiten stellen, toen ik schrok dat ik wel 8 hoofdstukken kon schrijven door de losse projecten, maar daar logischerwijs geen tijd meer voor had. Jordi, veel hebben we niet met elkaar te maken gehad, maar respect hoe jij de vakgroep hebt geleid gedurende het thuiswerken en het vertrouwen wat je in me hebt gehad in het laatste jaar. De administratieve staff, Marina, Sandra, Caroline en Kees wil ik bedanken voor hun vlotte medewerking op diverse zaken.

Bedankt Ronald voor het samen puzzelen naar werkbare data-assimilatie instellingen. Het moet soms best lastig geweest zijn om met een onderzoeker samen te werken die niet snel tevreden is. Reinder bedankt voor de fijne samenwerking in het schrijven van Nederlandse rapporten, je hebt de gave ook goed te kunnen schrijven voor ministeries. Ook bedankt voor de bijdrage aan de wetenschappelijke hoofdstukken/publicaties en de ondersteuning op het IT en computervlak. Natalie, bedankt voor het inwerken toen ik begon op de vakgroep aan mijn eerste project en de ondersteuning tot het indienen van de publicatie. Mijn proefschrift is in veel opzichten een vervolg op jouw PhD en werk op MAQ. Wellicht hebben we meteorologisch veel overlappende interesses, en ook je werk wat je toelichtte tijdens mijn bezoek in Reading vond ik inspirerend. Tenslotte, Albert bedankt voor onze samenwerking en je input voor o.a. klimaatscenario's, en Remko bedankt voor jouw advies en revisies in het ERA-urban project.

I would like to thank all members of the urban group. Aris thank you for the raised sharp questions during the urban meetings and discussions. I appreciate open you are for my and others research. Bert Heusinkveld, thank you for the good collaboration in the urban heat map project. It was a very interesting project and I enjoyed working with you. In addition, I like the nice conversations about cycling, holidays and the weather. Arjan, also thank you for the nice and fun breaks and I like your humor. Content-wise, I appreciate the lunch walks where I could clear my mind by dropping different ideas or occasionally complaints. Celia (Xi), thanks for the fine cooperation and for involving me in your interesting research. Iris thanks for being a helpful roommate in the first years of my PhD by supporting me with the radar data and programming code. I also like to thank my former office mates Ruben, Sjoerd, Auke (including forementioned Aris and Arjan) for the fun chats between our work.

Also, I would like to thank João and Sanda from the LAR group for the collaboration of the GreenQuays project on the microclimate restructuring in Breda. I got new insights from a different group and learned acquisition skills. Lee, thank you for your hospitality in England and I enjoyed the useful trip to the north to Lancaster. Joan and Sarah, thanks for involving me in the DARE community and the interesting workshop about data assimilation. Finally, I want to acknowledge the nice collaboration in different projects with the municipality of Breda, the municipality of The Hague, Ton de Nijs as project leader of the climate stress tests program from the RIVM, Climate Adaptation Services and the KNMI Datalab.

Tenslotte wil ik een aantal mensen bedanken buiten het vakgebied. Bedankt Herman, voor je interesse en discussies over mijn onderzoek en de leuke dingen die we gedaan hebben in Zweden en hier. Gino bedankt voor jou optimisme, humor en de leuke afleiding van het PhD werk. In zijn algemeenheid wil ik de mensen van tafeltennisvereniging Shot bedanken voor de gezelligheid en soms ook nuttige gesprekken des levens. Tenslotte, wil ik ouders en mijn broer en bedanken. Jan en Tjitske bedankt voor het meedenken aan de vormgeving van het proefschrift en jullie geduld en support de afgelopen jaren. Douwe bedankt voor je gastvrijheid en de tijd die je vaak voor mij hebt.

List of Publications

Peer reviewed Journal publications:

Zhang, X., Steeneveld, G. J., Zhou, D., Ronda, R. J., Duan, C., **Koopmans, S.**, & Holtslag, A. A. M. (2020). Modelling urban meteorology with increasing refinements for the complex morphology of a typical Chinese city (Xi'an), *Building and Environment*, **182**, 107109. <https://doi.org/10.1016/j.buildenv.2020.107109>

Koopmans, S., Heusinkveld, B. G., & Steeneveld, G. J. (2020). A standardized Physical Equivalent Temperature urban heat map at 1-m spatial resolution to facilitate climate stress tests in the Netherlands, *Building and Environment*, **181**, 106984. <https://doi.org/10.1016/j.buildenv.2020.106984>

Koopmans, S., Ronda, R. J., Steeneveld, G. J., Holtslag, A. A. M., & Klein Tank, A. M. G. (2018). Quantifying the effect of different urban planning strategies on heat stress for current and future climates in the agglomeration of The Hague (The Netherlands), *Atmosphere*, **9**(9), 353. doi:10.3390/atmos9090353

Steeneveld, G. J., Klompmaker, J. O., Groen, R. J. A., **Koopmans, S.**, & Holtslag, A. A. M. (2018). An urban climate assessment and management tool for combined heat and air quality judgements at neighbourhood scales. *Resources, Conservation and Recycling*, **132**, 204-217. doi:<https://doi.org/10.1016/j.resconrec.2016.12.002>

Koopmans, S., Theeuwes, N. E., Steeneveld, G. J., & Holtslag, A. A. M. (2015). Modelling the influence of urbanization on the 20th century temperature record of weather station De Bilt (The Netherlands). *International Journal of Climatology*, **35**(8), 1732-1748. doi:<https://doi.org/10.1002/joc.4087>

Steeneveld, G. J., **Koopmans, S.**, & Theeuwes, N. E. (2014). Refreshing the role of open water surfaces on mitigating the maximum urban heat island effect. *Landsc. Urban Plan.*, **121**, 92-96. doi:<https://doi.org/10.1080/00038628.2015.1105195>

Steeneveld, G. J., **Koopmans, S.**, Heusinkveld, B. G., van Hove, L. W. A., & Holtslag, A. A. M. (2011). Quantifying urban heat island effects and human comfort for cities of variable size and urban morphology in the Netherlands. *Journal of Geophysical Research: Atmospheres*, **116**(D20). doi:<https://doi.org/10.1029/2011JD015988>



*Netherlands Research School for the
Socio-Economic and Natural Sciences of the Environment*

D I P L O M A

for specialised PhD training

The Netherlands research school for the
Socio-Economic and Natural Sciences of the Environment
(SENSE) declares that

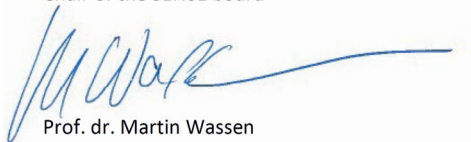
Sytse Koopmans

born on 27 March 1988 in Sneek, The Netherlands

has successfully fulfilled all requirements of the
educational PhD programme of SENSE.

Wageningen, 14 September 2021

Chair of the SENSE board



Prof. dr. Martin Wassen

The SENSE Director



Prof. Philipp Pattberg

The SENSE Research School has been accredited by the Royal Netherlands Academy of Arts and Sciences (KNAW)



K O N I N K L I J K E N E D E R L A N D S E
A K A D E M I E V A N W E T E N S C H A P P E N



The SENSE Research School declares that **Sytse Koopmans** has successfully fulfilled all requirements of the educational PhD programme of SENSE with a work load of 30.3 EC, including the following activities:

SENSE PhD Courses

- o Environmental research in context (2021)
- o Research in context activity: 'Two popular scientific articles and a co-presentation with a consultancy on a fair event' (2019-2021)

Other PhD and Advanced MSc Courses

- o Adaguc workshop, KNMI (2017)
- o DARE workshop, University of Reading (2017)
- o Brain friendly working and writing, Wageningen Graduate Schools (2019)
- o Presenter Course & workshop creating heat maps for consultancy, Wageningen University (2020)
- o Network training, Wageningen University (2021)

Management and Didactic Skills Training

- o Supervising MSc student with thesis entitled 'An assessment of the Dutch temperature 1 record using WRF infrastructure' (2017)
- o Supervising MSc student with internship (2017)
- o Teaching in the MSc course 'Urban Hydrometeorology' (2017-2019)
- o Teaching in the BSc course 'Meteorology and Climate' (2018)

Oral Presentations

- o *Using data assimilation in WRF to model the urban climate of Amsterdam.* EMS , 4-8 September 2017, Dublin, Ireland
- o **Invited talk:** *Using data assimilation to model the urban climate of Amsterdam.* DARE, Henley-on-Thames, UK
- o *Using weather radar observations for data assimilation to model the Amsterdam urban climate.* ERAD, 2-6 July 2018, Ede, The Netherlands
- o *Data assimilation of urban weather observations in WRF to model the urban climate of Amsterdam.* ISSR, 17-19 July 2018, Bonn, Germany
- o *Quantifying the effect of different urban planning strategies on heat stress in current and future climates in the Netherlands,* EMS, 3-7 September 2018, Budapest, Hungary
- o *Standardization urban heat maps of Physiological Equivalent Temperature.* EGU, 7-12 April 2019, Vienna, Austria

SENSE coordinator PhD education

Dr. ir. Peter Vermeulen

This research received funding from The Netherlands Organisation for Scientific Research (NWO) grant 'The Windy City' 864.14.007 and NWO-eScience project 'ERA-urban' 027.014.203.

This research received funding from the (Dutch) Ministry of Infrastructure and Water management.

This research received funding from UK EPSRC Senior Fellowship in Digital Technology for Living with Environmental Change, Data Assimilation for the Resilient City (DARE).

This research received funding from EU UIA project GreenQuays.

Financial support from Wageningen University for printing this thesis is gratefully acknowledged.

The reference stations of the Amsterdam Atmospheric Monitoring Supersite have been financially supported by the Amsterdam Institute for Advanced Metropolitan Solutions (AMS).

Cover design by Sytse Koopmans

Thesis Printed by ProefschriftMaken

